Dissertation
submitted to the
Combined Faculty of Mathematics, Engineering and Natural Sciences
of Heidelberg University, Germany
for the degree of
Doctor of Natural Sciences

Put forward by
Eric Rohr
born in: Richmond, Virginia, the United States of America
Oral examination: 28.11.2024

Jellyfish Galaxies and the Multiphase Nature of Gas Around Galaxies

Referees: Dr. Annalisa Pillepich

Prof. Dr. Cornelis Dullemond

Abstract

Gas is everywhere throughout the Universe, from the gas between galaxies, the intergalactic medium (IGM), to the gas surrounding a galaxy, the circumgalactic medium (CGM), to the gas within a galaxy, the interstellar medium (ISM). According to the standard paradigm, galaxies form at the centers of dark matter halos out of gas that cools from the otherwise hot gaseous atmospheres around them. In turn, the latter are influenced by accreting material from the IGM, by outflowing gas due to feedback, and by infalling satellite galaxies.

In this thesis, I investigate the complex relationship between satellite galaxies and the multiphase host halo gas using the cosmological magneto-hydrodynamical simulations TNG-Cluster and TNG50, the highest-resolution simulation from the IllustrisTNG suite. These simulations provide an unparalleled combination of resolution and sample size, coupled with a well-validated galaxy formation model, enabling several novel insights.

First, in TNG-Cluster, I affirm that massive cluster satellites, with masses similar to or larger than the Milky Way, are capable of retaining their own hot, X-ray-emitting gaseous atmospheres. These atmospheres should be statistically detectable with current and upcoming X-ray surveys and instruments. In contrast, for less massive satellites in smaller groups and clusters, I demonstrate that the ram pressure tails observed in TNG50 "jellyfish" galaxies originate from the satellite's interstellar medium. As this cool, metal-enriched gas is stripped from the jellyfish galaxies, it is deposited into the host halo. Consequently, satellites contribute more cool gas to galaxy groups and clusters than is present in them today.

Furthermore, I demonstrate that across cosmic time, the mass of the cool intracluster medium in cluster progenitors correlates with the number of gaseous satellites, affirming that satellites are a legitimate source of cool halo gas, according to TNG. Moreover, I illustrate the complex evolution of the cool intracluster medium, considering interconnected processes such as gas accretion from the intergalactic medium, gas heating and cooling, satellite stripping, star formation, and, most importantly, feedback from the central supermassive black hole. In TNG-Cluster, the total mass of the cool-phase intracluster medium unambiguously decreases since $z \approx 2-4$, over the past $\approx 10-12$ billion years, just after the onset of strong, kinetic-mode feedback from the central supermassive black hole.

These novel results challenge long-standing ideas about the evolution of both satellite and central galaxies, offering fresh insights into the role of environmental effects and feedback processes. I propose specific observational tests to validate these simulation predictions, providing a clear path for future empirical investigations. Comparing these simulation outcomes with data from current and upcoming surveys will sharpen our understanding of galaxy formation and evolution, ultimately guiding the development of more sophisticated galaxy formation models for next-generation cosmological simulations.

Zusammenfassung

Gas ist überall im Universum vorhanden, vom Gas zwischen den Galaxien, dem intergalaktischen Medium (IGM), über das Gas, das eine Galaxie umgibt, dem zirkumgalaktischen Medium (CGM), bis hin zum Gas innerhalb einer Galaxie, dem interstellaren Medium (ISM). Nach dem Standardparadigma bilden sich Galaxien, in den Zentren von Halos aus dunkler Materie, aus Gas, das sich von den ansonsten heißen Gasatmosphären um sie herum abkühlt. Letztere werden wiederum durch akkretierendes Material aus dem IGM, ausströmendes Gas aufgrund von Rückkopplungen und einfallende Satellitengalaxien beeinflusst.

In dieser Arbeit untersuche ich die komplexe Beziehung zwischen Satellitengalaxien und dem mehrphasigen Gas des Wirtshalos mithilfe der kosmologischen magneto-hydrodynamischen Simulationen TNG-Cluster und TNG50, der hochauflösendsten Simulation aus der IllustrisTNG-Suite. Diese Simulationen bieten eine beispiellose Kombination aus Auflösung und Stichprobengröße, gekoppelt mit einem gut validierten Galaxienentstehungsmodell, das mehrere neue Erkenntnisse ermöglicht.

Erstens zeige ich, dass in massereiche Haufensatelliten in TNG-Cluster, die eine ähnliche oder größere Masse als die Milchstraße haben, in der Lage sind, ihre eigenen heißen, Röntgenstrahlen emittierenden Gasatmosphären zu behalten. Diese Atmosphären sollten mit aktuellen und zukünftigen Röntgendurchmusterungen und Instrumenten statistisch nachweisbar sein. Im Gegensatz dazu zeige ich für weniger massereiche Satelliten in kleineren Gruppen und Haufen, dass die in TNG50-Quallengalaxien beobachteten Staudruckschweife aus dem interstellaren Medium der Satelliten stammen. Wenn dieses kühle, metallangereicherte Gas aus den Quallengalaxien entfernt wird, lagert es sich im Wirtshalo ab. Folglich tragen die Satelliten mehr kühles Gas zu den Galaxiengruppen und -haufen bei, als heute in ihnen vorhanden ist.

Zweitens zeige ich, dass über die kosmische Zeit hinweg die Masse des kühlen Intraclustermediums in den Vorläufern von Sternhaufen mit der Anzahl der Gassatelliten korreliert, was bestätigt, dass Satelliten gemäß TNG eine legitime Quelle für kühles Halo-Gas sind. Darüber hinaus veranschauliche ich die komplexe Entwicklung des kühlen Haufenmediums, indem ich miteinander verbundene Prozesse wie Gasakkretion aus dem intergalaktischen Medium, Gaserwärmung und -abkühlung, Satellitenstripping, Sternentstehung und vor allem die Rückkopplung durch das zentrale supermassereiche Schwarze Loch berücksichtige. In TNG-Cluster nimmt die Gesamtmasse des Intraclustermediums in der kühlen Phase seit $z \approx 2 - 4$ eindeutig ab, und zwar über die letzten $\approx 10 - 12$ Milliarden Jahre, unmittelbar nach dem Beginn der starken kinetischen Rückkopplung durch das zentrale supermassereiche Schwarze Loch.

Diese neuen Ergebnisse stellen langjährige Vorstellungen über die Entwicklung von Satelliten- und Zentralgalaxien in Frage und bieten neue Erkenntnisse über die Rolle von Umwelteinflüs-

sen und Rückkopplungsprozessen. Ich schlage spezifische Beobachtungstests vor, um diese Simulationsvorhersagen zu validieren und einen klaren Weg für zukünftige empirische Untersuchungen aufzuzeigen. Der Vergleich dieser Simulationsergebnisse mit Daten aus aktuellen und zukünftigen Durchmusterungen wird unser Verständnis von Galaxienentstehung und -entwicklung schärfen und letztlich die Entwicklung anspruchsvollerer Galaxienentstehungsmodelle für kosmologische Simulationen der nächsten Generation anleiten.

Acknowledgements

The feeling of having completed my Ph.D. thesis is indescribable, and there is no way that I could have done this by myself. There are too many people that I would like to thank for their guidance, support, and love over the past four years, from the lockdown during the pandemic to helping me with the final edits of this thesis.

Annalisa, you have been better than the best supervisor I could have imagined. You have taught me so much about simulations, galaxy evolution, and, most importantly, how to be an amazing scientist. You are truly a role model. When I present my work at other institutes or at conferences, I beam with confidence because I know that you support me and my work. I cannot imagine a Ph.D. without you as my supervisor, and I feel so prepared for whatever comes next, all thanks to you.

Dylan, thank you so much for all of your help over the past four years as my unofficial second supervisor. It cannot be stated how much you have helped not only me, but the entire community, with the documentation and example scripts to access and use the Illustris and IllustrisTNG data. You have provided me with excellent scientific advice on all three of my papers, and if it were not for your technical assistance, I would not have developed as much as a researcher. Thank you again, also for being my primary supervisor during Annalisa's parental leave.

Thanks as well to the other sources of guidance and advice during my PhD, namely to Ralf Klessen, as your input during the thesis committee meetings and Imladris meetings has been invaluable, in addition to your support for my post-doc to continue developing my own simulations, and to Hans-Walter Rix, who has met with me regarding each of my research projects and always supported my activities, both research and non-research realted. I would also like to thank all additional coauthors on my PhD papers – Reza, Elad, Gandhali, and Céline – and the first authors of papers on which I am a coauthor – Elad, Junia, Reza, Katrin, and Dylan. And to everyone else that has supported me professionally over the past years – Matthew, Morgan, Iva, Mila, Chris, Christian, Shane, Mark, Robert, Andrew, and Brett – thank you.

I also want to thank everyone that has given me feedback on the thesis: Annalisa, Evert, Nico, Horst, Hans-Walter, Reza, and Lukas. The thesis would not be what it is now without your help. I also want to thank Kees Dullemond for agreeing to be the second referee, in addition to Anna Pasquali and Luca Amendola for being the other examination committee members.

More personally, I would not be where I am today without the friends and family that have supported and motivated me along the way. There are way too many people to name here individually, but thank you to the GC theory group members, the MPIA family, everyone

from my IMPRS generation, my Heidelberg friends outside of astronomy that have kept me sane over the past years, my continued friends from UVa, from astronomy, Wertland/Shannon, and the volleyball team, and especially to the friends from Atlee and Aschreek that have been with me since the beginning.

An die Paula, ich weiß nicht, wie ich es ohne dich geschafft hätte, die Arbeit zu beenden. Du warst immer da und hast mich irgendwie stabil gehalten, egal wie schwierig oder stressig die Zeiten waren. Ich kann dir nicht genug dafür danken, dass du immer für mich da warst, und für alles, das du mir beigebracht hast. Danke für deine Liebe und Unterstützung.

Lastly, I would like to thank my family for everything they have done for me, and I know that you would have done so much had I let you. You have always been there and supported me and my decisions, even if you did not always understand why I did what I did. Mom and Dad, I am so grateful to have parents like you, and I cannot thank you enough for all of your love and support. Matthew, thanks for being my best friend for twenty-six years and always being there, both when I needed you and when I just wanted to have a nice zoom sesh. And of course I need to thank Entei, who was there for me during the worst part of my life and has only ever shown me love and excitement. I love you all so much very, and I cannot wait to see what comes next.

Contents

I. Introduction

1 Personal Motivation to Study Astronomy

Astronomy is the systematic, scientific search for answers to some of the most asked and most important questions in human history. Where did we come from? Are we special? Are there other places like ours? What will happen to us in the future? By "we", I mean the collective humanity since the dawn of civilization. Astronomy is perhaps the oldest science, where ancient cultures around the globe studied the motions of the stars and planets, trying to understand how it all makes sense, and how we fit into it all. It is really such a privilege to have been able to study astronomy as my main profession over the past few years.

It all started for me when I was 12 years old watching TED talks about space exploration that I fell in love with physics and astronomy. In Brian Cox's talk "Why We Need the Explorers?", he shows an image of the Earthrise, taken by Apollo 8 in 1968 as it was on the backside of the Moon (Fig. 1.1 left). Here, for the first time, we recognized that the Earth is merely a "small, fragile-looking world just hanging against the blackness of space", which motivated an entire generation to pursue innovation and even sparked the start of the environmental movement. Cox later returns to the symbolism of Earth's fragility with the Pale Blue Dot[1], taken in 1990 by the Voyager 1 spacecraft from about six billion kilometers away, which remains the most distant image of our home ever taken (Fig. 1.1 right). This image, the accompanying description from Carl Sagan, and the enthusiasm emanating from Cox as he explained why it is necessary to continue curiosity-driven pursuits inspired me join the movement. I decided to spend my free time learning as much as about physics and astronomy as possible, where cosmology ultimately caught my attention. I wanted to understand how the Universe works on the largest scales.

To understand the how the Universe looks and behaves on the largest scales, I chose to study galaxies. Galaxies are the building blocks of the Universe, and they are everywhere. The Hubble Deep Field, which is a composition of 342 individual images taken over 10 days in 1995 for a final exposure time of $\sim$ 100 hours, revealed $\approx$ 3000 galaxies in what was a seemingly dark, empty patch in the Northern sky (Fig. 1.2). The location was specifically chosen to be devoid of nearby galaxies and foreground stars from the Milky-Way. Everything we can see

[1] https://science.nasa.gov/mission/voyager/voyager-1s-pale-blue-dot/

Figure 1.1: **Earthrise from Apollo 8 and the Pale Blue Dot from Voyager 1.** Here are two of the most inspiring photographs ever taken from the Earth. On the left, the Earthrise as viewed from the back side of the Moon, showed for the first time the fragility of the Earth. On the right, the Pale Blue Dot as viewed from ≈ 6 billion kilometers away only amplifies this motif. These two images were used in Brian Cox's TED talk "Why We Need the Explorers", which ultimately inspired me to pursue astronomy. Images adapted from: NASA (left), NASA/JPL-Caltech (right).

in this image is another galaxy, is another collection of millions to billions of stars. Some of them are billions of light years away from Earth. When looking in different direction towards a different patch of dark sky in the southern sky, a similar image of thousands of galaxies emerged. The first location was not lucky or somehow special; the Universe looks similar in different directions (the Universe is isotropic), at least on large scales.

This brings me to the most fundamental concept in modern cosmology: the cosmological principle. The cosmological principle states:

> Viewed on sufficiently large scales, the properties of the Universe are the same for all observers. – *William Keel, 2007*

This formalism follows from the paradigm shift which began during the Copernican revolution: the Earth is not the center of the Universe but rather orbits around a common star, which is embedded in a common galaxy in an average place in the Universe. On large scales $\gtrsim$ 100 Mpc, the cosmological principle seems to hold very well; however, on smaller scales, there are clearly anisotropies and inhomogeneities, such as the mere existence of galaxies. While the two Hubble Deep Fields do not directly motivate the cosmological principle, they still suggest that the Universe is statistically similar in multiple directions. In essence, the Universe is homogeneous and isotropic on large scales, where a sufficiently large section of the

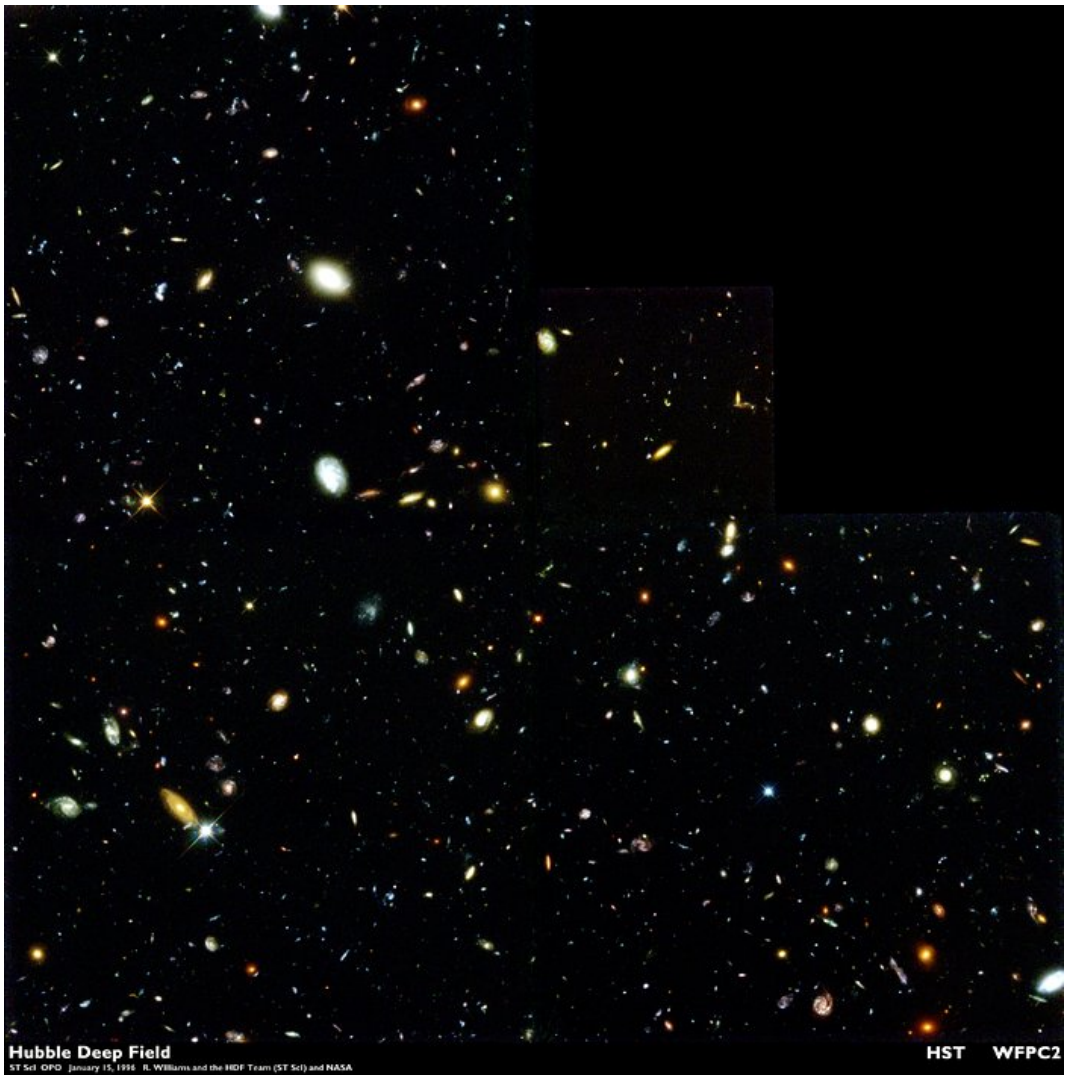

Figure 1.2: **The Hubble Deep Field.** When looking long enough at a seemingly dark patch of sky, it illuminates with thousands of galaxies. And this is true when looking in all directions, at all observable patches of the sky. The deeper one looks, the more galaxies one finds. Image credit: Robert Williams and the Hubble Deep Field Team (STScI) and NASA/ESA.

Universe can represent the entire observable Universe. Studying a portion of the Universe is equivalent to studying any other portion or even the entire Universe. The laws of physics are the same in all locations, at least to the best of our knowledge. However, the inhomogeneities are what make the Universe interesting. Every galaxy in the HDFs is a beautiful smudge on an otherwise uniform backdrop. These perturbations to the norm is where the real magic happens.

Astronomy is in essence just as philosophical as it is scientific. The scientific results hold philosophical implications. I personally find the same spiritual fulfillment learning about the structure of the Universe as many others may find, for example, in religion. When I feel overwhelmed and struggle with my daily life, I remember that the Universe does not care about my problems. This can be quite unsettling for some, but this humbling fact keeps me calm. The vastness and complexity of space comfort me.

1.1 Why study the cosmic gas

The earliest snapshot of the Universe comes from the cosmic microwave background (CMB). This faint microwave glow comes from the Big Bang, and its intensity is almost identical in every direction. The beauty of the CMB does not, however, come from the fact that it is nearly uniform in all direction but instead from the small scale perturbations, which are on the order of $\sim 10^{-5}$. The statistical properties of these small perturbations both encode the composition of and determine the fate of the Universe. Perhaps surprisingly, only $\approx 4\%$ of the total mass/energy of the Universe today comes from baryons, the normal everyday matter that makes up galaxies, black holes, and this thesis itself. The other 96% comes from dark matter and dark energy with minor contributions from photons and neutrinos.

At the time of the CMB, the entirety of the baryon budget consisted of primordial gas: Hydrogen and Helium with trace amounts of Lithium. The CMB perturbations of slightly over- or under-intensity translate to over or under-densities in the underlying distribution of gas. These overdensities would eventually collapse to form the galaxies we see today (Fig. 1.2). However, when summing all the galaxies in the Hubble Deep Fields, namely their stars which emit a majority of the optical light, in addition to all other galaxies observed with every other instrument, only a fraction of the expected total baryon mass emerges. When extrapolating the number and mass of all the stars in the visible Universe, the total mass is $\lesssim 15\%$, likely closer to $\approx 7\%$, of the total baryon mass (Fukugita et al., 1998). Where are the rest of the baryons? The answer lies in the gas that exists in, around, and between galaxies, which while universally expected has been difficult to observe due to its low surface brightness. With recent advancements in integral field spectroscopy, astronomers began observing that gaseous

reservoirs, which extend far beyond the stellar bodies of galaxies, illuminate. This is currently very time-intensive and can only be performed for individual objects, but future surveys will map out of the rest of the gas in, around, and between the galaxies.

The standard theory of galaxy formation states that primordial gas falls into spherical halos made of dark matter, forming a hot gaseous atmosphere. Some of this gas cools and falls towards the center of the halo and eventually forms the first stars. Gas is the fuel for star formation, for galaxy formation and evolution. The metals that form from nuclear fusion in stars and from their deaths as supernovae enrich the surrounding gas, facilitating further cooling and star formation. Supermassive black holes (SMBHs), which mostly inhabit galactic centers, form as the ultimate byproducts of gas collapse followed by gas accretion. All the stars, metals, and SMBHs that populate galaxies today formed out of primordial Hydrogen and Helium. SMBHs grow mainly by accreting galactic gas, called the interstellar medium (ISM). As the ISM fuels both the SMBHs and star formation, the gas surrounding the galaxy, called the circumgalactic medium (CGM), can cool and rain down onto the galaxy itself, replenishing the ISM. At even larger scales, the gravity of the galaxy and its dark matter halo pulls gas from outside the halo, called the intergalactic medium (IGM), into the CGM. At the same time, feedback from stars and SMBHs can heat up and blow out the ISM into the CGM, or even out into the IGM. This exchange of baryonic material across phases and spatial locations is called the "Cosmic Baryon Cycle" (Fig. 1.3; see also Tumlinson et al. 2017; Péroux & Howk 2020; Donahue & Voit 2022; Faucher-Giguère & Oh 2023 for recent reviews of the CGM and cosmic baryon cycle). This cycle is further complicated by the presence of multiple galaxies: what happens when two galaxies, each with their own CGM and baryon cycles, interact with each other? What happens when one galaxy is tens to hundreds of times more massive than the other? What about when one massive galaxy hosts hundreds of smaller ones? How does the CGM of the host galaxy effect the smaller, satellite galaxies, and how do the satellite galaxies, in turn, affect the host CGM? These are the main questions motivating this thesis. Using state-of-the-art cosmological simulations of galaxy formation and evolution, I will answer them.

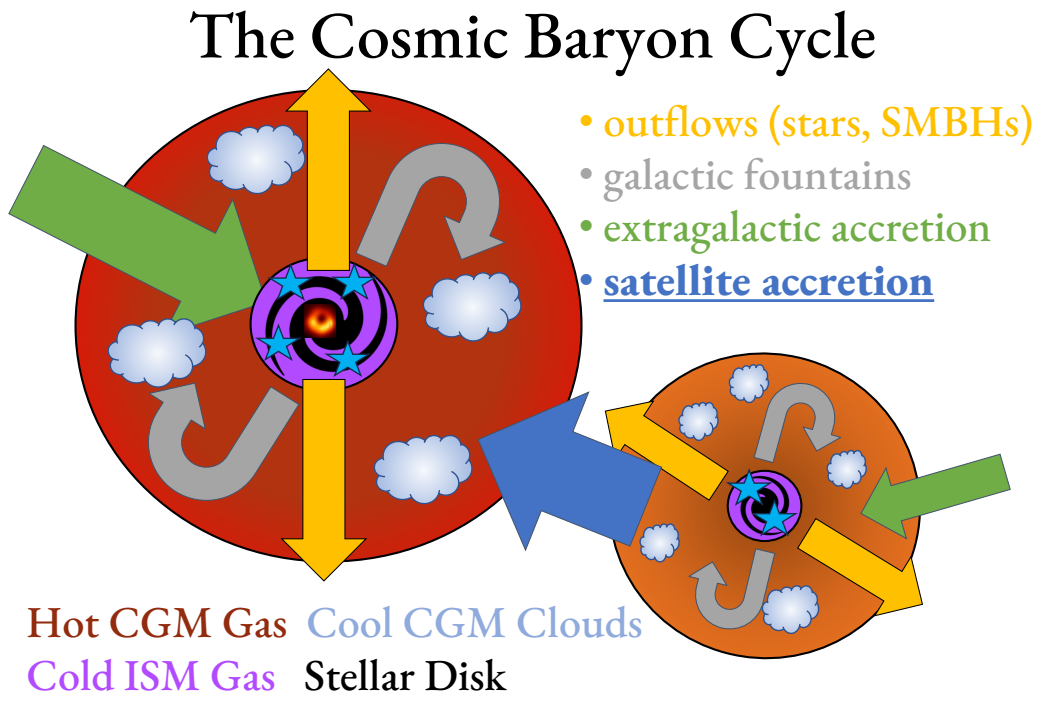

Figure 1.3: **The Cosmic Baryon Cycle.** The gas in (interstellar medium; ISM) and around (circumgalactic medium; CGM) galaxies can change phase and spatial locations due to, for example, outflows caused by stellar and supermassive black hole (SMBH) feedback, galactic fountains, extragalactic accretion, and satellite accretion of the smaller galaxy on the right into the larger galaxy on the left. The effects of the CGM from the massive galaxy on the satellite and vice versa is the main topic of this thesis. I also note the following concepts which I return to later: the average temperature of the hot CGM is higher in the larger galaxy, denoted by the redder color; the smaller galaxy has a larger fraction of its CGM in the cool phase (more light blue clouds); and the larger galaxy has both stellar and SMBH feedback shown, while the smaller galaxy has only stellar feedback. Image credit for the SMBH: Event Horizon Telescope Collaboration. Inspired by schematics from Dylan Nelson and Daniel Anglés-Alcázar.

2 Fundamental Concepts in a ΛCDM Universe

2.1 Observational evidence for a ΛCDM universe

Roughly one century ago, the world's leading astronomers debated the nature of the Andromeda nebula, trying to decide if belonged to our Milky Way or if it was its own "island universe", what later became known as a galaxy. Within the same decade of learning that other galaxies do in fact exist, the astronomers noticed something peculiar about these other galaxies: they are all moving away from Earth. Using Cepheid variable stars – variable stars with a known period-luminosity relationship Leavitt & Pickering (1912) – to measure their distances, it became clear that the farther away galaxies are, the faster they recede, called the Hubble-Lemaître law (Lemaître, 1927; Hubble, 1929):

$$v = H_0 d \tag{2.1}$$

where v is the recession velocity, d is the distances to the galaxy, and H_0 is the Hubble constant. The Universe is expanding. This discovery is the basis for modern cosmology. The Universe's expansion was consistent with the at-the-time recent formulation of general relativity,

$$G_{\mu\nu} + \Lambda g_{\mu\nu} = \kappa T_{\mu\nu} \tag{2.2}$$

where $G_{\mu\nu}$ is the Einstein tensor, $g_{\mu\nu}$ is the metric tensor, $T_{\mu\nu}$ is the stress-energy tensor, $\kappa = 8\pi G/c^4$ is the Einstein gravitational constant, where G and c are the Newtonian gravitational constant and speed of light, respectively, and Λ is the cosmological constant, which acts as a negative mass or energy of empty space to counteract the Universe contracting due to the gravitational attraction (Einstein, 1916). Specifically, an expanding homogeneous and isotropic Universe (at least on large scales) obeys the the Friedmann–Lemaître–Robertson–Walker metric

$$\mathrm{d}s^2 = \mathrm{d}t^2 - \frac{a(t)^2}{c^2}\left(\frac{\mathrm{d}r^2}{1-kr^2} + r^2 \mathrm{d}\Omega^2\right) \tag{2.3}$$

where k describes the spatial curvature of the Universe today at t_0, taking values -1, 0, or 1 if there is negative, null, or positive curvature, and $a(t) = \mathrm{d}\,t/\mathrm{d}\,t_0$ is the scale factor describing the expansion of the Universe, which is related to the cosmological redshift by $a(t) = 1/1+z(t)$ (e.g. Friedmann, 1922). The scale factor is defines such that today at time t_0, redshift 0, the scale factor is $a(t_0) = 1$. Importantly, the scale factor then relates the proper distance d_p to the comoving distance d_c, the distance that remains constant with the expansion of the Universe, by $d_p(t) = a(t)d_c$ such that $d_p(t_0) = d_c$ today. The solution to determine the expansion history of the Universe $a(t)$ is given by the set of Friedmann equations

$$H(t)^2 = \left(\frac{\dot{a}(t)}{a(t)}\right)^2 = \frac{8\pi G\rho}{3} - \frac{kc^2}{a(t)^2} + \frac{\Lambda c^2}{3} \tag{2.4}$$

$$\frac{\ddot{a}(t)}{a(t)} = -\frac{4\pi G}{3}\left(\rho + \frac{3p}{c^2}\right) + \frac{\Lambda c^2}{3} \tag{2.5}$$

where $H(t)$ is the Hubble parameter, ρ is the mass density, and p is the pressure.

There exists a critical density $\rho_{\mathrm{crit}}(t)$ such that the Universe becomes flat, where $k = 0$ in Eqn. 2.4,

$$\rho_{\mathrm{crit}}(t) = \frac{3H(t)^2}{8\pi G} \tag{2.6}$$

It is then convenient to express the densities $\rho_{x,0}$ of the given components of the Universe mentioned in Chapter 1 – namely vacuum density (dark matter) Λ, matter m, and relativistic particles γ – in units of the critical density, where $\Omega_{x,0} \equiv \rho_{x,0}/\rho_{\mathrm{crit},0}$. The first Friedmann equation (Eqn. 2.4) can then be rewritten as

$$H(t)^2 = H_0^2\left(\Omega_{\gamma,0}a(t)^{-4} + \Omega_{\mathrm{m},0}a(t)^{-3} + \Omega_{k,0}a(t)^{-2} + \Omega_{\Lambda,0}\right) \tag{2.7}$$

where $H_0 = H(t_0)$ is the Hubble constant today from Eqn. 2.1 and $\Omega_{k,0}$ is the spatial curvature density today. Eqn. 2.7 implies that with accurate measurements of the present-day Hubble constant and the density parameters, we then know the expansion history of the Universe. Due to the varying powers of $a(t)$ in Eqn. 2.7, the dominant component of the Universe can vary with cosmic time. But what exactly are the components of the Universe?

As mentioned in Chapter 1, the Universe today consists primarily of dark energy and dark matter. Lord Kelvin was the first to propose the existence of dark bodies based on the velocity dispersion of stars around the Sun in 1884, but it was not until 50 years later that dark matter[1] became widely accepted. In 1933, Fritz Zwicky studied the motion of galaxies in the Coma Cluster, and based on the necessary total mass as inferred by the virial theorem, concluded

[1] In fact, *dark* matter is a slight misnomer, since it does not absorb light but rather should be considered *transparent* or *clear* matter.

the presence of *dunkle Materie*, or dark matter. Quickly thereafter, observations of a flat rotation curve in Andromeda and other spiral galaxies implied high mass-to-light ratios in the galactic outskirts (Babcock, 1939; Oort, 1940), which would later be confirmed with improved observational techniques (Rubin & Ford, 1970; Ostriker et al., 1974; Einasto et al., 1974). Additional arguments for the existence of dark matter include the elevated stellar and globular cluster velocity dispersions around elliptical galaxies (Faber & Jackson, 1976), the hot temperatures of gas around galaxy clusters (King, 1972; Lea et al., 1973; Cavaliere & Fusco-Femiano, 1976), and gravitational lensing of galaxy clusters (Kaiser & Squires, 1993). As of writing this thesis, dark matter has still not been directly detected, but the evidence listed above confidently supports its existence and even rules out certain flavors of dark matter. Specifically, a cold dark matter (CDM) scenario is favored, where structure hierarchically build bottom-up (Peebles, 1982; Blumenthal et al., 1984), rather than a warm or hot dark matter scenario where larger structures would fracture (Bond et al., 1982; Blumenthal et al., 1982).

Measuring the precise value of the Hubble constant H_0 has proven to be a difficult challenge since its first discovery. While the initial measurement of the Hubble constant yielded a value of $\approx$ 500 km s^{-1} Mpc^{-1}, by the 1990s the estimated values began converging to $\approx$ 70 km s^{-1} Mpc^{-1} (Riess et al., 1995; Freedman et al., 2001, and references therein). In 1998, the year in which I was born, two competing teams used Type Ia Supernovae, which have approximately the same intrinsic luminosity (known as standard candles), to precisely measure the distances to far-away galaxies, finding a value of $\approx$ 70 km s^{-1} Mpc^{-1} (Riess et al., 1998; Perlmutter et al., 1999). In doing so, they discovered that not only is the Universe expanding, but it is speeding up. There must be some invisible energy in the Universe causing its expansion to accelerate: dark energy.

Over the past 25 years, the ΛCDM model has become the dominant model of the Universe we live in. Here, Λ refers to the cosmological constant, specifically to a possible form of dark energy that leads to the accelerating expansion of the Universe today; CDM is cold dark matter, which only interacts gravitationally, emitting no light. The ΛCDM model also assumes that Einstein's theory of general relativity is correct, where the Universe today is in fact expanding, and, based on measurements of the CMB, that the Universe has a flat geometry. While Λ and CDM make up $\approx$ 70% and $\approx$ 25% of the total mass-energy budget of the Universe today, no suitable candidates for dark energy or cold dark matter have been found. Regardless, this cosmological theory currently explains observations of the Universe better than any alternative theory, and the premise of this thesis accepts ΛCDM as being correct, or at least a very good approximation, to describing the Universe. The other $\approx$ 5% of mass-energy in the Universe today is in the form of baryonic matter, normal atoms and molecules that make up stars, galaxies, black holes, and cosmic gas.

Table 2.1: Currently accepted ΛCDM parameters, which are employed throughout this thesis, as given by Planck Collaboration et al. (2016). Note that this assumes a flat geometry where $\Omega_{\mathrm{tot},0} = 1$.

Parameter	Value	Description
H_0	$67.74\,\mathrm{km\,s^{-1}\,Mpc^{-1}}$	Hubble Constant
$\Omega_{\mathrm{bar},0}$	0.0486	baryon density
$\Omega_{\mathrm{dm},0}$	0.3089	dark matter density
$\Omega_{\gamma,0}$	$\sim 5 \times 10^{-5}$	relativistic particle density
$\Omega_{\Lambda,0}$	0.6911	dark energy density
n_s	0.9667	spectral scalar index
σ_8	0.8159	amplitude of the linear power spectrum on a scale of 8 Mpc h^{-1}

In this thesis I focus almost entirely on baryonic processes in an astrophysical context, naturally taking the gravitational effects of cold dark matter and cosmological expansion from dark energy into account. Today, there is also a minor contribution to the total mass-energy in the Universe from relativistic particles like photons and neutrinos on the order of $\sim 5 \times 10^{-5}$, which are mostly photons from the CMB (Hill et al., 2018). However, these photons are perhaps the most important ingredient for astronomy. Without these photons, especially those originating from astrophysical sources sources as stars and the cosmic gas, astronomy would be a much more difficult science, if it would even be possible to study.

Taking the present-day value for the Hubble parameter $H_0 \approx 70\,\mathrm{km\,s^{-1}\,Mpc^{-1}}$ as the Hubble constant today, the critical density of the Universe is

$$\rho_{\mathrm{crit},0} = \frac{3H_0^2}{8\pi G} \sim 10^{-29}\,\mathrm{g\,cm^{-3}} \sim 130\,\mathrm{M_\odot\,kpc^{-3}} \sim 5 \times 10^{-5}\,\mathrm{cm^{-3}} \tag{2.8}$$

where the latter is the equivalent hydrogen number density. CMB observations reveal the components of the Universe to consist of: dark energy density $\Omega_{\Lambda,0} \approx 0.7$, cold dark matter density $\Omega_{\mathrm{dm},0} \approx 0.25$, baryonic matter density $\Omega_{\mathrm{bar},0} \approx 0.05$, and radiation energy density $\Omega_{\gamma,0} \approx 5 \times 10^{-5}$, for a total energy density $\Omega_{\mathrm{tot},0} \approx 1$.

These parameters, the mass-energy densities and the Hubble constant, describe the Universe on the global, homogeneous scales. On smaller scales, however, the Universe is anything but homogeneous. This should come as no surprise since objects such as galaxies, planets, and people are in no way homogeneous and are orders of magnitude denser than $\rho_{\mathrm{crit},0}$. These inhomogeneities can be parameterized by the spectral scalar index n_s, which describes how the

density fluctuations vary with scale length, and the amplitude σ_8 of the linear power spectrum on scales of 8 Mpc h^{-1}, where $h = H_0/100\,\mathrm{km\,s^{-1}\,Mpc^{-1}}$. Table 2.1 summarizes these values from CMB measurements (Planck Collaboration et al., 2016).

2.2 Early universe and the cosmic microwave background

In the beginning there was nothing, but there was also everything. The leading hypothesis for the existence of our Universe details that the Big Bang initiated from a Gaussian fluctuation in an underlying quantum field, and these initial fluctuations became imprinted in the Universe. In these natal moments, the Universe was dense, hot, and expanding fast. The standard cosmological model predicts a period of exponential expansion, known as inflation, supported by a cosmological constant Λ, or any constituent with sufficient negative pressure (Guth, 1981; Linde, 1982; Starobinsky, 1982). In this context, parts of the Universe that were causally connected pre-inflation became disconnected. The curvature of the Universe evolves towards flatness. Any initial, microscopic perturbations grow to large, even super-horizon scale. Specifically, inflation predicts that a Gaussian random field describes the primordial density fluctuations, and that the initial power spectrum has a spectral index close to, but just below $n_s \sim 1$. These density perturbations have observable implications in the CMB.

After the inflationary period, the Universe was radiation dominated. As the Universe expanded adiabatically, it cooled. After a few minutes the elementary particles were able to form atomic nuclei, called big bang nucleosynthesis, where the theory predicts a cosmic mass ratio of Helium to Hydrogen of or 25% (Alpher et al., 1948). From an age of $\approx$ 5 minutes until $\sim$ 100, 000 years, the radiation-dominated Universe was still too hot for neutral atoms to exist. At redshift $\approx$ 3 300, the Universe transitioned to becoming matter-dominated, still expanding at a decelerating rate, albeit now decelerating slower than in the radiation-dominated era. At redshift $\approx$ 1300 at a cosmic time of $\approx$ 250, 000 years, free electrons and nuclei could finally form neutral Hydrogen and Helium in the poorly named process of recombination. Photons could still scatter off the still-free electrons until they fully decoupled, and after this last scattering off a free electron, the Big Bang photons could travel freely until today. The Universe was now transparent, and we can directly observe the Universe at this time of last scattering. The temperature of the photons was $\approx$ 3000 K but has now been redshifted to a temperature of $\approx$ 2.75 K, creating the CMB. Because the baryonic matter and photons were coupled and in equilibrium, the predicted CMB spectrum is a Black Body with small perturbations arising from matter density anisotropies and the baryonic acoustic oscillations.

I now transition from theory to the actual observations of the CMB, and specifically what the Planck Collaboration et al. (2016) have learned about the Universe from it.

The temperature of the nearly perfect blackbody CMB spectrum yields a direct measurement of the total photon energy density $\Omega_{\gamma,0}$ in the present-day Universe of $\approx 5 \times 10^{-5}$, assuming that the CMB photons dominate the total photon energy density (Hill et al., 2018). The CMB is at an average temperature of ≈ 2.75 K with Gaussian perturbations on the order of $\sim 10^{-5}$. The CMB exists in all directions of the sky with statistically consistent properties. Because the temperature perturbations can be described by a Gaussian random field – although some non-Gaussian features may exist – all statistical information is contained in the angular power spectrum. The large scale isotropy supports the theory of inflation, whereby regions on the sky separated by the sound horizon $\gtrsim 1$ deg were previously in causal contact before the inflationary period. On sub-sound-horizon scales of $\lesssim 1$ deg perturbations may exist due to motions in the photon-baryon fluid. The distribution of baryons, or more precisely, the baryonic anisotropies at the time of last scattering, determine the temperature fluctuations. Before recombination, the baryon-proton fluid provided a pressure to support itself against the gravitationally pull of dark matter on sub-horizon scales, while on super-horizon scales the baryons followed the already decoupled dark matter perturbations, which were growing with time. While the baryons were gravitationally attracted to the dark matter, the restoring pressure from the baryon-proton fluid led to the baryonic acoustic oscillations. Because the photon-baryon fluid was compressing and expanding adiabatically, the denser regions became hotter and vice versa. The angular power spectrum shows the most prominent peak at approximately the sound horizon at $\approx 1^{\circ}$. The exact position of this peak depends on the spatial curvature in the Universe, which can be constrained to being consistent with a flat Universe with a total mass-energy density of $\Omega_{\rm tot} \approx 1$. The exact shape of this peak depends also on the total matter density $\Omega_{\rm m} = \Omega_{\rm dm} + \Omega_{\rm bar}$, whose constraints require the presence of dark energy $\Omega_\Lambda = \Omega_{\rm tot} - \Omega_{\rm m} - \Omega_\gamma$. The second and third peaks at smaller angular scales constrain the dark matter and baryonic densities. The CMB is able to constrain the cosmological parameters in the early Universe, independently checking the methods and values measured in the late Universe explained above. The cosmological parameters measured in both the early and late Universe agree remarkably well, which is one of the strongest evidences for ΛCDM, although some minor discrepancies still persist (Di Valentino et al., 2021).

After the time of last scattering at $z \approx 1100$, when the Universe had recently transitioned from radiation- to matter-dominated, the Universe became transparent and optically dark. The baryons were decoupled from the photons and could follow the already decoupled dark matter, which had been continuously growing their primordial density perturbations. We now turn to the formation of dark matter halos and eventually to that of galaxies.

2.3 Formation of Dark Matter Halos

In a static Universe, any density perturbation in a pressure-less fluid, i.e., only under the influence of gravity, would continue to grow. In an expanding Universe or in the presence of some restoring pressure – either radiation or (magneto-)hydrodynamic pressure – the fate of density perturbations is less straightforward. Because dark matter is decoupled from photons and hydrodynamical effects, the pressure-free approximation holds; however, the expansion of the Universe cannot be ignored. Solving the evolution of a density perturbation in comoving coordinates yields a two-mode solution, where the growing mode is relevant for the the growth of structure. Further, a velocity perturbation can also grow such that the material falls radially inwards towards the perturbation, further increasing the density contrast. That is, certain density and velocity perturbations in our ΛCDM Universe can grow with time.

The linear perturbation theory is a good approximation for small perturbations on the order of or less than the average density of the Universe (Zel'dovich, 1970). Because these perturbations lead to runaway collapse, the linear approximation quickly breaks down, requiring the use of N-body numerical simulations to follow the collapse and structure of dark matter halos (Press & Schechter, 1974). In certain simplified cases, analytic solutions exist for the collapse of density perturbations in an expanding background. Namely, for a collisionless spherical overdensity, the sphere can collapse due to its own self-gravity (Gunn & Gott, 1972). In the more realistic scenario of a non-perfectly uniform sphere, the collapse is followed by a period of violent relaxation where the halo virializes. These collapsed structures can remain gravitationlly bound, despite the universal expansion, creating the first dark matter halos in the Universe. As the halos continue accreting dark matter, there is no physical barrier or boundary demarcating the end of the halo. It is common practice to characterize the halo radius as the radius R_{200c} at which the average total enclosed density is 200 times the critical density of the Universe, and the halo mass M_{200c} is the total mass enclosed by R_{200c}. The dark matter structure within a halo is surprisingly similar across a broad range of halo masses, when normalizing by the halo's virial radius (Einasto, 1965; Hernquist, 1990; Navarro et al., 1996). Despite this relatively arbitrary halo size definition, the local effects from the halo may indeed extend beyond this virial radius (see Section 3.3 for details).

2.3.1 Hierarchical growth of structure

In the ΛCDM Universe, small objects form first, which grow via accretion and mergers to become larger objects that exist today. For all halo masses above some minimum threshold, which is set by the streaming length of the dark matter (on the order of an Earth mass for cold dark matter), smaller halos outnumber more massive ones (Press & Schechter, 1974).

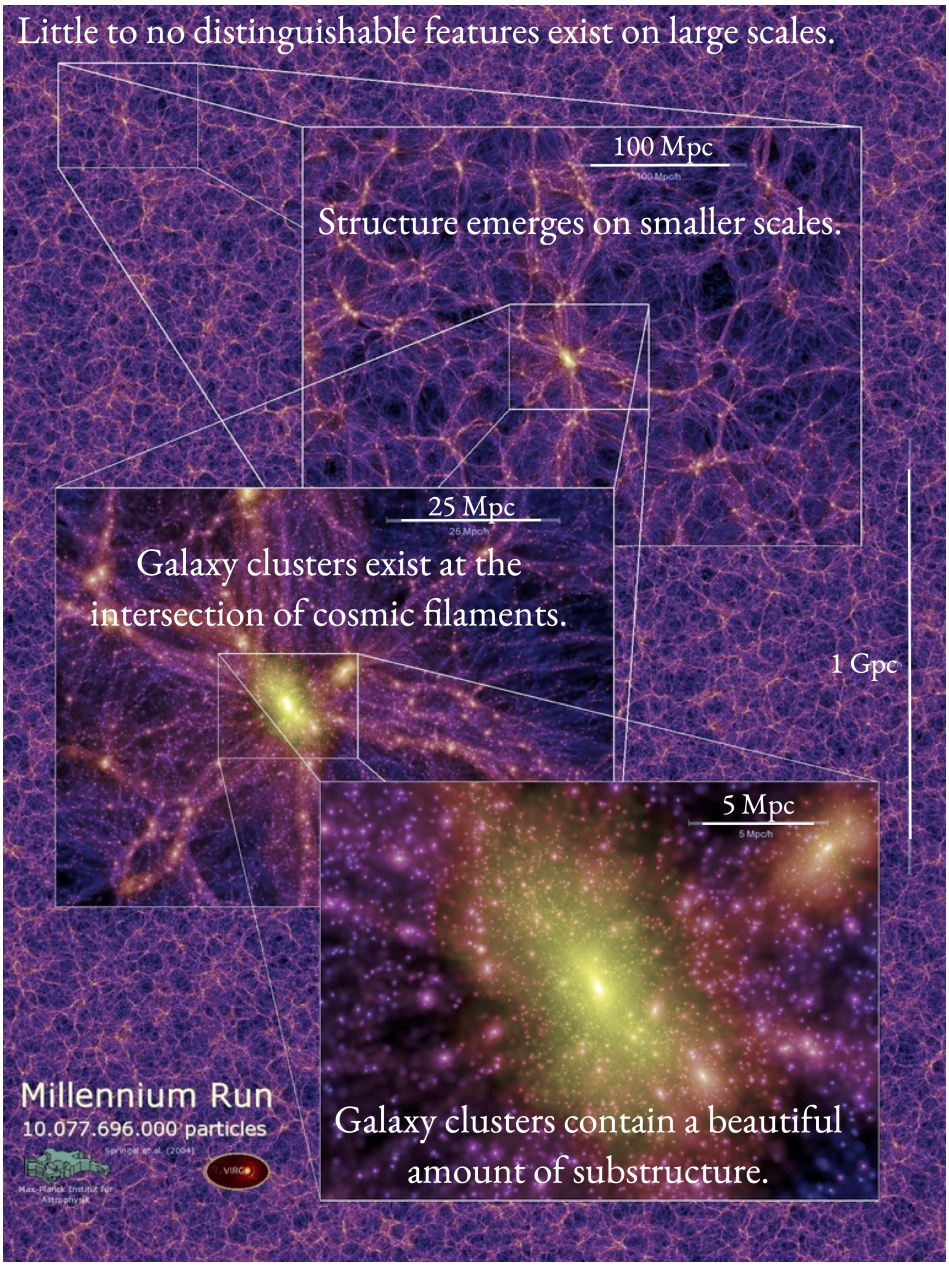

Figure 2.1: **Zoom in on a galaxy-cluster-sized halo in the Millennium Simulation**. The cosmic web beautifully emerges in the dark matter only Millennium simulation, which has an original volume of $\sim (750\ \mathrm{Mpc})^3$ with periodic boundary conditions. On the largest scales $\gtrsim 100$ Mpc, the simulation, and the Universe itself, is approximately uniform. Features begin appearing at smaller scales. Of particular interest is the intersection of cosmic filaments, where massive halos $\sim 10^{15}\ \mathrm{M}_\odot$ live and are expected to host massive galaxy clusters. Simulating the galaxies themselves, however, was not yet possible, and semi-analytic models were necessary to infer galaxy magnitudes and compare the results to observations. Figure adapted from the Millennium Simulation (Springel et al., 2005b).

Then halos grow by accreting more dark matter and smaller halos from the surrounding environment. Within a given volume at a given time, there is a maximum expected halo mass, with some stochasticity based on cosmic variance. This maximum mass depends depends on cosmological parameters, where this maximum mass increases with cosmic time, as this allows more time for gravitational accretion and mergers (Kauffmann et al., 1993).

Both the amplitude of the initial dark matter density perturbation and its location in space, that is, whether the peak randomly occurred near other overdensities or not, determine the eventual fate of the halo. To first order, halos forming from higher overdensities accrete at higher rates and become more massive groups and clusters today compared to halos forming from smaller overdensities. The halos forming out of smaller overdensities near larger, already collapsed halos may accrete onto them, further increasing the mass of the larger halo. Accretion events like these are common, especially in the denser early Universe, and a standard prediction from ΛCDM is that all halos today contain substructures in the form of accreted subhalos, where more massive halos host more subhalos (Moore et al., 1999; Klypin et al., 1999, see also Fig. 2.1). The hierarchical growth of structure leads to collapsed bridges of material that connect the halos (Klypin & Shandarin, 1983; Davis et al., 1985; White et al., 1987; Bond et al., 1996). This large scale structure forms the cosmic web, which consists of knots, filaments, sheets, and voids, and can be inferred by the positions of galaxies in all sky surveys, such as the CfA2 survey (Geller & Huchra, 1989), 2 Degree Field Galaxy Redshift Survey (2dFGRS; Colless et al., 2001), and the Sloan Digital Sky Survey (SDSS; York et al., 2000). The statistical properties of the large scale structure can be well modeled by simulations of the evolution of dark matter (Springel et al., 2005b, 2006, Fig. 2.1).

2.3.2 Galaxy clusters as the ultimate outcome of hierarchical assembly

The most massive halos in the Universe today, which are thought to host clusters of galaxies, live at the intersections of multiple overdense filaments, which is nicely visualized in Fig. 2.1. Fig. 2.1 displays the large scale distribution of dark matter from the Millennium simulation (Springel et al., 2005b). The original simulation volume is $\sim$ (750 Mpc)^3, and due to the periodic boundary conditions, the volume can be tessellated to appear much larger in the background image. On large scales $\gtrsim$ 100 Mpc, both the simulation and the Universe itself are approximately uniform. On smaller scales, however, structure emerges. Massive halos emerge at the intersections of cosmic filaments, and these halos host thousands of resolved subhalos, which likely translates to hundreds to thousands of observable satellite galaxies. The Millennium simulation only models the collisionless cold dark matter, so there are no explicit predictions for observable properties. However, When applying a semi-analytic model to

predict galaxy magnitudes from the simulation outputs (Kauffmann et al., 1993; Cole et al., 2000; Croton et al., 2006), the resulting large scale distribution of predicted galaxies matches the observed structure of galaxies (Springel et al., 2006).

Halos hosting galaxy clusters are the largest and rarest gravitationally collapsed structures in the Universe, and they are a primary area of study throughout this thesis. The collapse and creation of these halos is mostly determined by the initial conditions and gravitational collapse of cold dark matter; however, I am most interested in the baryons in and around the galaxies inhabiting these massive dark matter halos.

3 Galaxy Formation and Evolution in a Cosmological Context

The Hubble Deep Fields (Fig. 1.2) demonstrated the plethora of galaxies in a small patch of the night sky, where these galaxies clearly show a diversity in size, color, morphology, and age. All sky surveys (CfA2, 2DFGRS, SDSS) showed that the positions of galaxies map out a large scale cosmic web, similarly to the predictions from dark matter only simulations (Springel et al., 2005b, Fig. 2.1). But how do galaxies actually form, and why is their spatial distribution similar to the expected underlying dark matter distribution? After the birth of galaxies, namely after the first population of stars form, how do the galaxies evolve until today? How do galaxies interact with one another? And how do galaxies and their parent dark matter halos connect back to the large scale structure?

3.1 Gaseous halos and the birth of galaxies

The primordial gas, whose density perturbations at the time of the decoupling from the photons were on the order of $\sim 10^{-5}$, follow the dark matter, which was already decoupled from the radiation and could continue growing its density perturbations. Following the formation of the dark matter halo, the basic picture of gas collapse to form a galaxy comes from analytic arguments (Silk, 1977; Rees & Ostriker, 1977; White & Rees, 1978) and is summarized in Fig. 3.1.

The gaseous fluid is more complicated than the cold dark matter because the gas is collisional, creating a pressure to support itself against gravitational collapse. The infalling gas generates shocks in the halo, heating up to approximately the equivalent temperature of the gravitational potential energy of the halo, that is, the virial temperature $\gtrsim 10^6$ K. This creates a hot, hydrostatic halo that mostly pressure supports itself against collapse. The gas can cool by radiating energy away (Fig. 3.1, right panel), and, by the conservation of angular momentum, the cooling gas forms a compact disk in the center of the halo (Peebles, 1969; Fall & Efstathiou, 1980; Mo et al., 1998). The cold disk can grows by accreting hot halo gas that cools down, and the halo itself can grow by accreting material from the IGM. As the gas continues to grow

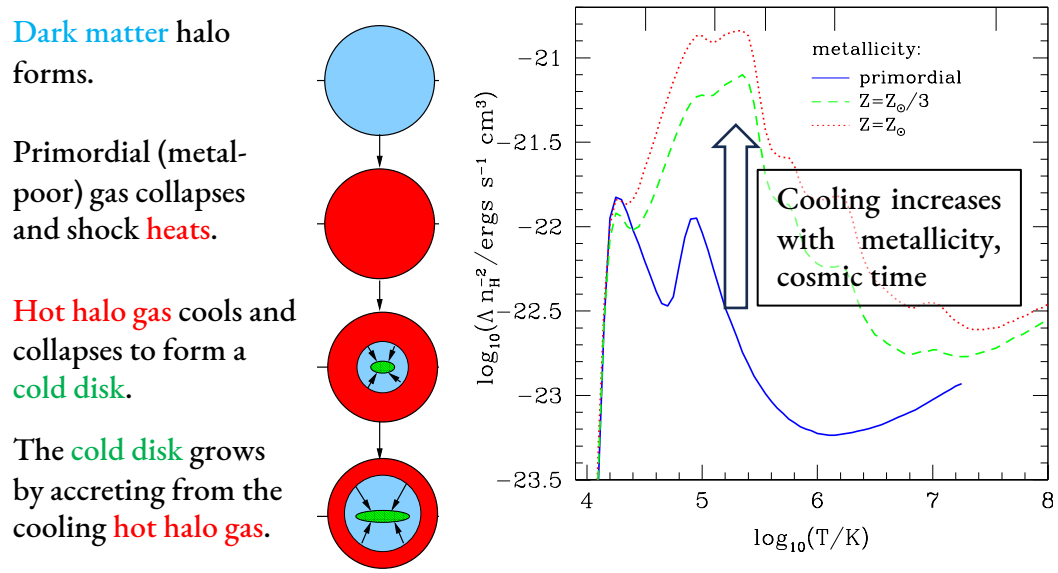

Figure 3.1: **Schematic for the formation of galaxies**. *Left*: After the formation of the dark matter halo, primordial gas falls into the halo's potential well and heats up via shocks. Some of the hot gas can then cool, and by the conservation of angular momentum, the cool gas forms a disk in the center of the halo. Lastly, the cool disk, which is supported by the hot atmosphere and parent dark matter halo, is able to grow by accreting hot halo gas that cools down. This picture for galaxy formation is based on the analytic arguments of (Rees & Ostriker, 1977; Silk, 1977; White & Rees, 1978), and the schematic is adapted from (Baugh, 2006). *Right*: The cooling function Λ for atomic and ionized gas, which assumes collisional ionization equilibrium (Sutherland & Dopita, 1993). Gas cooling becomes more efficient as the metallicity increases, where the average gas metallicity tends to increase with time, compared to the cooling of primordial gas, which consists of $\approx 76\%$ Hydrogen and $\approx 24\%$ Helium by mass. While gas can cool to temperatures $\lesssim 10^4$ K, the gas at these temperatures is fully neutral, and the collisions are not energetic enough to excite or free the electrons; molecular Hydrogen (and other molecules in metal-enriched gas) can exit, but this cooling is not tabulated here, nor is it included in much of the analysis of this thesis. Figure adapted from Baugh (2006).

denser in the disk, it eventually collapses to form the first stars of the Universe, commonly referred to as Population III (Pop. III) stars, which are essentially metal-free and likely quite massive $\sim 10^{2-5}\,M_\odot$ (Eggen et al., 1962; Klessen & Glover, 2023, and references therein). These Pop. III stars likely only lived for brief times, much shorter than the age of the Universe at their formation, and produced the first starlight in the Universe. The formation of the first Pop. III stars ended the cosmological dark ages; the Universe was beginning to light up.

These Pop. III stars produced the first metals in the Universe, beyond the trace amounts leftover from the Big Bang Nucleosynthesis. These stars shared their newly formed metals with the surrounding gas, likely through stellar winds and eventually supernovae explosions at the end of their lives. The surrounding, metal-enriched gas could then cool and fragment much more efficiently than the primordial gas, facilitating the formation of the second generation of stars, Population II (Pop. II) stars. The Pop. II stars were on average lower in mass than Pop. III stars, and thereby many of them could live for long times. Some of these Pop. II stars are likely still living today (Eggen et al., 1962). The centers of dark matter and gaseous halos now contain collections of gravitationally bound stars, gas, dark matter, and maybe the first black holes as well; these are the first galaxies in the Universe (Bromm & Yoshida, 2011).

3.2 The secular evolution of a central galaxy

The most common type of galaxy in the Universe today is a central galaxy, meaning that it is at the center of its dark matter halo. Every galaxy that has ever existed originally formed as a central galaxy. There exists today a broad range of central galaxy masses, ranging from small dwarfs of stellar mass $\sim 10^4\,M_\odot$ to massive brightest cluster galaxies (BCGs) weighing $\sim 10^{12.5}\,M_\odot$, in addition to a range of colors, morphologies, and star-forming activity. Central galaxies[1] have been observed to follow a number of relations:

i. For spiral galaxies, the H I line width, a proxy for the rotational velocity, increases with the galaxy's luminosity (Tully-Fisher relation; Tully & Fisher 1977).

ii. For elliptical galaxies, the stellar velocity dispersion increases with the galaxy's luminosity (Faber-Jackson relation; Faber & Jackson, 1976), and, when combined with the galaxy's effective radius, forms the fundamental plane for elliptical galaxies (Dressler et al., 1987).

iii. For star-forming galaxies, the galaxy's star formation rate (SFR) surface density increases with the galaxy's gas surface density (Kennicutt-Schmidt Law; Schmidt, 1959; Kenni-

[1] Here, by central galaxies, I am specifically referring to isolated galaxies, who have no significant satellite or neighboring galaxies that could affect the galaxy's evolution. In general, however, all central galaxies have some substructure within their halo.

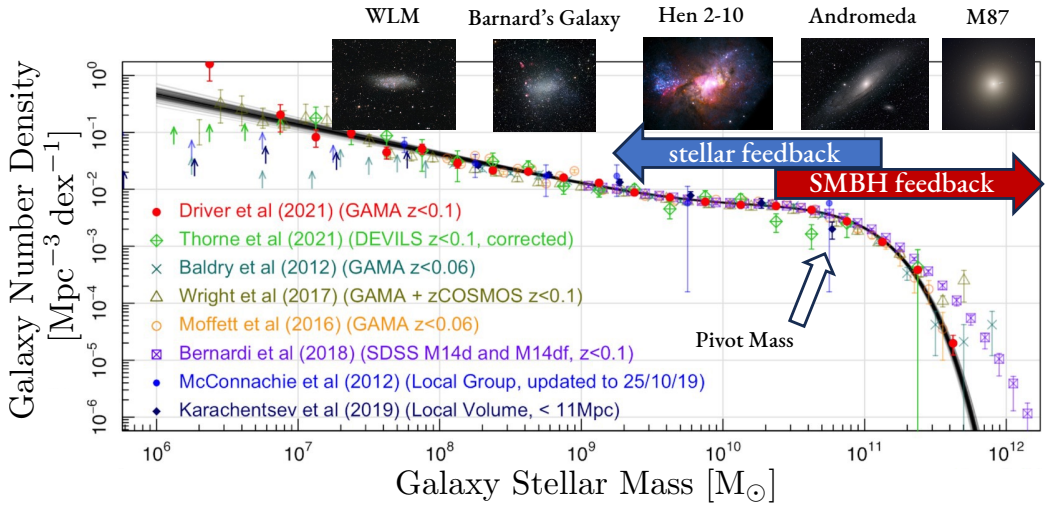

Figure 3.2: **Galaxy stellar mass function today**. The galaxy stellar mass function encodes average number of galaxies of a given mass in a given volume, where smaller galaxies are more frequent than larger galaxies. The shape of the galaxy stellar mass function, namely where the power law slope changes at the pivot mass $\sim 10^{10.5-11}$ M$_\odot$, hints at the dominant physical mechanism at play, i.e., stellar feedback at smaller masses and SMBH feedback at larger masses. I include example galaxies at their approximate stellar mass locations for reference. The galaxy stellar mass function is adopted from the Galaxy and Mass Assembly (GAMA) DR4 results (Driver et al., 2022). The galaxy image credits from left to right are: ESO and VST/Omegacam Local Group Survey (Wolf-Lundmark-Melotte; WLM); ESO (Barnard's Galaxy; NGC 6822); X-ray (NASA/CXC/Virginia/A.Reines et al), Radio (NRAO/AUI/NSF), and Optical (NASA/STScI) (Henize 2-10); Torben Hansen (Andromeda; M31); NASA, ESA and the Hubble Heritage Team (STScI/AURA), P. Cote, and E. Baltz (M87). Schematic inspired from Wechsler & Tinker (2018, fig. 2).

cutt, 1998); the galaxy's star formation rate increases with its stellar mass (star-forming main sequence; Gavazzi & Scodeggio, 1996; Brinchmann et al., 2004).

iv. Galaxies tend to separate on the color-magnitude diagram based on morphology, where late-type spirals tend to be bluer and early-type ellipticals tend to be redder[2] (de Vaucouleurs, 1961; Strateva et al., 2001; Bell et al., 2004).

v. The mass of the central SMBH increases with the central stellar velocity dispersion of the galaxy ($M_{\rm bh} - \sigma_\star$ or Magorrian relation; Magorrian et al., 1998; Ferrarese & Merritt, 2000; Gebhardt et al., 2000, see also Kormendy & Ho 2013 and references therein).

Items i and ii act as proxies for the distances to spiral and elliptical galaxies respectively, whereby measuring the either the H I rotational velocity or stellar velocity dispersion yields the luminosity or absolute magnitude of the galaxy. Items iii-iv demonstrate that various parts of a galaxy are connected to each other, implying that the physical mechanisms driving their evolution are, too, connected. a galaxy can grow its stellar mass by forming stars, but its star formation rate is limited to the amount of available gas and is somehow connected to the galaxy's current stellar mass (item iii). Bluer galaxies tend to be disky spirals, while redder galaxies tend to be ellipticals, suggesting that disky galaxies are able to from stars more efficiently than ellipticals, and there must be some morphological transition associated with the quenching of star-formation (item iv). Lastly, item v hints that the growth of the central SMBH is regulated by (or regulates) the growth of the galaxy.

These observational findings form the basis for theories of galaxy evolution. Namely, smaller galaxies form stars in disky morphologies, where the star-formation is regulated by the associated stellar feedback in the form of stellar winds and supernovae (Larson, 1974; Dekel & Silk, 1986; Silk, 1977). At a later stage, the central SMBH, which has been growing in mass along with the galaxy itself, switches from a mostly radiative "quasar" feedback mode to a mostly mechanical "radio" feedback mode, where the mechanical mode drives gaseous outflows and quenches star-formation (Silk & Rees, 1998; Di Matteo et al., 2005). The galaxies now have little gas within their stellar body, and without this fuel to form new stars, eventually turn red as the younger, bluer stars die out first. Without a thin star-forming disk, the morphologies slowly transform to being more elliptical in nature (with the help of mergers as well Toomre et al. 1972).

Fig. 3.2 summarizes this picture of galaxy evolution. Namely, I show the number density of galaxies as a function of galaxy stellar mass (where I include example galaxies at their

[2]Blue galaxies tend to have ongoing or recent star-formation, where the blue light comes from young O and B stars that have not yet died. Red galaxies tend to have little to no ongoing star-formation, and their stellar light comes from older stellar populations. This picture is complicated by dust extinction, but here I ignore the effects of dust.

approximate stellar mass), or the galaxy stellar mass function (GSMF), from the Galaxy and Mass Assembly (GAMA) collaboration (Driver et al., 2022). First, the galaxy number density decreases at at all galaxy stellar masses studied, similarly to the halo mass function for dark matter halos, where smaller halos outnumber larger ones. The galaxy number density decreases following an approximate power law at masses below the "pivot" mass; at masses above the pivot masses, the galaxy number density decreases exponentially with galaxy stellar mass. This sudden change suggests a switch in the physical process that dominates the galaxy's evolution at this mass: when star-formation regulated by stellar feedback transitions to quenching of star-formation from SMBH feedback (Wechsler & Tinker, 2018, and references therein).

Galaxies at this pivot (stellar) mass $\sim 10^{10.75-11}\,\mathrm{M}_\odot$ are commonly referred to as $L_\star$ galaxies, and M31 and our own Milky-Way are $L_\star$-like galaxies. These $L_\star$ galaxies today tend to have halo masses of $\sim 10^{12}\,\mathrm{M}_\odot$ and SMBH masses of $\sim 10^{8}\,\mathrm{M}_\odot$, where these numbers may be different at higher redshifts. At $z = 0$, however, galaxies like our own at the transition mass are of particular interest because both stellar and AGN feedback may effectively drive outflows and regulate the galaxy's evolution.

3.3 What happens when a central becomes a satellite

Satellite galaxies were central galaxies that have since fallen into the halos of more massive hosts. During first infall, the satellite still retains much of its own dark matter halo, CGM, and ISM, but this does not last long.

Observations show that compared to central galaxies of a similar mass, satellite galaxies tend to have more elliptical morphologies, redder colors, lower neutral H I fractions, higher gas metallicities, lower star-formation rates, higher quenched fractions, and suppressed active galactic nuclei (AGN) activity (Dressler, 1980; Giovanelli et al., 1985; Peng et al., 2010, 2012; Pasquali et al., 2012; Wetzel et al., 2012; Brown et al., 2016; Maier et al., 2019a,b). These findings all point to a picture where the local environment causes satellites to lose their gas and quench their star formation more efficiently or earlier on in their evolution than centrals.

A number of physical mechanisms have been proposed to explain these differences between satellites and centrals. Satellites galaxies are cutoff from the large scale structure and therefore have restricted access to accrete new gas (Larson et al., 1980; Balogh & Morris, 2000). In denser galactic environments, satellite-satellite interactions can efficiently remove gas and quench star-formation (Moore et al., 1996, 1998). Satellites can be tidally stripped of their dark matter, CGM, and, in the case of close encounter, the ISM and stars by the central galaxy (Toomre et al., 1972). Lastly, the hydrodynamic interaction of the ambient gas acting on the infalling satellite, called ram pressure, can directly remove the CGM and ISM from the satellite

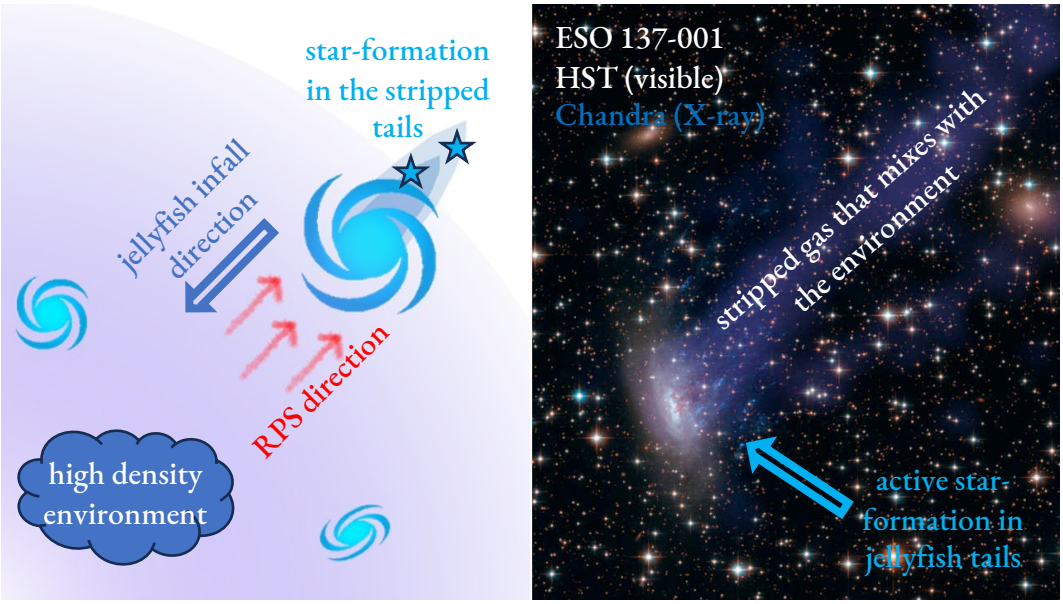

Figure 3.3: **Schematic of a jellyfish galaxy**. Jellyfish galaxies are satellite galaxies that have been visually identified to be undergoing ram pressure stripping (RPS), typically by long tails of stripped gas that point in the opposite direction of their own motion. Some of this stripped gas is able to form stars in the jellyfish tails, and some of the gas mixes with the ambient hot medium. Schematic (left) adopted from the Zooniverse Project Fishing for Jellyfish Galaxies (credit: Callum Bellhouse); Image (right) credits: NASA, ESA, CXC.

(Gunn & Gott, 1972). It is generally accepted that ram pressure is one of the most important environmental effects that leads to the removal of the gaseous reservoirs and quenching of star-formation of satellite galaxies *en masse*, especially satellites galaxies of lower stellar mass $\lesssim 10^{10}\,M_\odot$ (Cortese et al., 2021; Boselli et al., 2022). However, it has been suggested that massive SDSS satellites $\gtrsim 1010.5\,M_\odot$ still quench due to their own SMBH feedback (Goubert et al., 2024). In the rest of this thesis, I focus primarily on ram pressure as the dominant environmental effect that redistributes a satellite's gaseous reservoirs and eventually leads to its quenching, although all effects are, in theory, at play.

3.3.1 Jellyfish galaxies as examples of ram pressure stripping in action

Fig. 3.3 illustrates ram pressure in action as a jellyfish galaxy forms (left), alongside a composite *HST/Chandra* image (right) of an example jellyfish galaxy from cluster Abell 3627. As the gaseous satellite first falls into the dense environment of a more massive host, ram pressure from the ambient medium interacts with the satellite's gas, pulling the satellite's gas backwards relative the satellite and leaving the main stellar body unperturbed. The resultant galaxy

appears as and is affectionately referred to as a "jellyfish galaxy", where the unperturbed stellar body resembles the jellyfish head and the stripped gaseous tails mimic jellyfish tentacles (Bekki, 2009; Ebeling et al., 2014; McPartland et al., 2016). Traditionally they have been identified via stellar light in optical imaging and associated Hα emission coming from both the stellar body and the ram pressure stripped tails (Poggianti et al., 2017b). Some of the cold tail gas is even able to form stars, making jellyfish tails one of the only locations in the Universe where star formation occurs outside of the ISM in galaxies (e.g., Vulcani et al., 2018). Additionally, the tails can mix with the surrounding hot medium, creating a broad range of gas temperatures and metallicities (Franchetto et al., 2021). The combination of the multiphase gas in both the tails and the stellar body, coupled with the young and pre-existing older stellar populations, facilitate detecting jellyfish galaxies in the radio (synchrotron continuum and molecular emission lines), infrared, optical, ultraviolet, and X-ray (Gavazzi & Jaffe, 1987; Gavazzi et al., 2001; Kenney et al., 2004; Sun et al., 2006; Cortese et al., 2006; Smith et al., 2010; Jáchym et al., 2017; Poggianti et al., 2019; Ignesti et al., 2022).

Ram pressure is a hydrodynamical drag force, whose strength is proportional to the density of the ambient medium $\rho_{\rm cgm}$, in this case the CGM, and the square of the relative velocity $v_{\rm rel}$ between the ambient medium and the infalling satellite and the direction is anti-parallel to the relative velocity (Gunn & Gott, 1972). When the ram pressure on a given parcel of gas becomes stronger than the gravitational restoring force F_g, then the gas is removed:

$$\rho_{\rm cgm} v_{\rm rel}^2 > \frac{F_g}{\text{unit area}} \tag{3.1}$$

As the host mass increases, so does its gravitational potential, increasing the relative velocity of the infalling satellites. The average CGM density also increases with halo mass, and for a given host halo, both the density and relative velocity increase at closer host-centric distances. Thereby, the ram pressure can be rewritten as

$$p_{\rm ram} = p_{\rm ram}(M_{\rm halo}, d_{\rm sat}^{\rm host}) \propto \rho_{\rm CGM}(M_{\rm halo}, d_{\rm sat}^{\rm host}) v_{\rm rel}(M_{\rm halo}, d_{\rm sat}^{\rm host})^2 \tag{3.2}$$

Namely, for a fixed satellite stellar mass, ram pressure is expected to be more effective for larger host masses and at smaller host-centric distances, which are broadly consistent with observations (e.g., Presotto et al., 2012; Wetzel et al., 2012, 2013; Davies et al., 2019; Maier et al., 2019b; Roberts et al., 2019).

The gravitational restoring force is primarily provided by the satellite's stellar mass $M_\star^{\rm sat}$ and secondarily on the gas mass $M_{\rm gas}^{\rm sat}$. Specifically, the restoring force depends on the average enclosed surface density as a function of radius r from the satellite, where both $\Sigma_\star$ and $\Sigma_{\rm gas}$

decrease with satellite-centric radius. Assuming the restoring force is dominated by the stellar body, the gravitational restoring force can be rewritten as $F_g = F_g(M_\star^{\rm sat}, r)$. That is, the ram pressure on a given parcel of gas is opposed by restoring force of the stellar mass of the satellite and the distance from the gas to the center of the satellite. This implies that at a fixed host mass and host-centric distance, ram pressure should be more effective for lower-mass satellites and should remove gas in an outside-in fashion, both of which have been affirmed or assumed in observations (e.g., Warmels et al., 1988b; Cayatte et al., 1990; Balogh & Morris, 2000; Wetzel et al., 2013; Bluck et al., 2020; Vulcani et al., 2020). In practice, the binding energy of gas in the satellite's CGM and ISM are not just functions of radius, but local effects such as stellar or SMBH feedback are thought to contribute to the effectiveness of ram pressure stripping (Bahé & McCarthy, 2015; Emerick et al., 2016; Garling et al., 2024).

Jellyfish galaxies are, in general, a subset of the total satellite population. While a majority of observed satellites today are gas-poor with little to no active star-formation, jellyfish galaxies, by definition, still retain a sizeable amount of gas. This means that jellyfish galaxies are more likely to be recent infallers compared to the total satellite population. As all gaseous satellites are expected to undergo ram pressure, and as all satellites are expected to be gas-rich at infall[3], all satellite galaxies are expected to undergo ram pressure for some period of time. Whether this phase is observable and identifiable as a jellyfish phase in a given wavelength is another question. With this in mind, I proceed with the mindset that all gaseous satellites undergo ram pressure, where jellyfish galaxies represent a temporary phase of satellite galaxy evolution. That is, the lessons we learn from jellyfish can be applied to other satellites as well.

3.4 Putting it all back together: galaxies within the large scale structure

While the local environment, on scales of the virial radius of the halo $\lesssim 1$ Mpc, dominates the evolution of satellite galaxies, the larger environments, for example, whether a galaxy is in a void or a sheet, also impacts its evolution. For example, the closer a central galaxy is to a cosmic filament or sheet, the lower its specific star formation rate is likely to be (Winkel et al., 2021). In large scale overdensities, there are overall more galaxies, especially more massive groups and clusters (Borgani et al., 1999; Allen et al., 2011; Fumagalli et al., 2024), meaning that galaxy mergers and accretion occur more frequently. Further, galaxies are more often pre-processed, when a galaxy experiences environmental effects (ram pressure, for example) before falling into its $z = 0$ host (Dressler et al., 1999; Poggianti et al., 1999; Goto et al., 2003,

[3] I ignore here the effects of pre-processing, where a galaxy first falls into some other host, such as a galaxy group, before the host later falls into some more massive host, such as a galaxy cluster.

see also Fujita 2004; McGee et al. 2009; Donnari et al. 2021a for theoretical perspectives). Some simulation studies even suggest that low mass galaxies can even be ram pressure stripped by the cosmic web itself (Benítez-Llambay et al., 2013; Wright et al., 2019; Herzog et al., 2023). These larger scale effects are considered to be second order compared to the local satellite host mass. Throughout the remainder of this thesis, I focus on the local environmental effects, typically probed by the host mass.

3.4.1 The cosmic gas across scales: from the intergalactic to the interstellar medium

Galaxies form in the centers of their dark matter halos, where the galaxies can form stars out of the ISM and grow by accreting material from the CGM (§ 3.1). As the galaxy grows, galactic feedback from, for example, supernovae and SMBHs, returns some of the ISM back into the CGM and perhaps even into the IGM. The halos can grow by smoothly accreting gas and dark matter from the large scale structure or from infalling satellites and subhalos. As these satellites accrete onto their hosts, they experience the secular evolutionary processes (§ 3.2) in addition to the environmental processes that eventually lead to its gas removal and quenching of star-formation (§ 3.3). There is a continuous flow of gas across scales, where the gas can heat up, cool down, and even change phase in the form of star formation (Fig. 1.3).

Satellites can also affect their hosts. In the most extreme case, when a satellite has roughly equal mass to the central, called a "major merger", the entire morphology and properties of both galaxies can be disrupted, and the resultant, merged object may not appear or act as either of the preceding galaxies (Toomre et al., 1972). Mergers like these are cosmologically rare, but the general accretion of satellites is quite common. Our own Milky Way galaxy has two major satellite galaxies, the Large and Small Magellanic Clouds (L/SMC), and the halo contains many stellar streams, fossils of previous satellite galaxies that have been tidally stripped (Helmi, 2008). More massive galaxies, or more precisely, galaxies living in more massive halos, tend to have more detectable satellites and brighter stellar halos (Berlind & Weinberg, 2002, see also Fig. 2.1). One major theme of this thesis is to show that an analogous argument for the buildup of satellite galaxies and stellar halos exists for the halo gas; the difficulty here is that, unlike for stars in the halo, gas can mix and change phase on cosmologically short timescales.

Fig. 3.4 displays the cosmic gas from the largest scales of the IGM (left), to ICM/CGM (center), to the ISM (right), where each panel zooms-in by a factor of 10. Specifically, this is a series of images of a forming galaxy cluster at $z = 4$, which will become a massive galaxy cluster of total mass $\sim 10^{15}\,\mathrm{M}_\odot$ by $z = 0$, from the TNG-Cluster simulation suite (Nelson et al., 2024, Pillepich et al. in prep.). Amazingly, the gas in the IGM (left panel), some of which is megaparsecs away from the central galaxy at $z = 4$, will become part of the galaxy cluster by

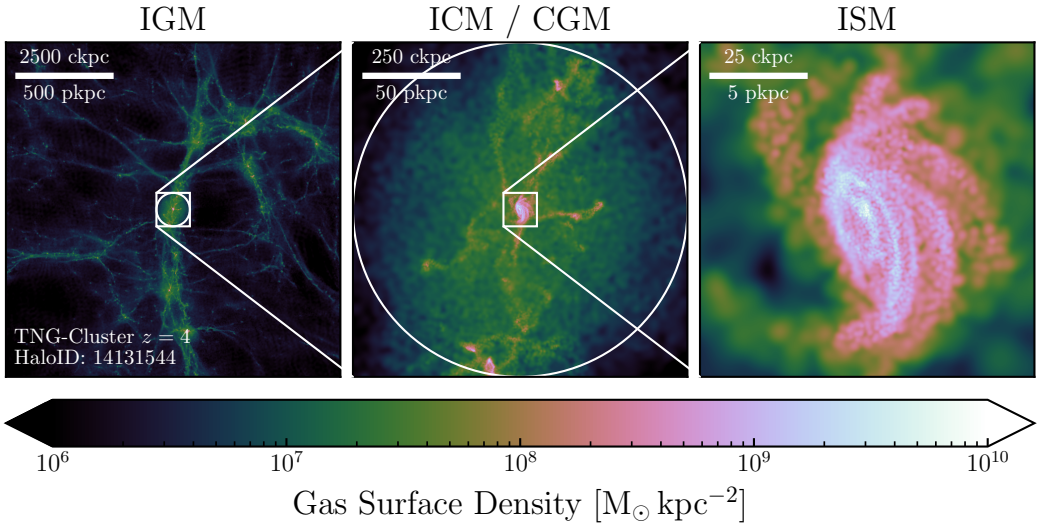

Figure 3.4: **The cosmic gas, from the intergalactic to the interstellar medium**. The cosmic gas is connected to itself across scales, going from the intergalactic medium (IGM; left panel), which shapes the filaments and voids in the large scale structure, to the intracluster or circumgalactic medium (ICM/CGM; middle panel), all the way down to the interstellar medium (ISM; right panel). Of particular interest to this thesis is the connection between the halo gas (ICM and CGM) and satellite galaxies, which are visible as the pink blobs in the ICM/CGM with their ram pressure stripped tails (middle panel).

$z = 0$. In the ICM (center), some substructure related to the large scale filaments and satellite galaxies with their ram pressure stripped tails are visible. In the ISM (right panel), the central galaxy still has a star-forming disk, before it later quenches due to its SMBH feedback. Fig. 3.4 illustrates the beauty of the cosmic gas and how it connects to itself across cosmic scales and time.

3.4.2 Cluster satellites as astrophysical laboratories

Studies of galaxy evolution have traditionally focused on self-regulating, central galaxies (e.g., Hopkins et al., 2012b). Many classic diagnostics and scaling relations (§ 3.2) used to calibrate galaxy formation models and cosmological simulations only consider central galaxies, since the evolution of satellites involves additional processes. This ensues that studies of satellite galaxies act as test beds for the leading theories, as these models were not necessarily calibrated to reproduce properties of satellite galaxy populations. Satellites are the sites of exotic branches of astrophysics, which are not always present in central galaxies. Lastly, satellites may play a crucial role in precision cosmology.

Central galaxies are commonly simulated as isolated, self-regulating disks, where the galaxies are always in a state of dynamic equilibrium (Springel & Hernquist, 2005). As gas builds up and cools, it collapses and forms stars, which then provide feedback to halt the cooling, before eventually cooling again and repeating the process (e.g., Scannapieco et al., 2012; Agertz & Kravtsov, 2015, see also Emsellem et al. 2022 for an observational perspective). This galactic baryon cycle does not apply the same way to satellite galaxies. The reservoirs of cooling gas, the satellite CGM, are typically stripped away quickly at infall (Larson et al., 1980; Balogh & Morris, 2000), leaving only the pre-existing ISM gas. Observations have shown that the ram pressure adds an additional pressure term that compresses the ISM gas, which may temporarily increase the galaxy's SFR (Gavazzi et al., 2001; Roberts & Parker, 2020; Grishin et al., 2021); an increase in the SFR then implies an increase in stellar feedback, making the surrounding gas more susceptible to being removed by the ram pressure. A similar story has been suggested for SMBH feedback, whereby the compressed ISM leads to more efficient SMBH growth and higher AGN fractions in satellite galaxies undergoing ram pressure compared to centrals of the same mass (Poggianti et al., 2017a; Maier et al., 2022; Peluso et al., 2022). The processes governing star formation in the ISM and SMBH feedback and the effects of the ensuing feedback are put to the test in satellite galaxies. At any given time, the satellite population represent a distribution of infall times and cumulative ram pressure, so population averages of quantities related to on-going or recent star-formation are the most informative tests (Vulcani et al., 2018, 2024).

Satellites further probe more exotic areas of astrophysics not necessarily present in centrals. First, the bulk motions of satellites are often supersonic, which are thought to drive shocks in the halo gas (Yun et al., 2019). These shocks, especially in the case of massive satellite compared to the central (major mergers), drastically alter the thermodynamic properties of the halo gas, causing, for example, large sloshing morphologies in galaxy clusters that are visible in the X-ray (Markevitch et al., 2000; Vikhlinin et al., 2001; Johnson et al., 2010), which may also heat up the ICM (Dekel & Birnboim, 2008; Bykov et al., 2015). This may also cause a bow shock in our own Milky Way CGM caused by the Large Magellanic Cloud (Setton et al., 2023). Outflows from satellites may heat up and/or redistribute the surrounding gas. In the case of ram pressure stripped gas (see Section 3.3.1 for details), the stripped satellite gas can cool to form stars, which is one of the only instances in the Universe where stars form outside of galaxies. The outer-layers of the cool tails constantly mix with the hot medium, creating some warm mixing layer that shields the inner tail regions and allows them to cool (see, e.g., Sun et al., 2009; Poggianti et al., 2019; Campitiello et al., 2021). Lastly, magnetic fields may be crucial the evolution of jellyfish tails, potentially preventing mixing of of the cool tail and hot halo gas (e.g., Müller et al., 2021; Ignesti et al., 2022, see also Sparre et al. 2024 for a theroetical perspective). Thus, the observations of these extreme cluster jellyfish galaxies probe exciting areas of astrophysics that are may not be available in studies of central galaxies[4]

Moreover, the thermodynamic structure of the surrounding medium is crucial to the evolution of satellite galaxies. In a full cosmological context, the halo gas is not spherically averaged and smoothly varying, like some early analytic theories of hydrostatic halos predict. The halo gas represents a distribution of temperatures, densities, and velocities. Importantly, inflows, outflows, and turbulence cause the gas often not to be at rest with respect to BCG and alter the density distribution of the gas as a function of host mass (Fabian, 1994; Cicone et al., 2014; Simionescu et al., 2019). The feedback processes affecting the halo gas, namely stellar feedback in low-mass halos and SMBH feedback from high-mass halos, and cosmological effects related to accretion from the large scale structure all ultimately affect the cumulative ram pressure that satellites undergo. That is, satellites are thought to experience varying amounts of ram pressure due to the local gas density and relative velocity, which vary throughout a satellite's orbit (Bahé & McCarthy, 2015; Ayromlou et al., 2019). The population average cumulative ram pressure sustained throughout an orbit then varies based on the structure

[4]The underlying physics governing the cool, stripped gas relative to the hot ambient medium under this Kelvin-Helmholtz instability, which is commonly studied in cloud-crushing experiments and a common test of a hydrodynamic solver, sets the longevity of the cool tails. Both the gas mixing, which is sensitive to the hydrodynamic solver, and the star-formation in the tails, which is sensitive to the galaxy formation model, must be accurately described to reproduce the observations of star-formation in jellyfish tails. Thus, the evolution of simulated jellyfish galaxies depends on the (magneto-)hydrodynamic solver, the galaxy formation model, and the inclusion of additional physics such as ideal MHD. See Chapter 4 for more details.

of the halo gas, which, for most satellites in group and cluster mass halos, likely depends on the SMBH feedback from the central galaxy (Hlavacek-Larrondo et al., 2022). It has already been shown that different SMBH feedback models produce different anisotropic satellite quenching signals – that is, where satellites along a galaxy's minor axis have lower quenched fractions than satellites along a galaxy's major axis because the SMBH feedback lowers the CGM density along the minor axis (Martín-Navarro et al., 2021). Thus, satellites are not only sensitive to their own feedback but also that from the central.

Outside of the evolution of satellite galaxies themselves, accurately simulating the effects of satellites is essential to precision cosmology. The halo mass function is most sensitive to the number of massive clusters (Allen et al., 2011), which implicitly depends on cosmological parameters related to the matter power spectrum and evolution of density perturbations, making accurate estimates of cluster mass essential to measure cosmological parameters (e.g., Pillepich et al., 2018c). Two such ways to estimate cluster masses involve the number of satellites above a given stellar mass or magnitude, called the halo occupation distribution (HOD; Berlind & Weinberg, 2002; Hansen et al., 2009), and the total cluster X-ray luminosity (Pratt et al., 2009; Vikhlinin et al., 2009; Pillepich et al., 2012). The satellite stellar mass function is mostly determined by the cluster mass, but the exact amount of post-infall satellite star-formation varies from model to model, thereby affecting the predicted HOD used to calibrate the observations. As the satellites affect the thermodynamic properties of the halo gas, they naturally affect the halo's X-ray luminosity. Satellites may also contribute to the total X-ray flux – for example via X-ray binaries, AGN, and-or their own X-ray emitting gas – potentially biasing X-ray selected clusters and their estimated masses. The study of satellite galaxies provide tests ranging from hydrodynamic shocks to small scale cloud-crushing to cosmology.

4 Cosmological simulations of galaxies

Observations of galaxies provide information at one snapshot of their lives, which we then interpret to understand their current state and past history. Assuming that cosmological simulations today represent realistic galaxy populations today, then when observed and simulated galaxies appear similarly, researchers can infer unobservable properties about the observed galaxies based on the simulations. The same can also be done for gas and dark matter, although observing dark matter is notoriously challenging. Differing cosmological simulations make different choices related to: (i) how to solve the gravity + (magneto-)hydrodynamic equations of motion; (ii) which physics modules to include and how to implement them; and (iii) simulation parameters, such as mass/spatial resolution, targets of interest, and general scope of the simulation. No matter simulation, all cosmological simulations of galaxies have a similar starting point.

4.1 Necessary inputs, approximations, and ingredients

Running a cosmological simulation of galaxies is challenging, and making these galaxies and their environments realistic was nearly impossible, before roughly one decade ago (Somerville & Davé, 2015). Modern cosmological simulations all roughly reproduce realistic galaxy populations, although they employ different methods and tools to do so. While this makes the problem of galaxy formation appear degenerate, careful comparisons of simulations and observations, especially in the gaseous halos, potentially reveal areas for improvement for the next generation of simulations (Crain & Van De Voort, 2023). Here, I briefly describe the necessary inputs, approximations, and ingredients that all modern cosmological simulations include, where Fig. 4.1 outlines the basic principles.

Generating Initial Conditions

Cosmological simulations typically begin when the linear approximation to the growth of density perturbations breaks down, at approximately $z \approx 100 - 150$ (Fig. 4.1 top row).

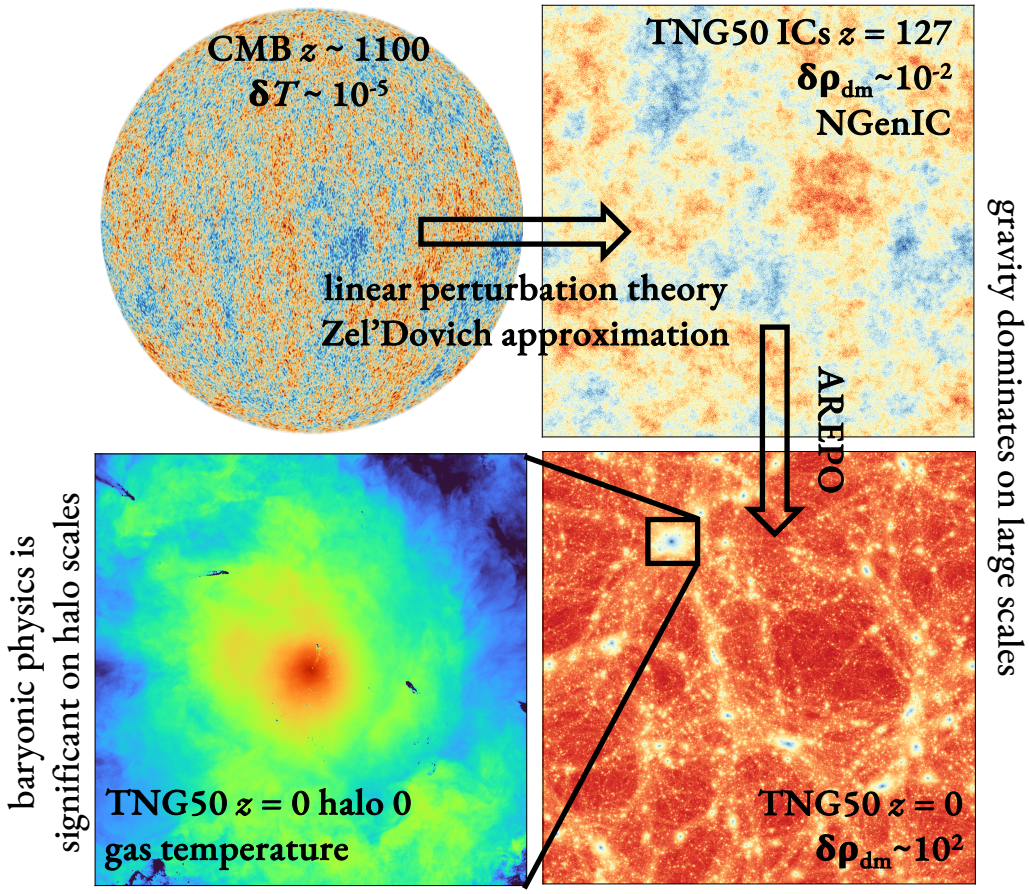

Figure 4.1: **Schematic for cosmological simulations of galaxies.** Cosmological simulations of galaxies start from the perturbations of the CMB at $z \sim 1100$, which are on the order of $\sim 10^{-5}$ (top left). The evolution of these temperature inhomogeneities can be well approximated using linear perturbation theory (the Zel'Dovich approximation Zel'dovich 1970) until $z \sim 130$ when the perturbations are on the order $\sim 10^{-2}$ (top right; here created with NGenIC, Springel et al. 2005b, as the initial conditions for TNG50, Pillepich et al. 2019; Nelson et al. 2019a), after which the gravitational collapse becomes non-linear, requiring a gravitational solver to accurately follow the collapse (AREPO, in this case for TNG50). At $z = 0$, the density perturbations are large, on the order of $\sim 10^2$ on halo scales ($\lesssim$ Mpc; bottom right). On halo scales and below, baryonic physics becomes significant, in addition to gravity, in determining the structure of the dark matter halo, the CGM, and the galaxy itself (bottom left; here, a gas temperature map of the most massive halo in TNG50). CMB image is adapted from (Planck Collaboration et al., 2020, credit: ESA and the Planck Collaboration).

The initial conditions are commonly generated using, NGenIC (Springel et al., 2005b) or MUSIC (Hahn & Abel, 2011). Specifically, these generators create a Gaussian random field of particles with positions, velocities, and masses that fill a given volume such that (i) the total matter density is consistent with Ω_m, and (ii) the initial positions satisfy the power spectrum. This requires a set of cosmological parameters – $\Omega_{m,0}$, $\Omega_{\rm bar,0}$, σ_8, n_s, and H_0 – within the flat ΛCDM context. The initial conditions generator then evolves the particle positions by solving the Poisson-Vlasov equation until the chosen redshift, typically using the Zel'Dovich approximation (Zel'dovich, 1970). This approach treats the cold dark matter as discretized particles; the gas follows the cold dark matter until this redshift, but there may be extra nuances related to how the main simulation discretizes the gas. Importantly, all cosmological simulations employ periodic boundary conditions, where the simulation volume is embedded in a larger universe, which is based on the cosmological principle that on large scales the Universe is isotropic and homogeneous.

Gravity + (Magneto-)Hydrodynamic Solvers

All modern cosmological simulation approximate cold dark matter and stars as collisionless particles. For a set of N collisionless particles, exactly solving the discretized Poisson-Vlasov equations scales $\propto N^2$, making such computations increasingly difficult for large numbers of particles. Computing the gravitational force on each discrete particle, which scales with the inverse square of the separation between two particles, requires a gravitational softening, such that the particles closer than this softening length do not form bound pairs, ensuing that the relaxation time of the system is cosmologically long and the collisionless approximation still holds (e.g., Thomas & Couchman, 1992; Merritt, 1995; Moore et al., 1998).

Ignoring direct summation methods, the softened gravitational force calculation can be using particle-mesh (PM) algorithms (Hockney & Eastwood, 1988), hierarchical multipole "tree" algorithms (Barnes & Hut, 1986; Dehnen, 2000), or some combination of the two (Bagla, 2002). Briefly, PM methods overlay a mesh on top of the particle distribution to obtain the mass density field, compute the potential in Fourier space using Green's function, calculate the force field from the potential, and update the accelerations at the original particle positions. While efficient and relatively simple to implement, the accuracy is limited to the size of the mesh cells, where small-scale errors may be large. Tree methods, specifically the Oct-Tree, hierarchically subdivide the simulation volume until each particle is alone in its own subvolume, or (sub-)node, where the empty subvolumes do not need to be stored. To compute the force on a given particle, one walks the tree and computes the partial force at each relevant (sub-)node, depending on some opening angle criterion setting the accuracy. After walking the tree for a single particle, the summation of each partial force yields the total

force, and this process for N particles scales as $\propto N \log_{10} N$. Tree methods, however, may scale sub-optimally when there is a large dynamic range of densities. Thus, combinations of the these methods are typically used to maximize accuracy and efficiency.

Two such noteworthy combinations are adaptive mesh refinement (AMR) methods (Villumsen, 1989; Couchman, 1991), which add additional levels of refinement on specific regions of interest (typically denser regions), and TreePM algorithms (Bagla, 2002), which separate the potential into long and short range forces, where PM algorithms solve the long range forces and Tree algorithms solve the short range forces. For most cases in cosmological simulations, besides for the dynamics around very dense regions such as star clusters and near SMBHs, the various codes are accurate enough, and significant difference are not expected for the dynamics of the collisionless dark matter and stellar particles.

The same cannot be said for the gas, however, which can exchange energy, momentum, and even mass between the resolution elements. The (magneto-)hydrodynamic equations for the gas are solved by approximating the gas as either particles in Lagrangian smoothed hydrodynamic particle (SPH; Lucy 1977; Gingold & Monaghan 1977; Monaghan 1992) codes, such as such as GADGET (Springel et al., 2001; Springel, 2005; Springel et al., 2021) and SWIFT (Schaller et al., 2016), or as cells that completely fill the simulation volume in Eulerian (mesh; Berger & Oliger, 1984; Berger & Colella, 1989) codes, such as RAMSES (Teyssier, 2002) and ENZO (Bryan et al., 2014). SPH codes naturally conserve the energy, momentum, and mass, but they may not capture discontinuities (shocks) and suppress mixing of multiphase gas (Springel, 2010a, and references therein). AMR codes, however, can better resolve shocks and mixing, but they are not Galilean invariant and may struggle to resolve fast-moving, high-density regions with complex geometries. There are newer methods that take the best parts of both SPH and AMR codes. GIZMO (Hopkins, 2015) is a meshless finite mass (or volume; using the Godunov method Gaburov & Nitadori, 2011) code based on GADGET, where the simulation region is split into overlapping cells based on the underlying particle distribution. Importantly, AREPO (Springel, 2010b; Pakmor et al., 2016; Weinberger et al., 2020) employs an unstructured dynamic mesh based on a Voronoi tessellation of the space based on mesh generating points, where the mesh naturally reshapes itself to better refine the densest regions. AREPO also has the benefit of being Galilean invariant and accurately treats discontinuities (shocks) and mixing between gas phases. The simulations used in this thesis were run using AREPO.

Simulating Baryonic Physics

In addition to the gravity and (magneto-)hydrodynamic solvers, simulations of galaxies require descriptions for baryonic physics. A majority of the processes are not resolvable in cosmolog-

ical simulations, requiring "subgrid" recipes to approximate the physical effects. Different cosmological simulations have slight differences in these subgrid routines, but a majority include the following processes:

- **Gas heating and cooling**: Gas is able to heat and cool following look-up tables based on the density, temperature and metallicity, where metal-line cooling is typically included (e.g., Sutherland & Dopita, 1993, see also Fig. 3.1). A UV background is typically included after reionization.

- **Multiphase ISM**: Most cosmological simulations allow gas cooling until temperatures of $\sim 10^4$ K, after which molecular cooling, dust, and local radiation effects (which are typically not modeled) become important (Wiersma et al., 2009a; Haardt & Madau, 2012). The ISM is then modeled as a two-phase medium, where the cold phase represents a majority of the mass and the hot phase, which has been heated by supernovae, represents a majority of the volume (Agertz et al., 2011; Dalla Vecchia & Schaye, 2012; Hopkins et al., 2012a).

- **Star formation**: Stars are able to form out of cool, collapsing gas, typically upon crossing a density threshold, e.g., $n > 0.1\,\mathrm{cm}^{-3}$, where the relation between density and temperature is determined by an effective equation of state (e.g., Springel & Hernquist, 2003). Individual stars are not resolved, but instead stellar particles represent entire populations based on some initial mass function (e.g., Kroupa, 2001; Chabrier, 2003).

- **Stellar evolution and feedback**: As the stellar populations evolve, they return mass, metals, and energy/momentum to the surrounding ISM via Type Ia and II supernovae, asymptotic giant branch stars, and neutron star mergers (Wiersma et al., 2009b; Vogelsberger et al., 2013). The supernovae, modeled either as thermal/kinetic energy injections or via decoupled hydrodynamics, in addition to stellar winds, photoionization, and radiation pressure can drive galactic outflows (Springel et al., 2005a; Hopkins et al., 2012b; Agertz et al., 2013; Hopkins et al., 2014, 2018).

- **SMBH seeding, growth, and merging**: SMBHs are seeded in the centers of halos, typically when the halo crosses some mass threshold. The SMBH is able to accrete gas from the surrounding ISM, typically via Bondi-Hoyle accretion with a maximum accretion rate determined by the Eddington limit (Springel et al., 2005a; Hopkins et al., 2006; Hopkins & Quataert, 2011). The SMBHs are usually re-positioned to stay at the centers of their host galaxies, and when two SMBHs approach either other, they merge.

- **SMBH feedback**: SMBHs return energy and/or momentum to the surrounding gas in the form of feedback. There are different approaches on how to model this feedback,

but some form of strong feedback is required to quench the star formation of massive central galaxies (Di Matteo et al., 2005; Sijacki et al., 2007; Weinberger et al., 2018).

Of particular importance are the stellar and SMBH feedback models, as these are crucial for regulating the star formation in low- and high-mass halos and reproducing the stellar to halo mass relation (Behroozi et al., 2010; Moster et al., 2013; Wechsler & Tinker, 2018).

In addition to the more/less required models listed above, additional physical processes can also be included. Including magnetic fields in the form of ideal MHD can provide non-thermal pressure support in the interstellar medium (Ferrière, 2001; Pakmor et al., 2011; Pakmor & Springel, 2013), and, in conjunction with cosmic rays, can drive galactic outflows (Field et al., 1969; Uhlig et al., 2012; Pakmor et al., 2016). Simulations of the epoch of reionization model radiation transfer (Rosdahl et al., 2018; Ocvirk et al., 2020; Kannan et al., 2022), which are also useful in simulating direct observables such as emission line fluxes (Katz et al., 2023). Lastly, on the fly dust production allows for more direct comparisons for observations and can inform observers about dust to gas mass ratios (Davé et al., 2019).

4.2 Overview of current cosmological galaxy simulations

Cosmological simulations of galaxies are a subset of both cosmological simulations and galaxy simulations, where cosmological simulations also encompass dark matter only simulations (such as the Millennium simulation; Fig. 2.1) and galaxy simulations could also be idealized (e.g., Springel & Hernquist, 2005, see also Naab & Ostriker 2017; Vogelsberger et al. 2020). In this thesis, I only consider cosmological simulations of galaxies, requiring cosmological initial conditions and baryon physics, which come in two flavors: full volume (also called uniform box) simulations and zoom-in simulations (zoom-ins, for short). Full volume simulations simulate the entire volume of the simulation at the same mass resolution and offer large sample statistics. Zoom-in simulations require a region of interest, chosen from a lower-resolution dark matter only (full volume) simulation, and increase the resolution only in this region, keeping the rest of the simulation volume at a lower, background resolution. While decreasing the sample size, this technique allows for much higher resolution than what would otherwise be feasible in a full volume simulation. Ideally, the best simulation would be a full volume, high resolution ($m_{\rm bar} \lesssim 10^2\,{\rm M}_\odot$), and large volume ($\sim {\rm Gpc}^3$) simulation, which includes all relevant physical processes, but this is not currently possible due to available computational resources. When designing a simulation, one must carefully consider the type of simulation, the resolution, and the volume (or specified regions for zoom-ins) and how this affects the

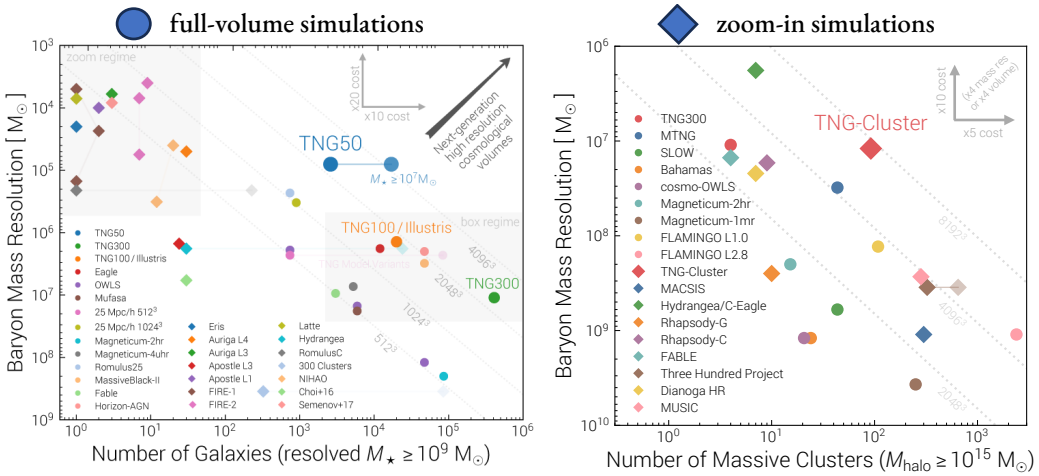

Figure 4.2: **Overview of cosmological simulations of galaxies and galaxy clusters.** A comparison of modern cosmological simulation in the mass resolution – number of resolved galaxies (left) or massive clusters (right) plane. Both TNG50 and TNG-Cluster are unparalleled in their combination of resolution and sample size, in addition to boasting a sophisticated, well-validated model for galaxy formation and evolution. Figures are adapted from (Nelson et al., 2019a, 2024).

scope of the simulation. In this thesis, I employ both cosmological simulations of galaxies, based on full volume simulations, and cosmological simulations of galaxy clusters, based on a collection of zoom-in simulations. Specifically, I use the TNG50 simulation, the highest resolution (full volume) simulation from the IllustrisTNG project, and TNG-Cluster, a collection of 352 zoom-in simulations of massive galaxy clusters. Here, I briefly put these two simulations into context with the other current simulations of galaxies and galaxy clusters, which is summarized in Fig. 4.2.

Cosmological Simulations of Galaxies

Fig. 4.2 (left panel) summarizes the current cosmological simulations of galaxies, where circle points refer to full volume (uniform box) simulations and diamonds refer to zoom-in simulations. These simulations focus on galaxies of stellar mass $\sim 10^{9-11}$ $M_\odot$, where each galaxy is composed of hundreds to thousands (or more) of resolution elements. TNG50 occupies an otherwise empty place in this phase space of mass resolution and sample size. Of particular interest are the other flagship simulations from the IllustrisTNG project, TNG100 (orange circle) and TNG300 (green circle), in addition to the other publicly released simulations Illustris (the predecesssor of IllustrisTNG; orange circle, as it has the same volume and resolution as TNG100; Vogelsberger et al., 2014b,a; Genel et al., 2014; Sijacki et al., 2015), EAGLE (red circle Crain et al., 2015; Schaye et al., 2015) and SIMBA (not included here, but with mass

resolution $m$bar $\approx 1.8 \times 10^7$ $M_\odot$ and slightly more resolved galaxies than TNG100, Illustris, and EAGLE Davé et al., 2019). These simulations, TNG100 (or TNG50, TNG300), EAGLE, and SIMBA, all employ different gravity-magneto-hydrodynamic solvers and galaxy formation models but still reproduce, for example, galaxy stellar mass functions that are consistent with observations. TNG100 and Illustris use the same initial conditions, where comparisons of these simulations with each other and with observations can be used to rule out galaxy formation models, since the large scale effects can be controlled (e.g. Martín-Navarro et al., 2021). Additionally, recent comparisons of the halo gas in these simulations find stark differences between the model predictions, where future observations of the CGM can be used to rule out certain models (Ayromlou et al., 2023b; Wright et al., 2024).

Cosmological Simulations of Galaxy Clusters

Fig. 4.2 (right panel) summarizes the current cosmological simulations of galaxy clusters, where galaxy clusters have total halo masses $\gtrsim 10^{15}$. As galaxy clusters are some of the rarest gravitationally collapsed objects in the Universe, simulating them requires large volumes, thereby decreasing the average resolution compared to simulations of galaxies. TNG-Cluster and its 352 galaxy clusters opens a new realm to statistically study galaxy clusters, BCGs, the ICM, and cluster satellites. Two other recent large volume simulations to note are MillenniumTNG (MTNG, blue circle; Pakmor et al., 2023), which uses the original Millennium simulation volume and the galaxy formation model from the IllustrisTNG project, and FLAMINGO (Schaye et al., 2023), whose $(2.8\ \mathrm{Gpc})^3$ volume is the largest hydrodynamic simulation of galaxy clusters that exists. MillenniumTNG and FLAMINGO are both uniform box simulations, where they both specialize in cosmological applications compared to the zoom-in nature of TNG-Cluster. In terms of philosophy and scope of the simulation, the Three Hundred Project (Cui et al., 2018) is the most similar to TNG-Cluster.

4.3 The IllustrisTNG and TNG-Cluster simulations

The IllustrisTNG[1] (hereafter, TNG; Pillepich et al., 2018b; Nelson et al., 2018a; Naiman et al., 2018; Marinacci et al., 2018; Springel et al., 2018) and TNG-Cluster[2] (Nelson et al., 2024, Pillepich et al. in prep.) simulations evolve CDM, gas, stars within an expanding universe based on a self-gravity and MHD framework (Pakmor et al., 2011; Pakmor & Springel, 2013) using the arepo code (Springel, 2010b; Pakmor et al., 2016; Weinberger et al., 2020) and with the TNG galaxy formation model (Weinberger et al., 2017; Pillepich et al., 2018a). The TNG production

[1] https://www.tng-project.org/
[2] www.tng-project.org/cluster/

simulations come in three volumes of side lengths ~ 50, 100, and 300 comoving Mpc, hereafter referred to as TNG50, TNG100, and TNG300 respectively. The TNG galaxy formation model was designed at the resolution of TNG100, with baryon mass resolution of $m_{\rm bar} = 1.4 \times 10^6\,{\rm M}_\odot$. The large volume TNG300 has baryon mass resolution $m_{\rm bar} = 1.1 \times 10^7\,{\rm M}_\odot$. The high resolution TNG50 simulation has mass resolution $m_{\rm bar} = 8.5 \times 10^4\,{\rm M}_\odot$ (Nelson et al., 2019b; Pillepich et al., 2019). These three simulations are publicly available in their entirety (Nelson et al., 2019a).

TNG-Cluster is a suite of 352 massive galaxy cluster simulations, spanning halo masses $M_{\rm 200c} \approx 10^{14.3-15.4}\,{\rm M}_\odot$. These halos were chosen from a $\approx$ 1 Gpc box-size parent dark matter only simulation. The 352 halos chosen for re-simulation are based only on $z = 0$ halo mass such that: (i) all ~ 90 halos with mass $> 10^{15}\,{\rm M}_\odot$ are included; and (ii) halos with mass $10^{14.3-15.0}\,{\rm M}_\odot$ were randomly selected in bins of 0.1 dex such that the halo mass distribution is flat over this mass range (see Nelson et al., 2024, for details). No other halo properties were considered in this mass range, such that the clusters are unbiased to properties such as the richness, relaxedness, or cool-coredness. The baryon mass resolution of TNG-Cluster is $m_{\rm bar} = 1.1 \times 10^7\,{\rm M}_\odot$, the same resolution as TNG300.

In the TNG and TNG-Cluster simulations, group and galaxy catalogs consist of the dark matter halos and galaxies. The dark matter halos are defined using the Friends-of-Friends (FoF) algorithm with a linking length $b = 0.2$, run using only the dark matter particles (Davis et al., 1985). The baryonic components – the gas, stars, and SMBHs – are connected to the same halos as the closest dark matter particle. Throughout this thesis, I use "FoF", "group", "FoF group", and "halo" synonymously. At time, I refer to halos of mass[3] ~ $10^{13-14}\,{\rm M}_\odot$ as "galaxy groups" and halos of mass ~ $10^{14-15.4}\,{\rm M}_\odot$ as "galaxy clutsers". The galaxies are identified using the SUBFIND algorithm, which connect gravitationally bound particles together (Springel et al., 2001; Dolag et al., 2009). I use the terms "subhalo" and "galaxy" synonymously even though, in general, SUBFIND objects may contain no stars and/or gas whatsoever. The most massive subhalo within a halo is then the "main" or "primary subhalo", also called the "central galaxy"; all other subhalos within a halo are "satellites", although at times I may add additional criteria. In all cases, I only consider subhalos of a cosmological origin as defined by the SubhaloFlag in Nelson et al. (2019a). I connect galaxies with their progenitors and descendants using SUBLINK_GAL, which searches for progenitors/descendants with common stellar particles and star-forming gas cells (Rodriguez-Gomez et al., 2015).

[3] Throughout this thesis, I refer to the halo mass as $M_{\rm 200c}$, the mass enclosed by the halo radius $R_{\rm 200c}$ such that the total average enclose density is equal to 200 times the critical density of the universe (Eq. 2.6) at that time.

The TNG galaxy formation model

The TNG galaxy formation model builds upon the largely successful Illustris model (Vogelsberger et al., 2014b,a; Genel et al., 2014; Sijacki et al., 2015). The fluid dynamics employ a Voronoi tessellation to spatially discretize the gas. Here, I briefly list the main elements of the TNG galaxy formation model:

- **Ideal MHD**: At the start of the simulation at $z = 127$, a uniform magnetic field of strength $\approx 10^{-14}$ G is seeded and allowed to evolve and amplify via small-scale dynamos, although the results are insensitive to the exact value of the seed field strength (Pakmor et al., 2011; Pakmor & Springel, 2013; Marinacci et al., 2015; Rieder & Teyssier, 2016; Pakmor et al., 2017).

- **Gas heating and cooling**: Gas is able to heat and cool, including metal-line cooling, based on the redshift, gas temperature, gas density, and gas metallicity following (Smith et al., 2008; Wiersma et al., 2009a) in the presence of a redshift-dependent UV background (Katz et al., 1992; Faucher-Giguère et al., 2009) and, for gas cells near SMBHs, the radiation field from the AGN (Vogelsberger et al., 2013).

- **Multiphase ISM** The TNG gas has a temperature floor at 10^4 K, and the relationship between temperature and density for star-forming gas is determined via an effective equation of state from Springel & Hernquist (2003). This model assumes a two-phase ISM, where the cold phase dominates the mass and the hot phase dominates the volume, and the relative pressure contributions of the two phases are affected by unresolved stellar feedback.

- **Star formation**: Cool gas denser than $n \gtrsim 0.1\,\mathrm{cm}^{-3}$ is able to form stars probabilistically based on the Kennicutt-Schmidt Law (Schmidt, 1959; Kennicutt, 1998) assuming a Chabrier initial mass function Chabrier (2003).

- **Stellar evolution and feedback**: After birth, stellar populations evolve and return mass and metals to the neighboring ISM via asymptotic giant branch stars, Type Ia, and Type II supernovae. While only the total metallicity (instead of individual abundances) is used for the gas cooling, the following individual abundances are tracked: H, He, C, N, O, Ne, Mg, Si, and Fe. Galactic winds, which are powered by ejecting star-forming gas cells by Type II supernovae, are decoupled from the hydrodynamics and travel until they reach a background density lower then $\lesssim 5 \times 10^{-3}\,\mathrm{cm}^{-3}$, $\approx 5\%$ that of the star formation threshold, or after 2.5% of the current Hubble time (Pillepich et al., 2018a).

- **SMBH formation, repositioning, and merging**: SMBHs are seeded at a mass of $\approx 1.2\times10^6\ M_\odot$ in the centers of halos with a total Friends of Friends mass $\approx 7.5\times10^{10}\ M_\odot$ that do not already have a SMBH. At every global time step, the SMBH is re-positioned to the minimum of the local gravitational potential over the nearest ≈ 1000 resolution elements, if it is not already there, and the velocity is set to the mass-weighted average of the local region. If there is another SMBH within this region, then the two SMBHs merge (Weinberger et al., 2017).

- **SMBH accretion and feedback**: SMBHs can accrete material from the surrounding ISM via Bondi-Hoyle-Lyttelton accretion (Hoyle & Lyttleton, 1939; Bondi & Hoyle, 1944; Bondi, 1952), where the maximum accretion rate is given by the Eddington limit. SMBHs can accrete in either a high or low accretion state, where the state depends on the Eddington fraction – the actual (Bondi) accretion rate normalized by the Eddington accretion rate. This pivot threshold is a function of the SMBH mass and is designed such that SMBHs of mass $\lesssim 10^8\ M_\odot$ usually accrete in the radiatively-efficient, "quasar", high-accretion mode, and SMBHs of mass $\gtrsim 10^8\ M_\odot$ tend to switch to a radiatively-inefficient, "radio", low-accretion state. In the high accretion state, the SMBH feedback is via a thermal energy injection to the local environment; in the low accretion state, the feedback is via kinetic energy injections in random directions that change for each injection, where the energy and momentum are conserved in a time-averaged sense. (Weinberger et al., 2017).

Early results and validations of the TNG model

At the time of writing this thesis, over 900 papers have used results from the IllustrisTNG simulations, making them the most used and cited cosmological simulations of galaxies that exist. In addition to the initial results from the TNG simulations (Springel et al., 2018; Nelson et al., 2018a; Naiman et al., 2018; Marinacci et al., 2018; Pillepich et al., 2018b), there are a number of earlier works and validations that are especially relevant for this thesis. Moreover, as TNG-Cluster is at the same resolution as TNG300, I expect the validations of TNG300 to hold as well for TNG-Cluster, although TNG-Cluster includes clusters more massive than those that exist in TNG300.

- (Yun et al., 2019) undertake a pilot study of jellyfish galaxies in TNG100, finding that jellyfish galaxies are more frequently found at intermediate and large host-centric distances, in more massive hosts, and with lower satellite stellar masses. The satellites tend to orbit supersonically and are correlated with the presence of bow shocks in the halo gas.

- Satellite galaxies in TNG simulations have atomic H I (Stevens et al., 2019) and molecular H II (Stevens et al., 2019) gas contents that are consistent with recent observations. Central and satellite quenched fractions are in good agreement with mass-matched results from SDSS (Donnari et al., 2021a).

- The overall properties of clusters in the TNG simulations are realistic in their, for example, ICM metallicity profiles (Vogelsberger et al., 2018), cool-core properties (Barnes et al., 2018), quenched fractions (Donnari et al., 2019), X-ray luminosities (Truong et al., 2020), and satellite populations (Stevens et al., 2019, 2021; Donnari et al., 2021a; Ayromlou et al., 2021a).

- The initial results from TNG-Cluster are also in general agreement with observations of the halo gas fraction, Faraday rotation, synchrotron emission, X-ray luminosities, thermal Sunyaev-Zeldovich signal (Nelson et al., 2024), cluster core properties (Lehle et al., 2024), gas motions and velocity dispersions (Ayromlou et al., 2023a), X-ray inferred kinematics of Perseus-like clusters (Truong et al., 2024), and radio relic morphologies (Lee et al., 2024).

5 Goals and rationale of the thesis

This thesis investigates the distribution and evolution of gas throughout halos, encompassing the different gaseous components such as the intracluster/circumgalactic medium, central galaxy, and satellite galaxies. The gaseous halos around galaxies have been shown by observations to be multiphase, where it is believed that the different components of such gaseous halos are affected by processes like accretion, feedback, and environmental interactions. By examining the flow of gas between these components and how they evolve over time, this thesis places particular emphasis on the role of environmental processes, specifically ram pressure stripping, in shaping the gas content of both satellite and central galaxies.

Particularly, the goal of this thesis is to study how the local halo environment affects the gaseous reservoirs of infalling satellite galaxies and, conversely, how satellite galaxies influence the physical properties and evolution of gaseous halos of their hosts. In this thesis, I challenge canonical ideas about the evolution of satellite and central galaxies, expand the applicability of these ideas to a broader range of systems, and propose observational tests to evaluate the simulation predictions. My approach involves visualizing the simulation outputs and analyzing how each physical process contributes to the bigger picture. I test my hypotheses using large datasets that allow for control over multiple variables simultaneously, revealing clearer distinctions between primary and secondary effects.

To achieve this, I track the evolution of both central and satellite galaxies, including their multiphase gaseous atmospheres, over the past $\approx$ 13 billion years. I utilize the cosmological magneto-hydrodynamic simulations TNG-Cluster, which consist of 352 zoom-in simulations of massive galaxy clusters at present, and TNG50, the highest-resolution simulation from the IllustrisTNG simulation suite. These simulations employ the well-tested TNG galaxy formation model and were run using the moving-mesh code AREPO. The unprecedented combination of sample size and resolution in these simulations allows for more detailed and accurate studies of these topics than have been possible before.

The objectives of the three scientific chapters that follow are as follows:

1. Introduce or reintroduce the relevant background literature, fundamental concepts, key questions to be addressed, and the tools and datasets used to answer those questions;

2. Address the scientific questions of each chapter using novel tools and samples, determining whether the new results align with or challenge canonical literature;
3. Investigate the physical processes driving these results by considering new or additional mechanisms or by approaching the problems from fresh perspectives;
4. Discuss the broader implications of these findings, considering how they can expand existing theories of galaxy evolution and/or propose observational tests to evaluate the simulation results and underlying TNG galaxy formation model;
5. Review the limitations of the chapter and suggest future directions for improving, expanding, or testing these novel results.

5.1 Outline for the remainder of the thesis

Fig. 5.1 outlines Part II: The Main Scientific Results:

- In Chapter 6, I answer whether $z = 0$ cluster satellites are able to retain their own CGM. Using the $\approx 90,000$ satellites of present-day stellar mass $\sim 10^{9-12}\,M_\odot$ in 352 clusters of mass $\sim 10^{14.3-15.4}\,M_\odot$ in TNG-Cluster, I present a demographic overview of the satellites and their multiphase gaseous reservoirs and the relevant physical processes, namely ram pressure and SMBH feedback. I provide interpretations for current and upcoming soft X-ray observations of galaxy clusters based on the spatially extended X-ray emission of cluster satellites. I propose a stacking experiment to statistically constrain the physics across populations of cluster satellites. Lastly, I quantify the covering fraction and overall satellite contribution to the total soft X-ray emission in galaxy clusters.
- In Chapter 7, I explore when, where, and for how long ram pressure stripping of cold gas (temperatures $\lesssim 10^{4.5}$ K) in jellyfish galaxies occurs. I track ≈ 500 unique jellyfish branches from TNG50 of stellar mass $\sim 10^{8-10.5}\,M_\odot$, currently living in hosts of mass $\sim 10^{12-14.3}\,M_\odot$, from when they were centrals through infall until today. Specifically, I use the Monte Carlo tracer particles to determine how much cold gas is lost due to ram pressure throughout their orbits. I demonstrate the diversity in ram pressure stripping timescales and their dependencies on host mass, stellar mass, and orbital parameters, where there are also clear connections between stripping of cold gas and quenching of star formation. Moreover, I compute how much cold gas is deposited into the host halos by ram pressure and compare this to the amount of cold gas that exists in halos today.

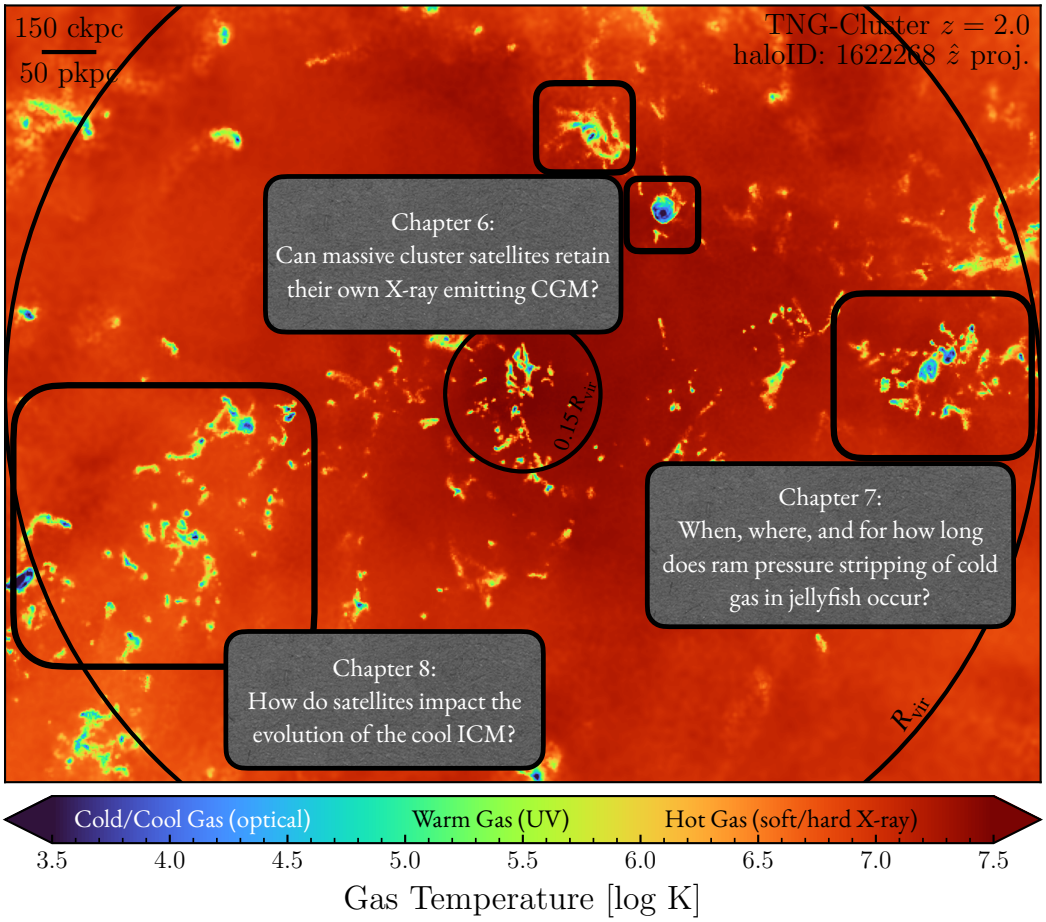

Figure 5.1: **Outline for the main science chapters.** This temperature projection of a $z = 2$ cluster from TNG-Cluster shows a hot ICM ICM with many cool clouds connected to satellites scattered throughout. I juxtapose the main question of each science chapter with examples of the relevant physics at play. The (inner) outer circles mark (0.15) R_{200c}.

- In Chapter 8, I present the evolution of the cool ICM in TNG-Cluster over the past $\approx$ 13 billion years, since $z \sim 7$, and attempt to explain the physical processes responsible for its evolution. Namely, I consider the effects of gas accretion from the large scale structure, gas heating and cooling, infalling satellite galaxies, and SMBH feedback on the evolution of the cool ICM mass. I suggest that some of the star-forming ICM originates from satellite galaxies, either as gas that was directly removed or perturbed to cool by the passage of the satellite, and that this star formation could be observable. Lastly, I predict the Mg II column density around galaxy clusters as functions of cluster mass and redshift, explicitly showing how satellites and other interloping halos in projection contribute Mg II ions to the ICM and compare the predictions with recent observations.

In Chapter 9, I summarize the main results from Chapters 6, 7, and 8, emphasizing the results that challenge long-standing beliefs about galaxy evolution and-or propose observational tests of the simulations. In Chapter 10, I put these results in context with recent literature, discuss the limitations of the thesis, and introduce some future work to address these limitations. Finally, I conclude with some final thoughts in Chapter 11.

II. Main Scientific Results

6 The Hot Circumgalactic Media of Massive Cluster Satellites in the TNG-Cluster Simulation: Existence and Detectability

This chapter is based on the article Rohr et al. (2024), which I led as the first author, where I conducted the main scientific direction of the paper, performed the analysis, created the figures, and wrote the text. Additional authors and their contributions include: Annalisa Pillepich, who assisted in the scientific direction, helped organize the final structure of the paper, and significantly edited the text; Dylan Nelson, who computed the soft X-ray luminosities, assisted in the scientific direction, and edited the text; Mohammadreza Ayromlou, who computed the instantaneous ram pressure for all satellites and provided comments to the text; and Elad Zinger, who provided comments to the text.

This paper was part of the TNG-Cluster first results splash, where the following papers were released on arXiv on the same day: Nelson et al. (2024); Ayromlou et al. (2023a); Lee et al. (2024); Lehle et al. (2024); Rohr et al. (2024); Truong et al. (2024). I contributed as a co-author to Nelson et al. (2024); Ayromlou et al. (2023a); Lehle et al. (2024), primarily by contributing insights during the initial data analysis and providing comments to the texts. The TNG-Cluster simulation was led by PIs Dylan Nelson and Annalisa Pillepich and executed on a various machines: the HoreKa supercomputer, funded by the Ministry of Science, Research and the Arts Baden-Württemberg and by the Federal Ministry of Education and Research; the bwForCluster Helix supercomputer, supported by the state of Baden-Württemberg through bwHPC and the German Research Foundation (DFG) through grant INST 35/1597-1 FUGG; the Vera cluster of the Max Planck Institute for Astronomy (MPIA), as well as the Cobra and Raven clusters, all three operated by the Max Planck Computational and Data Facility (MPCDF); and the BinAC cluster, supported by the High Performance and Cloud Computing Group at the Zentrum für Datenverarbeitung of the University of Tübingen, the state of Baden-Württemberg through bwHPC and the German Research Foundation (DFG) through grant no INST 37/935-1 FUGG.

TNG-Cluster is based on the AREPO code and employs the TNG galaxy formation model from the IllustrisTNG team (PI: Volker Springel; additional references can be found on the TNG website here), which is a follow-up of the original Illustris simulation. Additional analysis was carried out on the Vera supercomputer from the MPCDF.

ABSTRACT

The most massive galaxy clusters in the Universe host tens to hundreds of massive satellite galaxies $M_\star \sim 10^{10-12.5}\,\mathrm{M}_\odot$, but it is unclear if these satellites are able to retain their own gaseous atmospheres. We analyze the evolution of $\approx$ 90,000 satellites of stellar mass $\sim 10^{9-12.5}\,\mathrm{M}_\odot$ around 352 galaxy clusters of mass $M_{200c} \sim 10^{14.3-15.4}\,\mathrm{M}_\odot$ at $z = 0$ from the new TNG-Cluster suite of cosmological magneto-hydrodynamical galaxy cluster simulations. The number of massive satellites per host increases with host mass, and the mass–richness relation broadly agrees with observations. A halo of mass $M_{200c}^{\mathrm{host}} \sim 10^{14.5}$ (10^{15}) $\mathrm{M}_\odot$ hosts $\sim$ 100 (300) satellites today. Only a minority of satellites retain some gas, hot or cold, and this fraction increases with stellar mass. lower-mass satellites $\sim 10^{9-10}\,\mathrm{M}_\odot$ are more likely to retain part of their cold interstellar medium, consistent with ram pressure preferentially removing hot extended gas first. At higher stellar masses $\sim 10^{10.5-12.5}\,\mathrm{M}_\odot$, the fraction of gas-rich satellites increases to unity, and nearly all satellites retain a sizeable portion of their hot, spatially extended circumgalactic medium (CGM), despite the ejective activity of their supermassive black holes. According to TNG-Cluster, the CGM of these gaseous satellites can be seen in soft X-ray emission (0.5-2.0 keV) that is, $\gtrsim$ 10 times brighter than the local background. This X-ray surface brightness excess around satellites extends to $\approx 30 - 100$ kpc, and is strongest for galaxies with higher stellar masses and larger host-centric distances. Approximately 10 percent of the soft X-ray emission in cluster outskirts $\approx 0.75 - 1.5 R_{200c}$ originates from satellites. The CGM of member galaxies reflects the dynamics of cluster-satellite interactions and contributes to the observationally inferred properties of the intracluster medium.

6.1 Introduction

Since the 1950s, astronomers have been observing absorption lines in the spectra of background sources due to gas along the line of sight, including in the gaseous halos of intervening galaxies. This circumgalactic medium (CGM) is an enigmatic component of the baryonic Universe, and a necessary element for a comprehensive picture of galaxy evolution (see Tumlinson et al., 2017; Faucher-Giguère & Oh, 2023, for recent reviews). The CGM is the interface between gas that is expelled from the galaxy due to stellar and active galactic nucleus (AGN) feedback, and gas flowing into the halo from the intergalactic medium (IGM), as well as from satellite galaxies (hereafter satellites).

To first approximation, the CGM is a thermally pressure-supported atmosphere in rough hydrostatic equilibrium (Rees & Ostriker, 1977; Silk, 1977; White & Rees, 1978). With increasing halo mass and virial temperature, the CGM also becomes hotter and emits at progressively higher energies. Inflowing gas is expected to be shock-heated to approximately the same virial temperature or, depending on galaxy mass and redshift, to penetrate toward the inner regions (Kereš et al., 2005; Dekel & Birnboim, 2006; Faucher-Giguere et al., 2011; Nelson et al., 2016). However, outflows, inflows, and the quasi-static CGM are all multiphase, and can contain cold, molecular components as well as hot, virialized phases. As a result, the CGM is a complex component of the galactic ecosystem that is shaped by the complex interplay

of physical processes including gas cooling, magnetic fields, galactic feedback, filamentary inflows, and galaxy mergers and satellites (e.g., Sarazin, 2002; Voit, 2005; Peeples et al., 2019; Nelson et al., 2020; Ramesh et al., 2023a). Within the current cosmological paradigm, all massive central galaxies (hereafter centrals) are expected to be surrounded by a gaseous halo or CGM, embedded within a halo of cold dark matter. The picture for satellites orbiting within the halo of a more massive central galaxy is, however, less clear. It is unknown if satellites can retain their own CGM after they begin interacting with their host halo.

Satellite and central galaxies differ in many respects. Observationally, satellites have higher elliptical and S0 fractions, higher quenched fractions, lower (specific) star formation rates (SFRs), redder colors, lower neutral and molecular gas fractions, elevated gas metallicities, reduced X-ray emission, and suppressed AGN activity compared to centrals of the same mass (e.g., Dressler, 1980; Giovanelli et al., 1985; Wetzel et al., 2013; Peng et al., 2010, 2012; Brown et al., 2016; Maier et al., 2019a,b; Cortese et al., 2021; Boselli et al., 2022). A number of physical mechanisms have been invoked to explain these differences (see Cortese et al., 2021, for a recent review), many of which are related to the hydrodynamical interaction between the gas of the satellites and the ambient gaseous halo of their hosts.

Starting from the outermost scales and working inward, satellites are thought to be cut off from the intergalactic medium (IGM), removing a source of gas replenishment (Larson et al., 1980). Satellite gas is vulnerable to ram pressure stripping (RPS), which directly removes gas preferentially from the outside in (Gunn & Gott, 1972; McCarthy et al., 2008; Boselli et al., 2022, for a recent review). First, the gaseous halo of the satellite is stripped, after which it is no longer able to accrete from its own CGM (Balogh & Morris, 2000). Moreover, gas accretion from the ambient medium is expected to be strongly suppressed (van de Voort et al., 2017; Wright et al., 2020). Finally, ram pressure can also directly remove the interstellar medium (ISM) of satellites, likely in an outside in fashion as inferred by observations of truncated disks (e.g., Warmels et al., 1988a; Cayatte et al., 1990, 1994; Vollmer et al., 2001; Lee et al., 2022b). Consequently, RPS deposits the CGM and ISM of satellites into the gaseous halos of their hosts (e.g., Rohr et al., 2023; Roy et al., 2024).

Simultaneously with these environmental effects, the ISM and CGM gas of satellites is subject to internal stellar and AGN feedback processes. These feedback processes increase the effectiveness of RPS (e.g., Bahé & McCarthy, 2015; Ayromlou et al., 2021b; Kulier et al., 2023). Several observations suggest that ram pressure may compress the ISM and temporarily enhance star formation (e.g., Gavazzi et al., 2001; Vulcani et al., 2018; Roberts et al., 2022a) and AGN activity (e.g., Poggianti et al., 2017b; Peluso et al., 2022, contra: Roman-Oliveira et al. 2018) before eventually removing most satellite gas. This ram pressure driven increase in ISM gas density has also been seen in some idealized simulations of individual satellites (Lee

et al., 2020; Choi et al., 2022; Zhu et al., 2024) and to cause bursts of star formation also in cosmological volume galaxy simulations (Göller et al., 2023).

The effectiveness of RPS increases with host mass. Furthermore, at fixed host mass, ram pressure stripping is expected to become more important with decreasing satellite stellar mass, since the satellite stellar body acts as the gravitationally restoring force opposing ram pressure (e.g., Wright et al., 2022; Zinger et al., 2024). However at galaxy stellar masses $\gtrsim 10^{10.5}\mathrm{M}_{\odot}$ AGN feedback is expected and inferred to become more efficient at ejecting gas and quenching galaxies (e.g., Silk & Rees, 1998; Schawinski et al., 2007; Fabian, 2011), both in centrals and satellites (e.g., Bluck et al., 2020; Joshi et al., 2020; Donnari et al., 2021b). After the ISM has been largely ejected, it becomes more susceptible to ram pressure removal. As a result, the retention of hot CGM and cold ISM gas reservoirs, on timescales of Myr to Gyr, depends sensitively on both satellite mass as well as host halo mass.

The low density and surface brightness of the CGM have made it difficult to directly observe in emission, but recent instrumentation and surveys have detected the CGM of single and stacked galaxies in the optical/UV (e.g., Hayes et al., 2013; Leclercq et al., 2022; Dutta et al., 2023), X-ray (e.g., Bogdan et al., 2013; Comparat et al., 2022; Chadayammuri et al., 2022), and even the radio (Chen et al., 2024). For satellites, the first detection of a gaseous corona in emission was the Large Magellanic Cloud (LMC) using *Hubble Space Telescope* spectra (Wakker et al., 1998; Krishnarao et al., 2022). Using *Chandra*, Sun et al. (2007) detect X-ray galactic coronae with temperatures $kT \approx 0.5 - 1.1$ keV in ≈ 60 percent of super-L_* galaxies residing in clusters, implying CGM stripping timescales of several Gyrs. Goulding et al. (2016) detect X-ray emission within the stellar effective radius of 33 early-type systems in the MASSIVE survey, a fraction of which are not the central of their group or cluster. Babyk et al. (2018) extract X-ray scaling relations out to five times the stellar effective radius of 94 early-type galaxies in the local Universe, many of which are satellites of nearby groups and clusters. Zhang et al. (2019) find in stacked SDSS spectra suppressed Hα + [N II] emission from the CGM of $\sim$ L$_\star$ galaxies that are in denser environments (see also Burchett et al. 2018). Lastly, Hou et al. (2024) and Zhang et al. (2024) find X-ray emission around satellites in stacked *Chandra* and eROSITA observations (see also Hou et al. 2021). However, it remains unclear what percentage of satellites today retain hot gas reservoirs, and to what extent their CGM have been damaged by the environment of their hosts, especially if these are massive groups and clusters of galaxies.

Despite the relatively low number statistics for detected CGM gas around satellites, its existence is consequential. For example, Lucchini et al. (2020) find that such a satellite CGM is necessary to reproduce the observed kinematics and mass of the Large and Small Magellanic Cloud system. Moreover, the high surviving HI fractions of a Hydra galaxy cluster subgroup

suggest a surviving intragroup medium actually shields the group members from the hotter intracluster medium (ICM; Hess et al., 2022). Lastly, Churazov et al. (2012) infer that the largest fluctuations in resolved X-ray maps of the Coma cluster are due to cluster members.

The stripping and loss of gas from satellites have been studied with cosmological hydrodynamical galaxy simulations. For example, using the GIMIC simulations, Bahé et al. (2013) find that group and cluster hosts with total mass $\sim 10^{13-15.2}\,\mathrm{M}_\odot$ are able to strip infalling galaxies of their CGM already when the latter are at distances of $\sim 5R_{200c}^{\mathrm{host}}$. More recently, Wright et al. (2022) study the orbital histories of EAGLE satellites around groups and clusters, finding that satellites begin to lose their CGM at $\approx 2-3R_{200c}^{\mathrm{host}}$, while gas removal is more efficient for clusters and lower-mass satellites. The emerging phenomenology of diverse satellite CGM properties and removal timescales depends on satellite-host configurations (e.g., Kawata & Mulchaey, 2008; McCarthy et al., 2008; Bekki, 2009; Zinger et al., 2018a; Kulier et al., 2023). This has also led to the revision of simplified assumptions previously adopted in semi-analytical models. Typically, these models have only accounted for gas stripping in satellites within the virial radius (e.g., Henriques et al., 2015), with some even removing the entire satellite CGM gas once a satellite crosses into the halo boundary (e.g., Lacey et al., 2016; Lagos et al., 2018). Updated semi-analytical models, which include both the stripping of satellites and centrals beyond the halo boundary, as well as a gradual approach to gas stripping, demonstrate improved alignment with observational data (e.g., Ayromlou et al., 2021a). However, the majority of the theoretical analyses so far focus on galaxy groups and low-mass clusters rather than the largest clusters in the Universe, where environmental effects are maximal. Moreover, no previous simulation work has connected the possible survival of the CGM around satellites and its observability.

In this work, we use the new TNG-Cluster simulation suite (Nelson et al., 2024, Pillepich et al. in prep) to address the question: do $z = 0$ satellites in massive galaxy clusters retain, or not, their CGM. We specifically target the massive end of the host distribution to focus on the harshest environments and to maximize the mass range of satellite galaxies. TNG-Cluster includes 352 galaxy clusters with total mass $M_{200c}^{\mathrm{host}} \sim 10^{14.3-15.4}\,\mathrm{M}_\odot$ and over 90,000 satellites with stellar mass larger than $\sim 10^9\,\mathrm{M}_\odot$ at $z = 0$. It therefore provides an unprecedented sample size of satellites, including thousands of satellites more massive than our own Milky Way and Andromeda. These are simulated with the well-tested IllustrisTNG galaxy formation model (TNG hereafter) within a full ΛCDM cosmological context, and with competitive spatial and mass resolution. Despite important simplifications (such as no explicit modeling of the multiphase ISM, influencing results related to the cold gas – see Zinger et al. 2018a and Kukstas et al. 2022), the TNG model returns satellite quenched fractions and gas contents

that are broadly consistent with observations (e.g., Stevens et al., 2019; Donnari et al., 2021b; Stevens et al., 2021).

Moreover, as shown in a series of companion papers that showcase first results from TNG-Cluster, the simulated halos exhibit X-ray luminosity scaling relations and other global properties of the ICM (Nelson et al., 2024), fractions of cool cores (Lehle et al., 2024), gas kinematics (Ayromlou et al., 2023a), levels of turbulence in the cores (Truong et al., 2024), and morphologically diverse radio relics (Lee et al., 2024) that are all broadly consistent with observations.

The goals of this work are: a) to quantify the predictions from TNG-Cluster for the population of cluster satellites and their hot and cold gas reservoirs; by doing so, we aim to b) provide interpretation for current X-ray observations of cluster galaxies and their spatial extent; c) suggest an experiment to constrain the physics of satellites in massive hosts, beyond X-ray observations of individual systems; and d) quantify the covering fraction of the CGM of satellites versus the ICM of the host.

We begin by describing the new simulation suite, sample selection, and our methods (§ 6.2). In § 6.3, we present the clusters and their satellite demographics, the gaseous content of the satellites, the spatial extent of the satellite CGM, and the causes of satellite-to-satellite variations. We discuss details and caveats of our results in § 6.4, and in § 6.4.1 we present a statistical stacking experiment to detect the soft X-ray emission from satellite CGM. We discuss implications of our findings in § 6.4.2 and § 6.4.3 and summarize our main results in § 6.5.

6.2 Methods

6.2.1 TNG-Cluster

TNG-Cluster[1] is a suite of 352 massive galaxy cluster simulations, spanning halo masses $M_{200c} \approx 10^{14.3-15.4}\,M_\odot$ (Nelson et al., 2024, Pillepich et al. in prep). These halos were chosen from a $\approx$ 1 Gpc box-size parent dark matter only simulation, TNG-Cluster-Dark. The 352 halos chosen for re-simulation are based only on $z = 0$ halo mass such that: (i) all $\sim$ 100 halos with mass $> 10^{15}\,M_\odot$ are included; and (ii) halos with mass $10^{14.3-15.0}\,M_\odot$ were randomly selected in bins of 0.1 dex such that the halo mass distribution is flat over this mass range (see Nelson et al., 2024, for details).

The TNG-Cluster simulation employs the well-tested TNG galaxy formation model (Weinberger et al., 2017; Pillepich et al., 2018a). The baryon mass resolution of TNG-Cluster is $m_{\rm bar} = 1.1 \times 10^7 M_\odot$, the same resolution as TNG300 from the original TNG simulation

[1] www.tng-project.org/cluster/

Table 6.1: Summary of the definitions and notation used throughout this work.

Name	Notation	Notes
host halo size	$R_{\rm 200c}^{\rm host}$ [Mpc]	radius at which the average enclosed density is 200 times the critical density of the Universe
host halo mass	$M_{\rm 200c}^{\rm host}$ [$\rm M_\odot$]	total mass enclosed within the halo size $R_{\rm 200c}^{\rm host}$
satellite stellar size	$R_{\rm half,\star}$ [kpc]	half mass radius of the total gravitationally bound stellar mass, computed via SUBFIND
satellite stellar mass	$M_{\star}^{\rm sat}$ [$\rm M_\odot$]	stellar mass of the satellite galaxy within $2R_{\rm half,\star}$
satellite gas mass	$M_{\rm gas}^{\rm sat}$ [$\rm M_\odot$]	total gravitationally bound gas mass, computed via SUBFIND
satellite hot gas mass	$M_{\rm HotGas}^{\rm sat}$ [$\rm M_\odot$]	$M_{\rm gas}^{\rm sat}$ but only for hot $> 10^{4.5}$ K gas; used as a proxy for X-ray bright gas
satellite cold gas mass	$M_{\rm ColdGas}^{\rm sat}$ [$\rm M_\odot$]	$M_{\rm gas}^{\rm sat}$ but only for cold $< 10^{4.5}$ K gas; used as a proxy for ISM gas
satellite CGM gas mass	$M_{\rm CGM}^{\rm sat}$ [$\rm M_\odot$]	circumgalactic medium; $M_{\rm gas}^{\rm sat}$ but only for $> 2R_{\rm half,\star}$ gas; includes hot and cold gas
host-centric distance	$d_{\rm sat}^{\rm host}$ [$R_{\rm 200c}^{\rm host}$, kpc]	distance from the center of the host cluster to the center of the satellite, in 2D projection unless otherwise noted.
infall time	$\tau_{\rm FirstInfall}$ [Gyr]	the first time a galaxy became a satellite[a]

[a] The first time the galaxy was a Friends-of-Friends satellite for at least 3 consecutive snapshots in a host of mass $M_{\rm 200c}^{\rm host} > 10^{12}\,\rm M_\odot$.

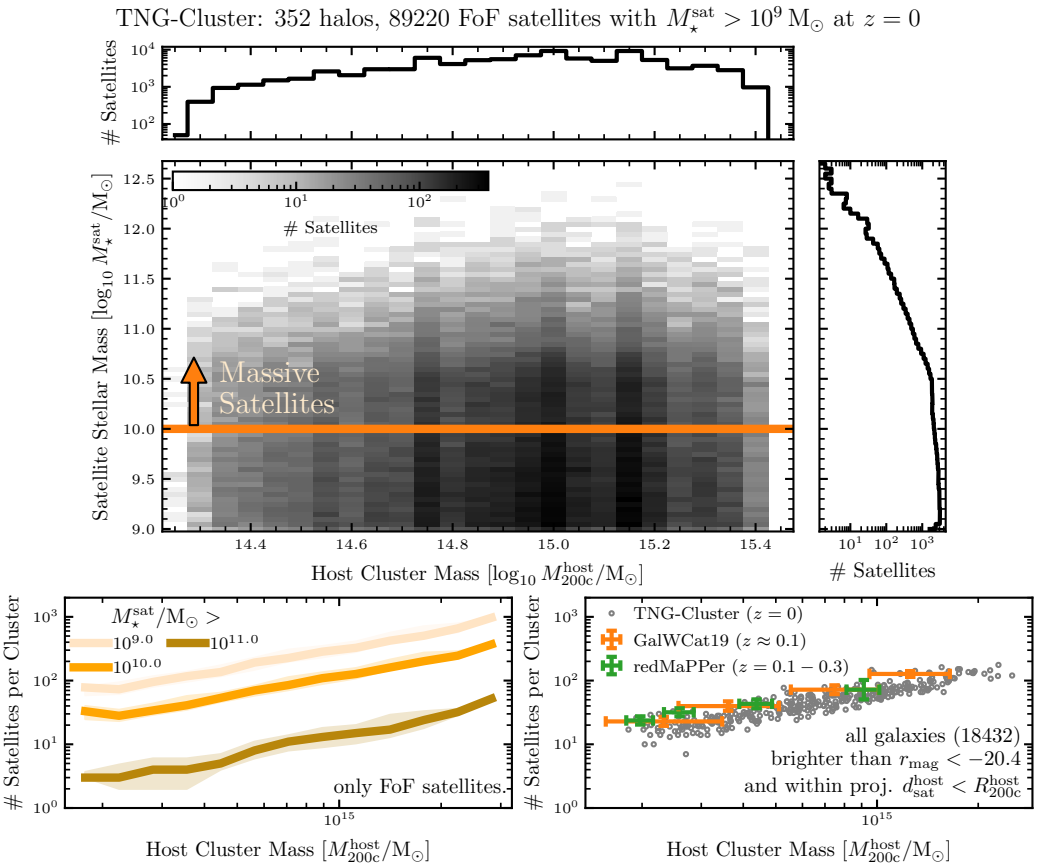

Figure 6.1: **Cluster and satellite demographics in TNG-Cluster.** *Top panels:* We plot the number of satellite galaxies of the 352 clusters in bins of satellite stellar $M_\star^{\rm sat}$ and host halo $M_{\rm 200c}^{\rm host}$ mass at $z = 0$. The one-dimensional histograms for $M_\star^{\rm sat}$ and $M_{\rm 200c}^{\rm host}$ are included in the right and top panels. The number of satellites per stellar mass bin decreases with satellite stellar mass, where there is a sharp decrease in the number of super-L$_\star$ galaxies $M_\star^{\rm sat} > 10^{10.5}\,{\rm M}_\odot$. The number of satellites per host mass bin increases at lower cluster masses $M_{\rm 200c}^{\rm host} \sim 10^{14.3-15}\,{\rm M}_\odot$, and then decreases for the most massive clusters $M_{\rm 200c}^{\rm host} \sim 10^{15-15.4}\,{\rm M}_\odot$, which reflects the TNG-Cluster halo mass function (see text and Nelson et al., 2024, for details). *Bottom panels:* For each of the 352 hosts, we plot the number of FoF satellites above given stellar masses (left), where the medians and 16th and 84th percentiles are the solid curves and shaded regions respectively. Additionally, we qualitatively compare the TNG-Cluster results to spectroscopic (GalWCat19; Abdullah et al., 2020, 2023) and photometric (redMaPPer; Costanzi et al., 2019) SDSS observations, considering all galaxies brighter than $r_{\rm mag} < -20.4$ and within a projected distance $d_{\rm sat}^{\rm host} < R_{\rm 200c}$ as satellites (right panel; see text for details). The TNG-Cluster mass-richness relation is qualitatively consistent with observations.

suite (Pillepich et al., 2018b; Nelson et al., 2018a; Naiman et al., 2018; Marinacci et al., 2018; Springel et al., 2018). We note that the TNG galaxy formation model at the TNG-Cluster mass resolution (the same as TNG300) has already been at least partially validated in the low-mass cluster regime (e.g., Nelson et al., 2018a; Donnari et al., 2021a; Truong et al., 2020; Donnari et al., 2021b). Here we briefly summarize the model.

The TNG simulations, including TNG-Cluster, evolve gas, cold dark matter, stars, and super massive black holes (SMBHs) within an expanding universe, based on a self-gravity + magneto-hydrodynamic framework (Pakmor et al., 2011; Pakmor & Springel, 2013) using the Arepo code (Springel, 2010b). The fluid dynamics employ a dynamic, moving Voronoi tessellation of space. Gas has a cooling floor at 10^4 K, and the relationship between temperature and density for star-forming gas is determined via a two-phase sub-grid pressurization model Springel & Hernquist (2003). For this analysis, we manually set the temperature of star-forming gas to 10^3 K, its cold-phase value. The TNG galaxy evolution model includes: gas heating and cooling; star formation; stellar population evolution and chemical enrichment from AGB stars and type Ia + II supernovae; supernova driven outflows and winds (Pillepich et al., 2018a); the formation, merging, and growth of SMBHs; and two main SMBH hole feedback modes: a thermal "quasar" mode, and a kinetic "wind" mode (Weinberger et al., 2017).

Catalogs contain halos as well as galaxies. Dark matter halos are identified using the Friends-of-Friends (FoF) algorithm with a linking length $b = 0.2$, run only using the dark matter particles (Davis et al., 1985). Then the baryonic components are connected to the same halos as their closest dark matter particle. Throughout this paper, we use "FoF," "group," "FoF group," and "halo" synonymously. Galaxies are then identified using the subfind algorithm, which identifies gravitationally bound sets of particles and cells (Springel et al., 2001; Dolag et al., 2009). We use the terms "subhalo" and "galaxy" synonymously even though, in general, subfind objects may contain no stars and/or gas whatsoever. Typically, the most massive subhalo within a halo is the "main" or "primary subhalo," also called the "central galaxy;" all other subhalos within a halo are "satellites." We follow the evolution of galaxies using sublink_gal , which constructs merger trees for subhalos by searching for descendants with common stellar particles and star-forming gas cells (Rodriguez-Gomez et al., 2015). The TNG simulations are publicly available in their entirety, and TNG-Cluster will likewise be released in 2024 (Nelson et al., 2019a, 2024). Our analyses adopt the same ΛCDM cosmology as TNG, consistent with the Planck Collaboration et al. (2016) results: $\Omega_{\Lambda,0} = 0.6911$, $\Omega_{\rm m,0} = \Omega_{\rm bar,0} + \Omega_{\rm dm,0} = 0.3089$, $\Omega_{\rm bar,0} = 0.0486$, $\sigma_8 = 0.8159$, $n_s = 0.9667$, and $h = H_0/(100\,{\rm km\,s^{-1}\,Mpc^{-1}}) = 0.6774$, where H_0 is the Hubble parameter.

6.2.2 Halo and Satellite Galaxy Sample Selection

In this work, we exclusively focus on the 352 primary zoom targets from the TNG-Cluster simulation[2]. Moreover, we only consider satellite galaxies with stellar mass $M_\star^{\rm sat} > 10^9\,{\rm M}_\odot$, corresponding to $\gtrsim 100$ stellar particles each.

As is common practice with TNG, we define galaxy stellar mass $M_\star$ as the total SUBFIND stellar mass within twice the stellar half mass radius $M_\star \equiv M_\star(< 2R_{\rm half,\star})$. For galaxy gas mass $M_{\rm gas}$, we take the total gravitationally bound SUBFIND gas mass, regardless of galactic-centric distance. At times, we consider only cold $\leq 10^{4.5}$ K, hot $> 10^{4.5}$ K, ISM ($< 2R_{\rm half,\star}$), or CGM ($> 2R_{\rm half,\star}$) gas, where all star-forming gas is cold by definition. The median (10th, 90th percentiles) gas cell size in the satellite CGM is 5.2 (3.0, 8.6) kpc. Table 6.1 summarizes all quantities and definitions.

Unless noted otherwise, we consider galaxies as satellites based on their Friends-of-Friends membership, and do not enforce any explicit restriction on the cluster-centric distance. In some analyses, we rather consider satellites as all galaxies within a 2D projected cluster-centric distance, to mimic observational samples (see § 6.4.1 for more details). In all cases, we only consider subhalos of cosmological origin as defined by the SubhaloFlag in Nelson et al. (2019a). All FoF satellite galaxies considered are uncontaminated at $z = 0$, meaning that they contain zero dark matter low resolution elements. However, in general, it is possible that low resolution gas, stars, or dark matter are present, particularly at large distances away from clusters, but this is not expected to influence our results.

6.3 The Circumgalactic Medium of Cluster Satellites According to TNG-Cluster

6.3.1 Clusters and Their Satellite Demographics

TNG-Cluster provides an unprecedentedly large set of simulated massive cluster galaxies whose basic demographics are consistent with observations of cluster richness. In particular, in Figure 6.1 we plot the 2D histogram of all well-resolved satellites with $M_\star > 10^9\,{\rm M}_\odot$ across the 352 clusters in the $z = 0$ satellite stellar $M_\star^{\rm sat}$ - host halo $M_{\rm 200c}^{\rm host}$ mass plane (main panel). The color shows the number of galaxies in each bin, which span 0.1 dex in each axis, with 1D histograms for host halo and satellite stellar mass on the top and right subpanels, respectively.

The 352 galaxy clusters spanning 1 dex in host mass contain a total of $\approx 90,000$ satellites, covering 3.5 dex in stellar mass. The maximum satellite stellar mass increases with halo mass,

[2]We note that there are other halos that happen to be within the individual re-simulation regions (Nelson et al., 2024), but we do not include these objects in our analysis.

as no satellite galaxy may be more massive than its brightest cluster galaxy (BCG) by definition. For example, the BCG stellar mass within a $10^{14.5}$ (10^{15}) $M_\odot$ cluster is $\approx 10^{12}$ ($10^{12.2}$) $M_\odot$. This is, for example, visible in the 2D histogram (central panel) as a triangular region lacking satellites in the upper left corner. Throughout this work, we refer to satellites $M_\star^{\rm sat} > 10^{10}\,M_\odot$ as massive, and focus primarily on these systems.

It should be kept in mind that the TNG-Cluster (+TNG300) halo mass function is approximately flat at masses $M_{\rm 200c}^{\rm host} \approx 10^{14.3-15.1}\,M_\odot$, whereas there is a sharp decrease in the number of halos at the highest-mass end $M_{\rm 200c}^{\rm host} \approx 10^{15.1-15.4} M_\odot$, where the sample is volume limited (see fig. 1 from Nelson et al., 2024). As a consequence, in TNG-Cluster, the number of satellites per host mass bin increases with halo mass for lower-mass clusters to then decrease again toward the most massive systems in our sample: this is because more massive clusters on average host more satellites, but more massive clusters are also rarer. On the other hand, the TNG-Cluster satellite stellar mass function (top right subpanel) exhibits the typical shape characteristic also of central galaxies, with a slow decrease for $M_\star^{\rm sat} \sim 10^{9-10.5}\,M_\odot$, and a fast drop-off for massive super-$L_\star$ satellites $M_\star^{\rm sat} \gtrsim 10^{10.5}\,M_\odot$ (e.g., Baldry et al., 2012).

In Fig. 6.1 (bottom left panel), we show a theoretical richness-mass relation, that is,the average number of satellites per host above a given stellar mass threshold, as a function of host mass $M_{\rm 200c}^{\rm host}$. Solid curves represent medians across the cluster sample, with the 16th and 84th percentiles as shaded regions. As expected, the number of satellites per host above any given stellar mass increases with host mass. For example, at a mass $M_{\rm 200c}^{\rm host} \approx 10^{14.5}$ (10^{15}) $M_\odot$, each cluster hosts ≈ 100 (300) satellite galaxies of mass $M_\star^{\rm sat} > 10^9\,M_\odot$ (light orange). Also as expected, at a fixed halo mass, the number of galaxies above a given stellar mass threshold increases as the mass threshold decreases. In TNG-Cluster, nearly all clusters host a few extremely massive satellite galaxies $M_\star > 10^{11}\,M_\odot$ (dark orange).

Finally, in Fig. 6.1 (bottom right panel), we qualitatively compare the richness-mass relation predicted by TNG-Cluster with spectroscopic (GalWCat19; Abdullah et al., 2020, 2023) and photometric (redMaPPer; Costanzi et al., 2019) SDSS observations. In particular, we plot the number of satellites per host brighter than $r < -20.4$ mag, corresponding to $\sim M_\star^{\rm sat} \gtrsim 10^{10.4}\,M_\odot$. Here by satellites we mean all galaxies within the high-resolution zoom region of depth $\sim 5 R_{\rm 200c}^{\rm host} \sim 7-12$ Mpc and within a projected distance $< R_{\rm 200c}^{\rm host}$, regardless of the FoF membership. Even though we do not create synthetic observations to match the SDSS data and hence even though these comparisons are at face value, the result is encouraging: the TNG-Cluster richness-mass relation is qualitatively consistent with SDSS (see also Nelson et al., 2024, and their fig. 16).

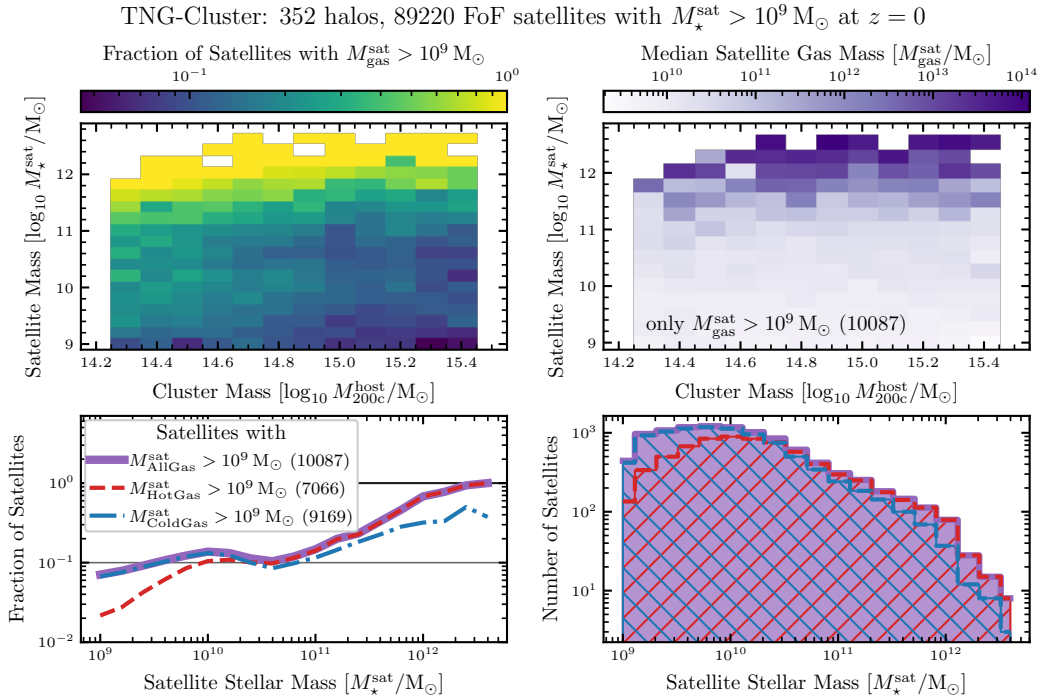

Figure 6.2: **How the TNG-Cluster satellite gas mass varies with the satellite stellar and host halo mass.** *Top left panel:* for the ≈ 90,000 TNG-Cluster satellites with $M_\star^{\rm sat} > 10^9\,{\rm M}_\odot$, the fraction of satellites that retain gas reservoirs $M_{\rm gas}^{\rm sat} > 10^9\,{\rm M}_\odot$ today as satellites is shown in bins of satellite stellar $M_\star^{\rm sat}$ and cluster $M_{\rm 200c}^{\rm host}$ mass. *Top right panel:* only 10,000 (10 percent) of the TNG-Cluster satellites retain gas masses $M_{\rm gas}^{\rm sat} > 10^9\,{\rm M}_\odot$ today. For these gaseous satellites, we show the median satellite gas mass $M_{\rm gas}^{\rm sat}$ in bins of satellite stellar $M_\star^{\rm sat}$ and host halo $M_{\rm 200c}^{\rm host}$ mass. *Bottom panels:* We show the fractions (left panel) and numbers (right panel) of satellites with all (purple, solid, filled), hot (red, dashed, "\" hatched), and cold (blue, dashed-dotted, "/" hatched) gas masses $> 10^9\,{\rm M}_\odot$ within a given stellar mass bin at $z = 0$. We mark 100 percent and the global average of 10 percent with black lines, and include the total number of gaseous satellites in the legend. While a given satellite is more likely to retain gas if it has a higher stellar mass, a given gaseous satellite is more likely to have a lower stellar mass because there are simply more lower-mass satellites.

6.3.2 The Gas Content of Cluster Satellites

Of the ≈ 90,000 TNG-Cluster satellites with $M_\star^{\rm sat} > 10^9 {\rm M}_\odot$, only ≈ 10,000 (10 percent) retain at least some gas today. Throughout the paper, by this we mean at least $M_{\rm gas}^{\rm sat} > 10^9\,{\rm M}_\odot$ of gravitationally bound gas reservoirs, that is,a well resolved amount of gas. We motivate this choice in Appendix 6.6 and, we have checked that adding an additional criterion on the gas mass fraction $f_{\rm gas} \equiv M_{\rm gas}^{\rm sat}/(M_{\rm gas}^{\rm sat} + M_\star^{\rm sat}) > 10^{-2},\ 10^{-1}$ would remove an unimportant subset of galaxies, that is, 40 (0.4 percent), 777 (7.7 percent) of the gaseous satellites.

In Fig. 6.2 (top left panel), we explore how this fraction of gas-rich satellites varies with satellite stellar $M_\star^{\rm sat}$ and host cluster $M_{\rm 200c}^{\rm host}$ mass. At a fixed satellite stellar mass (a given row), the fraction of gas-rich satellites tends to decrease with increasing host mass, broadly consistent with expectations from RPS. Namely, ram pressure increases with host mass, thereby driving down the fraction of gas-rich satellites. Moreover, at a fixed halo mass (a given column), the fraction of gas-rich satellites increases with satellite stellar mass, and this trend exists at all considered stellar masses. The restorative gravitational pull from the stellar body acts as the primary foil to ram pressure, thereby increasing the fraction of gas-rich satellites with increasing satellite mass (e.g., Wright et al., 2022; Rohr et al., 2023; Kulier et al., 2023).

In Fig. 6.2 (top right panel), we further show that, for the ≈ 10,000 gas-rich satellites, the average satellite gas mass generally increases with satellite stellar mass. In fact, this applies to the most massive satellites and is not the case for those with mass $M_\star^{\rm sat} \sim 10^{9-11}\,{\rm M}_\odot$, which all exhibit a rather uniform $M_{\rm gas}^{\rm sat} \lesssim 10^{10}\,{\rm M}_\odot$ of gas reservoir[3]. Indeed, about 100 TNG-Cluster satellites retain gas masses $M_{\rm gas}^{\rm sat} \sim 10^{13-14}\,{\rm M}_\odot$ today: these are the most massive satellites in the simulation, and would be in general some of the most massive galaxies in the Universe. We note that these could in fact be considered merging sub clusters (see the companion paper by Lehle et al., 2024). Interestingly, for all gas-rich satellites, the average gas mass does not depend on host mass across the TNG-Cluster mass range. We speculate two origins for the null-trend of median (gas-rich) satellite gas mass with cluster mass. First, and only applying to satellites of mass $M_\star^{\rm sat} \sim 10^{9-11}\,{\rm M}_\odot$, the average satellite gas mass $M_{\rm gas}^{\rm sat} \sim 10^{9-10}{\rm M}_\odot$ is just above our threshold for being considered gas-rich $M_{\rm gas}^{\rm sat} > 10^9\,{\rm M}_\odot$ (see Appendix 6.6 for more details). Many of these satellites are likely undergoing environmental processes en route toward becoming gas-poor; they have not yet been cluster-members long enough to have been stripped of their gas. Second and related, these satellites may have had their gas reservoirs first preprocessed by other groups before falling into their current cluster hosts (e.g., Jung et al., 2018; Donnari et al., 2021a).

[3] For these low-mass satellites, we have checked that the infall look-back time – that is,the total time the galaxy has been suffering from environmental effects such as ram pressure – primarily determines how much gas the satellites retain (not shown).

With this intuition that gas retention is primarily determined by satellite mass, in Fig. 6.2 (bottom panels), we show how the fraction (bottom left panel) and number (bottom right panel) of satellites that retain significant gas reservoirs at $z = 0$ vary with satellite stellar mass. We split the gas (purple, solid, filled) into hot (red, dashed, '/' hatch) and cold (blue, dash-dotted, '\' hash) phases. Across all stellar masses considered, $\approx$ 91 percent of the gaseous satellites retain at least some cold gas. For the hot gas, this only applies to $\approx$ 70 percent of the gaseous satellites.

At low stellar masses $M_\star^{\rm sat} \sim 10^{9-10}\,{\rm M}_\odot$ the fraction (left) and number (right) of gas-rich satellites increases with stellar mass for all, hot, and cold gas. Nearly all gas-rich satellites retain cold gas at these stellar masses, and the fraction of gas-rich satellites that retain hot gas increases rapidly with stellar mass. This is consistent with ram pressure removing hot, spatially extended gas preferentially first, while the cold ISM gas tends to be more resistant to these environmental effects (e.g., Wright et al., 2022; Rohr et al., 2023, Fig. 6.3).

At intermediate stellar masses $M_\star^{\rm sat} \sim 10^{10-10.5}\,{\rm M}_\odot$, the fraction of gas-rich satellites (left panel) slightly decreases from $\approx$ 16 to $\approx$ 13 percent, where the fraction with cold gas (blue, dashed-dotted) drops to $\approx$ 12 percent. The decrease in gas retention at these stellar masses is likely due to the onset of the kinetic-mode of AGN feedback (Weinberger et al., 2017; Nelson et al., 2018a; Zinger et al., 2020; Truong et al., 2020; Ayromlou et al., 2021a, see below: Figs. 6.3, 6.4 right panels). At high stellar masses $M_\star^{\rm sat} \sim 10^{10.5-11.75}\,{\rm M}_\odot$, the fraction of (cold) gaseous satellites increases with stellar mass to a maximum of $\approx$ 60 percent ($\approx$ 30 percent). More massive galaxies retain more gas as they (i) have deeper gravitational potential wells; and (ii) tend to be later infallers (into any host; see Table 6.1 for details), thereby decreasing the amount of time they have been experiencing environmental effects.

While the fraction of gaseous satellites generally increases with mass (top panel), the total number of gaseous satellites decreases with stellar mass (bottom panel), because that the total number of satellites decreases with stellar mass (Fig. 6.1). Thus, while a given satellite is more likely to retain gas if it has a higher stellar mass, a given gas-rich satellite is more likely to have a lower stellar mass, because there are in general many more low-mass satellites.

6.3.3 The Spatial Extent of the Satellite Gas: the Case for the Satellite Circumgalactic Medium

To assess the extent of and understand how various physical processes reshape the multiphase gas reservoirs in and around satellites, we turn to the gas radial profiles of the $\approx$ 10,000 gas-rich satellites in TNG-Cluster. In Fig. 6.3 (top panels), we show the median gas radial profiles (see Fig. 6.4 for the individual profiles to see the galaxy-to-galaxy variation and Fig. 6.6 for the time evolution for an example satellite) separated into all (purple), hot (red), and cold

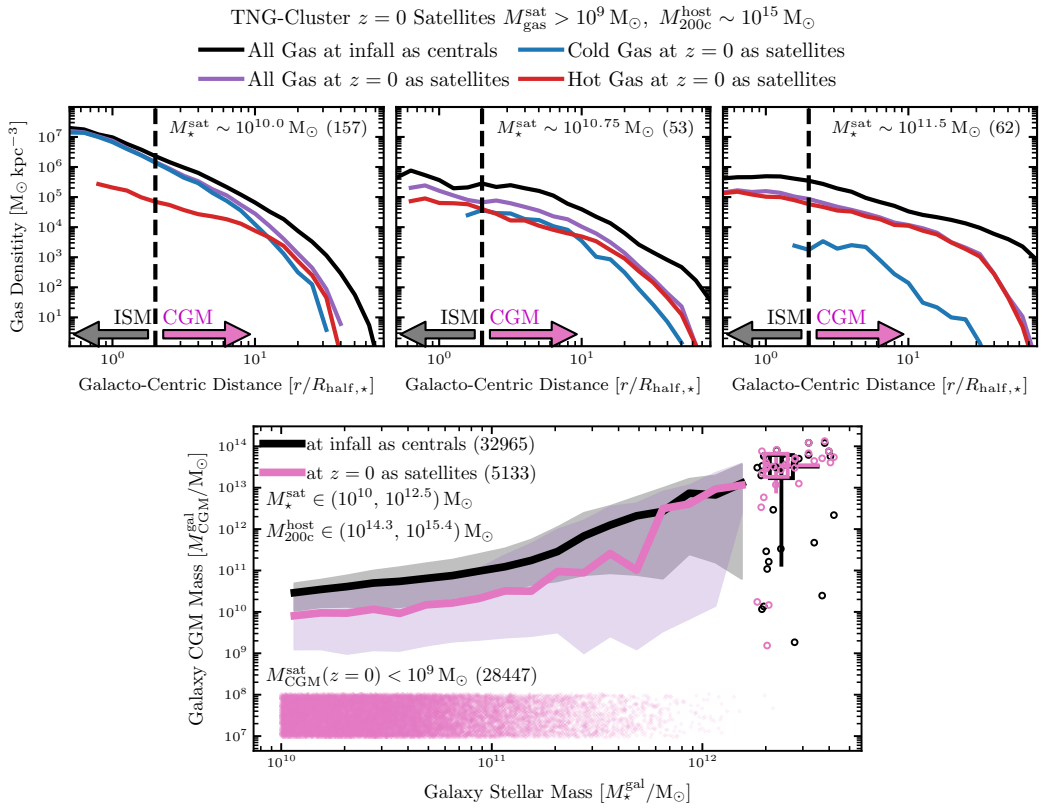

Figure 6.3: **Spatial extent of satellite gas in TNG-Cluster.** Of the ≈ 5,000 gas-rich $M_{\rm gas}^{\rm sat} > 10^9\,{\rm M}_\odot$ massive satellites $M_\star^{\rm sat} > 10^{10}\,{\rm M}_\odot$ at $z = 0$, we examine the spatial extent of all (hot and cold) gas at a fixed host cluster mass $M_{\rm 200c}^{\rm host} \sim 10^{15}\,{\rm M}_\odot$ and at three stellar masses $M_\star^{\rm sat} \sim 10^{10}$, $10^{10.75}$, $10^{11.5}\,{\rm M}_\odot$ (top panels, left to right respectively). Moreover, we compare the total gas density (purple) at $z = 0$ of cluster members as satellites with that at infall as centrals (black). All curves show the median profiles of all galaxies in the bin; see Fig. 6.4 for the individual profiles to see the galaxy-to-galaxy variation. We define all gas outside $> 2R_{\rm half,\star}$ as the circumgalactic medium (CGM). We then plot total CGM mass $M_{\rm CGM}^{\rm sat}$ as a function of galaxy stellar mass $M_\star^{\rm sat}$ (bottom panel) at infall as centrals (black), and at $z = 0$ as satellites (pink). The curves are the medians of the CGM masses (only the galaxies with nonzero CGM mass for the satellites), and for the most massive galaxies we plot the individual objects (circles) and the median stacks (squares). We manually place the ≈ 28,000 CGM-poor $M_{\rm CGM}^{\rm sat} < 10^9\,{\rm M}_\odot$ satellites at masses $\sim 10^{7-8}\,{\rm M}_\odot$. All stacks use stellar, host, and gas masses at $z = 0$, and the radial profiles are normalized to $R_{\rm half,\star}$ at the considered time (infall or today). More than 5,000 cluster satellites retain a CGM despite residing in harsh cluster environments.

(blue) phases at $z = 0$ as satellites at a fixed host cluster mass $M_{200c}^{\rm host} \sim 10^{15}\,{\rm M}_\odot$ and at fixed satellite stellar masses $M_\star^{\rm sat} \sim 10^{10}$, $10^{10.75}$, $10^{11.5}\,{\rm M}_\odot$ (left to right, respectively). All stacks and $M_\star^{\rm sat}$ measurements are at $z = 0$. For comparison, we include the total gas profile at infall when the galaxies were centrals (black). We consider all gas within $2R_{\rm half,\star}$ as the interstellar medium (ISM) and all gas at $> 2R_{\rm half,\star}$ as the circumgalactic medium (CGM).

Across all considered stellar masses and at all galactic-centric distances, galaxies have higher gas densities at infall as centrals, compared to today as satellites. As a result, satellites have lower gas masses and higher quenched fractions than their central counterparts (e.g., Stevens et al., 2019; Donnari et al., 2021a, for TNG). In detail, the differences between the gas density at infall and $z = 0$ vary both with galactic-centric distance and satellite stellar mass. Moreover, the most prevalent gas phase (hot, red; or cold, blue) today also depends on these two quantities. Complicating the issue, at higher stellar masses $M_\star^{\rm sat} \gtrsim 10^{10.5}\,{\rm M}_\odot$, nearly all galaxies in the TNG model experience strong AGN kinetic-mode feedback. That is, high-mass satellites are subject to both external and internal processes that impact their gas reservoirs.

At lower stellar masses $M_\star^{\rm sat} \sim 10^{10}\,{\rm M}_\odot$ (left panel), the total gas density today is composed primarily of cold gas, especially within the ISM. Only at large distances $\gtrsim 5R_{\rm half,\star}$ does the hot gas begin to contribute significantly to the total gas density. Within the ISM, the total gas density is largely unchanged for central versus satellite status. However, at the outskirts $\gtrsim 10R_{\rm half,\star}$, there is a clear truncation in gas profiles. These differences are consistent with expectations from ram pressure removal, where the spatially extended gas is removed preferentially earlier than the tightly bound ISM (Balogh & Morris, 2000).

At intermediate stellar masses $M_\star^{\rm sat} \sim 10^{10.75}\,{\rm M}_\odot$ (middle panel), the total gas density today is composed of similar amounts of hot and cold gas at all distances. Unlike lower-mass galaxies, these have experienced episodes of AGN feedback which partially ejects nearby, mostly cold, ISM gas (Nelson et al., 2019b), reducing its density. At large distances in the CGM $> 2R_{\rm half,\star}$, the total gas density both at infall and $z = 0$ extend to farther distances than at smaller stellar masses. The higher-mass satellites retain sizeable gas reservoirs at large distances up to $\gtrsim 30R_{\rm half,\star}$.

This trend continues to the highest stellar mass bin $M_\star^{\rm sat} \sim 10^{11.5}\,{\rm M}_\odot$ (right panel). Here, the gas density is comprised almost entirely of hot gas at all distances. In fact, there is little to no cold gas within the ISM, that is,galaxies at these masses are largely quenched, regardless of central or satellite status (Donnari et al., 2021a). The differences between the total gas density profiles as centrals versus as satellites are roughly constant at all distances. The CGM density is highest for these high-mass galaxies, and this satellite CGM gas extends to larger physical distances.

In the bottom panel of Fig. 6.3, we provide one of the key quantitative findings of this analysis: the CGM mass $M_{\rm CGM}^{\rm gal}$ of satellites as a function of stellar mass $M_\star^{\rm sat}$ (pink), and at infall as centrals (black). The curves are the medians of the CGM masses (only the galaxies with nonzero CGM mass for the satellites), and for the most massive galaxies we plot the individual objects (circles) and the median stacks (squares). Here by CGM we mean the gas reservoir that extends beyond the main stellar body of a galaxy. According to TNG-Cluster, more than 5,000 massive $M_\star^{\rm sat} > 10^{10}\,{\rm M}_\odot$ satellites retain their own CGM or gaseous atmosphere despite the harsh cluster environments. Further, on average, the retained CGM mass increases with satellite stellar mass, while the differences between infall and $z = 0$ decrease. higher-mass satellites are more resistant to environmental effects and are able to retain spatially extended gas reservoirs. Beyond the average trends, however, there remains a large galaxy-to-galaxy variation in the ability of retaining CGM mass, and we study exactly this diversity next.

6.3.4 The Diversity of Satellite Circumgalactic Media

We now consider individual galaxies to explore the diversity of satellite CGM. In Fig. 6.4 we plot the total gas density radial profiles for all gas-rich $M_{\rm gas}^{\rm sat} > 10^9\,{\rm M}_\odot$ satellites at a fixed host halo $M_{\rm 200c}^{\rm host} \sim 10^{15}\,{\rm M}_\odot$ and satellite stellar mass $M_\star^{\rm sat} \sim 10^{10},\ 10^{10.75}$. We color the profiles by their instantaneous ram pressure[4] (left column) and supermassive black hole (SMBH) mass (right column), and we overplot the medians of the top and bottom quartiles of ram pressure and SMBH mass. We also examine the effect of time since infall, a proxy for the integrated environmental effects, on the radial profiles and find similar results that of the instantaneous ram pressure (not shown).

At lower stellar masses $M_\star^{\rm sat} \sim 10^{10}\,{\rm M}_\odot$, satellites experiencing more ram pressure have lower CGM densities, and their spatial extent is truncated (top left panel). This result also holds for higher satellite masses (lower left panel). In the ISM $< 2R_{\rm half,\star}$, gas densities tend to increase with ram pressure, but the effect is small. At higher stellar masses $M_\star^{\rm sat} \sim 10^{10.75}\,{\rm M}_\odot$ (bottom left panel), this effect is stronger. Recent simulations and radio observations predict and infer that ram pressure can compress a satellite's ISM (e.g., Vulcani et al., 2018; Roberts et al., 2022a; Kulier et al., 2023), and our results qualitatively agree.

To examine the effect of SMBH feedback we use SMBH mass as a proxy. This is the integral of the SMBH accretion history, and so it is a proxy of and proportional to the total feedback energy ever released. At lower stellar masses $M_\star^{\rm sat} \sim 10^{10}\,{\rm M}_\odot$ (top left panel), SMBHs do not seem to have an impact on satellite gas densities. Within the TNG model, the SMBHs in these

[4] We compute the instantaneous ram pressure by measuring the local background environment using an adaptive spherical shell and Gaussian mixture estimator (Ayromlou et al., 2019, 2021b). The ram pressure is then the background density multiplied by the relative velocity squared.

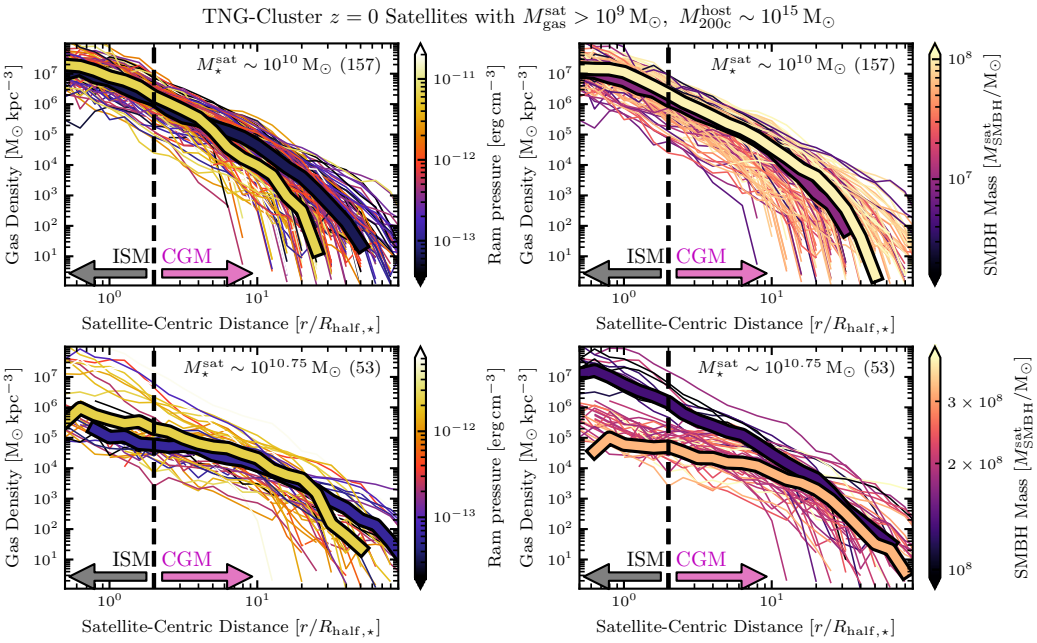

Figure 6.4: **How ram pressure and SMBHs affect the gas contents of TNG-Cluster satellite galaxies.** For the gas-rich $M_{\rm gas}^{\rm sat} > 10^9\,{\rm M}_\odot$ satellites at a fixed cluster $M_{\rm 200c}^{\rm host} \sim 10^{15}\,{\rm M}_\odot$ and satellite $M_\star^{\rm sat} \sim 10^{10}$, $10^{10.75}\,{\rm M}_\odot$ (top versus bottom panels) mass, we show total gas density radial profiles colored by current ram pressure (left column) and SMBH mass (right column). The thick curves show the medians of the top and bottom quartiles of ram pressure and SMBH mass, and the thin curves are the profiles of the individual satellites. Ram pressure tends to truncate the gas profiles at large distances and slightly compress the ISM gas, while SMBH feedback tends to eject and decrease the density of the ISM gas for more massive satellites.

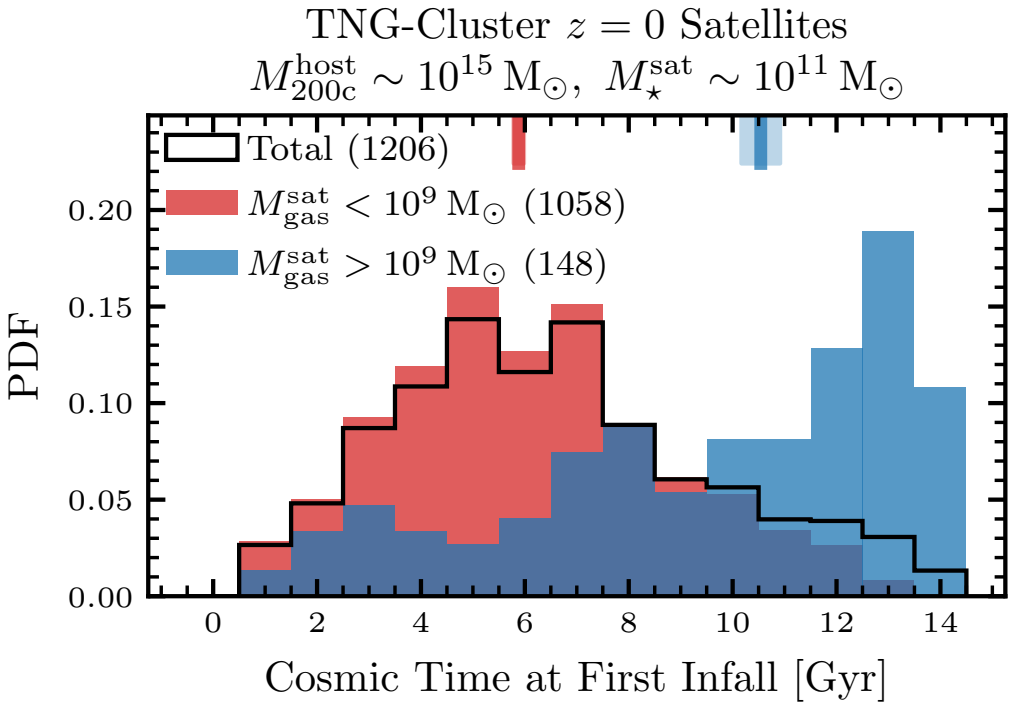

Figure 6.5: **Gas-rich satellites today are typically late infallers.** We plot the probability distribution functions (PDFs) of the infall times of all (black), gas-poor $M_{gas}^{sat} < 10^9\,M_\odot$ (red), and gas-rich $M_{gas}^{sat} > 10^9\,M_\odot$ (blue) TNG-Cluster satellites at a fixed host halo $M_{200c}^{host} \sim 10^{15}\,M_\odot$ and satellite stellar $M_\star^{sat} \sim 10^{11}\,M_\odot$ mass. We mark the medians and errors of the distributions as hashes on the top x-axis. The infall time is the first infall into any host, regardless if the galaxy has been preprocessed or not. At a fixed host halo and satellite stellar mass, the infall time is the primary driver determining whether satellites remain gas-rich or gas-poor today: more recent infallers are more likely to retain large gas reservoirs.

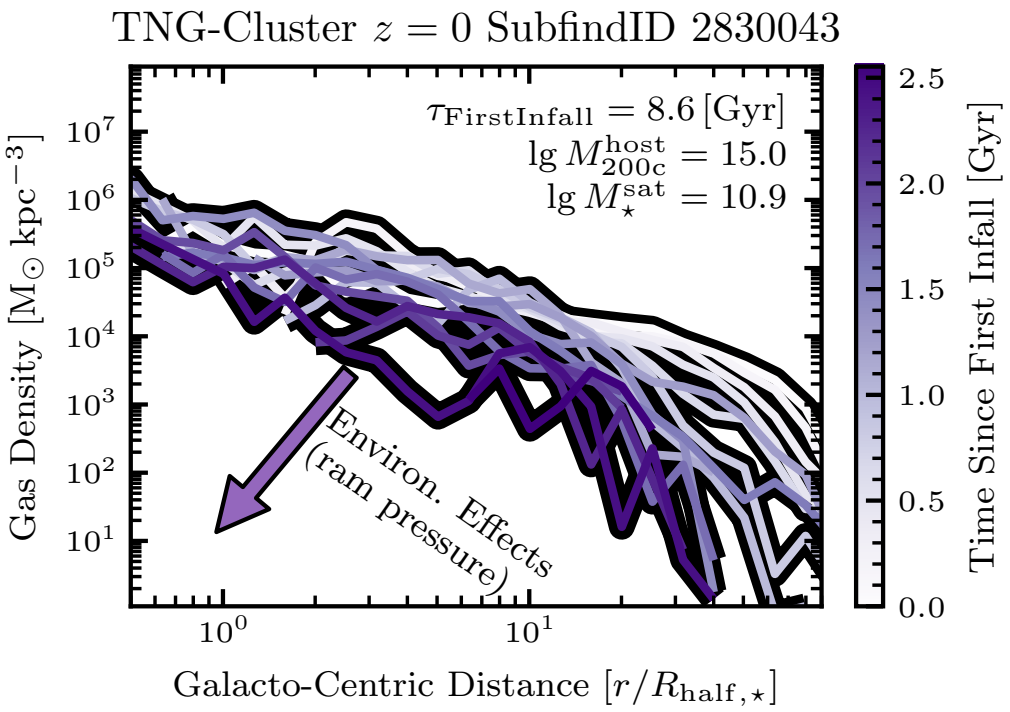

Figure 6.6: **How the environment removes gas from an example satellite.** For an example gas-poor satellite today of mass $M_\star^{\rm sat}(z = 0) \approx 10^{10.9}\,{\rm M}_\odot$ in a cluster of mass $M_{\rm 200c}^{\rm host}(z = 0) \approx 10^{15.0}\,{\rm M}_\odot$, we study the time evolution of the gas radial profiles since first infall ($\tau_{\rm FirstInfall} \approx 8.6$ Gyr i.e., look-back time ≈ 5 Gyr) until it becomes gas-poor today. The cumulative environmental effects, namely the integrated ram pressure since infall, and secular processes, namely feedback from the SMBH, remove the satellite's gas, leaving a gas-poor, quenched satellite today.

galaxies are largely in the quasar mode, where the corresponding feedback couples poorly to the gas, and is thus not ejected (Weinberger et al., 2018).

At higher stellar masses $M_\star^{\rm sat} \sim 10^{10.75}$ M$_\odot$ (bottom right panel), SMBHs are more important. At these masses and by $z = 0$, most of these satellites have experienced episodes of kinetic AGN feedback. Those with lower SMBH masses have higher ISM densities by $\sim 1-2$ dex than those with higher-masses. This effect extends into the CGM, to $\sim 10 R_{\rm half,\star}$. When SMBHs begin accreting at low rates, exerting wind mode feedback and expelling the ISM gas, they partially remove their own source of fuel for gas accretion. Without a supply of nearby cold gas, SMBHs grow more slowly. As a result, finding SMBHs in satellites that are much more massive is rare, although in central galaxies they can continue to grow via mergers (Joshi et al., 2020). At large radii $\gtrsim 10 R_{\rm half,\star}$ there is little impact from SMBH feedback. So, in summary, SMBH feedback tends to eject and decrease the density of the ISM gas for more massive, gas-rich satellites $M_\star \gtrsim 10^{11}$ M$_\odot$, which are typically quenched as a result but can still hold on to their CGM.

Now as seen in the previous sections, while many massive satellites manage to retain their own CGM today, at stellar masses $M_\star^{\rm sat} \lesssim 10^{11.5}$ M$_\odot$ a majority of TNG-Cluster satellites have actually lost their gas reservoirs due to combinations of secular and environmental processes. Moreover, among the gas-rich massive satellites, the retained CGM mass can vary by 2 or 3 orders of magnitude (Fig. 6.3, main panel).

For high-mass satellites $M_\star^{\rm sat} \sim 10^{11}$ M$_\odot$, we therefore study why most ($\sim$ 80 percent; Fig. 6.2, bottom left panel) end up gas-poor at $z = 0$. Fig. 6.5 shows the probability distribution functions (PDFs) of infall times for satellites at a fixed host halo $M_{\rm 200c}^{\rm host} \sim 10^{15}$ M$_\odot$ and satellite stellar $M_\star^{\rm sat} \sim 10^{11}$ M$_\odot$ (total, black), split into those that are gas-poor $M_{\rm gas}^{\rm sat} < 10^9$ M$_\odot$ (red), and those that are gas-rich $M_{\rm gas}^{\rm sat} > 10^9$ M$_\odot$ (blue) today. The infall time is the first infall into any host, regardless if the galaxy has been preprocessed or not. Gas-rich satellites tend to be late-infallers, experiencing environmental effects for a shorter period of time than gas-poor satellites.

We further explore the cumulative environmental effects in Fig. 6.6, where we show the time-evolution since infall ($\tau_{\rm FirstInfall} \approx 8.6$ Gyr, i.e., look-back time ≈ 5 Gyr ago) of the gas radial profiles for an example gas-poor satellite today ($M_\star^{\rm sat}(z=0) \sim^{11}$ M$_\odot$ in a cluster of mass $M_{\rm 200c}^{\rm host}(z=0) \sim 10^{15}$ M$_\odot$). As the time since infall increases, the gas density at a fixed galactocentric distance decreases, and the maximum extent of the CGM truncates, approximately following the direction of arrow. After sufficient time in the cluster environment, subject to ram pressure from its passage through the ICM, the galaxy loses all of its gas, becoming a gas-poor, quenched satellite today.

6.4 Implications of Satellite CGM in Clusters

As we have seen in the previous sections, massive satellite galaxies can retain a spatially extended, mostly hot CGM, and each cluster hosts a few to tens such massive satellites. One would then expect the satellite CGM to emit in the X-ray and to contribute to the total X-ray flux from galaxy clusters. Moreover, satellite CGM could contribute to absorption lines on background quasar spectra in the near UV. We thereby study the possibility to statistically detect this satellite CGM in observations.

These results and the following discussion depend on a number of assumptions: the TNG galaxy formation model, the Friends-of-Friends halo finder for defining the halos and their members, the SUBFIND algorithm for determining the galaxies' bound resolution elements, the TNG-Cluster halo sample, and the numerical resolution of TNG-Cluster itself (see Appendix 6.6 for more details on the gas resolution).

6.4.1 Detecting Extended Soft X-ray Emission Around Satellites

We now turn to answer the following question: Can the hot CGM retained by satellites be detected, above the background ICM (Schuecker et al., 2001). This hot satellite gas emits thermally via bremsstrahlung in the X-ray, similarly to the ICM. However the gas temperature is much lower for satellite CGM gas $\approx 0.5 - 2$ keV compared to the ICM at $\approx 5 - 10$ keV (see also Truong et al., 2024). We therefore focus on the soft X-ray $0.5 - 2$ keV emission, computed using the collisional ionization tables of AtomDB from the Astrophysical Plasma Emission Code (Smith et al., 2001, following Nelson et al. 2023).

In Fig. 6.7 we show examples of broad-band soft X-ray emission around 16 TNG-Cluster satellite galaxies. These galaxies are necessarily within a projected distance $d < 1.5 R_{200c}^{\rm host}$ of one of the 352 TNG-Cluster BCGs. Each image is 600×600 kpc^2 in size, and we include information about each galaxy and its host in the panels. The X-ray emission around these galaxies is clearly visible against the background ICM, even without a background subtraction. The X-ray morphologies are diverse; while many examples are roughly circular, many also show asymmetries and filamentary features. These morphologies could be caused by both internal (for example, SMBH feedback, such as for SubfindIDs 256830, 4373716, 7596594) and/or external processes (for example, ram pressure, such as for SubfindIDs 7596594, 7929001). These are some of the most prominent spatially extended X-ray emission around satellites, but each cluster hosts several such examples[5] (Nelson et al., 2024).

[5] We include three projections of each cluster in the soft X-ray in an online gallery, where satellites can clearly be seen against the background: https:/www.tng-project.org/cluster/gallery/.

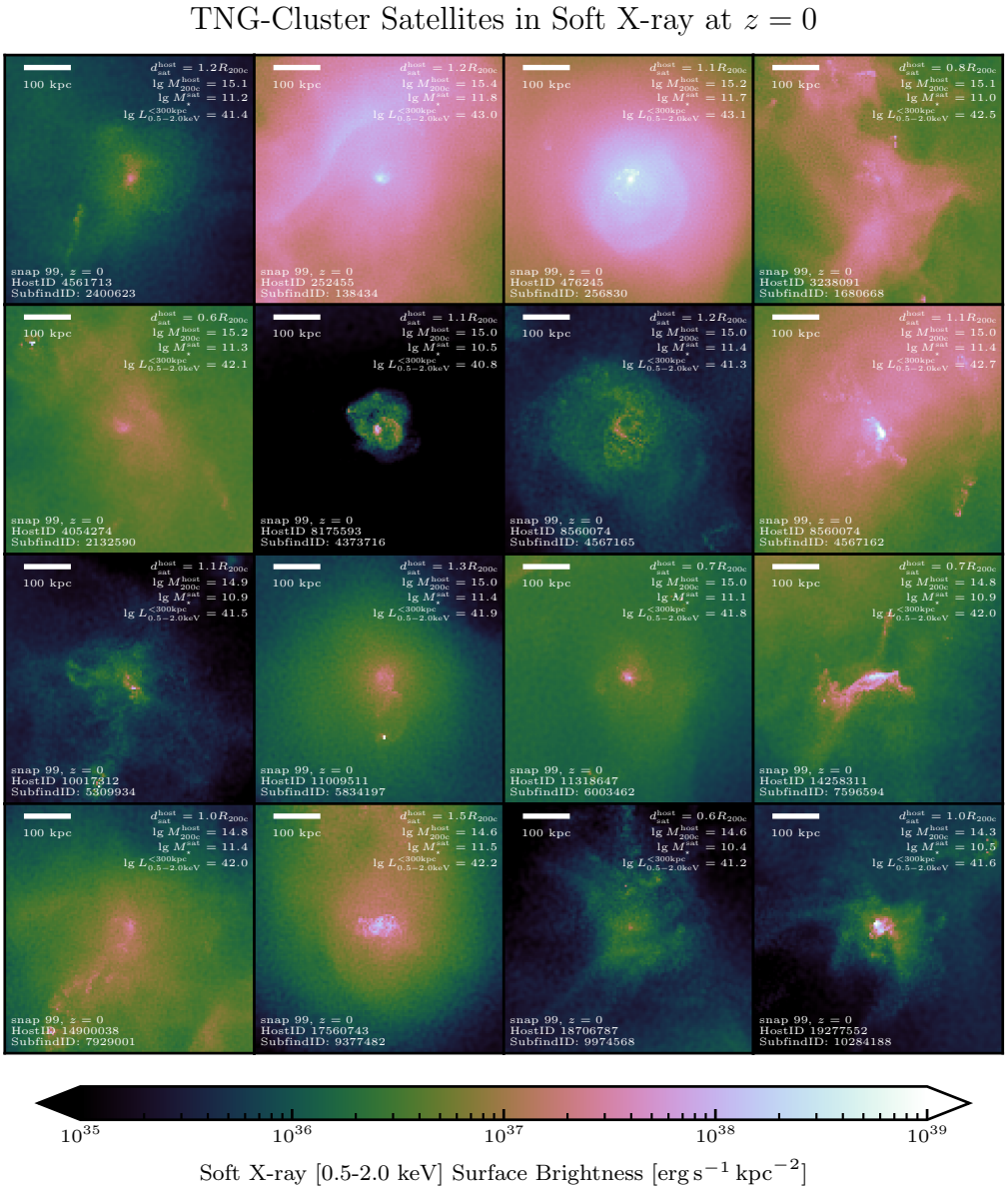

Figure 6.7: **Poster of the diversity of TNG-Cluster satellites in soft X-ray emission.** We show the soft X-ray (0.5-2.0 keV) surface brightness for 16 example TNG-Cluster satellite galaxies at $z = 0$. Each image is 600×600 kpc^2 in size (scale bar in the upper left). These galaxies are necessarily within a projected distance of $1.5R_{200c}$ of their host. We include information about the galaxy and its host in the upper right and lower left corners; the units of the cluster M_{200c}^{host} and satellite $M_{\star}^{sat}$ mass are [$\log_{10}$ M$_\odot$], and the soft X-ray luminosity $L_{0.5-2.0keV}^{<300kpc}$ is the total X-ray luminosity within a projected aperture of 300 kpc in units of [$\log_{10}$ erg s^{-1}]. Many of the maps display morphological signatures of SMBH feedback, with dome-like inflated bubbles and/or ram pressure, with gas tails extending in specific directions.

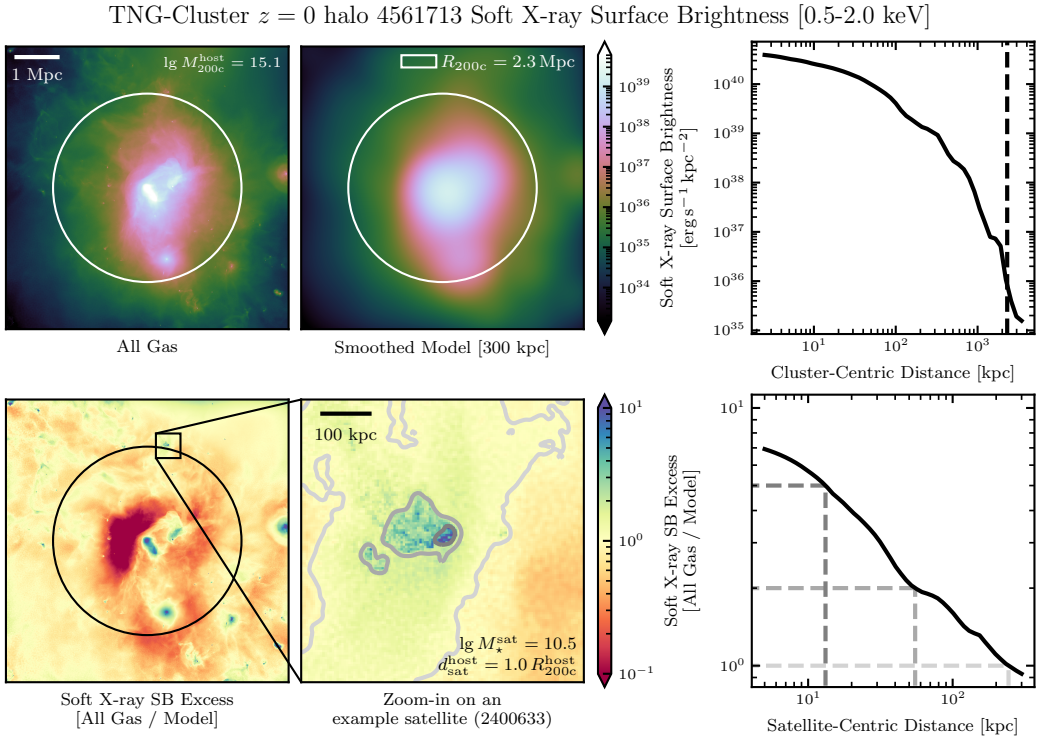

Figure 6.8: **Schematic detailing how we detected satellites' circumgalactic media and measured their radial profiles.** For a given halo (halo mass $M_{200c}^{host} \approx 10^{15.1}\,M_\odot$) at $z = 0$, we compute the soft X-ray (0.5 – 2.0 keV) continuum surface brightness (SB) on $5 \times 5\,kpc^2$ pixels (top left). We then smooth the image using a Gaussian kernel of standard deviation 300 kpc (top center). The white circles indicate the virial radius. We include the azimuthally averaged radial profile, where the dashed line marks the virial radius (top right). We compute the soft X-ray surface brightness excess as the ratio of all the gas in the image to the smoothed model (bottom left), and zoom in on an individual example satellite (bottom center; stellar mass $M_\star^{sat} \approx 10^{10.5}\,M_\odot$ at projected cluster-centric distance $d_{sat}^{host} \approx 1.0 R_{200c}^{host}$). We include the contours of {1, 2, 5} times the background on the zoom-in and on the satellite's excess radial profile (bottom right). In this satellite we detect a soft X-ray surface brightness excess out to ≈ 200 kpc from the satellite's center, and the morphology suggests the satellite's X-ray emitting gas is experiencing environmental effects. The soft X-ray excess profile for this example satellite is similar to others of the same stellar mass and cluster-centric distance (see Fig. 6.9 and text).

We now quantify the spatial extent of the X-ray emitting gas compared to the ambient background for all > 30,000 massive satellite galaxies around TNG-Cluster hosts. Fig. 6.8 displays a schematic of our methodology. We start with the projected soft X-ray map of an entire cluster (top left panel; this example has mass $M_{\rm 200c}^{\rm host} \approx 10^{15.1}\,{\rm M}_\odot$), where the image is $3R_{\rm 200c}$ (≈ 6.9 Mpc) in size in each direction and the white circle marks $R_{\rm 200c}$. We include all gas in the simulation in this projection, with a depth of $\sim 5R_{\rm 200c} \sim 10$ Mpc. We then smooth the X-ray map using a Gaussian kernel with a fixed physical width of 300 kpc (top center panel). This choice of smoothing length enables us to detect excesses and deficits compared to the background on scales smaller than 300 kpc. On larger scales, the signal is smoothed out and tends toward the background medium. We vary this smoothing scale between 100 and 1,000 kpc, finding qualitatively similar results. The projected soft X-ray surface brightness radial profile (top right panel) decreases with halo-centric radius, where the dashed line marks the halo radius. This radial profile itself does not provide a good background estimate, as the ICM can be far from spherically symmetric (e.g., Truong et al., 2021).

We compute the soft X-ray surface brightness excess map (bottom left) as the normal X-ray map divided by the smoothed model. In this map the perturbations – both excess (green-blue) and deficits (orange-red) – are clearly visible. Satellites and their CGM produce many of these perturbations, both point-like and extended excess sources. Here, we zoom in on one example satellite of mass $M_\star^{\rm sat} \approx 10^{10.5}\,{\rm M}_\odot$ and at projected host-centric distance $d_{\rm sat}^{\rm host} \approx 1.0R_{\rm 200c}^{\rm host}$ (bottom center panel), where the zoom region is 600 kpc per side. The contours mark where the X-ray surface brightness reaches {1, 2, 5} times the smoothed background. The region of excess X-ray emission (inside the outermost contour) extends to large distances and has a complex morphology. The inner, brighter regions show signs of ram pressure removal. We show the projected radial profile (lower right panel), and find that the excess X-ray emission decreases with satellite-centric distance, reaching the background value at ≈ 200 kpc. This example X-ray excess profile is similar to the average of all satellites of this mass and distance, although the maximum excess at small satellite-centric distances for this example is lower than average (see text below and Fig. 6.9, bottom right panel).

We next consider all massive galaxies $M_\star^{\rm sat} > 10^{10}\,{\rm M}_\odot$ within a projected cluster-centric distance $d_{\rm sat}^{\rm host} < 1.5R_{\rm 200c}^{\rm host}$, ignoring the FoF membership. This yields $\approx 37,000$ satellites around the 352 clusters. We zoom-in on the positions of each of these satellites and compute the soft X-ray surface brightness excess radial profile. Fig. 6.9 shows the mean-stacked profiles in bins of satellite stellar mass $M_\star^{\rm sat}$ (top center), host halo mass $M_{\rm 200c}^{\rm host}$ (bottom left), and cluster-centric distance (bottom right). As a reminder, ≈ 85 percent of these satellites are gas-

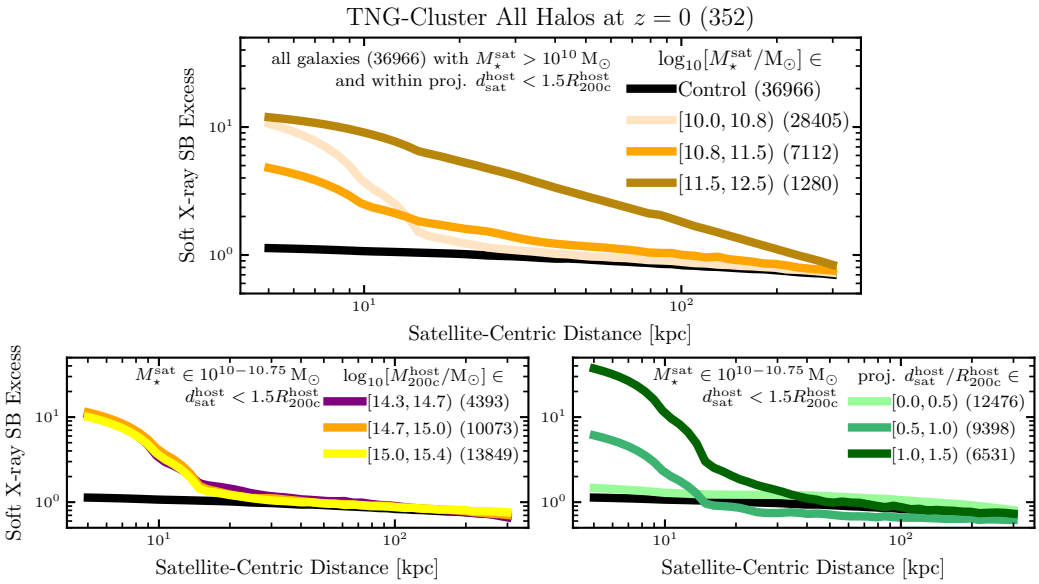

Figure 6.9: **Stack of the $z = 0$ satellite soft X-ray surface brightness excess radial profiles around all 352 TNG-Cluster halos.** We compute the soft X-ray (0.5-2.0 keV) surface brightness (SB) excess around all $\approx$ 37,000 galaxies with $M_\star^{\rm sat} > 10^{10}\,{\rm M}_\odot$ and within a projected distance $d_{\rm sat}^{\rm host} < 1.5R_{\rm 200c}^{\rm host}$ of the 352 hosts. We then mean-stack these radial profiles in bins of satellite stellar mass $M_\star^{\rm sat}$ (top panel), and within a fixed stellar mass bin, we further stack in bins of host cluster mass $M_{\rm 200c}^{\rm host}$ (bottom left) and cluster-centric distance (bottom right). In all panels, the control sample represents the same measurement, at random locations such that the distributions of cluster-centric distances match that of the satellites. Across all satellites, the X-ray excess extends to $\sim 20-100$ kpc, although individual satellites or specific stacks may exhibit excesses out to $\approx$ 300 kpc from the satellites.

poor and do not contribute to the total emission, but we still include them in stacks[6] . Some of these galaxies lie in projection near other X-ray excesses (deficits) and would still contribute (negatively) to the stacked profile. It is not clear a priori if the excesses and deficits cancel each other out. We therefore construct a control sample stack that matches the distribution of cluster-centric distances. While we construct control samples for each stack (in satellite mass, host mass, and cluster-centric distance), the differences between the controls of each stack are negligible, and all show a surface brightness excess of ≈ 1. We simplify by plotting the total control sample (black curves) in each panel.

In Fig. 6.9 (top center), all three stellar mass $M_\star^{\rm sat}$ bins display X-ray excesses compared to the control. The most massive satellites $M_\star^{\rm sat} \sim 10^{11.5-12.5}\,{\rm M}_\odot$ (dark orange), have an excess of nearly ≈ 10× the background at small satellite-centric distances $\lesssim$ 10 kpc, and the excess extends out to ≈ 300 kpc. The intermediate $M_\star^{\rm sat} \sim 10^{10.75-11.5}\,{\rm M}_\odot$ (orange) and lower $M_\star^{\rm sat} \sim 10^{10-10.75}\,{\rm M}_\odot$ (light orange) bins also display extended X-ray excesses out to ≈ 100 and ≈ 30 kpc respectively. The satellites in the lower-mass bin have a higher peak X-ray excess at small distances than those in the intermediate mass bin. As shown in Fig. 6.3 (top panels), the hot gas density at small distances $\lesssim R_{\rm half,\star}$ is higher for lower-mass satellites $M_\star^{\rm sat} \sim 10^{10}\,{\rm M}_\odot$ than for intermediate-mass satellites $M_\star^{\rm sat} \sim 10^{10.75}\,{\rm M}_\odot$. Using hot gas density as a proxy for soft X-ray luminosity, we would then expect these lower-mass satellites (light orange) to be brighter at small distances than intermediate-mass satellites (orange). We speculate that the lower hot gas density in the centers of high-mass satellites could be caused by the AGN feedback redistributing gas to larger distances (e.g., Ayromlou et al., 2023b).

To distinguish from the effects of satellite mass, we now further stack the X-ray excess radial profiles by host mass $M_{\rm 200c}^{\rm host}$ (bottom left) and cluster-centric distance $d_{\rm sat}^{\rm host}$ (bottom right) only for the satellites in the lowest-mass bin $M_\star^{\rm sat} \in 10^{10-10.75}\,{\rm M}_\odot$. In the X-ray excess radial profiles stacked by host mass $M_{\rm 200c}^{\rm host}$ (bottom left), all three halo mass bins display similar maximum excess of ≈ 10× the background at small distances and similar extents to ≈ 50 − 100 kpc. There are no significant differences between different host masses, in agreement with our earlier result that the gas mass of gas-rich satellites $M_{\rm gas}^{\rm sat} > 10^9\,{\rm M}_\odot$ does not vary with halo mass (Fig. 6.2, top right panel).

Lastly, in the stack by projected cluster centric distance $d_{\rm sat}^{\rm host}$ (bottom right), satellites at larger projected cluster-centric distances have both higher peak X-ray excesses and extend to farther satellite-centric distances. Satellites at projected distances $d_{\rm sat}^{\rm host} \approx 1.0 - 1.5 R_{\rm 200c}^{\rm host}$ (dark green) have maximum excesses of $\gtrsim$ 30× the background and extend out to ≈ 50 kpc from

[6] When instead using median-stacks rather than mean-stacks, X-ray excesses around the most massive satellites ($M_\star^{\rm sat} \in 10^{11.5-12.5}\,{\rm M}_\odot$) and satellites at the largest cluster-centric distances ($d_{\rm sat}^{\rm host}/R_{\rm 200c}^{\rm host} \in 1.0 - 1.5$) remain, but all other stacks are indistinguishable from the control.

the satellite. Greater excesses at large distances arise because these satellites retain more of their CGM. They likely consist of mostly first infallers into the clusters, and so have not been experiencing the cluster-environment effects for as long as other satellites. Since the satellites at the closest projected distances $d_{\rm sat}^{\rm host} \lesssim 0.5 R_{\rm 200c}^{\rm host}$ (light green) are, and have been, experiencing stronger ram pressure removal of their gas, it is natural that they have no significant excess X-ray emission compared to the control.

According to our theoretical experiment and on the outcome of TNG-Cluster, stacking the soft X-ray excess emission around the positions of optically selected satellites can yield a clear signal of the satellite CGM emission. We expect these results to qualitatively hold in X-ray surveys, and such an experiment could be conducted with the eROSITA all sky survey, albeit only for a sample of nearby clusters (e.g., Comparat et al., 2022; Zhang et al., 2024). Recently, Hou et al. (2024) stack the archival *Chandra* observations (0.5-2.0 keV) of 21 star-forming, edge-on, late-type galaxies in the Virgo cluster. They find three detections without the need for stacking, and, when stacking by satellite SFR, they detect a signal for the highest SFR bin, with an X-ray luminosity $L_x \sim 10^{38}\,{\rm erg\,s^{-1}}$ per galaxy. While all of the brightest example TNG-Cluster satellites exceed this luminosity (Fig. 6.7), we speculate that many of the fainter TNG-Cluster satellites would emit at approximately this luminosity. Finally, although we have focused on the broad-band soft X-ray as an example for satellite CGM detectability, we also expect the CGM to be detectable in SZ, by using, for example, X-ray hardness (e.g., Truong et al., 2021), and in ratios of X-ray emission lines using XRISM or LEM (Kraft et al., 2022).

6.4.2 Implications of Satellite CGM for ICM Emission Studies

Considering that each cluster hosts tens to hundreds of massive satellites and that many can retain their own CGM, we turn to the covering fraction of satellite CGM on a cluster by cluster basis. While the overall luminosity and mass fractions of satellite CGM compared to the total ICM may be small, it may be an important component of observable soft X-ray emission from the ICM.

In Fig. 6.10, we split the total (left column) soft X-ray emission of four example clusters into its two main components: gas gravitationally bound to the main halo or BCG (second column); gas gravitationally bound to satellite galaxies (third column). We consider all galaxies within the projected field of view as satellites, regardless of stellar mass or FoF membership. A majority of the TNG-Cluster soft X-ray emission within $R_{\rm 200c}$ (circles) comes from the gas bound to the BCG, but there are also many satellites with their hot CGM that contribute. We compute and show the fractional contribution from satellites to the total soft X-ray emission (rightmost column).

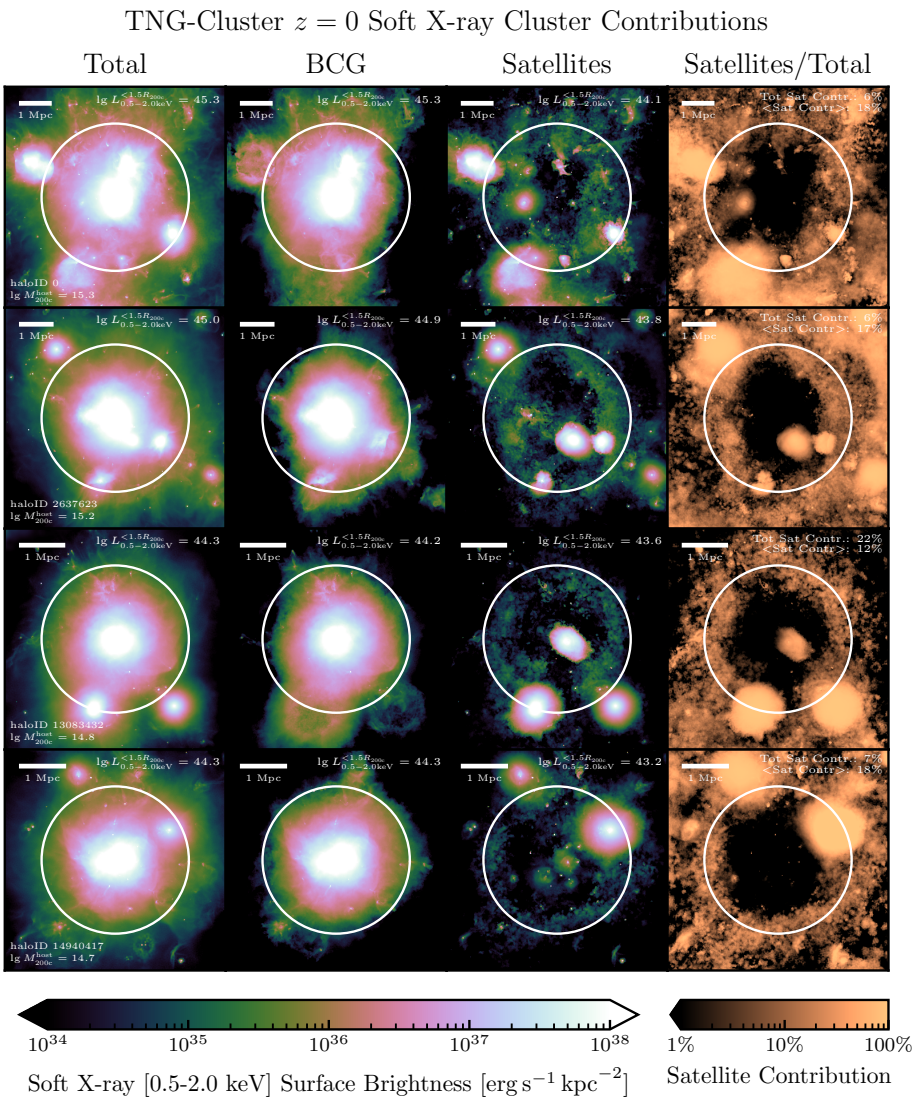

Figure 6.10: **Separating cluster soft X-ray emission into its main sources, for four clusters in TNG-Cluster.** We break down the total soft X-ray emission (Total) of an example cluster into its main components: gas that is gravitationally bound to the main halo, i.e., brightest central galaxy (BCG), and gas bound to the satellite galaxies (Satellites). Here, satellites are all galaxies besides the BCG that lie within the field of view of the image $3R_{200c} \times 3R_{200c}$. We include the haloID and mass M_{200c}^{host} in units of [$\log_{10}$ $M_\odot$] in the lower left in the Total image, and the soft X-ray luminosity $L_{0.5-2.0keV}^{<1.5R_{200c}}$ within a projected aperture $1.5R_{200c}$ in units of [$\log_{10}$ erg s^{-1}] in the top right of each panel. We compute the fractional contribution from satellites to the total soft X-ray emission (Satellites / Total), and include both the total soft X-ray contribution from satellites and the mean satellite contribution per pixel in the upper right corner. In all panels the circles denote R_{200c}. The satellite contributions vary from halo-to-halo, but in general satellites contribute $\sim$ 10 percent of the total soft X-ray flux within $\lesssim 1.5R_{200c}$ of the clusters.

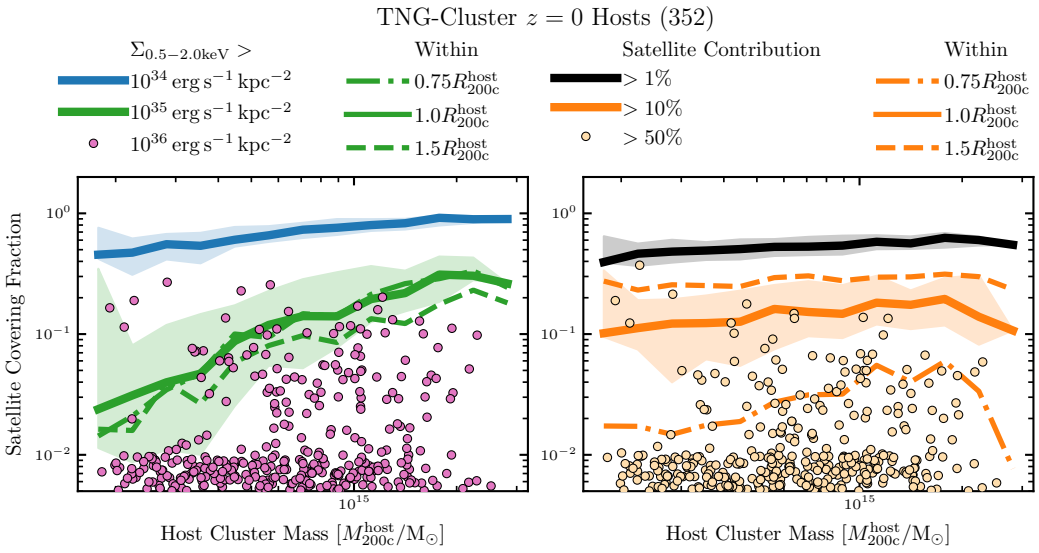

Figure 6.11: **Covering fraction of X-ray emission from satellite circumgalactic media in TNG-Cluster.** We measure the projected covering fraction of satellites soft X-ray (0.5-2.0 keV) emission to total for the 352 clusters at $z = 0$ for two cases: above a given fixed satellite surface brightness threshold (left panel) and above a given satellite-to-total fractional local threshold (right panel). The fiducial threshold choices are shown for varying cluster-centric apertures. Thick curves are the medians across all clusters, shaded regions enclose the 16th and 84th percentiles, and points are the individual clusters, where we manually place clusters with satellite covering fractions $< 10^{-2}$ between 10^{-2} and $10^{-2.5}$. In both panels when varying the minimum threshold we use the fiducial aperture of $< 1.0R_{200c}$, and when varying the aperture we use the intermediate threshold ($> 10^{35}$ erg s^{-1} kpc^{-2} in the left panel; > 10 percent contribution in the right panel). The collection of satellite CGM can contribute to a significant portion of the cluster's projected area, and at larger surface brightness or satellite-to-total fractional thresholds there is more halo to halo variation.

In the cluster centers, satellites do not contribute significantly to the total X-ray flux, except for, locally, around the positions of particularly bright satellites. In the outskirts, however, satellites contribute more significantly to the total X-ray. In each cluster here there are at least a few satellites with bright, spatially extended CGM, and all clusters host many satellites with visible CGM emission.

We quantify the projected covering fraction of soft X-ray emission from bound satellite gas in Fig. 6.11. We compute the projected covering fraction of satellite soft X-ray (0.5-2.0 keV) emission within a given aperture for the 352 clusters at $z = 0$ in two ways: a) above a given surface brightness threshold (left panel) or satellite-to-total fractional threshold – that is,above a given threshold of local satellite-to-total fractional emission on a pixel by pixel basis (right panel). Thick curves are the medians, shaded regions enclose the 16th and 84th percentiles, and points are the individual clusters.

Above any of the considered physical surface brightness thresholds (left panel, different colors), the satellite covering fractions increase with cluster mass. As the cluster mass increases, the number of satellites and average satellite mass increase, while higher-mass satellites are also more likely to retain larger, brighter CGM. At a surface brightness above 10^{34} erg s^{-1} kpc^{-2} (blue), nearly all clusters have a satellite covering fraction of $\approx 0.7 - 1$, suggesting that with deep enough X-ray observations a majority of cluster-sightlines intercept some satellite circumgalactic gas. That is, while the current eROSITA all sky survey (eRASS:4) can detect X-ray surface brightness down to $\sim 10^{35}$ erg s^{-1} kpc^{-2} (at least via stacking; Zhang et al., 2024), we speculate that at ~ 1 dex deeper imaging more than of pixels would contain emission from satellites. Detecting this satellite contribution would depend on the signal to noise, or using X-ray spectra to distinguish the satellite CGM from the ICM emission.

Above 10^{35} erg s^{-1} kpc^{-2} (green; the level currently achievable in eRASS:4), the satellite covering fraction increases from $\approx$ 3 percent at $M_{200c}^{\rm host} \sim 10^{14.3}$ M$_\odot$ to $\approx$ 30 percent at $M_{200c}^{\rm host} \sim 10^{15.4}$ M$_\odot$. Above 10^{36} erg s^{-1} kpc^{-2} (pink) the median satellite covering fraction is $\lesssim 10^{-1}$ for halo masses $\lesssim 10^{15}$ M$_\odot$ (not shown). There are however a number of individual clusters at all masses with high covering fractions, that is,> 0.1 within $R_{200c}^{\rm host}$. Finally, at a surface brightness threshold of $> 10^{35}$ erg s^{-1} kpc^{-2}, the covering fractions are similar within $0.75R_{200c}^{\rm host} \approx R_{500c}^{\rm host}$ (dashed-dotted) and $R_{200c}^{\rm host}$ (solid), decreasing at larger radii $\approx 1.5R_{200c}^{\rm host}$ (dashed).

Roughly half the cluster project area within the virial radius has > 1 percent contribution from satellites (Fig. 6.11, black line). Only ≈ 10 percent of the pixels have satellite contributions above the fiducial 10 percent threshold. At the highest satellite-to-total threshold of > 50 percent, meaning that at least half of the total soft X-ray flux per pixel originates from satellites, only ≈ 3 percent of clusters have significant satellite covering fractions > 10 percent.

As can been seen from the images in Fig. 6.10, the X-ray emission in cluster cores is dominated by the gas bound to the BCG. In the outskirts however, satellites contribute more significantly to the total flux. Considering the region from $0.75 - 1.5\ R_{200c}^{\rm host}$ ($\approx 1.0 - 2.0\ R_{500c}^{\rm host}$), the covering fractions above the fiducial > 10 percent satellite contribute are the highest at ≈ 0.75. Overall, satellites contribute $\gtrsim 10$ percent of the total soft X-ray emission to cluster outskirts $\approx 0.75 - 1.5 R_{200c}^{\rm host}$.

6.4.3 Implications for Satellite Galaxy Evolution

The presence of a CGM, or not, affects the evolution of a given satellite galaxy and how the satellite interacts with its surrounding medium. From the perspective of the satellites themselves, the presence of an extended CGM gaseous halo and reservoir will modify their evolution in high-density environments, versus if they were directly exposed to the cluster environment (Li et al., 2023). Conversely, from the perspective of the cluster-satellite interactions, feedback from the satellites will have different effects on the surrounding host medium if they have their own CGM (Bahe et al., 2012). Finally, from the perspective of the CGM and/or ICM of massive haloes, whether satellites are surrounded by their own gas will affect the interpretation of the ICM itself also via, for example, absorption line studies (Anand et al., 2022).

Satellites that have already had their CGM removed have lost their barrier or protection against the ICM. If there is continued star formation or black hole accretion, then the ensuing outflows would interact with the ICM, heating up and becoming unbound from the satellite, that is being directly deposited into and mixed with the ICM (McGee et al., 2014). As a majority of satellites in TNG-Cluster are gas-poor today, many satellites have deposited their CGM and ISM into cluster atmospheres, and these satellites could potentially act as a source of metals in cluster outskirts (see Nelson et al., 2024).

Satellites that still retain their CGM behave differently. First, the CGM will roughly co-move with the satellite, shielding it from ram pressure stripping. To an extent, satellites with a spatially extended, roughly spherical CGM may continue evolving similarly to central galaxies of the same mass, that is forming stars, growing their central SMBHs, and even accreting cold gas from their own CGM. However, there remain key differences between these massive satellites and their central counterparts (e.g., Engler et al., 2020). For example, in TNG100 massive satellites $M_\star^{\rm sat} \sim 10^{10.6-11.6}\ {\rm M}_\odot$ that quench as satellites tend to have reduced SMBH accretion rates compared to centrals (Joshi et al., 2020). This could be caused by lower gas accretion rates from a disturbed or partially stripped CGM. The existence of the CGM for satellite galaxies modulates not only their secular evolution but also the impact of environment, as well as the strength and nature of interactions with the parent cluster ICM.

6.5 Summary and Main Conclusions

In this work we study the gas content, circumgalactic medium retention, and observability of ≈ 90, 000 satellite galaxies in and around 352 host clusters from the new TNG-Cluster simulation (Nelson et al., 2024, Pillepich et al. in prep). This simulation provides statistical and representative samples of satellites at high resolution $m_{\rm bar} \sim 10^7\,{\rm M}_\odot$ with the well-validated TNG galaxy formation model (Weinberger et al., 2017; Pillepich et al., 2018a). We focus on satellites with stellar mass $M_\star^{\rm sat} \sim 10^{9-12.5}\,{\rm M}_\odot$ around clusters with total mass $M_{\rm 200c}^{\rm host} \sim 10^{14.3-15.4}\,{\rm M}_\odot$ at $z = 0$. Our main results are:

- The number of satellites per cluster above a given stellar mass threshold increases with cluster mass such that a cluster of mass $M_{\rm 200c}^{\rm host} \sim 10^{14.5}$ (10^{15}) ${\rm M}_\odot$ hosts ∼ 100 (300) satellites today (Fig. 6.1, § 6.3.1). Of these satellites, ∼ 40 (100) are massive $M_\star^{\rm sat} \sim 10^{10-12.5}{\rm M}_\odot$. Each cluster hosts at least a few extremely massive satellites $M_\star^{\rm sat} \sim 10^{11-12.5}\,{\rm M}_\odot$, that is,as or more massive than Andromeda. The TNG-Cluster satellite-richness relation broadly agrees with SDSS observations.

- Across all studied stellar and host masses, only a minority (10 percent) of satellites retain significant gas reservoirs $M_{\rm gas}^{\rm sat} > 10^9\,{\rm M}_\odot$ at $z = 0$. The fraction of gas-rich satellites increases with satellite stellar mass (Fig. 6.2, § 6.3.2), where more massive satellites have higher gas masses. There is little trend with host cluster mass.

- lower-mass satellites $M_\star^{\rm sat} \sim 10^{9-10}\,{\rm M}_\odot$ are more likely to retain, if at all, a mostly cold interstellar medium (ISM) as opposed to a hot CGM, as ram pressure preferentially removes the CGM first (Figs. 6.3, 6.4, § 6.3.2,§ 6.3.4). higher-mass satellites $M_\star^{\rm sat} \sim 10^{10.75-12.5}{\rm M}_\odot$ are more likely to retain a mostly hot, spatially extended CGM because of their stronger self-gravity, and the ejective impact of AGN feedback on ISM gas (Figs. 6.3, 6.4).

- With a sample of over 5,000 satellites that retain a sizeable amount of their CGM gas, we find that CGM gas mass increases with satellite stellar mass (Fig. 6.3). More massive satellites lose less CGM mass since infall, reflecting their resistance to environmentally driven gas-removal processes.

- We predict that many gas-rich TNG-Cluster satellites should be visible in the soft X-ray (0.5-2.0 keV), even without a background subtraction (Fig. 6.7, § 6.4.1).

- We quantify the soft X-ray excess around satellites by subtracting a smoothed model from the total X-ray surface brightness maps (Fig. 6.8). When mean-stacking all 37, 000

satellites of mass $M_\star^{\rm sat} \sim 10^{10-12.5}\,{\rm M}_\odot$ within a projected distance $< 1.5 R_{\rm 200c}^{\rm host}$, there is an excess in the X-ray surface brightness up to $\approx 10\times$ the background, extending to $\approx 50-100$ kpc (Fig. 6.9). The excess is the largest for satellites with high masses and large cluster-centric distances.

- We contrast the soft X-ray contribution from satellites to the total ICM emission (Figs. 6.10, 6.11; § 6.4.2). Satellites can contribute significantly to the X-ray emission over large portions of the projected areas of clusters, that is,they have a high covering fraction. Approximately 10 percent of the soft X-ray emission in cluster outskirts $\approx 0.75-1.5 R_{\rm 200c}$ originates from satellite galaxies.

In conclusion, massive satellite galaxies are able to retain at least some of their hot, spatially extended, X-ray emitting CGM, despite living in harsh cluster environments. The gaseous atmospheres around some of these satellites should be visible in the soft X-ray, sometimes without a background subtraction. These results have numerous implications related to the evolution of satellite galaxies and interpretation of X-ray surveys and background quasar absorption studies. The presence or not of a satellite CGM affects how the ICM can remove the ISM of the satellite, how the outflows from the satellite interact with the surrounding medium, and to what extent the satellite is able to accrete from the surrounding medium. We predict a fraction of satellites do in fact retain a sizeable amount of their CGM, and these extended gas reservoirs contribute to the X-ray flux of their host clusters. The average cluster has a high covering fraction of satellite CGM, especially in the outskirts, and these CGM contribute absorbers along the line of sight to background quasars. Future studies can model the TNG-Cluster satellite CGM to compute quantitatively the column densities of specific ions, also in the UV, such as Mg II or O VI, whose absorbing strength depend on the thermodynamic properties of the gas. As we expect these properties to differ between the gas in the satellite CGM and that in the ICM, the absorption features could be dominated by the interloping satellite CGM rather than the ICM. Future observational studies of both quasar absorption features and X-ray clusters should consider the possible influences from the satellite population.

6.6 Appendix A: Defining a Gas Mass Threshold for Gas-Rich Satellites

Fig. 6.12 shows the number of satellites per host, as a function of host halo mass, with a gas mass above a given threshold. Halos with mass $M_{\rm 200c}^{\rm host} \approx 10^{14.5}\,{\rm M}_\odot$ host ≈ 100 satellites (Fig. 6.1 bottom left panel), but only ≈ 10 (≈ 10 percent) of those galaxies retain gas masses

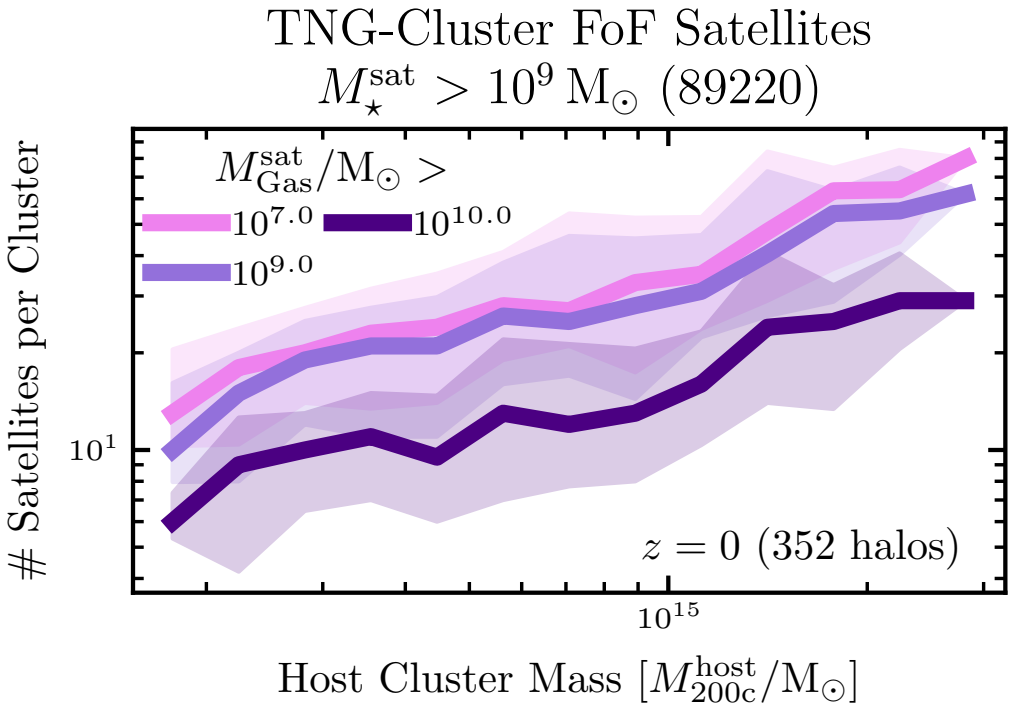

Figure 6.12: Similar to Fig. 6.1 (bottom left panel) except we show the number of satellites per host with a given gas mass $M_{\rm gas}^{\rm sat}$ or higher. The medians and 16th and 84th percentiles are the solid curves and shaded regions respectively. The number of satellites per host above a given gas mass increases with host mass. While ≈ 90 percent of satellites have gas masses $M_{\rm gas}^{\rm sat} < 10^7\,{\rm M}_\odot$, 90 percent of those with gas mass $M_{\rm gas}^{\rm sat} \geq 10^7\,{\rm M}_\odot$ (~ 1 gas cell) actually have $M_{\rm gas}^{\rm sat} \gtrsim 10^9\,{\rm M}_\odot$ (≈ 100 gas cells), suggesting that the gaseous TNG-Cluster satellites are sufficiently resolved.

above our resolution limit at $z = 0$. In fact, the majority of satellites have negligible gas masses $M_{\rm gas}^{\rm sat} \lesssim 10^7\,{\rm M}_\odot$. The curves for the numbers of satellites with $M_{\rm gas}^{\rm sat} > 10^7\,{\rm M}_\odot$ (light purple) and $M_{\rm gas}^{\rm sat} > 10^9\,{\rm M}_\odot$ (purple) are remarkably similar: there are only ≈ 10 percent more of the former. This suggests that satellites with nonzero gas content $M_{\rm gas}^{\rm sat} > 10^7\,{\rm M}_\odot$ (that is, at least one gas cell, or above the TNG-Cluster resolution limit) are reasonably resolved and relatively gas rich $M_{\rm gas}^{\rm sat} \gtrsim 10^9\,{\rm M}_\odot$ ($\gtrsim 100$ gas cells).

As a result, we consider satellites with $M_{\rm gas}^{\rm sat} > 10^9\,{\rm M}_\odot$ gas-rich and those with $M_{\rm gas}^{\rm sat} < 10^9\,{\rm M}_\odot$ gas-poor. We check that adding an additional criterion that the gas fraction $f_{\rm gas} \equiv M_{\rm gas}^{\rm sat}/(M_{\rm gas}^{\rm sat} + M_\star^{\rm sat}) > 10^{-2},\ 10^{-1}$ removes 40 (0.4 percent), 777 (7.7) percent of the gaseous satellites, and excising these galaxies does not significantly affect the results.

Moreover, the difference between these two $M_{\rm gas}^{\rm sat} > 10^7,\ 10^9\,{\rm M}_\odot$ (light purple, purple) populations is much smaller than between the $M_{\rm gas}^{\rm sat} > 10^9,\ 10^{10}\,{\rm M}_\odot$ (purple, dark purple) populations. This well-defined difference suggests that the processes removing gas from satellites are spatially and temporarily resolved at gas masses $M_{\rm gas} \sim 10^{9-10}\,{\rm M}_\odot$, but perhaps not at lower gas masses $M_{\rm gas}^{\rm sat} \lesssim 10^9\,{\rm M}_\odot$. That is, once a gas reservoir drops to $\sim$ a few $\times 10^2$ cells, it quickly becomes gas-poor. A resolution convergence study with the IllustrisTNG boxes can quantitatively assess possible numerical effects on satellite gas contents and physical properties (e.g., Joshi et al., 2020; Donnari et al., 2021b; Stevens et al., 2021).

7 Jellyfish Galaxies With the IllustrisTNG Simulations -- When, Where, and For How Long Does Ram Pressure Stripping of Cold Gas Occur?

This chapter is based on the article Rohr et al. (2023), which I led as the first author, where I conducted the main scientific direction of the paper, performed the analysis, created the figures, and wrote the text. Additional authors and their contributions include: Annalisa Pillepich, who coordinated the Cosmological Jellyfish Project, assisted in the scientific direction, helped organize the final structure of the paper, and significantly edited the text; Dylan Nelson, who provided valuable insights regarding the Monte Carlo tracer particles, assisted in the scientific direction, and edited the text; Elad Zinger, who led the analysis and provided the final classifications for the Cosmological Jellyfish Project, assisted in the scientific direction, and provided comments to the text; Gandhali D. Joshi, who helped conduct the Cosmological Jellyfish Project and provided comments to the text; and Elad Mohammadreza Ayromlou, who provided comments to the text.

This paper was part of the Cosmological Jellyfish Project where the following papers were released on arXiv on the same day: Zinger et al. (2024); Göller et al. (2023); Rohr et al. (2023), where I contributed as a co-author to the other papers. I created the jellyfish branches, which track inspected galaxies across snapshots, which have been publicly released along with the rest of the Cosmological Jellyfish Project data[1]. Additionally, I provided insights to the analysis of each paper, especially so to Göller et al. (2023), and comments to the final texts.

The TNG50 simulation was led by PIs Annalisa Pillepich and Dylan Nelson and excited on the Hazel Hen supercomputer at the High Performance Computing Center Stuttgart under the Gauss Centre for Supercomputing (GCS) Large-Scale Project GCS-DWAR (2016). The TNG50 simulation uses the AREPO *code and TNG galaxy formation model from the IllustrisTNG team*

[1] https://www.tng-project.org/data/docs/specifications/#sec5_3

(PI: Volker Springel; additional references can be found on the TNG website here), which is a follow-up of the original Illustris simulation. Additional analysis was carried out on the Isaac, Raven, and Vera supercomputers at the Max Planck Computing and Data Facility.

ABSTRACT

Jellyfish galaxies are prototypical examples of satellite galaxies undergoing strong ram pressure stripping (RPS). We analyze the evolution of 512 unique, first-infalling jellyfish galaxies from the TNG50 cosmological simulation. These have been visually inspected to be undergoing RPS sometime in the past 5 billion years (since $z = 0.5$), have satellite stellar masses $M_\star^{\rm sat} \sim 10^{8-10.5}$ M$_\odot$, and live in hosts with $M_{\rm 200c} \sim 10^{12-14.3}$ M$_\odot$ at $z = 0$. We quantify the cold gas ($T \leq 10^{4.5}$ K) removal using the tracer particles, confirming that for these jellyfish, RPS is the dominant driver of cold gas loss after infall. Half of these jellyfish are completely gas-less by $z = 0$, and these galaxies have earlier infall times and smaller satellite-to-host mass ratios than their gaseous counterparts. RPS can act on jellyfish galaxies over long time scales of $\approx 1.5 - 8$ Gyr. Jellyfish in more massive hosts are impacted by RPS for a shorter time span and, at a fixed host mass, jellyfish with less cold gas at infall and lower stellar masses at $z = 0$ have shorter RPS time spans. While RPS may act for long periods of time, the peak RPS period – where at least 50 per cent of the total RPS occurs – begins within ≈ 1 Gyr of infall and lasts $\lesssim 2$ Gyr. During this period, the jellyfish are at host-centric distances $\sim 0.2 - 2R_{\rm 200c}$, illustrating that much of RPS occurs at large distances from the host galaxy. Interestingly, jellyfish continue forming stars until they have lost ≈ 98 per cent of their cold gas. For groups and clusters in TNG50 ($M_{\rm 200c}^{\rm host} \sim 10^{13-14.3}$ M$_\odot$), jellyfish galaxies deposit more cold gas ($\sim 10^{11-12}$ M$_\odot$) into halos than exist in them at $z = 0$, demonstrating that jellyfish, and in general satellite galaxies, are a significant source of cold gas accretion.

7.1 Introduction

At a fixed galaxy stellar mass, observations show that there are a number of differences between field and satellite galaxies (satellites for short). Namely with the Sloan Digital Sky Survey (SDSS), it has been shown that the population of satellites has a higher quenched fraction, lower (specific) star-formation rates (SFR, or sSFR), and redder colors compared to central galaxies of the same stellar mass (Peng et al., 2010, 2012; Wetzel et al., 2012). Moreover, satellite galaxies exhibit on average lower neutral HI gas fractions, elevated gas metallicites, reduced circumgalactic X-ray emission, and suppressed active galactic nucleus (AGN) activity compared to their mass-matched analogs in the field (Giovanelli et al., 1985; Brown et al., 2016; Maier et al., 2019a,b).

These observational trends suggest that, in addition to the secular processes of galaxy evolution, satellite galaxies undergo additional environmental phenomena. It is generally accepted that ram-pressure stripping (RPS) is one of the most impactful among such environmental phenomena (Gunn & Gott, 1972, see Boselli et al., 2022 for a recent review).

Ram pressure is proportional to ρv^2, where ρ is the density of the surrounding ambient medium, and v is the relative velocity of the infalling galaxy (or a given parcel of gas) and the ambient medium. This effect is expected to increase with host mass ($M_{\rm 200c}$) because satellites in more massive hosts tend to fall in with higher velocities and more massive hosts tend to

have denser circumgalactic media (CGM)[2], also depending on the stellar and AGN feedback of the central galaxy. Moreover for a given host, this pressure should increase with decreasing distance both because the surrounding medium is denser at smaller radii, and galaxies move faster when they are deeper into their hosts' potential wells. These expected results are broadly consistent with observations (e.g., Maier et al., 2019b; Roberts et al., 2019) With respect to removing single parcels of gas from the infalling satellite, RPS acts against the satellite's gravitational restoring force, dominated by the stellar body. Consequently the effectiveness of RPS is expected to increase with decreasing satellite stellar mass.

For a given satellite galaxy, ram pressure first strips the hot or less gravitationally-bound gas, a feature that has been inferred observationally (Balogh & Morris, 2000) and assumed in semi-analytic models (Cole et al., 2000; Somerville et al., 2008; Lagos et al., 2018; Ayromlou et al., 2019). With respect to the satellite's intersteller medium (ISM), RPS is thought to work outside-in, as observationally inferred via truncated disks (Warmels et al., 1988b; Cayatte et al., 1990, 1994; Vollmer et al., 2001; Lee et al., 2022a) and leading to outside-in quenching (Schaefer et al., 2017, 2019; Bluck et al., 2020; Vulcani et al., 2020; Wang et al., 2023, contra: Wang, 2022).

Ram pressure is also thought to compress the satellite's gas, especially on the galaxy's leading edge. This is inferred to cause temporary periods of enhanced star formation (Gavazzi et al., 2001; Vulcani et al., 2018; Roberts & Parker, 2020; Grishin et al., 2021; Roberts et al., 2022a) and AGN activity (Poggianti et al., 2017a; Maier et al., 2022; Peluso et al., 2022, contra: Roman-Oliveira et al., 2018). In turn, the feedback from star-formation and AGN may lower the binding energy of the ISM gas, potentially facilitating RPS (Garling et al., 2024). Thus the physical mechanism responsible for the loss of satellite ISM gas is likely a combination of RPS and stellar/AGN-driven outflows. However, despite these temporary periods of enhanced star-formation and AGN activity, RPS ultimately leads to the removal of ISM gas and to the quenching *en masse* of satellites (e.g., Wetzel et al., 2013; Maier et al., 2019a; Boselli et al., 2022, see Cortese et al., 2021 for a recent review). We note, however, that the timescales related to environmental quenching are highly debated, ranging from short $\lesssim$ 500 Myr to long $\gtrsim$ 4 Gyr times, typically but not always measured from the first R_{200c} crossing (Cortese et al., 2021, and references therein).

Conversely, satellite galaxies are not only affected by their environment, but they have the potential to perturb the ambient medium in a number of ways. First, the bulk motion of the satellites is thought to affect the CGM kinematics by inducing turbulence and by bringing

[2]Throughout this paper, we define the CGM to be the entire multiphase gaseous medium around central galaxies regardless of their stellar or total host mass, unless explicitly referred to as intragroup medium (IGrM) for galaxy groups ($M_{200c} \sim 10^{13-14}$ M$_\odot$) or intracluster medium (ICM) for clusters ($M_{200c} \sim 10^{14-14.3}$ M$_\odot$).

in gravitational energy, which heats the CGM via dynamical friction and shocks (e.g., Dekel & Birnboim, 2008). As the infalling galaxies may travel faster than the ambient medium's sound speed, some satellites are also expected to create bow shocks in CGM (Yun et al., 2019). This shock and the induced turbulence may act as perturbations, triggering the warm/hot $T \sim 10^{6-8}$ K CGM to cool into $T \sim 10^{4-5}$ K clouds. Moreover, the gas that has been ram-pressure stripped, namely the satellite's cold ISM, is expected to be deposited into the host's halo. For groups and clusters with many satellite galaxies, there could be a substantial amount of accreted halo gas originating from the stripped satellites. However, this has never been quantified. Finally, while currently still highly debated, such cold gas clouds in the CGM, regardless of their origin, could be long-lived (e.g., Li et al., 2020; Sparre et al., 2020; Gronke et al., 2022; Fielding & Bryan, 2022), and satellite-induced cold gas clouds may be a source of cold gas found in the CGM today (Nelson et al., 2020; Rodríguez et al., 2022).

Observed satellites that have been visually identified to be undergoing RPS have been called jellyfish galaxies (from now on, jellyfish for short), where their stellar bodies (the jellyfish heads) remain relatively unperturbed but their gaseous disks are being stripped in the direction opposite of motion, forming the jellyfish tails (e.g., Bekki, 2009; Ebeling et al., 2014; McPartland et al., 2016). These jellyfish and their stripped tails are multi-wavelength objects and have been observed in the X-ray, UV, optical, and radio (e.g., Gavazzi & Jaffe, 1987; Gavazzi et al., 2001; Kenney et al., 2004; Sun et al., 2006; Cortese et al., 2006; Smith et al., 2010; Jáchym et al., 2017; Poggianti et al., 2019; Ignesti et al., 2022). However, many of these studies have focused on single or a few objects. Observers have recently pushed for systematic surveys of jellyfish galaxies, where the largest uniform samples come from the GAs Stripping Phenomena in galaxies with MUSE (GASP; Poggianti et al., 2017b; Gullieuszik et al., 2020, 54 galaxies), the OSIRIS Mapping of Emission-line Galaxies (OMEGA; Chies-Santos et al., 2015; Roman-Oliveira et al., 2018, 70), and the LOw-Frequency ARray (LOFAR; Shimwell et al., 2017; Roberts et al., 2021a,b, 95 in clusters and 60 in groups for 155 jellyfish in total). The largest statistical studies of jellyfish galaxies come from Smith et al. (2022), who use 106 jellyfish with radio continuum emission from the LoTSS survey, and from Peluso et al. (2022), who use 131 jellyfish with information on the central ionizing mechanism.

Despite these recent efforts, unanswered questions still remain, such as: when with respect to infall and where with respect to the host does RPS begin; for how long does RPS act; did the quenched, low gas-fraction galaxies we see today go through a jellyfish phase; what determines how long RPS will take to totally remove a jellyfish's gas; how does the RPS of jellyfish galaxies compare to other satellites; where is the stripped gas being deposited, and more generally, how much cold gas do satellites bring into their hosts' halos?

The answers to these questions can provide both insights into environmental quenching of satellites as well as important implications for the evolution of massive hosts and their surrounding halo gas in the context of the cosmic baryon cycle. While we have reached a general consensus that RPS is necessary to remove satellite cold gas and reproduce the aforementioned environmental trends, the timescales and locations of RPS and the associated satellite quenching remain highly debated. Thus, we turn to numerical simulations with temporal evolution to investigate the satellite-host interaction. Idealized simulations have been able to reproduce jellyfish by imposing an external wind, mimicking the RPS felt during infall through the CGM (e.g., Tonnesen & Bryan, 2009; Lee et al., 2020; Choi et al., 2022). With the perspective of satellite quenching, zoom-in and full cosmological hydrodynamical galaxy simulations have studied more or less explicitly the RPS of satellites, finding a wide range of quenching timescales that broadly agree with observational inference (e.g., Bahé & McCarthy, 2015; Jung et al., 2018; Wright et al., 2019; Yun et al., 2019; Oman et al., 2021; Rodríguez et al., 2022; Pallero et al., 2022; Wright et al., 2022; Samuel et al., 2023). However, quantitative and statistically-robust simulation predictions as to the timings and modalities of RPS are still missing. And so, to understand satellite quenching, we must first quantify the effects of perhaps its most relevant process: RPS.

In this work, we use the high-resolution, ~ 50 Mpc magneto-hydrodynamical simulation TNG50 from the IllustrisTNG project (TNG thereafter) to study the satellite-host interaction in a realistic, cosmological context. In particular, we aim at quantifying when, where, and for how long the RPS of cold gas occurs. We focus on cold gas as this is the source of star formation in galaxies and because its existence within the otherwise hot CGM of massive halos is a compelling open question. Moreover, we focus on jellyfish galaxies because these are satellites that, by identification and hence by construction, are surely undergoing RPS. Among its advantages, the TNG50 simulation produces thousands of galaxies and hosts ranging over 5 orders of magnitude in mass, and it naturally includes many environmental processes such as pre-processing, tidal stripping, harassment, strangulation, starvation, and RPS. The TNG simulations do not include possibly-relevant environmental processes such as viscous momentum transfer or thermal evaporation, and there is no explicit modelling of the multiphase ISM (Cowie & Binney, 1977; Nulsen, 1982, see Zinger et al., 2018a and Kukstas et al., 2022 for discussions). However, the TNG model has been shown to return satellite populations whose quenched fractions and gas content are broadly consistent with observations (e.g. Stevens et al., 2019; Donnari et al., 2021b; Stevens et al., 2021).

In a companion paper, Zinger et al. (2024) visually inspect TNG satellites to identify jellyfish galaxies using the citizen science Cosmological Jellyfish project hosted on Zooniverse, yielding an unprecedented number of more than 500 unique, first-infalling jellyfish galaxies

in the TNG50 volume alone. In another companion paper, Göller et al. (2023) study the star-formation activity of these jellyfish both temporally and across populations. In this paper, we employ the Monte Carlo Lagrangian tracer particles to follow the flows of gas in and out of satellite galaxies, quantifying the cold gas sources and sinks across cosmic time from when the galaxies were centrals, through their jellyfish phases, and in some cases until they have been completely stripped of all gas, existing as quenching, gas-poor satellites at $z = 0$.

We begin by introducing the methods (§ 7.2), namely by summarizing the TNG50 simulation (§ 7.2.1), the Cosmological Jellyfish project (§ 7.2.2), the tracking of galaxies across cosmic time (§ 7.2.3), how we employ the tracer particles (§ 7.2.5.1), and how we identify the onset and end of RPS (§ 7.2.5.2). We then present our main results (§ 7.3). We start by comparing the jellyfish galaxy population with that of the inspected and general $z = 0$ satellite populations (§ 7.3.1), and then comment on the origin of the jellyfish gaseous tails (§ 7.3.2). After quantifying the strength of RPS post infall (§ 7.3.3) and determining a subsample of jellyfish that are devoid of cold gas at $z = 0$ (§ 7.3.4), we answer when, where, and for how long RPS occurs (§ 7.3.5, 7.3.6). We then discuss how we can generalize our jellyfish results with all $z = 0$ satellites (§ 7.4.1), connect the the cold gas loss via RPS with satellite quenching times (§ 7.4.2, and illustrate how much and where cold gas is deposited via RPS into halos (§ 7.4.3). We end by summarizing the main results and restating the conclusions (§ 7.5).

Unless otherwise noted, all analysis including the TNG simulations adopt a ΛCDM cosmology consistent with the Planck Collaboration et al. (2016) results: $\Omega_{\Lambda,0} = 0.6911$, $\Omega_{m,0} = \Omega_{\rm bar,0}+\Omega_{\rm dm,0} = 0.3089$, $\Omega_{\rm bar,0} = 0.0486$, $\sigma_8 = 0.8159$, $n_s = 0.9667$, and $h = H_0/(100\,{\rm km\,s^{-1}\,Mpc^{-1}}) = 0.6774$, where H_0 is the Hubble parameter, and the subscript "0" denotes that the quantity is measured today.

7.2 Methods and TNG50 Jellyfish Galaxies

7.2.1 The TNG50 Simulation

The IllustrisTNG project[3] (Pillepich et al., 2018b; Nelson et al., 2018a; Naiman et al., 2018; Marinacci et al., 2018; Springel et al., 2018) consists of a series of cosmological volume ΛCDM simulations, including gravity + magneto-hydrodynamics (MHD) and a galaxy formation model (see method papers for details: Weinberger et al., 2017; Pillepich et al., 2018a). Here we briefly summarize the TNG simulations.

The TNG production simulations come in three volumes of side lengths ~ 50, 100, and 300 comoving Mpc, hereafter referred to as TNG50, TNG100, and TNG300 respectively. The

[3] https://www.tng-project.org/

TNG galaxy formation model was designed at the resolution of TNG100, which includes 2×1820^3 resolution elements with baryon mass resolution of $m_{\rm bar} = 1.4 \times 10^6$ $M_\odot$. The large volume TNG300 has 2×2500^3 resolution elements with mass resolution $m_{\rm bar} = 1.1 \times 10^7$ $M_\odot$. The high resolution TNG50 simulation has 2×2160^3 resolution elements with mass resolution $m_{\rm bar} = 8.5 \times 10^4$ $M_\odot$ (Nelson et al., 2019b; Pillepich et al., 2019). The minimum gas resolution in TNG50 at $z = 0$, i.e. the smallest non-vanishing gas mass in any given galaxy, is $\approx 4 \times 10^4$ $M_\odot$. These three simulations are publicly available in their entirety (Nelson et al., 2019a). In this paper, we work exclusively with the highest-resolution run TNG50.

The TNG simulations evolve gas, cold dark matter, stars, and super massive black holes (SMBHs) within an expanding universe, based on a self-gravity + MHD framework (Pakmor et al., 2011; Pakmor & Springel, 2013) using the Arepo code (Springel, 2010b). The fluid dynamics employ a Voronoi tessellation to spatially discretize the gas. The TNG gas has a temperature floor at 10^4 K, and the relationship between temperature and density for star-forming gas is determined via an effective equation of state from Springel & Hernquist (2003). For this analysis, we manually set the temperature of star-forming gas to 10^3 K. The TNG galaxy evolution models includes the following processes: gas heating and cooling; star formation; stellar population evolution + chemical enrichment from AGB stars and type Ia + II supernovae; supernova driven outflows and winds (Pillepich et al., 2018a); formation, merging, and growth of SMBHs; and two main SMBH hole feedback modes: a thermal 'quasar' mode, and a kinetic 'wind' mode (Weinberger et al., 2017). The TNG simulations have reproduced many observational relations and properties across orders of magnitude in mass and spatial scales.

The group and galaxy catalogs consist of the dark matter halos and the dark matter plus baryonic galaxies. The dark matter halos are defined using the Friends-of-Friends (FoF) algorithm with a linking length $b = 0.2$, run only using the dark matter particles (Davis et al., 1985). Then the baryonic components are connected to the same halos as their closest dark matter particle. Throughout this paper, we use "FoF", "group", "FoF group", "halo" synonymously. The galaxies are identified using the subfind algorithm, which connect together all gravitationally bound particles (Springel et al., 2001; Dolag et al., 2009). We use the terms "subhalo" and "galaxy" synonymously even though, in general, subfind objects may contain no stars and/or gas whatsoever. Typically albeit not always, the most massive subhalo within a halo is the "main" or "primary subhalo", also called the "central galaxy"; all other subhalos within a halo are "satellites". In all cases, we only consider subhalos of a cosmological origin as defined by the SubhaloFlag in Nelson et al. (2019a).

7.2.2 The Cosmological Jellyfish Project on Zooniverse

In this paper, we study jellyfish galaxies from the TNG50 simulation and identify them based on the classification of the Zooniverse Cosmological Jellyfish project[4]. The Zooniverse Cosmological Jellyfish project presented images of TNG50 satellite galaxies – in addition to TNG100 galaxies, not studied here – on the Zooniverse platform for classification by citizen scientists. Here several thousand volunteers underwent a training session and classified whether the given galaxy resembles a jellyfish or not (Zinger et al., 2024).

Following the pilot project that visually classified a subset of TNG100 satellites (Yun et al., 2019), the term "jellyfish galaxy" was associated with a satellite with a visually identifiable signature of RPS in the form of asymmetric gas distributions in one direction. The visual inspection is based on images of gas column density – i.e. all gas irrespective of phase, temperature, etc. – with stellar mass contours, projected in random orientations in a field of view of 40 times the 3D stellar half mass radius $R_{\rm half,\star}$. Each image was classified by at least 20 inspectors (trained volunteers) whose proficiency was measured when tallying the votes. A galaxy image received a score between 0 and 1 based on these votes, whereby we employ a threshold of 0.8 and above to identify jellyfish galaxies, as recommended by Zinger et al. (2024).

Galaxies meeting the following criteria had their images posted for inspection for the Zooniverse project:

- non central, i.e. satellite;
- of cosmological origin, as defined by the SubhaloFlag in Nelson et al. (2019a);
- $M_\star^{\rm sat} \equiv M_\star^{\rm sat}(< 2 \times R_{\rm half,\star}) > 10^{8.3}$;
- $f_{\rm gas} \equiv M_{\rm gas}^{\rm sat} / M_\star^{\rm sat} > 0.01$, where $M_{\rm gas}^{\rm sat}$ is the satellite's total (i.e. gravitationally-bound) gas mass.

All galaxies satisfying the above criteria were inspected at each available snapshot since $z = 0.5$ (every ~ 150 Myr in cosmic time; snapshots 99-67), and at redshifts 0.7, 1.0, 1.5, and 2.0 (every ~ 1 Gyr in cosmic time; snapshots 59, 50, 40, and 33).

According to the results of the Zooniverse Cosmological Jellyfish project for TNG50, 4,144 of the total 53,610 (7.7 per cent) galaxy images are jellyfish. See Zinger et al. (2024) for more details on the Zooniverse Cosmological Jellyfish project and related results for both TNG50 and TNG100.

[4] https://www.zooniverse.org/projects/apillepich/cosmological-jellyfish

7.2.3 Tracking Galaxies Along the Merger Trees

Based on the selection for the Zooniverse Cosmological Jellyfish project, frequently an individual galaxy was inspected multiple times at different points in time along its evolutionary track.

In this paper, we connect the galaxies that were inspected at multiple times using SUBLINK_GAL (Rodriguez-Gomez et al., 2015). Briefly, SUBLINK_GAL constructs the merger trees at the subhalo level by searching for descendant candidates with common stellar particles and star-forming gas cells. Then SUBLINK_GAL chooses the descendant by ranking all candidates with a merit function that takes into account the binding energy of each particle/cell, and choosing the candidate with the highest score as the descendant.

In this paper, we chiefly work with and follow the unique evolutionary tracks of galaxies, branches, inspected in the Cosmological Jellyfish project. In total, there are 5,023 unique galaxy branches in TNG50 among the inspected images. The analysis of these satellite galaxy populations along their evolutionary tracks requires following the merger tree branches both of the individual galaxies and their (sometimes temporary) hosts. We give results on this in §7.3.1 and more details in Appendix 7.6.

7.2.4 Galaxy Sample Selection of This Analysis

With respect to the Zooniverse Cosmological Jellyfish project, we apply additional selection criteria to be able to start from a sample of satellites defined at $z = 0$ that does not include backsplash and pre-processed galaxies. Please see Appendix 7.6 for details regarding how we classify the galaxies as backsplash and/or pre-processed.

Of the 5,023 inspected galaxy branches in TNG50, we apply the following sample selection criteria. At each criterion, we list the number of remaining branches in the simulation, and the number excised by this criterion in parentheses[5].

1. The galaxy must survive until the end of the simulation at $z = 0$. That is, the main descendant branch must track the subhalo until snapshot 99: 3,018 (2,005 excised).

2. There must be at least one snapshot since $z \leq 0.5$ when the galaxy was inspected in the Zooniverse project (and therefore meeting the criteria outlined in §7.2.2): 2,398 (620).

3. The galaxy must be a satellite galaxy at $z = 0$, i.e., not a backsplash galaxy at snapshot 99: 2,062 (336).

[5]The number excised is the number from the previous criterion. For example, criterion (ii) excises x branches from the y branches remaining after applying criterion (i). This now leaves $y - x$ branches after applying criterion (ii).

4. The galaxy must not have been pre-processed by a host group other than its $z = 0$ host: 1,610 (452).

5. The galaxy must have a well defined infall time (must have been a central galaxy for at least one snapshot before becoming a satellite): 1,543 (67).

Thus our total number of cleaned, first-infalling inspected branches in TNG50 is 1,543. Of these branches, we separate them into those that have at least one jellyfish classification since $z = 0.5$, called "jellyfish" branches, and those without a jellyfish classification since then, called "non-jellyfish" branches. The numbers of jellyfish and of non-jellyfish branches in TNG50 are 512 (33 per cent) and 1,031 (67 per cent), respectively[6] (see §7.3.1 for additional results). We note that at the time of infall all inspected branches (jellyfish and non-jellyfish) are star-forming; see § 7.4.2 for a discussion regarding the quenching times and Göller et al. (2023) for details on the star-forming properties of these galaxies.

7.2.5 On Cold Gas, Infall Time, Tracer Particles, and Measuring Ram Pressure Stripping

In this work, we study the gravitationally-bound cold gas of TNG50 satellite galaxies: by cold gas, throughout this paper, we mean gas with a temperature $T_{\rm ColdGas} \leq 10^{4.5}$ K (including star-forming gas; see § 7.2.1 for more details).

Throughout this paper, we define infall as the first time in cosmic history that a galaxy becomes a satellite member of its $z = 0$ FoF host, irrespective of distance.

7.2.5.1 Following the Gas with Tracer Particles

As TNG50 is based on a moving-mesh code to follow the evolution of the underlying fluid field, we must employ the Monte-Carlo-Lagrangian tracer particles to follow the history and evolution of individual gas parcels (Genel et al., 2013; Nelson et al., 2013). Briefly, AREPO treats the gas as a fluid field through a Voronoi mesh. There is no innate method to follow the flow of matter between the mesh elements and across time. Thus the tracers are introduced, acting as test particles within the fluid. TNG50 was run with one tracer per gas cell at the initial conditions. The tracers have a constant identifying number (ID) throughout the simulation, and at each snapshot each tracer has exactly one baryonic parent resolution element: a gas cell, a stellar or wind particle, or a SMBH. This means that any given tracer represents 8.5×10^4 $M_\odot$ of baryonic mass with the properties of its parent. For example, if a single tracer has a gas

[6] In TNG50, there are 8 cleaned, inspected branches that have a jellyfish classification before $z = 0.5$ but not afterwards. We exclude these galaxies from the jellyfish sample.

parent at one time and a star parent at the next time, then the tracer represents 8.5×10^4 $M_\odot$ of gas mass being converted into stars. In this way, one can track the flow of matter by following a given tracer and its parent's properties across cosmic time. In TNG50 the parents of the tracers are output at each snapshot, describing the exchange of parcels of baryonic material across resolution elements at time intervals of $\sim$ 150 Myr. As the tracer particles are Monte Carlo in nature, we make only statistical statements about the behavior of thousands to millions of tracers.

In practice, at each snapshot and for each galaxy of interest, we find all tracers whose parents are bound, cold gas cells. While not every gas cell necessarily has an associated tracer and some gas cells may have multiple child tracers, the total tracer cold gas mass (total number of tracers times $m_{\rm bar} = 8.5 \times 10^4$ $M_\odot$) agrees with the total amount of cold gas mass measured by gas cells (see § 7.3.3 for more details and an example). Then we follow the tracers and their parents across snapshots in order to measure the cold gas mass that is stripped or launched in an outflow, becomes hot, participates in star formation, transforms into a wind particle, and gets accreted into a SMBH.

We proceed as follows, on a galaxy by galaxy basis along its main descendant branch (MDB). Starting from the first snapshot that the galaxy is identified in the merger trees, we find all tracers whose parents are bound, cold gas cells of this galaxy. Then at the next snapshot for the galaxy along its MDB, we find which tracers belong to one of the following mutually exclusive and completely exhaustive groups:

1. are recorded in both snapshots: bound, cold gas that remains bound, cold;
2. are recorded in the current snapshot but not in the previous one: currently bound, cold gas that previously was either not bound or not cold;
3. are recorded in the previous snapshot but not the current one: previously bound, cold gas that no longer is;

Potential physical origins of tracers in group (ii) include inflows, cooling, stellar mass return, or wind re-coupling. The group (iii) tracers could either a) go from cold gas cells into one of the following: star particles (star formation denoted SF, or SFR for star formation rate); SMBH sink particles (i.e. SMBH accretion); bound, warm/hot gas cells (heating); or b) be no longer bound gas cells (stripping + outflows). We denote the latter "RPS+outflows" and will be focusing on this quantity throughout the paper. We include tracers whose parents become unbound and hot in the same time step in this category. We note that tidal stripping may be included in RPS+outflows, although visual inspection shows that ram-pressure stripping is the dominant mechanism of jellyfish galaxies, and a majority of galaxies do not reach host-centric distances $\lesssim 0.2 R_{\rm 200c}$. Moreover, the Zooniverse inspectors were specifically asked *not*

to classify an image as a jellyfish if there was a close companion or gaseous tails were visible on both sides of the galaxy (Zinger et al., 2024).

7.2.5.2 Identifying the Onset and End of Ram Pressure Stripping

Throughout our analysis, prior to infall (host FoF membership; see above), we assume that the RPS + outflows category is dominated by outflows, namely outflows driven from stellar- and/or SMBH-feedback. As we further justify in § 7.3.3, for most jellyfish the amount of outflows before infall is approximately constant. Immediately after infall, there is commonly an increase in the RPS + Outflows category, indicating that another physical process has become present, namely RPS. Moreover between infall and pericenter, many satellites experience bursts of star formation and/or AGN accretion, which has also been seen in observations, reproduced by simulations, and thought to be caused by ram pressure compressing the ISM gas (Gavazzi & Jaffe, 1987; Bahé & McCarthy, 2015; Mistani et al., 2016; Zoldan et al., 2017; Vulcani et al., 2018; Roberts & Parker, 2020; Grishin et al., 2021; Peluso et al., 2022; Göller et al., 2023; Garling et al., 2024). These bursts of star formation and/or AGN accretion would in turn induce turbulence in the ISM and drive outflows, which then facilitate ram-pressure stripping (e.g., Bahé & McCarthy, 2015). Attempting to distinguish the relative contributions from outflows and ram pressure becomes a chicken-and-egg problem. Thus, we consider the time of infall to be the onset of RPS, and after infall relabel the quantity "RPS+Outflows" as "RPS". We note that we have estimated the onset of RPS using two alternative methods, and find that for most jellyfish the difference between the various methods is $\lesssim$ 450 Myr ($\lesssim$ 3 snapshots): see Appendix 7.7 and Fig. 7.14 for more details.

The end of ram-pressure stripping is either when the galaxy's cold gas mass falls below our resolution limit (namely below $\approx 4 \times 10^4$ M$_\odot$ i.e. $f_{\rm gas} \lesssim 5 \times 10^{-4}$ for a galaxy at our minimum stellar mass of $\mathcal{M}_\star^{\rm sat} = 10^{8.3}$ M$_\odot$), or the end of simulation at $z = 0$. In our sample, 259/512 ($\approx$ 50 per cent) galaxies lose all their cold gas at or before $z = 0$.

We denote the onset of RPS as the infall time τ_0 and its end as τ_{100} (when 100 per cent of the RPS has occurred), so that the difference between these two times returns in principle the maximum time span over which RPS has acted on any given galaxy:

$$\tau_{\rm RPS} = \tau_{100} - \tau_0, \tag{7.1}$$

where τ_{100}, τ_0 are the ages of the universe at the given points. This RPS time span is the longest duration over which RPS has acted for the galaxies that have lost their cold gas prior to $z = 0$. On the other hand, for those satellites that still have some gas today, the above-defined timescale

of RPS is likely a lower estimate, while we speculate that these galaxies would continue being stripped in the future. See §7.3.4 for differences between these two ending states.

Throughout the paper, we will compare the times of RPS with estimates of the quenching time, i.e. of the most recent and last time that a galaxy has fallen 1 dex below the star-forming main sequence (SFMS) for its mass and redshift, as per definitions of Pillepich et al. (2019) and catalogs from Joshi et al. (2021); Donnari et al. (2021b).

7.3 Results

7.3.1 TNG Jellyfish Galaxies Across Their Unique Branches

According to the Cosmological Jellyfish project on Zooniverse, 4,144 of the 53,610 images from TNG50 are jellyfish galaxies (7.7 per cent; Zinger et al., 2024). Using the merger trees to identify when the same galaxies were imaged at multiple points in cosmic time in TNG50 and applying our selection criteria (§7.2.4), we now focus on our sample of 512 first-infalling unique jellyfish galaxies, among 1,543 unique, inspected branches (33 per cent).

Fig. 7.1 shows our selection of Jellyfish (green histograms) and Inspected (dark gray histograms) satellites at $z = 0$. We now quote numbers in terms of unique branches such that Fig. 7.1 is the branch- or merger tree-based counterpart of similar histograms in Zinger et al. (2024, see their fig. 2). In each of the panels, we include the medians and 1σ errors (hashes and shaded regions on the top x-axis) for the Inspected and Jellyfish samples. We note that for each of the distributions (except $M_\star^{\rm sat}(z = 0)$, see text below), the 2-sample Kolmogorov-Smirnov (KS) and Anderson-Darling (AD) tests suggest at $\geq$ 95 per cent confidence that the Inspected and Jellyfish samples were not drawn from the same parent distribution, i.e. that the two samples are significantly different. We include for comparison the general population of $z = 0$ satellites with $M_\star^{\rm sat}(z = 0) \geq 10^{8.3}\,{\rm M}_\odot$, which is generally similar to the Zooniverse inspected sample, except that the general $z = 0$ satellite population includes pre-processed satellites. See § 7.4.1 for a more detailed discussion on how representative the jellyfish sample is compared to all $z = 0$ satellites above stellar mass.

Firstly, Fig. 7.1 shows, thanks to TNG50, that we can study satellite galaxies, and hence jellyfish and RPS, in a rather extended range of stellar masses and host masses. Namely we study satellites with stellar masses $\sim 10^{8-12}\,{\rm M}_\odot$ orbiting in hosts with total masses $\sim 10^{10.5-14.3}\,{\rm M}_\odot$ at $z = 0$. However we cannot make statements about satellites in the most massive clusters $M_{\rm 200c} \sim 10^{15}\,{\rm M}_\odot$.

As shown in the top left panel, jellyfish galaxies (green) tend towards lower stellar masses $M_\star^{\rm sat}(z = 0)$ compared to the inspected galaxies (dark gray), and especially to the non-jellyfish galaxies that have been inspected (not shown, but would be dark gray minus green). Since the

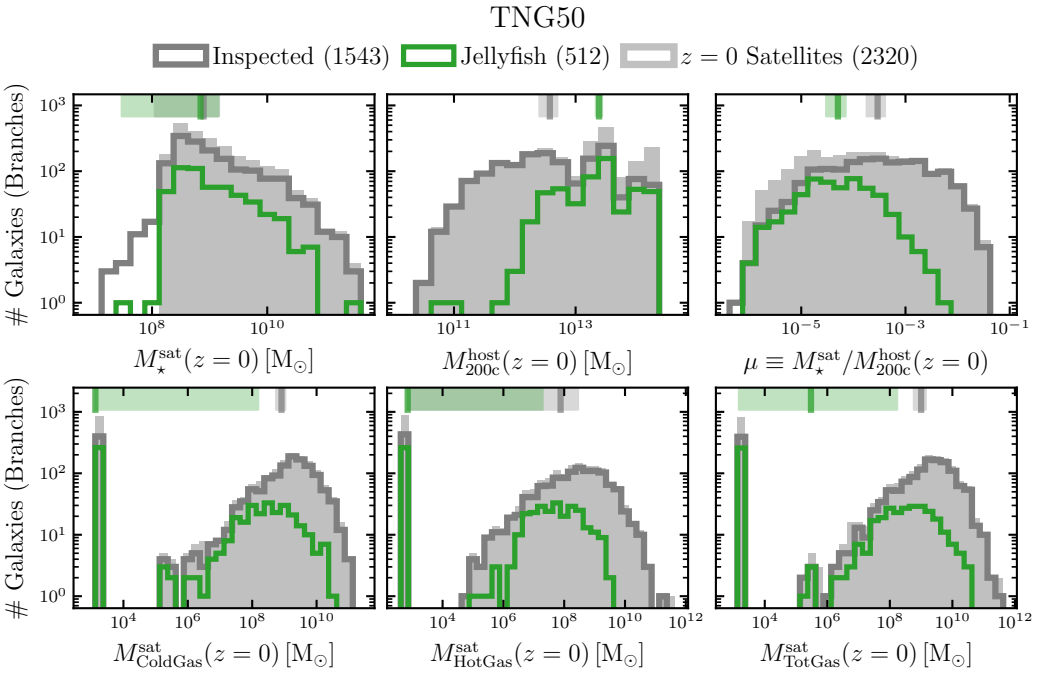

Figure 7.1: **Selection of TNG50 galaxies studied in this work and the abundance of jellyfish, along their unique branches.** The Inspected sample (dark gray) includes a subset of all satellite branches from TNG50, selected for the identification of galaxies with clear signatures of RPS: this chiefly excludes satellites with $M_\star^{\rm sat} < 10^{8.3}$ M$_\odot$ and less than 1 per cent of gas mass fraction at the time of inspection, as well as pre-processed and backsplash galaxies. The Jellyfish sample (green) also requires at least one jellyfish-classified snapshot at $z \leq 0.5$. See §7.2.2 and 7.2.4 for more details. The medians and 1σ errors of the Inspected and Jellyfish galaxy distributions are marked by the hash marks and shaded regions on the top x-axis. For comparison, we show all TNG50 $z = 0$ satellites with $M_\star^{\rm sat} > 10^{8.3}$ M$_\odot$ (light gray). For the gas properties in the bottom row, the galaxies with gas masses below our resolution limit are placed manually at $\sim 10^3$ M$_\odot$. Cold gas has temperatures $\leq 10^{4.5}$ K; hot gas has temperatures $> 10^{4.5}$ K.

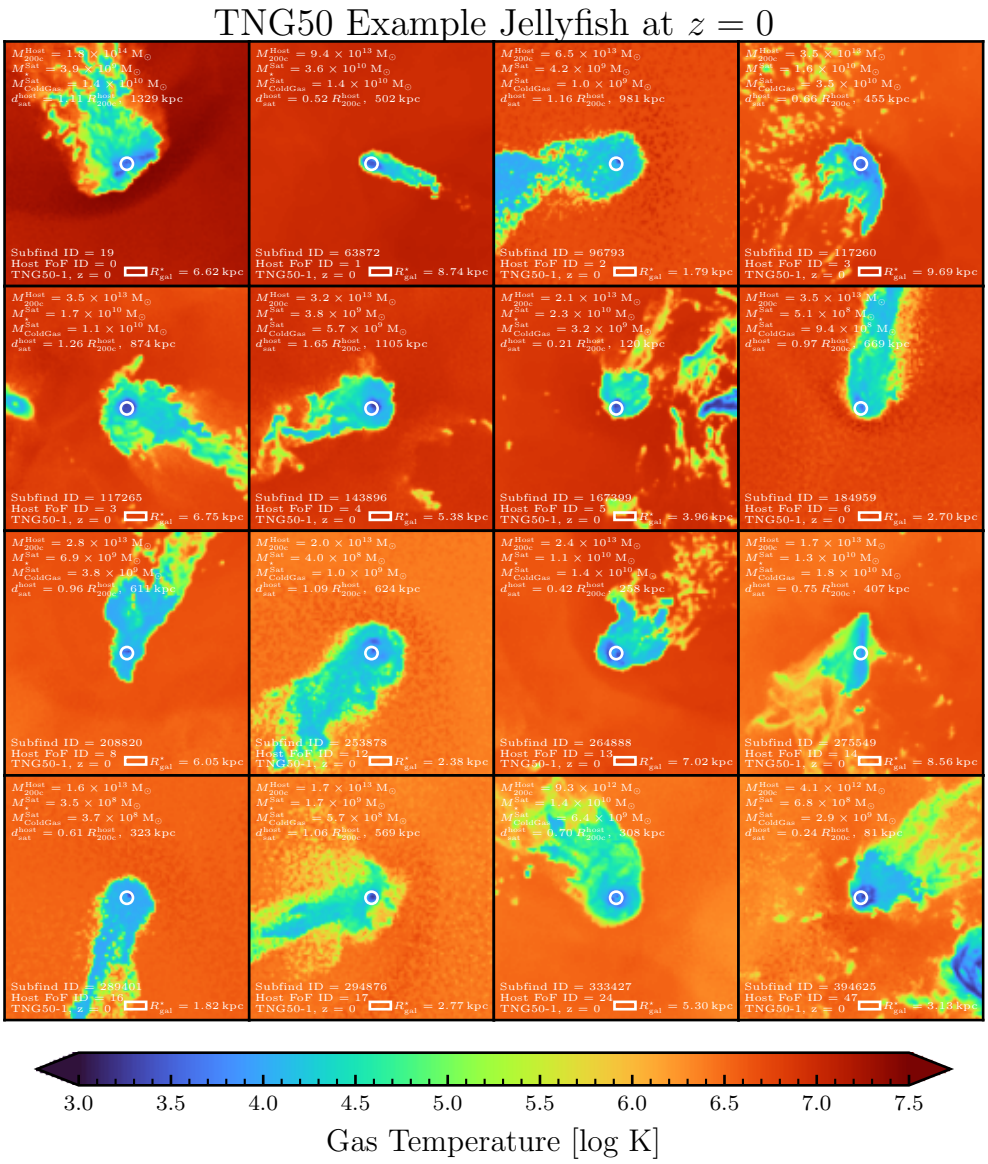

Figure 7.2: **The coldness of the ram-pressure stripped gas in TNG50 jellyfish galaxies.** We show gas temperature maps of 16 TNG50 jellyfish galaxies, randomly chosen at $z = 0$. Each image is $(40 \times R_{\mathrm{half},\star})^3$ in size and depth, with 100×100 pixels (~ kpc sized pixels) in the same orientation as the jellyfish were posted to Zooniverse (i.e., random and along the z-axis). Here, we measure the mass-weighted-average temperature map of all (FoF i.e. ambient) gas within the cube, and overplot the jellyfish (i.e. gravitationally-bound) gas. The white circle shows the galaxy stellar radius ($R_{\mathrm{gal}} = 2 \times R_{\mathrm{half},\star}$), and information about the jellyfish galaxy and its host are in the top- and bottom- left corners. Star-forming gas is placed at the nominal temperature of 10^3 K, so all dark blue locations represent active star-forming regions. The gas in the jellyfish tails is typically and on average cold-cool ~ 10^{4-5} K.

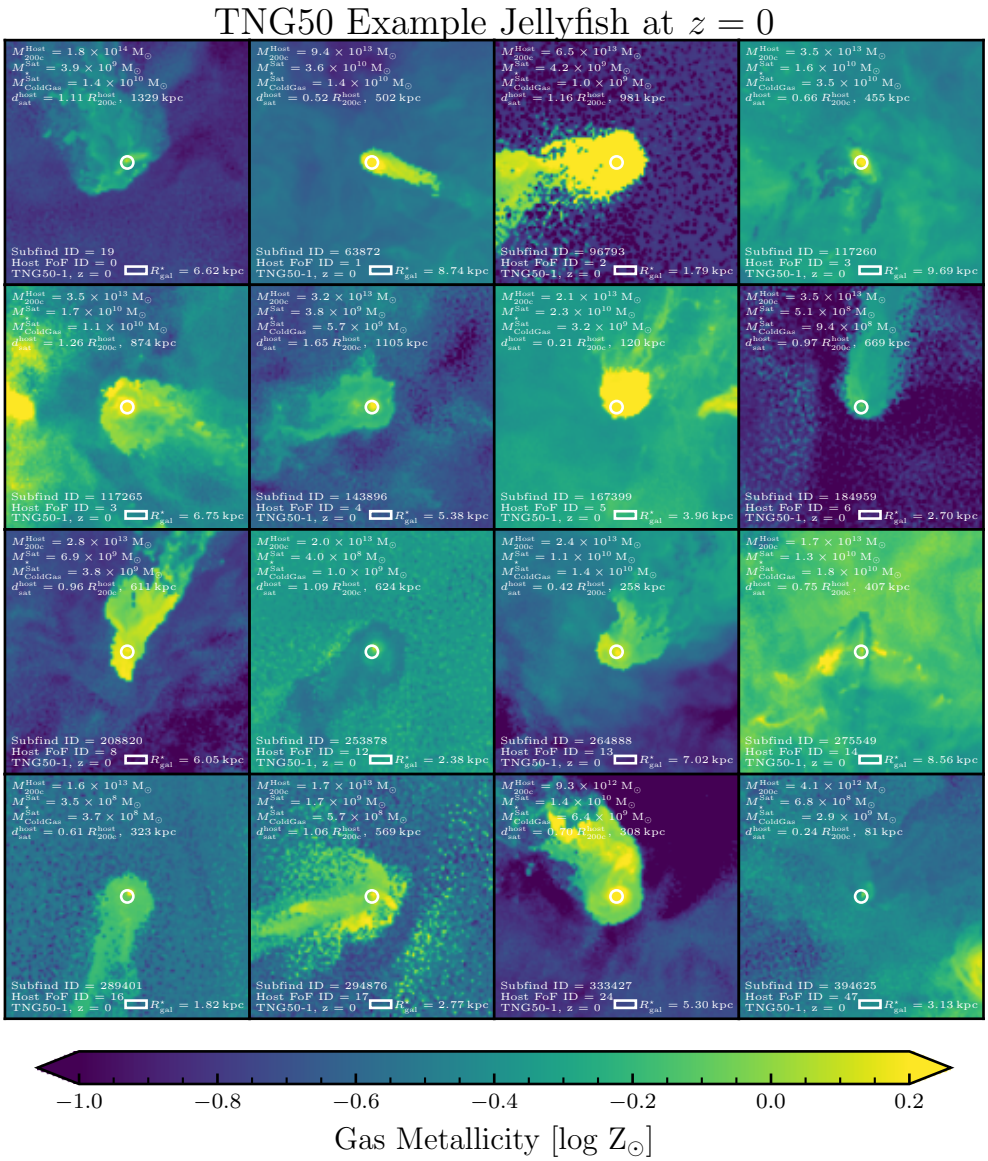

Figure 7.3: **The metallicity of the ram-pressure stripped gas in TNG50 jellyfish galaxies.** Similar to Fig. 7.2 but here showing the mass-weighted gas metallicity rather than the temperature. The tails of jellyfish are as enriched as the main body of the satellites they stem from, but depending on the host, the tails may or may not be more enriched than the ambient gas.

stellar body is the primary foil to RPS, providing the gravitational binding energy for the gas to remain in the galaxy, galaxies with a weaker restoring force are naturally more susceptible to RPS, in line with other studies of TNG jellyfish (Yun et al., 2019; Zinger et al., 2024). Because we only inspect galaxies with $M_\star^{\rm sat} > 10^{8.3}\,{\rm M}_\odot$ at the time of inspection, we see a decrease in the number of galaxies at lower masses. This inspection criterion is only at the snapshot of inspection, so galaxies that later lose stellar mass due to either tidal stripping or stellar mass return may have stellar masses below this lower limit. The fact that only 2/512 (0.39 per cent) of jellyfish branches compared to 26/1,031 (2.5 per cent) of non-jellyfish branches have stellar masses below the inspection criterion suggests that we are able to separate galaxies undergoing tidal vs ram-pressure stripping. At the high-mass end, $M_\star^{\rm sat} \gtrsim 10^{10.5}\,{\rm M}_\odot$ there are only a few jellyfish galaxies. We speculate that this is a combination of two effects: more massive satellites in hosts of this mass range better retain their cold gas against stripping; at these stellar masses, the TNG kinetic mode of SMBHs expels much of the galaxy's gas (e.g. Terrazas et al., 2020; Zinger et al., 2020), often at infall and before the peak effectiveness of RPS. While the AD test suggests confidence at the ≈ 95 per cent level that the two distributions are distinct, the KS test suggests only ≈85 per cent confidence, and the medians of the two distributions are not significantly different.

In the top middle panel, we see that jellyfish typically live in more massive hosts, and almost all inspected galaxies in massive hosts $M_{\rm 200c}^{\rm host} \gtrsim 10^{13}\,{\rm M}_\odot$ have been classified at some point since $z = 0.5$ as jellyfish. The number of satellite galaxies increases with the host halo mass due to hierarchical structure formation. With increasing host mass the gravitational potential well deepens, which in turn leads to both better retention of stellar- and SMBH-driven outflows from the central and more cosmological gas accretion from the large scale structure. These effects generally lead to a denser CGM or ICM. Moreover, deeper potential wells increase the infall velocities of satellite galaxies, sometimes even to supersonic speeds (Yun et al., 2019). The denser ambient medium and the increased relative velocity both increase the strength of ram-pressure stripping (e.g. Yun et al., 2019). However in the past five billion years, MW-mass halos $M_{\rm 200c}^{\rm host} \sim 10^{12}\,{\rm M}_\odot$ have also hosted a number of jellyfish galaxies.

In the top right panel Fig. 7.1, by combining the effects of satellite stellar mass and host mass, we see that jellyfish galaxies typically have small mass ratios $\mu \equiv M_\star^{\rm sat}/M_{\rm 200c}^{\rm host}$, and nearly every inspected galaxy with a mass ratio $\mu \lesssim 10^{-4}$ is a jellyfish.

The satellite stellar mass distribution of the inspected galaxies (dark gray) is slightly below but quite similar to that of the $z = 0$ satellites (light gray) for stellar masses $M_\star^{\rm sat} \sim 10^{8.3-10.5}\,{\rm M}_\odot$ (top left), and the distributions are nearly identical for masses $M_\star^{\rm sat} \sim 10^{10.5-11.8}\,{\rm M}_\odot$. Compared to the $z = 0$ satellites, the inspected galaxies have an under-population of high mass hosts $M_{\rm 200c}^{\rm host} \sim 10^{13.5-14.3}\,{\rm M}_\odot$ (top middle) and low mass ratios $\mu \lesssim 10^{-4}$ (top right). We

speculate that many of these $z = 0$ satellites are pre-processed and therefore have been excluded from this analysis, but they may also have had too low of gas masses and their fractions to be inspected (bottom panels).

In the bottom panels of Fig. 7.1, we see that jellyfish galaxies typically exhibit, at $z = 0$ lower amounts of gravitationally-bound cold gas $M^{\rm sat}_{\rm ColdGas}$ with temperatures $T_{\rm ColdGas} \leq 10^{4.5}$ K (or star-forming; bottom left), hot gas $M^{\rm sat}_{\rm HotGas}$ with temperatures $T_{\rm HotGas} > 10^{4.5}$ K (bottom middle) and total gas $M^{\rm sat}_{\rm TotGas}$ (bottom right) compared to the inspected branches. A larger fraction of jellyfish (≈ 50 per cent) compared to non-jellyfish (≈ 12 per cent) have gas masses below our resolution limit, plotted here at $M^{\rm sat}_{\rm Gas} \sim 10^3\,{\rm M}_\odot$. We have explicitly checked that the non-jellyfish inspected galaxies with large $z = 0$ gas reservoirs are typically late-infallers and have higher mass ratios, causing weaker ram-pressure stripping. Conversely, the non-jellyfish inspected satellites without any gas at $z = 0$ are typically early-infallers, namely they joined their $z = 0$ hosts when galaxies were inspected only every ~ 1 Gyr, compared to every ~ 150 Myr after $z = 0.5$. Additionally, there are a few cases of massive galaxy mergers where the FoF-identified central galaxy switches between the two galaxies; this means that these quasi-central galaxies meet the inspection criteria but are not truly classical satellites.

7.3.2 Jellyfish Tails Stem from the Stripped, Cold ISM

In this work, we study the ram-pressure stripping of cold gas because the long-lived jellyfish tails originate mostly from the cold ISM of satellite galaxies. We provide arguments for this as follows.

Firstly in Fig. 7.2 we show the gas temperature maps of 16 TNG50 jellyfish at $z = 0$. Each image is $(40 \times R_{\rm half,\star})^3$ in size and depth, with 100×100 pixels ($\sim$ kpc sized pixels) in the same orientation as the jellyfish were posted to Zooniverse (i.e., random and along the z-axis). We measure the mass-weighted-average temperature map of all (FoF i.e. ambient) gas within the cube, and overplot the jellyfish (i.e. gravitationally-bound) gas. In each image, the jellyfish tails' temperature matches, or is at a similar temperature of, the ISM gas, which we roughly denote as the gas enclosed by the white circles of radius $2 \times R_{\rm half,\star}$. In some cases, a bow shock is also present, which appears as a stark contrast in temperature in the opposite direction of the tails (e.g., top left; see also other manifestations of bow shocks in front of TNG100 jellyfish galaxies in fig. 10 of Yun et al., 2019).

Fig. 7.3 showcases the metallicity maps for the same 16 TNG50 jellyfish galaxies. Generally, the metallicity of the jellyfish tails is similar to that of the main body of the galaxy (the jellyfish head). Unlike the temperature, the metallicity of the background halo gas is not always so distinct from the jellyfish (e.g., bottom right), as it depends on the satellite-to-host mass ratio.

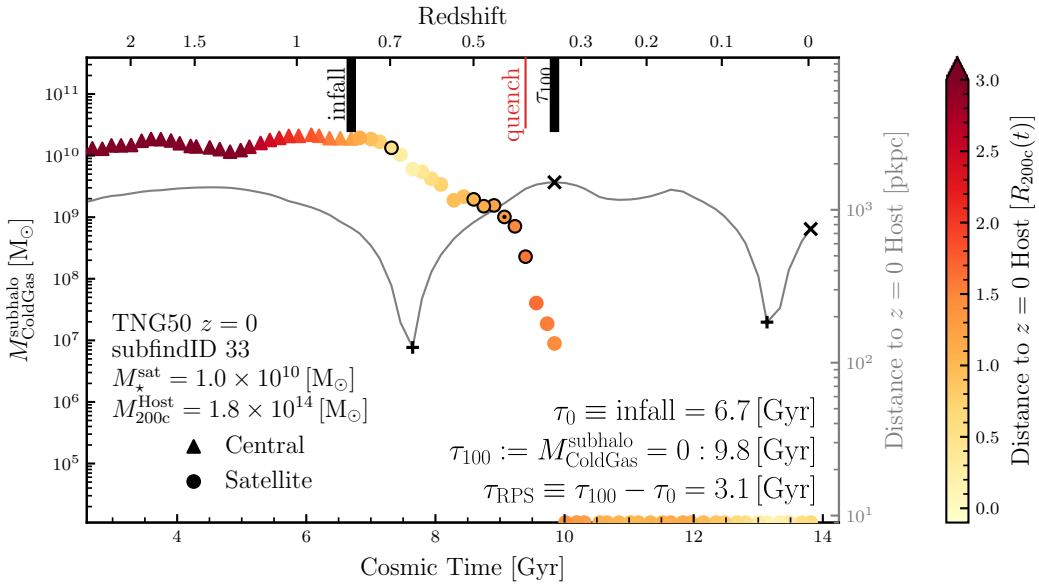

Figure 7.4: **Time evolution of the total gravitationally-bound cold gas $M_{\rm ColdGas}^{\rm subhalo}$ of a TNG50 jellyfish galaxy.** The marker style denotes the FoF membership of the galaxy, as either a central (triangle) or satellite (circle), whereas the color indicates the distance to the $z = 0$ host in normalized units of $[R_{\rm 200c}(t)]$. The host-centric distance in physical units (thin gray curve) uses the right y-axis, and we mark the pericentric and apocentric passages with black "+" and "x" symbols respectively. The snapshots when this galaxy has been visually inspected are outlined with a thick black circle and the snapshot(s) when it has been classified as a jellyfish are indicated with a central black dot. We place by hand the times after τ_{100} when the cold gas mass $M_{\rm ColdGas}^{\rm subhalo}$ is below our resolution limit ($\lesssim 4 \times 10^4\,{\rm M}_\odot$) at the lower y-limit (along the bottom x-axis). The thick black ticks denote the onset of RPS as the infall time (τ_0) and the end of RPS (τ_{100}), in this case when $M_{\rm ColdGas}^{\rm subhalo}(t) = 0$. The red tick marks when the galaxy quenches, defined as when the galaxy falls at least one dex below the star-forming main sequence for the last time.

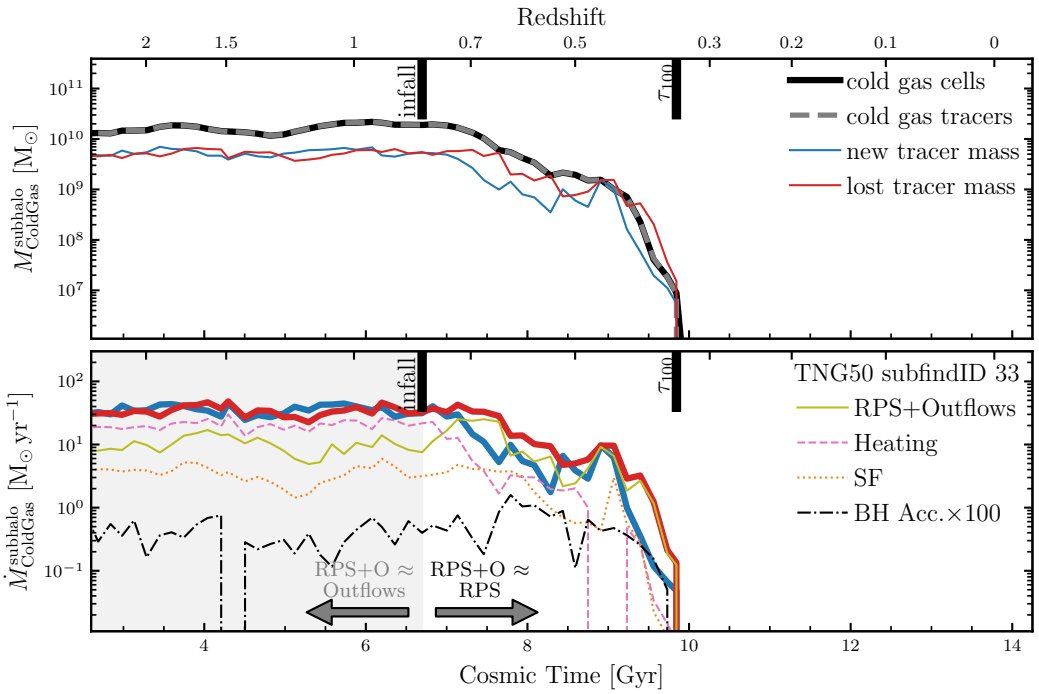

Figure 7.5: **Time evolution of the tracer quantities for an example TNG50 jellyfish galaxy, the same galaxy as in Fig. 7.4.** In the top panel, we see that the total cold gas mass (thick black curve) and tracer mass with cold gas parents (gray dashed curve) agree. The thin blue curve shows the the total new cold gas, the tracer mass whose parents are now cold gas cells but previously were not, such as cooling or inflowing gas. The thin red curve shows the opposite, and we further separate the various physical mechanisms of cold gas loss in the bottom panel, now normalized by the time between snapshots. The contribution to net lost tracers from star formation (orange dotted) is small at all times, while heating (pink dashed) is dominant only while the galaxy is a central. The cold gas mass lost via SMBH accretion (black dot-dashed) is shown here multiplied by 100 and negligible at all times. When the galaxy becomes a satellite at infall (black tick mark, cosmic time 6.7 Gyr, $z \sim 0.8$), RPS (olive) becomes the dominant source of cold gas loss. Throughout this paper and following the inspection of the evolutionary tracks of all selected galaxies, we assume that before infall, RPS + Outflows is dominated by outflows, and that after infall RPS is dominant.

These images exemplify that, at the time when a RPS tail is identifiable in gas column density, the physical properties of the gas in the tails are similar to those in the ISM in the main body of the satellite galaxy undergoing RPS. The tail gas is cold and is typically as metal enriched as the jellyfish head.

Furthermore, we have checked that, at the time of infall, $\approx$ 75 (60) per cent of the gravitationally-bound gas mass is cold for jellyfish galaxies with stellar masses at infall of $M_{\star}^{\rm sat}(\tau_0) = 10^{8-9}$ (10^{9-10}) $\rm M_{\odot}$.

As a note, this ISM-origin of the RPS'ed gas does not preclude the jellyfish tails to reveal themselves across a wide range of wavelengths (see § 7.1 for references). Namely, although the bulk of the tail gas is cold or cool according to TNG50, it can also manifest itself in e.g. soft X-ray (see fig. 12 from Kraft et al., 2022, for a mock 100 ks exposure from the Line Emission Mapper for an example TNG100 jellyfish galaxy in the soft X-ray continuum and at the OVII f line).

7.3.3 The Majority of the Cold Gas Loss after Infall is Due to Ram-Pressure Stripping

According to TNG50, RPS is the dominant source of cold gas loss after infall for jellyfish galaxies. This is somewhat to be expected, given the jellyfish nature of the selected galaxies under inspection. However, we have demonstrated this for all 512 TNG50 jellyfish galaxies, using the tracer particle analysis described in Section 7.2.5.1. We showcase this result with one example galaxy below.

Fig. 7.4 shows the time evolution of the gravitationally-bound cold gas mass $M_{\rm ColdGas}^{\rm subhalo}$ for one example TNG50 jellyfish galaxy. Prior to infall (at cosmic times $\lesssim$ 6.5 Gyr) and at large distances ($\gtrsim 2R_{\rm 200c}^{\rm host} \sim 10^3$ kpc), the cold gas associated to the galaxy is approximately constant. After infall, $M_{\rm ColdGas}^{\rm subhalo}$ decreases significantly through the first pericentric passage until the satellite has effectively no cold gas remaining, which we denote as τ_{100} (see §7.2.5.2 for more details). The galaxy quenches its star formation for the last time shortly before τ_{100}, at $\approx$ 3 Gyr after infall.

Fig. 7.5 graphs the evolution of cold gas mass and the associated tracers for the same galaxy as in Fig. 7.4. In the top panel, $M_{\rm ColdGas}^{\rm subhalo}$ measured using the gas cell data (thick black curve) is identical to that in Fig. 7.4; moreover, $M_{\rm ColdGas}^{\rm subhalo}$ measured using the tracers (dashed gray curve; the number of tracers with cold gas parents times the baryonic mass resolution) closely matches the cold gas mass measured using SUBFIND at all times. This affirms that the tracers robustly measure the cold gas mass (see § 7.2.5 and Appendix 7.6 for more details).

In the top panel of Fig. 7.5, while the galaxy is a central before infall at cosmic times $\lesssim$ 6.7 Gyr, the net new (thin blue curve) and lost (thin red curve) cold gas tracers roughly

balance each other, leading to the approximately constant total $M^{\rm subhalo}_{\rm ColdGas}$. This likely reflects a quasi-equilibrium galactic fountain scenario, where inflows and outflows approximately cancel out to yield a constant $M^{\rm sat}_{\rm ColdGas}$, at least for the depicted galaxy. At infall, there is an immediate drop in new cold gas – the cold gas that the galaxy acquired via cold gas inflows or gas cooling – which qualitatively agrees with the results from the EAGLE simulation (Wright et al., 2019, 2022). The lost cold gas mass remains approximately constant for $\sim$ 1 Gyr after infall before eventually declining. After infall, the lost cold gas is always similar to or higher than the new cold gas, leading to the net decline in cold gas mass until $M^{\rm subhalo}_{\rm ColdGas} < 4\times10^4\,{\rm M}_\odot$. However it is interesting that the new cold gas remains nonzero for Gyrs after infall, including during the pericenter passage.

In the bottom panel of Fig. 7.5, we show again the net new (thick blue curve) and lost (thick red curve) tracers of cold gas, now shown as cold gas mass rates normalized by the time between snapshots. Further, we split the lost tracers into the various sinks of RPS+outflows (solid olive), gas heating (dashed pink), star-formation (SF; dotted orange) and SMBH accretion multiplied by 100 (BH acc.; black dot-dashed). See § 7.2.5.1 for additional technical inputs.

Before infall, gas heating is the dominant mechanism of cold gas loss, followed by RPS+outflows and SF. During this time, the shapes of the RPS+outflows, SF and SMBH accretion×100 are quite similar, suggesting that SF and/or SMBH accretion are the primary drivers of outflows for this galaxy. For the first ~Gyr after infall, the SF remains roughly constant while the RPS+outflows increases, confirming the onset of RPS. Moreover there is a simultaneous net gas loss, translating into an increase in the "efficiency" of RPS+outflows and SF, where efficiency here denotes RPS+outflows or SF normalized by $M^{\rm sat}_{\rm ColdGas}$. During this period, the cold gas lost via heating also decreases significantly. SMBH accretion is the least dominant cold gas sink at all times, at least for this galaxy. This galaxy has in fact experienced little to no kinetic AGN feedback, though in general 45 of the 512 ($\approx$ 9 per cent) of jellyfish galaxies have $M^{\rm sat}_\star(z=0) > 10^{10}\,{\rm M}_\odot$ and have experienced kinetic AGN feedback. Through pericenter until the jellyfish has a gas mass below our resolution limit, RPS+outflows remains the dominant physical mechanism of cold gas removal.

As discussed and anticipated in §7.2.5.1, outflows and RPS are closely intertwined, for example as outflowing gas is less gravitationlly bound and therefore more susceptible to RPS. We hence avoid distinguishing between cold gas that is lost (and becomes unbound) because of RPS or because of a combination of RPS and high velocities, and we conclude that that RPS (+outflows) is the dominant source of cold gas loss after infall for jellyfish galaxies in TNG50.

7.3.4 Why Do Half of the TNG50 Jellyfish Have, or not Have, Cold Gas Today?

The 512 jellyfish galaxies provided by TNG50 span orders of magnitude in their $z = 0$ stellar mass, host mass, and importantly their (cold) gas mass (Fig. 7.1). Why do half of the jellyfish galaxies retain significant amounts of cold gas until $z = 0$, while the others do not?

As a reminder, in this paper we analyse TNG50 satellite galaxies that survive, in terms of their galaxy stellar mass, through $z = 0$ (see §7.2.2 and §7.2.4 for more details). In Fig. 7.6, we show the satellite-to-host mass ratio μ vs. the infall time for the population of jellyfish branches that end up with cold gas masses above (blue circles) or below (red circles) our resolution limit ($4 \times 10^4\,M_\odot$) at $z = 0$. Here, the 16/84th percentiles and medians are marked with the shaded regions and vertical lines respectively. We note that the results remain qualitatively similar when using the satellite-to-host mass ratio at infall rather than at $z = 0$.

The average infall occurs ~ 2 Gyr earlier for those jellyfish galaxies with little to no cold gas remaining than for those that still retain some cold gas at $z = 0$. While the host halo masses might have not had as much time to grow at earlier times and the $z = 0$ mass ratios are $\mu \sim 10^{-3} - 10^{-5}$, most of the early infallers (with infall times $\gtrsim 5$ Gyr ago) have had enough time until $z = 0$ to undergo secular and environmental processes to lose their cold gas. Even if these galaxies required multiple pericentric passages to lose their gas, they have had enough time before $z = 0$ to have done so. Conversely, the largest majority of late-infalling jellyfish (i.e. with infall times as recent as a few Gyr ago) that have lost their gas by $z = 0$ exhibit very low $z = 0$ mass ratios (in the range $\mu \sim 10^{-4} - 10^{-6}$), whereas those with cold gas today typically have $\mu \sim 10^{-3} - 10^{-5}$, either because they are more massive or because they orbit in less massive hosts.

We speculate that the galaxies with non-vanishing cold gas masses that remain satellites (i.e. do not become backsplash galaxies) would eventually lose all their cold gas, i.e. if the simulation ran longer in time.

Whereas the characterization of Fig. 7.6 is not surprising, it reminds us that, the longer a satellite has interacted with its host, the more time environmental processes, such as RPS, have had to act upon it. And even though some secondary effects may be in place – such as galaxy selection, orbital trajectories, numbers of pericentric passages, edge-on vs. face-on orientation of the satellite as it falls into the host, and/or satellite-satellite interactions – this zeroth-order picture is in line with what has already been quantified by Donnari et al. (2021b); Joshi et al. (2021) for all TNG simulations: satellites that have spent more time in their hosts are more likely to be quenched compared to those that are still infalling or on their first infalling trajectory.

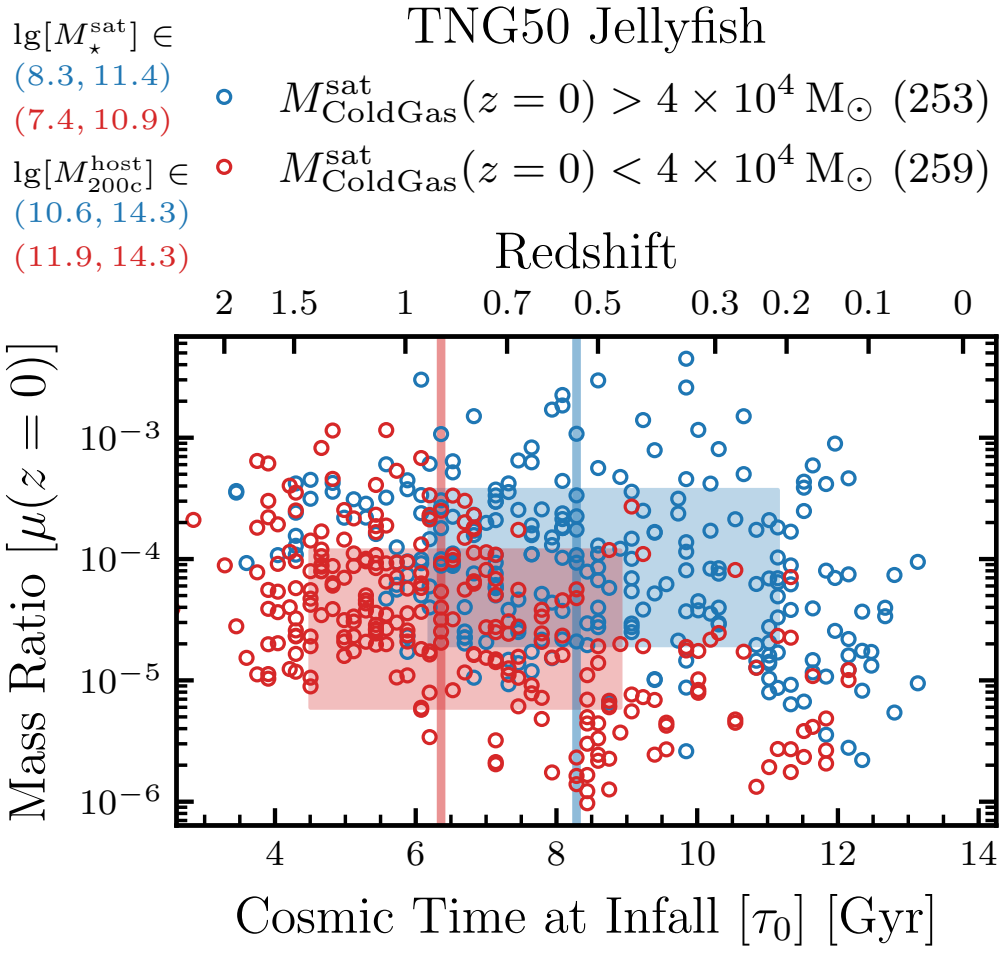

Figure 7.6: **Why do some jellyfish retain significant amounts of cold gas until $z = 0$, while others do not?** The shaded regions and vertical lines mark the 16th/84th percentiles and medians of the distributions, respectively. The TNG50 jellyfish with cold gas masses below our resolution limit at $z = 0$ ($M^{\rm sat}_{\rm ColdGas} < 4\times10^4\,{\rm M}_\odot$, red circles) typically have earlier infall times τ_0 and lower mass ratios $\mu \equiv M_\star^{\rm sat}/M_{\rm 200c}^{\rm host}(z=0)$ than the jellyfish with $M^{\rm sat}_{\rm ColdGas} > 4\times10^4\,{\rm M}_\odot$ today (blue circles).

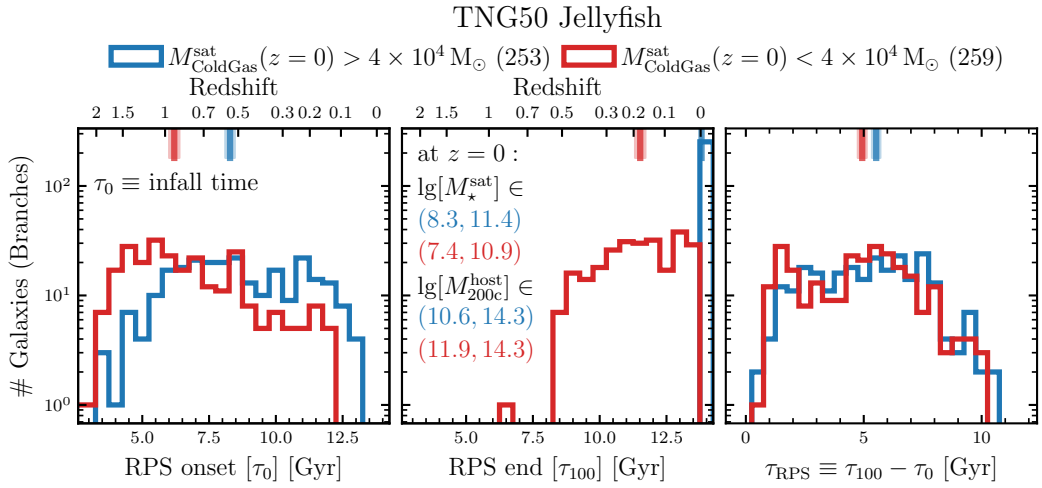

Figure 7.7: **Distributions of onset, end, and duration of ram-pressure stripping (RPS) for TNG50 jellyfish with cold gas masses at $z = 0$ above (blue) and below (red) our resolution limit.** The onset of RPS τ_0 (left panel) is defined as cosmic time at infall. The end of RPS τ_{100} (center panel) is defined as when the cold gas mass drops below our resolution limit ($M^{\rm sat}_{\rm ColdGas} \lesssim 4\times10^4\,{\rm M}_\odot$) or the end of the simulation at $z = 0$, if the galaxy always has $M^{\rm sat}_{\rm ColdGas} \gtrsim 4\times10^4\,{\rm M}_\odot$. The total RPS timescale $\tau_{\rm RPS}$, i.e. the total duration of RPS (right panel), is the difference between the end and onset of RPS. The jellyfish with substantial cold gas masses at $z = 0$ all have $\tau_{100} = 13.8$ Gyr (the end of the simulation) by definition, causing the $\tau_{\rm RPS}$ distribution to be a reflection of the τ_0 distribution. The medians and 1σ errors of the distributions are marked by the hash marks and shaded regions on the top x-axis. For the jellyfish with $M^{\rm sat}_{\rm ColdGas}(z = 0) < 4\times10^4\,{\rm M}_\odot$, the $\tau_{\rm RPS}$ distribution appears bimodal, with peaks at $\approx 1.5 - 2.0$ and $4.5 - 6.5$ Gyr. We examine this distribution in detail in §7.3.5.1.

7.3.5 For How Long Is Ram Pressure Stripping in Action?

We are hence ready to quantify for how long RPS acts or has acted on TNG50 jellyfish galaxies.

Fig. 7.7 shows the distributions of the onset of RPS (τ_0 i.e. infall time; left), the end of RPS (τ_{100}; middle), and the duration of RPS ($\tau_{\rm RPS}$; right), for TNG50 jellyfish with cold gas masses below (red) and above (blue) our resolution limit ($4\times10^4\,{\rm M}_\odot$) at the current epoch.

As we have seen in Fig. 7.6 and now again in the left panel, the jellyfish with little to no cold gas at $z = 0$ are typically early infallers, with a majority falling in at $\tau_0 \approx 4.5 - 7$ Gyr after the Big Bang and a tail of late infallers at $\tau_0 \gtrsim 10$ Gyr after the Big Bang. After the RPS onset, the TNG50 jellyfish continue losing cold gas until sometime in the past few billion years ($\tau_{100} \approx 9 - 14$ Gyr). We only select galaxies which have been jellyfish since $z = 0.5$, so we exclude galaxies that have been totally stripped of cold gas before $z = 0.5$.

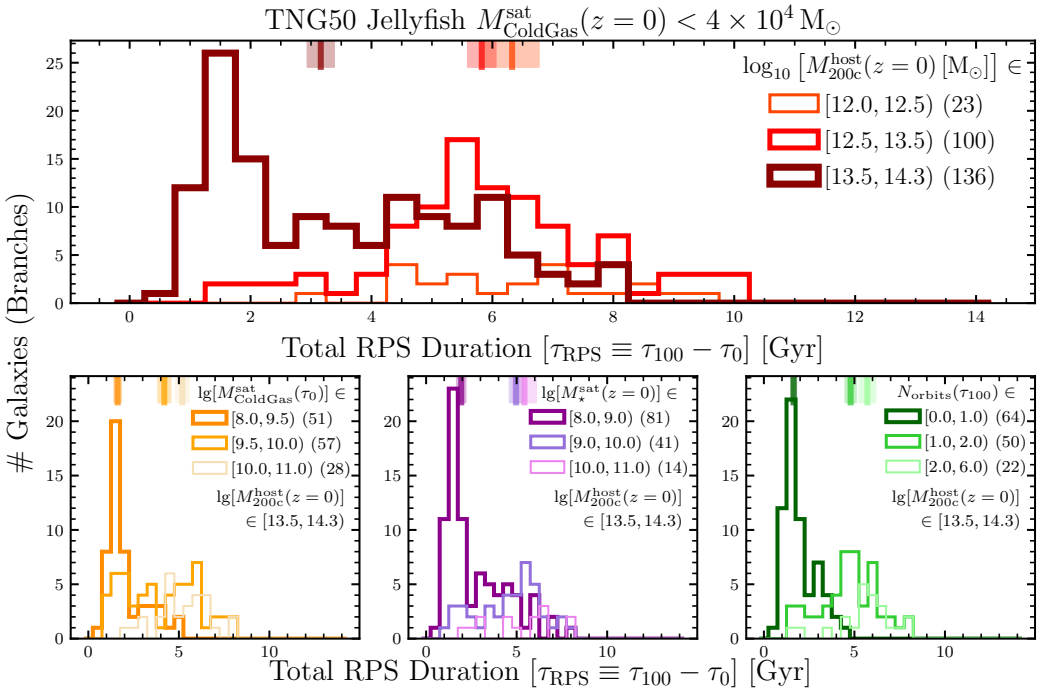

Figure 7.8: **Given that a given jellyfish loses all of its cold gas, what determines how long it will take?** Of all the TNG50 jellyfish with $M^{\rm sat}_{\rm ColdGas}(z=0) < 4\times10^4\,{\rm M}_\odot$, we bin the ram-pressure stripping (RPS) timescales $\tau_{\rm RPS}$ by host mass $M^{\rm host}_{\rm 200c}(z=0)$ in the top panel. Here, only cluster mass hosts (dark red, $M^{\rm host}_{\rm 200c} = 10^{13.5-14.3}\,{\rm M}_\odot$, 8 hosts in total) have many jellyfish with both short and long RPS timescales. Then in the bottom panels we further bin the jellyfish orbiting in cluster-mass hosts by satellite cold gas mass at infall $M^{\rm sat}_{\rm ColdGas}(\tau_0)$ (bottom left), satellite stellar mass today $M^{\rm sat}_{\star}(z=0)$ (bottom middle), and the number of orbits by the end of RPS $N_{\rm orbits}(\tau_{100})$, where the number of orbits is the number of apocentric passages, and the end of RPS (τ_{100}) is the first time the satellite's cold gas mass falls below our resolution limit (see text for details). In all panels, the number of galaxies within each histogram is in parentheses in the panel legend; the medians and 1σ errors are marked by the hash marks and shaded regions on the top x-axis.

Finally, according to TNG50, the distribution of the RPS duration ($\tau_{\rm RPS}$, right panel) can be very wide, even for both subsets of jellyfish galaxies. For the jellyfish with substantial cold gas masses at $z = 0$ all have $\tau_{100} = 13.8$ Gyr (the end of the simulation) by definition, causing the $\tau_{\rm RPS}$ distribution to be a reflection of the τ_0 distribution. Thereby for these $z = 0$ gaseous jellyfish, environmental effects, and hence RPS, have acted on them for as many as billions of years. For the jellyfish with cold gas masses below our resolution limit at $z = 0$, the $\tau_{\rm RPS}$ distribution appears somewhat bimodal (see below for more details). Among these jellyfish, a fraction have undergone RPS for about $\approx 1.5 - 2.5$ Gyr and a larger fraction has undergone RPS for as long as $\sim 4.5 - 7.5$ Gyr. As a reminder, these numbers represent the maximum time span over which RPS has acted (§7.2.5.2); we see in the next Sections whether RPS may be more effective on shorter timescales.

7.3.5.1 Physical Origin of the Diversity of RPS Duration

What are the important factors in determining how long a given jellyfish needs to be stripped of its cold gas? We focus from now on only on those jellyfish that have cold gas masses below our resolution limit at the current epoch $M^{\rm sat}_{\rm ColdGas}(z = 0) < 4 \times 10^4\,{\rm M}_\odot$.

In the top panel of Fig. 7.8, we extract the distribution of the duration of RPS $\tau_{\rm RPS}$ for the TNG50 jellyfish without substantial cold gas today, stacked by halo mass $M^{\rm host}_{\rm 200c}$ of their current host. The number of jellyfish (not the number of hosts) belonging to each host mass bin is in parentheses in the upper right corner.

Jellyfish in clusters ($M^{\rm host}_{\rm 200c} = 10^{13.5-14.3}\,{\rm M}_\odot$, dark red histogram) exhibit the shortest median RPS duration (vertical dark red line), although the distribution peaks at even shorter time spans: $\tau_{\rm RPS} \sim 1.5 - 2$ Gyr. Then there is a valley at intermediate stripping times $\tau_{\rm RPS} \sim 2.5 - 4$ Gyr, followed by a slight increase from $\tau_{\rm RPS} \sim 4.5 - 6$ Gyr. The longest timescale for any jellyfish in this host mass bin is 8 Gyr. The jellyfish in groups ($M^{\rm host}_{\rm 200c} = 10^{12.5-13.5}\,{\rm M}_\odot$, red histogram) show RPS timescales that are single-peaked, with the median and mode coinciding at $\tau_{\rm RPS} \approx 5.5$ Gyr. While not shown but explicitly checked, jellyfish in group-mass hosts typically require at least 2 pericenteric passage to become fully stripped of cold gas. There are only ≈ 10 (≈ 10 per cent) galaxies in this host mass bin with stripping times shorter than 4 Gyr. This agrees with our earlier argument that RPS is more effective in higher host masses. Moreover, the jellyfish in approximately Milky-Way mass halos ($M^{\rm host}_{\rm 200c} = 10^{11.5-12.5}\,{\rm M}_\odot$, light red) require at least 4 Gyr, or in some cases much longer, to be fully stripped of their cold gas today. In general as RPS becomes more effective with increasing host mass, there are typically more jellyfish galaxies per host with increasing host mass (see also fig. 14 from Zinger et al., 2024). However, even for these MW-mass hosts, the satellite-to-satellite variation is very large:

there are TNG50 jellyfish that undergo RPS for as long as 10 billion years in both group- and MW-mass hosts, and as long as 8 billion years for cluster-mass hosts.

The trend whereby shorter RPS time spans occur, on average, for satellites in more massive hosts is consistent with expectations described in § 7.1. However, here we quantify it for the first time with a large number of jellyfish across a wide range of host and satellite masses. Moreover, this trend is in place (physically vs. hierarchical growth of structure) even though more massive hosts exhibit in fact overall more recent infall times of their $z = 0$ satellites than less massive hosts (not shown but explicitly checked).

In the bottom row of Fig. 7.8, we focus on the TNG50 jellyfish with no remaining cold gas at $z = 0$ in the 8 cluster hosts ($M_{200c}^{\rm host} = 10^{13.5-14.3}\,{\rm M}_\odot$) to investigate which additional physical properties imprint secondary trends on the duration of RPS. In practice, we show the $\tau_{\rm RPS}$ distributions binned by the satellites' cold gas mass at infall (left), stellar mass at $z = 0$ (middle), and number of apocentric passages by τ_{100} (right).

In the bottom left panel of Fig. 7.8, we see that satellites with the smallest (dark orange) and largest (light orange) amount of cold gas at infall are both single peaked at $\tau_{\rm RPS} \approx 1.5$ and 5 Gyr respectively. Conversely, the intermediate bin (orange) has an approximately uniform distribution from $\tau_{\rm RPS} \approx 1.5 - 6$ Gyr. Galaxies with less strippable material at infall tend to have shorter stripping durations. While not shown but explicitly checked, this trend remains for galaxies in a fixed host halo and galaxy stellar mass bin.

In the bottom middle panel, lower mass jellyfish (dark purple) are typically stripped of all their cold gas faster, on average in $1 - 2$ Gyr, although a non-negligible fraction of them still require $3 - 6$ Gyr to be fully stripped of their cold gas. The intermediate (purple) and high (light purple) bins of satellite's stellar mass have similarly flat distributions with both a median RPS duration of ~ 5 Gyr.

Lastly in the bottom right panel of Fig. 7.8, we show that satellites with the shortest RPS durations are those with the fewest orbits by being totally stripped $N_{\rm orbits}(\tau_{100})$, where $N_{\rm orbits}(\tau_{100})$ is the number of apocentric passages before τ_{100}. The jellyfish with the shortest RPS duration are those that get stripped of all their cold gas before or immediately after their first pericentric passage (dark green), whereas satellites that require longer RPS time spans to be fully stripped of their cold gas are characterized by more than one apocentric passage (green and light green histograms).

7.3.6 When and Where Does Ram Pressure Strip Most of a Jellyfish's Cold Gas?

While most TNG50 jellyfish are stripped of their cold gas within $\sim 1 - 7$ Gyr after infall (Fig. 7.7 right panel; Fig. 7.8 top panel), the amount of gas being stripped is not constant

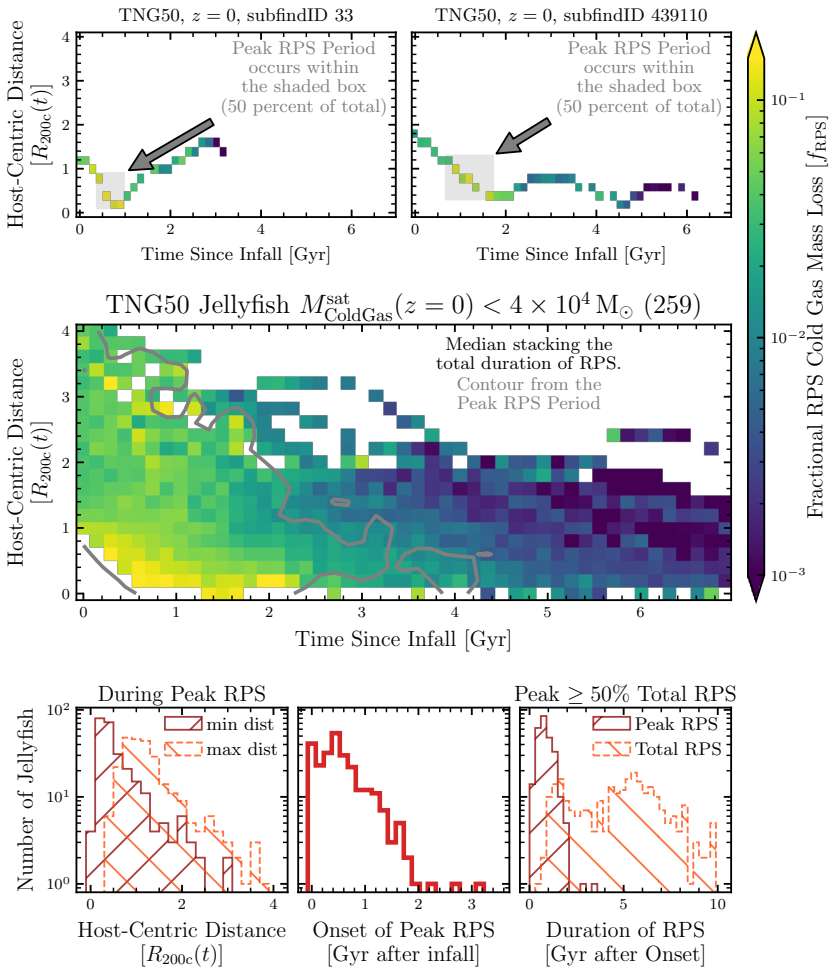

Figure 7.9: **When after infall, where within the host halo, and for how long does 50 per cent of RPS occur?** Top panels: the cold gas mass loss due to RPS at each snapshot normalized by the total amount of cold gas lost due to RPS through the satellite's life for two example galaxies (i.e. fractional RPS loss as per equation (7.2)). The peak RPS period – the minimum amount of time for 50 percent of the total RPS to occur (equation (7.3)) – is within the gray box. The galaxy in the top left panel is the same as in Figs. 7.4, 7.5. Central panel: Median stacking of the fractional RPS loss of all 259 TNG50 Jellyfish with $M^{sat}_{ColdGas}(z = 0) < 4 \times 10^4\,M_\odot$. The gray contour marks the phase space obtained when stacking only the peak RPS periods of all 259 jellyfish. Bottom panels: Histograms detailing the peak RPS period of the 259 TNG50 Jellyfish with $M^{sat}_{ColdGas}(z = 0) < 4 \times 10^4\,M_\odot$. Bottom left panel: the distributions of minimum (dark red, '/' hatch, solid outline) and maximum (light red, '\' hatch, dashed outline) host-centric distances $[R_{200c}(t)]$ within the peak RPS period. Bottom center panel: the distribution of onsets of the Peak RPS periods [Gyr after infall]. Note that the total RPS time span τ_{RPS} begins at infall which is at 0 Gyr on this plot. Bottom right panel: the distributions of the peak RPS (dark red, '/' hatch, solid outline) and total RPS (light red, '\' hatch, dashed outline) time spans. Note that the total RPS time span distribution is identical to that in the right panel of Fig. 7.7.

throughout this period. The halo gas is denser at closer distances to the central galaxy, and jellyfish move faster at closer distances while they are deeper in their host's potential well. Both of these effects increase the ram pressure stripping acting on satellites at closer distances. We quantify this increase in RPS with decreasing distance in Fig. 7.9. In the top panels for two example galaxies, we show the fractional RPS loss $f_{\rm RPS}(t_i)$ – the amount of cold gas lost due to RPS since the last snapshot $\Delta t_{\rm snap_i} = t_i - t_{i-1}$, normalized by the total amount of cold gas lost due to RPS in the satellite's life:

$$f_{\rm RPS}(t_i) = \frac{\int_{t_{i-1}}^{t_i} {\rm RPS}(t)\,{\rm d}t}{\int_{\tau_0}^{\tau_{100}} {\rm RPS}(t)\,{\rm d}t} \tag{7.2}$$

where τ_0 and τ_{100} define the total time span of satellite RPS. In general, the fractional RPS increases as a jellyfish approach pericenter, followed by a decrease as it approaches apocenter. For galaxy with SubhaloID 439110 (right panel), the fraction of total gas lost is higher during the first pericentric passage compared to the second because $M^{\rm sat}_{\rm ColdGas}$ – the total amount of cold gas able to be stripped – is an order of magnitude higher at infall than after its first orbit (at apocenter). There is still an increase in fractional RPS during the second pericentric passage compared to at apocenter, but the majority of RPS for this jellyfish occurs during the first infall through pericentric passage.

We characterize the period of most effective RPS, the peak RPS period, by finding the minimum amount of time required for 50 per cent of the total cold gas loss via RPS to occur. That is, we minimize the difference in bounds $(t_{\rm stop} - t_{\rm start})$ such that the integral of the fractional RPS $f_{\rm RPS}(t)$ is at least 50 percent:

$$\text{peak RPS} := {\rm MIN}\Big(t_{\rm stop} - t_{\rm start}\Big)\Big|\int_{t_{\rm start}}^{t_{\rm stop}} f_{\rm RPS}(t)\,{\rm d}t \geq 0.5\,. \tag{7.3}$$

We highlight the peak RPS periods for the two examples galaxies in Fig. 7.9, top, with gray boxes, which in both cases occur during the first infall towards pericenter.

In the central panel of Fig. 7.9, we stack all 259 TNG50 jellyfish with $M^{\rm sat}_{\rm ColdGas}(z=0) < 4\times10^4\,{\rm M}_\odot$, taking the median fractional RPS loss in the bins with more than one galaxy. Additionally, the gray contour denotes the phase space region obtained when stacking only the peak RPS periods of the jellyfish. Based on the fractional RPS loss (color of bins) and the peak RPS contour, a majority of the RPS occurs within the first few Gyrs after infall and over a wide range of host-centric distances. At a fixed time since infall (single column), there is a higher fractional RPS loss at closer distances. However and especially at times $\lesssim 2$ Gyr after

infall, there is a significant amount of RPS occurring at large host-centric distances, up to $\approx 3R_{200c}$. At later times $\gtrsim 2.5$ Gyr after infall, the peak RPS only occurs at closer host-centric distances $\approx 0.2 - 1.0R_{200c}$. The smallest host-centric bin $< 0.1R_{200c}$ is largely unpopulated (no color) or with few galaxies (not shown but checked). This means that their pericentric passages are at distances $\gtrsim 0.1R_{200c}$, and that they are being stripped of their cold gas in the halos rather than directly into central galaxy. This again supports the claim that tidal stripping is likely not a significant mechanism for cold gas removal for this jellyfish sample.

In the bottom panels of Fig. 7.9, we show the distributions of the peak RPS period quantities. In the bottom left panel, we show the minimum (dark red, '/' hatch, solid outline) and maximum (light red, '\' hatch, dashed outline) host-centric distances during the peak RPS periods. The minimum peak RPS distance distribution has its peak (mode) at $0.3R_{200c}$, and the median (16, 84 percentiles) are 0.43 (0.22, 1.1) R_{200c}. The maximum peak RPS distance distribution peaks at R_{200c}, with median (16, 84 percentiles) at 1.2 (0.75, 1.9) R_{200c}. These distributions reflect that the peak RPS period starts at large distances in the halo (which has been discussed in, e.g., Bahé et al., 2013; Zinger et al., 2018a) and continues until approximately the pericentric approach, which for our sample of jellyfish that lose all cold gas by $z = 0$ tends to be at $\gtrsim 0.2R_{200c}$ (see Zinger et al., 2024, for more details about TNG jellyfish at large distances $d_{\rm sat}^{\rm host} > R_{200c}$). The cold gas is being stripped in, and thereby deposited into, the host halos; we extensively expand on this in § 7.4.3 and Fig. 7.10.

In the bottom center panel, we see that the onset of the peak RPS occurs at or just after ($\lesssim 1$ Gyr) infall. Only ≈ 15 per cent of these jellyfish galaxies begin their peak RPS period > 1 Gyr after infall, suggesting that the infall time is a reasonable definition for the start of the total RPS time span.

In the bottom right panel, we show the peak RPS (dark red, '/' hatch, solid outline) and total RPS (light red, '\' hatch, dashed outline) time spans. The two distributions here have different times of onset; the peak RPS onset is that given in the bottom center panel, while the total RPS onset is the infall time, which would be 0 in the bottom center panel. The total RPS time span is identical to that in Fig. 7.7. While the total RPS duration spans a broad range of times $\approx 1 - 7$ Gyr, the peak RPS period is much narrower, spanning only $\lesssim 2$ Gyr after onset. Thus while the total RPS time span may be quite long, a majority of the RPS occurs in a relatively short period. While not shown here, the distribution of peak to total RPS time span ranges from $\approx 0.1 - 0.4$, with the mode and median at ≈ 0.15 and 0.20 respectively.

We note an alternative method for characterizing the effectiveness or peak RPS as the specific RPS (sRPS): RPS / $M_{\rm ColdGas}^{\rm sat}$. Typically for the TNG50 jellyfish without cold gas at $z = 0$, the specific RPS + outflows is approximately constant before infall. At infall, the sRPS typically increases through pericenter and near apocenter either plateaus or decreases, sometimes to its

pre-infall value. For the galaxies that lose all their cold gas only at or after second pericenter (subfindID 439110 in the top right panel of Fig. 7.9 for example), the sRPS increases again and always reaches its maximum value at or shortly before τ_{100}. See Appendix 7.7 for more details and Fig. 7.13 for an example.

7.4 Discussion

7.4.1 How Do These Jellyfish-Based Results Generalize to All Satellite Galaxies?

Throughout this paper, we have focused on jellyfish galaxies, as these are satellites with manifest signs of ongoing RPS. In particular, we have followed satellites along their evolutionary tracks through cosmic epochs and dubbed the inspected galaxies as jellyfish only if they have at least one jellyfish classification since $z = 0.5$. This is when the temporal sampling of the images on Zooniverse transitioned from every ≈ 1 Gyr to every ≈ 150 Myr. We also restate that the images posted to Zooniverse used a fixed gas column density colorbar in the range $\Sigma_{\rm gas} \in 10^{5-8}\,{\rm M}_\odot\,{\rm kpc}^{-2}$ and did not include background subtraction, mimicking a surface brightness limited sample. Hence to have been classified as a jellyfish galaxy, the stripped tails must have been dense enough to have been distinguishable against the background. Lastly, we expect that at any given snapshot, we miss $\approx 30-40$ per cent of jellyfish galaxies due to projection effects (Yun et al., 2019; Zinger et al., 2024).

As shown in Fig. 7.1 and discussed in § 7.3.1, jellyfish galaxies tend towards lower stellar masses $M_\star^{\rm sat}$, higher host masses $M_{\rm 200c}^{\rm host}$, and lower satellite-to-host mass ratios μ at $z = 0$ compared to the inspected galaxies and the general $z = 0$ population of satellites. Conversely, the inspected galaxies that were *not* identified as jellyfish tend towards the opposite. First 163 of the 1,031 (≈ 15 per cent) non-jellyfish galaxies have stellar masses $M_\star^{\rm sat} > 10^{10}\,{\rm M}_\odot$, and may have experienced phases of kinetic AGN feedback, ejecting much of their gas. Of the lower mass non-jellyfish galaxies $M_\star^{\rm sat} < 10^{10}\,{\rm M}_\odot$, we affirm that many of these satellite galaxies are still undergoing or have undergone RPS (see Figure 7.11), and the question becomes why have they not been identified as jellyfish. These non-jellyfish galaxies have a median satellite-to-host mass ratio $\mu = 7.8 \times 10^{-4}$, ≈ 15 times higher than that for the jellyfish $\mu = 5.0 \times 10^{-5}$. We generally expect and have shown in Fig. 7.8 that with increasing satellite-to-host mass ratio RPS is weaker and acts over longer time spans. Accordingly, some of the gaseous tails may not have been identifiable in gas column density compared to the ambient medium. Moreover, the non-jellyfish galaxies have a median infall time at 9.2 ± 1.2 Gyr, ≈ 1.7 Gyr later than the jellyfish galaxies at 7.5 ± 1.0 Gyr. So it is also possible that these late-infalling non-jellyfish have not yet had enough time to undergo enough RPS to form the recognizable tails, although

the timescales associated with the appearance and disappearance of the jellyfish tails is largely unconstrained (Smith et al., 2022).

While 259/512 (≈ 51 per cent) of the jellyfish galaxies have cold gas masses below our resolution limit at $z = 0$, this is only the case for 125/1,031 (≈ 12 per cent) of the non-jellyfish galaxies. Then how can these 125 gas-less satellites have lost all of their cold gas without being identified as jellyfish? Of the galaxies with $M^{\rm sat}_{\rm ColdGas}(z = 0) < 4 \times 10^4\,{\rm M}_\odot$, the RPS duration for jellyfish includes both short and long time spans $\tau_{\rm RPS} \approx 1.5 - 8$ Gyr, while for the non-jellyfish the time spans are only long $\tau_{\rm RPS} \approx 3.5 - 7.5$ Gyr. Again, this demonstrates that the RPS for the non-jellyfish with higher mass ratios is slower, potentially causing the gaseous tails to be unidentifiable. Furthermore, these $z = 0$ gas-less non-jellyfish tend to have even earlier infall times than their jellyfish counterparts. In fact, almost all of the non-jellyfish have infall times before $z = 0.5$, before the temporal sampling of the images on Zooniverse transitioned from every ≈ 1 Gyr to every ≈ 150 Myr. So before $z = 0.5$, we may be missing some jellyfish simply by not inspecting their images often enough. Based on the statistical, physical differences between the general jellyfish and non-jellyfish galaxies, and that we may be missing some high-redshift, jellyfish-like galaxies, we conclude that our primary sample of jellyfish galaxies is pure, but perhaps not complete. And when generalizing the results of the RPS time spans from the jellyfish to all satellites, the time spans would only increase. We have also checked that the peak RPS periods are slightly longer and still occur in the halos for the non-jellyfish galaxies. However, our results only apply to first-infalling galaxies, i.e not to pre-processed galaxies, which is more significant for less massive satellites in more massive hosts. Extending this analysis to pre-processed galaxies would require distinguishing how much RPS occurs in each host, and when the infalling group's intragroup medium gets stripped.

7.4.2 The Connection Between Ram Pressure Stripping and Quenching Timescales

The 259 TNG50 jellyfish that are gas-poor at $z = 0$ were star forming galaxies – on the star forming main sequence (SFMS) – before infall and are instead quenched at $z = 0$ – at least than one dex below the SFMS. The question becomes, when between the RPS onset at infall and its end at τ_{100} do these jellyfish quench. We calculate the amount $f_{\rm RPS}(< \tau_{\rm quench})$ of RPS that has already occurred by the time of last quenching $\tau_{\rm quench}$ via

$$f_{\rm RPS}(< \tau_{\rm quench}) = \int_{\tau_0}^{\tau_{\rm quench}} f_{\rm RPS}(t)\,{\rm d}t \tag{7.4}$$

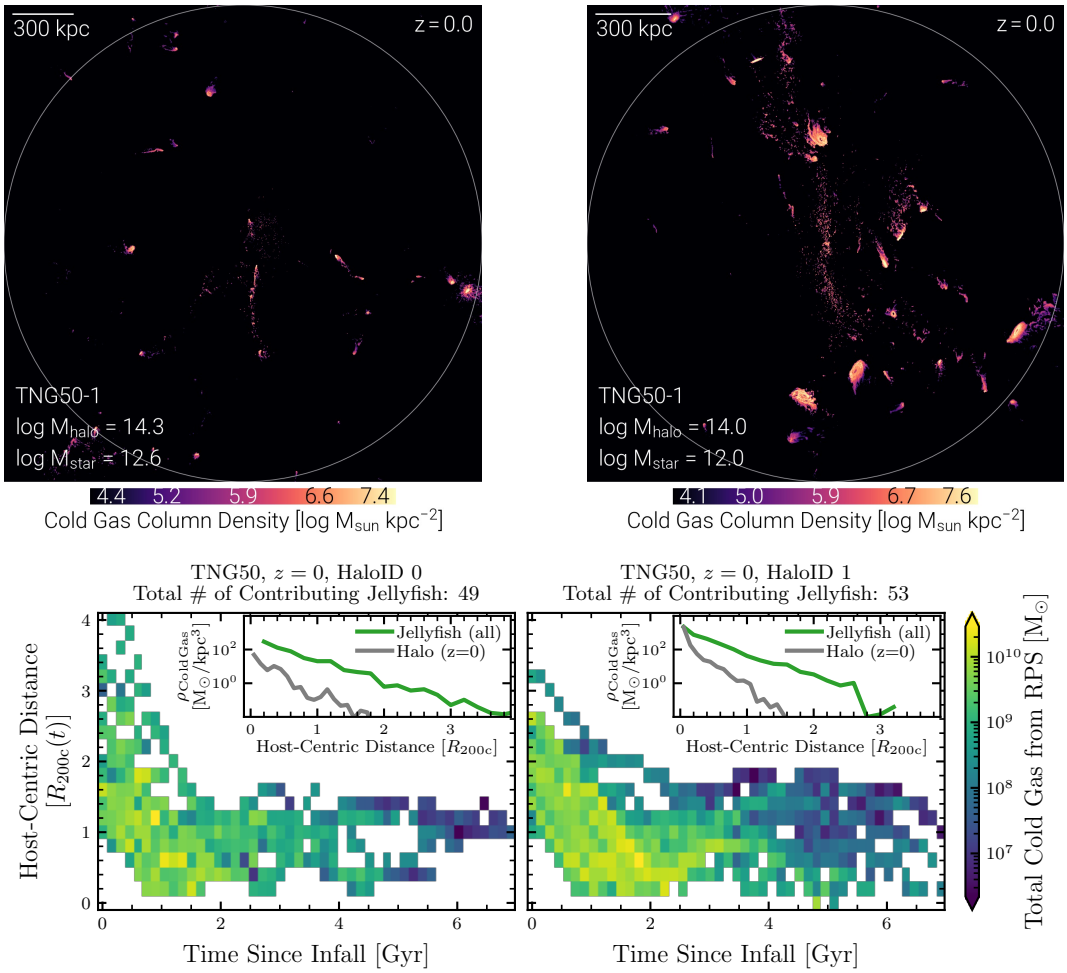

Figure 7.10: **TNG jellyfish deposit a significant amount of cold gas into their host halos.** For the most (left) and second most (right) massive clusters in TNG50 ($M_{200c}^{host}(z=0) \approx 10^{14}\,M_\odot$), we plot the cold gas column density at $z = 0$ (top panels; all halo gas with temperatures $\leq 10^{4.5}$ K, including gas gravitationally bound to satellites) and the total amount of cold gas deposited in the host halos from all TNG50 jellyfish in bins of host-centric distance and time since infall (bottom panels). For both halos, the total amount of cold gas deposited into the halos from ram-pressure stripped jellyfish is $\sim 10^{12}\,M_\odot$ over the last 5 billion years. In the insets (bottom panels), we compare the radial distributions of the cold gas deposited via RPS from all jellyfish at $z \lesssim 0.5$ (green) with the cold gas that exists in and around the halos at $z = 0$ (gray, excluding cold gas bound to satellite galaxies). Together with Fig. 7.11, this shows that jellyfish, and more generally satellites, contribute a significant amount of cold gas into their host halos.

where the fractional RPS $f_{\rm RPS}(t)$ is defined in equation (7.2), and $\tau_{\rm quench}$ is the last time that the galaxy falls at least one dex below the SFMS for the last time (Pillepich et al., 2019; Joshi et al., 2021; Donnari et al., 2021b).

On average, the jellyfish do not quench until $\gtrsim$ 99 per cent of the total RPS has occurred. Only 5/259 ($\approx$ 2 per cent) of the jellyfish quench before $f_{\rm RPS}(< \tau_{\rm quench}) = 97$ per cent. Moreover, these jellyfish have already lost $\gtrsim$ 98 per cent of their cold gas by the time they quench. Of the 259 jellyfish galaxies with $M^{\rm sat}_{\rm ColdGas}(z = 0) > 4 \times 10^4\,{\rm M}_\odot$), only 74 ($\approx$ 30 per cent) have quenched whereas the others are still forming stars (see also Göller et al., 2023). These quenched jellyfish also have already lost $\approx$ 98 per cent of their cold gas before quenching. While the peak period of RPS typically occurs during the first infall through pericenter, lasting $\lesssim$ 2 Gyr, the jellyfish do not quench for the last time until nearly all of their cold gas has been stripped on time spans that can be $\gtrsim$ 5 Gyr after infall. This does not necessarily imply that the galaxies are on the SFMS for the entire duration between infall and τ_{100}, but instead that they quench for the last time only after being stripped of almost all of their cold gas. Jellyfish galaxies are able to continue forming stars well after infall and after they have lost almost all of their cold gas due mostly to RPS.

To define a quenching timescale, one also needs to define the onset of quenching (See Cortese et al., 2021, for a review of various definitions used in the literature). If we assume the infall time τ_0 as the onset of quenching, then the distribution of quenching timescales is approximately the same as the RPS timescale distribution in Fig. 7.7 (right panel, red histogram). Thus, the quenching timescales for the TNG50 jellyfish studied here and without cold gas at $z = 0$ range from $\approx 1 - 7$ Gyr after infall. However, we note that many of these jellyfish undergo brief ($\lesssim$ 1 Gyr) bursts of star-formation between infall and first pericentric passage (Göller et al., 2023). While it may seem counter-intuitive for the onset of quenching – in this case, infall – to be directly before a burst of star-formation, this starburst coincides exactly with the time span that most jellyfish incur their peak gas loss due to RPS (Fig. 7.9). Thus the RPS and burst of star-formation may act together and enhance each other to remove cold gas from jellyfish, eventually quenching them. This is consistent with the satellite post-starburst quenching scenario, where ram pressure induces a burst of star-formation before the satellite eventually quenches and has signature of a post-starburst galaxy Poggianti et al. (2017b); Gullieuszik et al. (2017); Vulcani et al. (2020); Grishin et al. (2021); Werle et al. (2022).

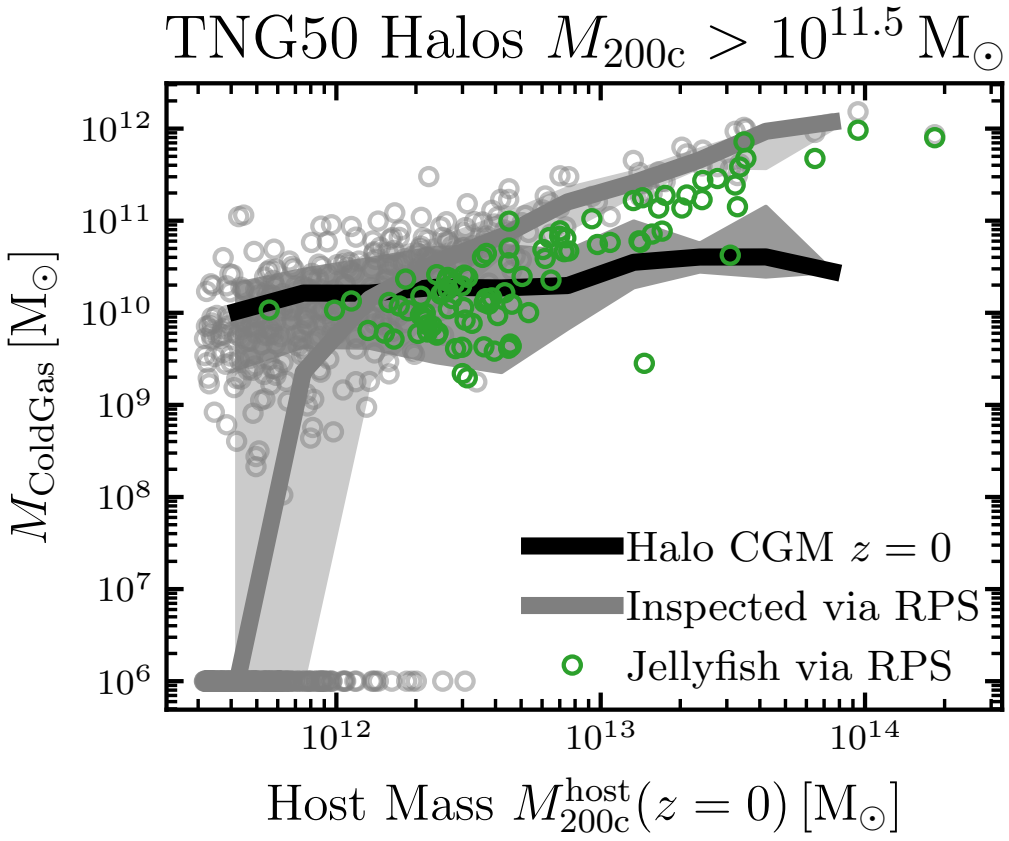

Figure 7.11: **TNG satellites (both jellyfish and inspected satellite branches) are a significant source of cold gas for their host halos.** We extend the analysis from Fig. 7.10 now to include all inspected branches and hosts down to mass $M^{\rm host}_{\rm 200c} = 10^{11.5}\,M_\odot$. We compare the the cold circumgalactic medium (CGM) excluding cold gas bound to satellites (black curve and shaded region denote the median and 16/84th percentiles) to the amount of cold gas brought in over the past ~ 5 Gyr by jellyfish (green circles) and all inspected galaxies (jellyfish + non-jellyfish; gray circles, where the gray curve and shaded region denote the median and 16/84th percentiles) from ram pressure stripping (RPS). We place by hand the halos without any cold gas deposited from inspected galaxies at $M_{\rm ColdGas} = 10^6\,M_\odot$. At host masses $\gtrsim 10^{13}\,M_\odot$, the inspected satellite galaxies have brought more cold gas into the halos over the past ~ 5 billion years than exists in the CGM today.

7.4.3 RPS Deposits Satellite ISM into the Halo

In addition to being stripped of their cold gas, jellyfish galaxies, and more generally satellite galaxies, also provide a source of cold gas to the halo. For a given host, how much cold gas comes directly from ram-pressure stripped jellyfish galaxies?

In Fig. 7.10, we combine all jellyfish galaxies (regardless if they have substantial cold gas at $z = 0$ or not) in the the two most massive clusters $M_{200c}^{host}(z = 0) \approx 10^{14}\,M_\odot$ in TNG50, and show the total amount of deposited cold gas in the time since infall – host-centric distance space, similarly to Fig. 7.9. We also show the cold gas column density maps for these clusters for reference. The two clusters have hosted 49 and 53 total contributing jellyfish since approximately $z \sim 0.5$, depositing a total of $\sim 10^{12}\,M_\odot$ of cold gas mass into the hosts. This is a substantial amount of cold gas: it is about one tenth of the total amount of gas in these halos at any given time, it is of a similar order of magnitude as the stellar mass of the central galaxy of the host at $z = 0$, and it is orders of magnitude more than the amount of ionized and molecular gas that have been recently observed around several brightest central galaxies (e.g. McNamara et al., 2014; Russell et al., 2019).

We can integrate the contributed cold gas along the host-centric distance, yielding the 1D distribution of the deposited cold gas from RPS in time since infall. For the most massive halo in TNG50, the median (16/84 percentiles) of the cold gas from RPS distribution occurs 0.9 (0.3/1.8) Gyr after infall; for the second most massive halo, 1.2 (0.4/2.4) Gyr after infall. Again, while some jellyfish contribute cold gas to the hosts over long periods $\gtrsim$ 3 Gyr, a majority of the RPS occurs shortly after infall, qualitatively agreeing with the results discussed in § 7.3.6 shown in Fig. 7.9 (bottom center and right panels).

Additionally, we can integrate the contributed cold gas along the time since infall, yielding the host-centric radial distribution of deposited gas from RPS. For the most massive halo in TNG50, the median (16/84 percentiles) of the cold gas from RPS distribution occurs at 1.0 (0.6/2.4) R_{200c}; for the second most massive halo, 0.8 (0.2/1.8) R_{200c}. Thus, we see that the majority of contributed cold gas from RPS is deposited into the outskirts of the gaseous halos (i.e., CGM or ICM) of these most massive hosts in TNG50. In the figure insets, we compare the radial-density distributions of cold gas deposited via RPS from all jellyfish (green) with the cold gas that exists in the halos at $z = 0$ (gray, excluding cold gas bound to satellites). For these two cluster-mass hosts, more cold gas has been brought into their halos via RPS over the last many billion years than exists in their intra-cluster media today.

We extend this analysis in Fig. 7.11 now to include all inspected satellite branches (gray circles) and group- ($M_{200c}^{host}(z = 0) \sim 10^{13}\,M_\odot$) and Milky-Way-mass ($M_{200c}^{host}(z = 0) \sim 10^{12}\,M_\odot$) hosts. According to our analysis and to TNG50, over the past $\sim$ 5 billion years satellite galaxies have deposited more than $10^{10}\,M_\odot$ of cold gas mass via RPS in the CGM

of halos more massive than $10^{12.5}\,M_\odot$. The amount of cold gas in the CGM at $z = 0$ (black circles) increases with halo mass until $\sim 10^{13.5}\,M_\odot$, and afterwards is approximately constant. The amount of cold gas deposited by inspected galaxies in low mass hosts $M_{200c}^{host} \lesssim 10^{12}\,M_\odot$ is bimodal, where many hosts have 0 inspected branches. Of the low-mass hosts with inspected branches, the amount of cold gas deposited by ram pressure stripping (RPS) increases with halo mass, which continues with all studied halo masses.

Of the amount of cold gas deposited by RPS of the inspected galaxies, the relative contribution of jellyfish galaxies increases with halo mass, reflecting the trend that a higher percentage of inspected galaxies are jellyfish at the higher host masses (see Fig. 7.1). At host masses $\gtrsim 10^{13}\,M_\odot$, the inspected galaxies have brought more cold gas into the halos over the past ~ 5 billion years than exists in the CGM today.

Thereby, we claim that jellyfish, and the more generally inspected or satellite galaxies, bring a significant amount of cold gas in the CGM/ICM of massive halos. The question then becomes, what happens to the stripped cold gas between being deposited and $z = 0$. We speculate that this gas could either (i) remain cold in the CGM, (ii) remain cold and rain down on the central galaxy, (iii) mix and heat up with the surrounding hot medium, and/or (iv) be heated up and/or pushed outside of the halo by kinetic AGN feedback (e.g., Ayromlou et al., 2023b). Conversely, one could start with the cold CGM clouds at $z = 0$ and follow their histories back in time, quantifying how much came from satellites (Nelson et al., 2020). We postpone the task of quantifying the fate of the cold gas brought by satellites into the CGM around galaxies for a future work.

7.5 Summary and Conclusions

In this work, we use the high-resolution, ~ 50 Mpc magneto-hydrodynamical simulation TNG50 from the IllustrisTNG project to study the satellite-host interaction in a cosmological context for ≈ 5 orders of magnitude in satellite stellar and host total mass. In particular, we quantify when, where, and for how long the ram pressure stripping (RPS) of cold gas occur, by focusing on jellyfish galaxies, i.e. satellites with manifest signs of RPS.

We use the results from Zinger et al. (2024), which is a follow up from the pilot Zooniverse study from Yun et al. (2019), to identify jellyfish galaxies via visual inspection. Namely, Zinger et al. (2024) report and discuss the visual inspection via Zooniverse of 53,610 satellite galaxies from TNG50 with $f_{gas} < 0.01$ and $M_\star^{sat} > 10^{8.3}\,M_\odot$, in the TNG50 simulation. For this paper, we track the 53,610 inspected images across cosmic time, finding a total of 5,023 unique galaxy branches. In the main analysis of this work, we focus on the galaxy branches that survive until $z = 0$, were inspected in the Zooniverse project since $z \leq 0.5$, are satellites at $z = 0$, have

not been pre-processed, and have well-defined infall times; this returns a pure sample of 1,543 galaxies. 512 of these 1,543 branches (≈ 33 per cent) are jellyfish galaxies, meaning that they were classified as a jellyfish galaxy for at least one snapshot since $z \leq 0.5$.

Compared to the inspected galaxies and general $z = 0$ satellites with $M_\star^{\rm sat} > 10^{8.3}\,{\rm M}_\odot$, the TNG50 jellyfish galaxies tend to have lower stellar masses, higher host masses, lower satellite-to-host mass ratios, and less gas (Fig. 7.1). The tails of the jellyfish galaxies are made up of mostly cold gas ($\leq 10^{4.5}$ K) with similar metallicities to the gas within the stellar body, suggesting that the tails stem from the interstellar media (Figs. 7.2, 7.3), though the jellyfish tails may also be observable in, e.g., soft x-rays.

We employ the Monte-Carlo-Lagrangian tracer particles to quantify the relative importance of each cold gas sink, namely SMBH accretion, star-formation (SF), gas heating, and ram-pressure stripping (RPS) + outflows. As individual galaxy tracks suggest, we assume that before infall, i.e. the first time the galaxy becomes a member of its Friends-of-Friends (FoF) host group, RPS+outflows category is dominated by outflows, and after infall RPS is dominant. Then we define the onset τ_0 of RPS as the infall time and the end τ_{100} of RPS as either when the galaxy's cold gas mass falls below our resolution limit of $m_{\rm gas} \approx 4\times10^4\,{\rm M}_\odot$ ($f_{\rm gas} \lesssim 5\times10^{-4}$) or at the end of the simulation at $z = 0$; then the total RPS time span $\mathcal{T}_{\rm RPS}$ is the difference between $\tau_{100} - \tau_0$. With this sample of 512 jellyfish and method to measure RPS, our main results are:

- For an individual example, we show that a single jellyfish branch loses all of its cold gas between infall and apocenter (Fig. 7.4), and during this period RPS is the dominant channel of cold gas loss (Fig. 7.5). We check and find that RPS dominates the post-infall cold gas loss for all other jellyfish in the sample.

- Approximately half 259/512) of the jellyfish have been stripped of all cold gas by $z = 0$. The jellyfish without cold gas at $z = 0$ (i.e. with cold gas mass $< 4 \times 10^4\,{\rm M}_\odot$) tend to have smaller satellite-to-host mass ratios and earlier infall times than the jellyfish that retain some cold gas at $z = 0$ (Figs. 7.6, 7.7).

- For the 259 jellyfish galaxies without cold gas at $z = 0$, the total RPS durations span $\mathcal{T}_{\rm RPS} \approx 1 - 7$ Gyr (Fig. 7.7). The dominant factor for determining the RPS time span is the host mass, whereby jellyfish in higher-mass hosts have shorter RPS durations (Fig. 7.8, top panel). Secondarily, RPS durations decrease with satellite cold gas mass at infall, the stellar mass at $z = 0$, and the number of orbits by τ_{100} (Fig. 7.8, bottom panels respectively).

- While the total RPS duration may be quite long, most jellyfish incur a majority of their cold gas mass loss via RPS within a short peak RPS period, beginning $\lesssim$ 1 Gyr after infall and lasting $\lesssim$ 2 Gyr (Fig. 7.9 top, bottom center, and bottom right panels). Typically this peak RPS period occurs within $\approx 0.2 - 2R_{200c}$ of the host and during the first infall.

- Jellyfish galaxies continue forming stars for billions of years after infall, until they have lost $\approx$ 98 per cent of their cold gas mass. They quench for the last time only after $\approx$ 99 per cent of the RPS has occurred (§ 7.4.2).

- In the two most massive $\sim 10^{14}\,M_\odot$ halos in TNG50, jellyfish galaxies contribute $\approx 10^{12}\,M_\odot$ of cold gas into the intra-cluster medium over the past $\sim$ 5 billion years (ICM; Fig. 7.10). The radial distribution of cold gas brought in via jellyfish RPS is significantly higher than the amount of cold gas existing in the ICM today. In fact, satellite galaxies deposit over the past $\sim$ 5 billion years $\gtrsim 10^{10}\,M_\odot$ of cold gas in the CGM of $\gtrsim 10^{12.5}\,M_\odot$ TNG50 halos (Figs. 7.11). For massive hosts, this cold gas contribution is of the same order of magnitude as the stellar mass in the central galaxy today. Therefore, jellyfish galaxies, and the more general population of satellites, bring a significant amount of cold gas into the CGM/ICM of massive hosts.

In summary, we have shown that, according to TNG50, RPS is the dominant cause of loss of cold gas in satellites after they start to interact with their $z = 0$ hosts and that satellite galaxies are significant contributors of cold gas to the CGM and ICM. RPS acts on infalling galaxies for very long periods of time, i.e. *many* billion years on average, even though the majority of the cold gas mass loss occurs faster, with half of the cold gas of satellites being stripped in the span of about 2 billion years or less. This cold gas is typically deposited by the satellites all the way from intermediate host-centric distances to beyond the virial radii of their hosts.

We note that these results apply only to the satellite stellar and total host masses studied in this work, within the TNG model of galaxy formation. For the most massive satellites, $M_\star \sim 10^{10-11}\,M_\odot$, it is possible that their stellar potential is deep enough to retain some of their own CGM post-infall, shielding some of their ISM gas. At these masses, the TNG kinetic mode of SMBH feedback also becomes important, and is thought to dominate, along with RPS, the quenching of these satellites (Donnari et al., 2021a). In a future work, we extend these results to more massive satellite and host masses using the upcoming TNG-Cluster project that focuses on massive hosts $M_{200c}^{\rm host} \sim 10^{14-15.4}\,M_\odot$ using the TNG galaxy formation model.

7.6 Appendix A: Tracking Individual Galaxies Across Epochs

In the Cosmological Jellyfish project, whose results we use here and are summarized and discussed by Zinger et al. (2024), gas-map images were posted of TNG50 (and TNG100, though not discussed here) satellite galaxies meeting the criteria summarized in § 7.2.2 at all 33 snapshots since $z = 0.5$ (snapshots 99-67), plus at four additional snapshots corresponding to redshifts $z = 0.7, 1.0, 1.5, 2.0$ (snapshots 59, 50, 40, 33). Many galaxies were inspected at multiple snapshots. However, for this work we focus on the unique evolutionary tracks, or branches, of individual galaxies using SUBLINK_GAL (Rodriguez-Gomez et al., 2015). In practice, we load the main progenitor branch (MPB) of every galaxy inspected at $z = 0$ (snapshot 99), saving the galaxies' subfindIDs at all previous snapshots. Then at each earlier inspection snapshot (98, 98, ..., 67, 59, 50, 40, 33), we check which galaxies' MPB have already been saved. If not, then we save the MPB and continue to the next snapshot. Within the 53610 inspected galaxy images in TNG50, there 5023 are unique branches.

As summarized in § 7.2.4, throughout this work we exclude galaxies if they do not exist at $z = 0$, are backsplash galaxies at $z = 0$, or have been pre-processed. For each branch that is not inspected at $z = 0$ (snapshot 99), we load the main descendant branch (MDB). With the MDB, we find the last snapshot at which the galaxy exists, typically either when the galaxy merges with another more massive galaxy (subhalo coalescence) or at $z = 0$. We are interested only in galaxies that exist as satellites at $z = 0$, so we exclude 2,341 branches that do not exist as satellites at $z = 0$. To determine whether the remaining galaxies that are satellites at $z = 0$ are have been pre-processed, we examine both the galaxies' and their $z = 0$ hosts' MPBs (technically the MPBs of their $z = 0$ hosts' main subhalos). Then at each snapshot, we classify each galaxy's Friends-of-Friends (FoF) group membership into exactly one of three categories:

- the main (central) subhalo of the group;
- a satellite of its $z = 0$ host;
- a satellite of a group other its $z = 0$ host.

Then using these categorizations across the snapshots, we can determine whether the galaxy was pre-processed; if the galaxy spent at least $N_{\rm snaps} = 5$ consecutive snapshots as a satellite in a host – other than its $z = 0$ host – of mass $M_{\rm 200c}^{\rm host} > M_{\rm LowLim} = 10^{11}\,{\rm M}_\odot$. If the galaxy instead spent these $N_{\rm snaps}$ snapshots in its $z = 0$ host, then spent some snapshots as a central galaxy, before eventually being a satellite in the same group, then we do not consider the galaxy to

be pre-processed and include the galaxy in the analysis. We exclude a total of 341 TNG50 pre-processed galaxies[7].

In general, we classify all TNG50 $z = 0$ galaxies at all snapshots as one of the three above categories. Then for all $z = 0$ systems, we further flag and exclude current backsplash galaxies, i.e. galaxies that have spent $N_{\rm snaps} = 5$ consecutive snapshots in a host of mass $M_{\rm 200c}^{\rm host} > M_{\rm Lowlim} = 10^{11}\,{\rm M}_\odot$ before eventually being a central galaxy at $z = 0$. This definition is nearly equivalent to that used by Zinger et al. (2020), except that they use $N_{\rm snaps} = 3$ and $M_{\rm Lowlim} = 0$ (i.e., no criterion for host mass). Additionally we note that, especially during massive mergers, SUBFIND may confuse which galaxy is actually the central and which is the satellite. Consequently some galaxies (such as central galaxy of the most massive cluster in TNG50) may be classified as a backsplash galaxy due to this "swapping problem", so we recommend using caution when physically interpreting these backsplash galaxies.

Further, we check whether each $z = 0$ satellite subhalo was pre-processed or previously a backsplash galaxy. The pre-processing definition is above. A galaxy was previously a backsplash galaxy if it spent at least $N_{\rm snaps} = 5$ in any host of mass $M_{\rm 200c}^{\rm host} > M_{\rm LowLim} = 10^{11}\,{\rm M}_\odot$, then spent at least $N_{\rm snaps}$ consecutive snapshots as a central, before eventually being a satellite at $z = 0$. A given $z = 0$ satellite may be a previous backsplash but not pre-processed if the previous host is also the $z = 0$ host; pre-processed but not previously a backsplash if the galaxy falls into a pre-processing host and this pre-processing host falls into the $z = 0$ host; both a previous backsplash and pre-processed; or neither. Previously Donnari et al. (2021b) combined these two flags – pre-processed and previous backsplash – as one general "pre-processing" flag, while in this analysis we include previous backsplash galaxies. Additionally, Donnari et al. (2021b) use $N_{\rm snaps} = 3$ and $M_{\rm LowLim} = 10^{12}\,{\rm M}_\odot$, and the catalogs utilize SUBLINK rather than SUBLINK_GAL (Rodriguez-Gomez et al., 2015).

7.7 Appendix B: Comparisons of the Onset of RPS

Throughout the paper, we define the onset τ_0 of ram-pressure stripping (RPS) as the infall time, as the first time a galaxy becomes a member of its $z = 0$ Friends-of-Friends (FoF) host group. The FoF algorithm decides group membership based on the relative positions of dark matter particles, and there are a-priori no constraints on the shape or total size of the halo; that is, we do not assume spherical halos where galaxies become satellite members upon crossing the virial radius $R_{\rm 200c}$. Consequently, there is a range of infall distances $d_{\rm sat}^{\rm host}(\tau_0)$, ranging from $\approx 1 - 4R_{\rm 200c}$ (see Fig. 7.9, middle panel). Throughout this paper, we consider this

[7] The most massive TNG50 halo accretes a group $M_{\rm 200c} \sim 10^{13}\,{\rm M}_\odot$ at $z \approx 0.7$, and we therefore exclude many of this group's pre-processed jellyfish.

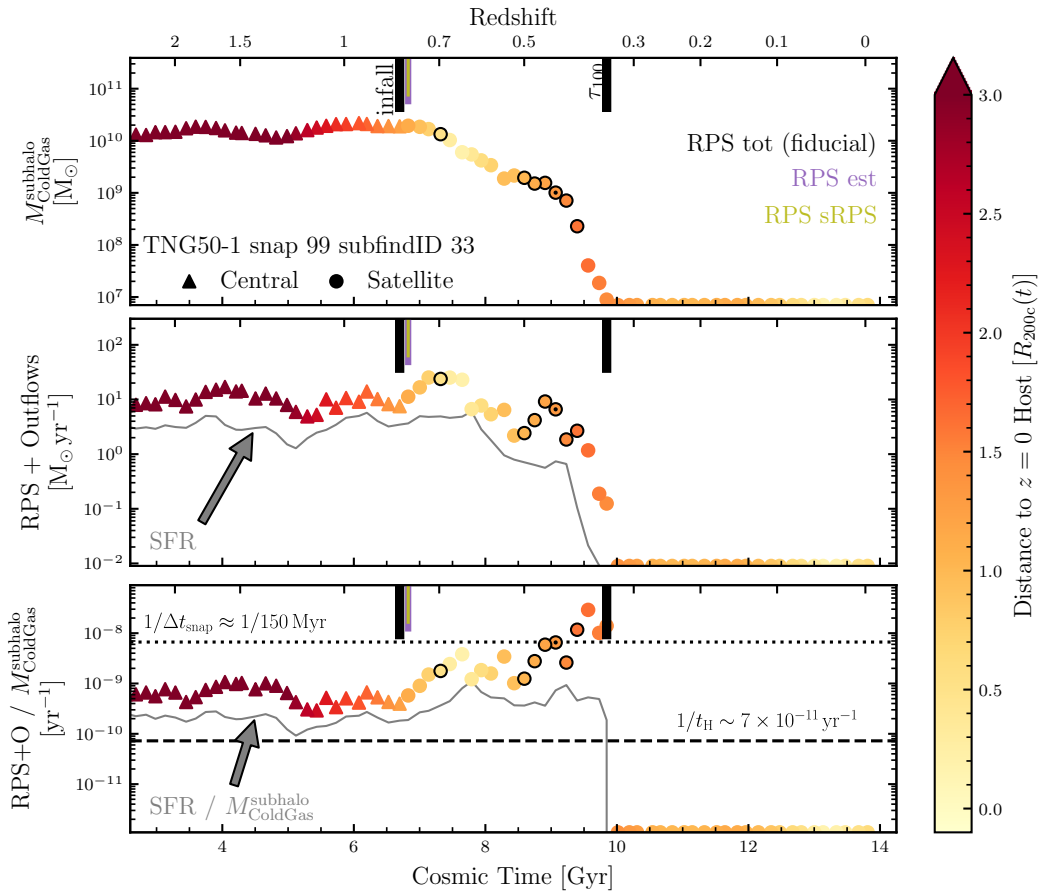

Figure 7.12: **Time evolution of the cold gas content and associated tracers of a TNG jellyfish galaxy that is stripped of all cold gas between first and second pericentric passage.** The marker style denotes the FoF membership and the color the distance to the $z = 0$ host in units of $[R_{\rm 200c}^{\rm host}(t)]$. The inspected snapshots are outlined, and the jellyfish classified have a black dot. We plot snapshots where the y-axis quantity is below our resolution limit at the lower y-limit (along the bottom x-axis). The thick black ticks denote the fiducial start (infall) and end (when $M_{\rm ColdGas}^{\rm subhalo} = 0$) times of ram-pressure stripping (RPS), while the purple ("RPS est") and olive ("RPS sRPS") ticks denote two alternative methods of measuring the start of RPS. See the text for additional details regarding the definitions of RPS est and RPS sRPS. For this galaxy, the three definitions yield similar results for the onset of RPS. Top panel: the total gravitationally-bound cold gas mass $M_{\rm ColdGas}^{\rm subhalo}$. Middle panel: RPS+outflows and instantaneous SFR as the thin gray curve. Bottom Panel: sRPS = RPS+outflows / $M_{\rm ColdGas}^{\rm subhalo}$, in addition to SFR / $M_{\rm ColdGas}^{\rm subhalo}$ as the thin gray curve; the dashed line denotes $1/t_H$, where t_H is the Hubble Time; the dotted line denotes the approximate inverse time between snapshots $1/\Delta t_{\rm snap} \approx 1/150\,{\rm Myr} \approx 7\times10^{9}\,{\rm yr}^{-1}$.

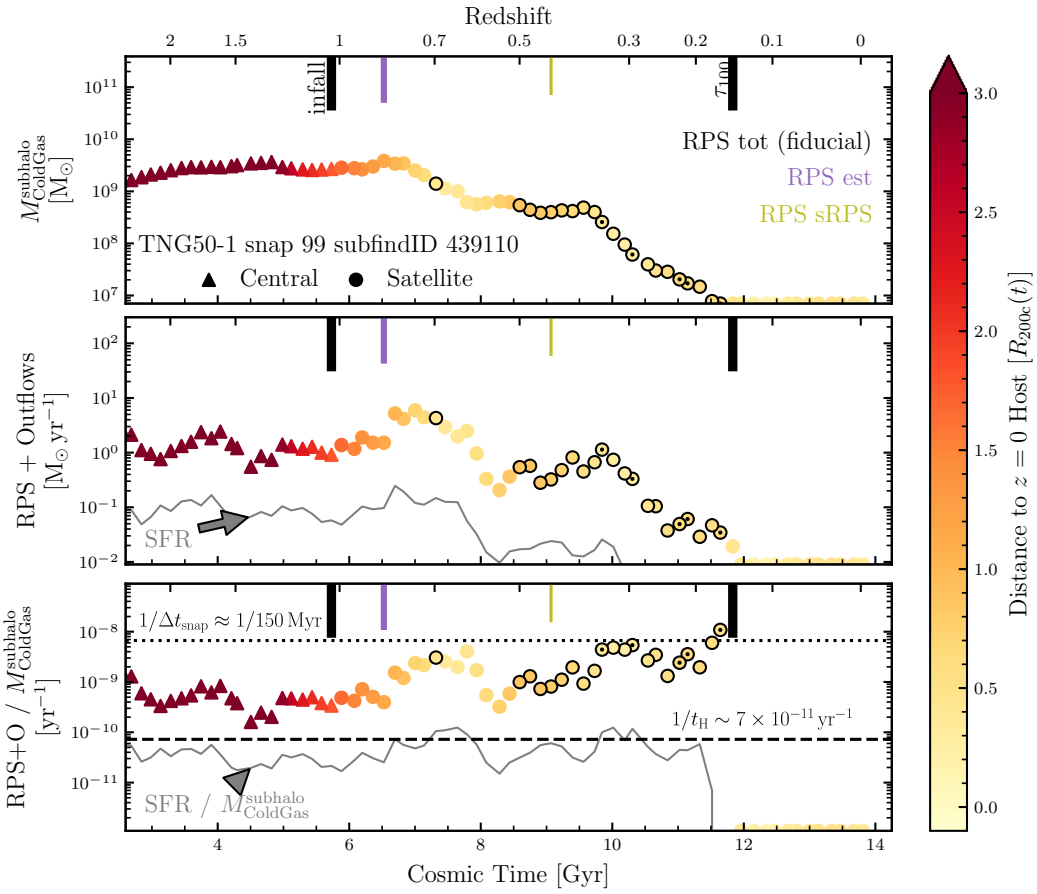

Figure 7.13: **Time evolution of the cold gas content and associated tracers of a TNG50 jellyfish galaxy that is stripped of all cold gas only after its second pericentric passage.** Similar to Fig. 7.12, except for this example the onset of RPS τ_0 for "RPS est" (purple) and "RPS sRPS" (olive) are significantly later than the infall time (black, fiducial). This represents a non-common case, so that we can safely take the infall time, i.e. the first time a galaxy becomes part of the Fof of its $z = 0$ host, as the onset of RPS.

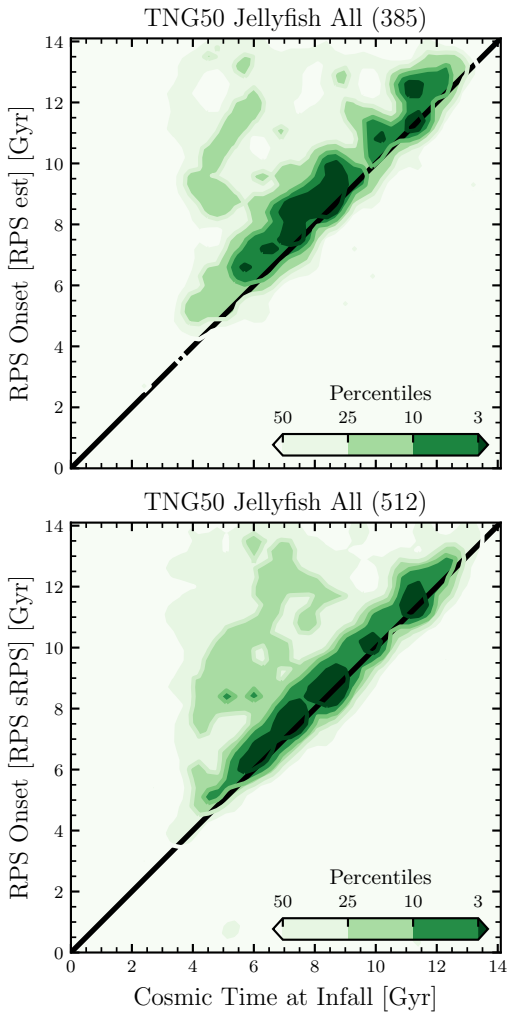

Figure 7.14: Alternative methods for measuring the onset of RPS compared to the fiducial choice of infall time.

FoF infall time to be onset of environmental effects for these first-infalling, not pre-processed jellyfish. Moreover, using this infall time as the onset and the time when galaxies lose all cold gas as the end of RPS allows us to measure the entire RPS time span $\tau_{\rm RPS} = \tau_{100} - \tau_0$, at least for the galaxies that lose all cold gas by the end of the simulation at $z = 0$.

We have checked our results using two additional definitions for measuring the onset of RPS τ_0. First, we assume that the pre-infall outflows are primarily star-formation-driven outflows. Then we measure each galaxy's cold gas loading factor $\eta_{\rm ColdGas}$ as the median cold gas loss due to outflows divided by the star-formation rate (SFR)

$$\eta_{\rm ColdGas} = \text{median}\left(\frac{\text{Outflows(<infall time)}}{\text{SFR(<infall time)}}\right) \tag{7.5}$$

where "Outflows" is the (RPS + Outflows) total cold gas mass loss from RPS + outflows directly measured using the tracer particles, before infall assumed to be entirely outflows. Then after infall, we estimate the amount of star-formation-driven outflows as the product of $\eta_{\rm ColdGas}$ and the SFR. Thus, we attempt to separate the measured RPS+Outflows into the two components:

$$\begin{aligned} \text{RPS est}(t) &= (\text{RPS + outflows})(t) - \text{outflows}(t) \\ &= (\text{RPS + outflows})(t) - \eta_{\rm ColdGas} \times \text{SFR}(t) \end{aligned} \tag{7.6}$$

where "RPS est" is the estimated RPS and (RPS + outflows) is the quantity measured using the tracer particles. Then we find the peak of "RPS est" and go backwards in time until the this estimated RPS vanishes, i.e. until the (RPS + outflows) can be fully estimated by just star-formation-driven outflows. In practice, we calculate the running median of the estimated outflows and total RPS + outflows over $N_{\rm snaps} = 7$ consecutive snapshots ($\sim$ 1 Gyr), and find where the difference, the estimated RPS, peaks. Then we go backwards in time until the running median of the estimated RPS vanishes, where this time marks the onset of RPS. In Fig. 7.12, the onset of RPS using this "RPS est" is shown with a purple tick, where this estimated onset of RPS is 2 snapshots ($\approx$ 300 Myr) after the infall time. In the middle panel after infall, there is an increase in the total RPS + outflows (triangles and circles) while the SFR (gray) remains approximately constant. Thus, the "RPS est"-onset is similar to the infall time.

While this method attempts to separate the relative amounts of cold gas loss via (RPS + outflows) into RPS and outflows, there are a number of disadvantages. First, this method assumes that the cold gas mass loading factor $\eta_{\rm ColdGas}$ – which varies with galaxy stellar mass, cold gas mass, and SFR – is approximately constant before and after infall. Then as a number

of galaxies experience a burst of star-formation between infall and first pericentric passage, the approximations of $\eta_{\rm ColdGas}$ may break down. For the example jellyfish in Fig. 7.13, there is both an increase in the RPS + outflows and in the SFR after infall, delaying the "RPS est"-onset of RPS by 7 snapshots ($\sim$ 1 Gyr). In fact, for 127/512 ($\approx$ 25 per cent) jellyfish galaxies, the $\eta_{\rm ColdGas}$-estimated outflows account for the entire budget of cold gas mass loss via (RPS + outflows), meaning that the estimated RPS is null. For this sample of visually-inspected galaxies to be undergoing RPS, we conclude that this method overestimates the contribution from outflows and thereby may inaccurately determine the onset of RPS.

The increased star-formation in jellyfish galaxies during infall may be caused by the RPS-induced compression of gas, especially on the leading side (e.g., Roberts et al., 2022a). Then the star-formation-driven outflows fight against the gravity of the stellar body, making the gas more susceptible to RPS (e.g., Garling et al., 2024). In this context, separating the total RPS and outflows may be futile. Both outflows and RPS work to remove the galaxy's cold gas, the fuel for star-formation, and deposit the galaxy's ISM into the halo.

In spite of this, for the remaining 385 jellyfish galaxies with non-vanishing estimated RPS contributions, the "RPS est" onset of RPS is typically $\lesssim$ 3 snapshots ($\lesssim$ 450 Myr) later than the infall time (Fig. 7.14, top panel). The difference between this and the fiducial onset is significantly shorter than the total RPS time span, where the end of RPS is the same for both definitions (when $M_{\rm ColdGas} = 0$). Thus, when attempting to capture the entire duration of RPS, we choose infall time over the "RPS est" start as the fiducial onset of RPS.

As a second alternative, we use the specific RPS and outflows (sRPS+O), namely the cold gas mass loss due to RPS and outflows (RPS+O) divided by the total amount of cold gas $M_{\rm ColdGas}^{\rm subhalo}$. Here, the units are [time^{-1}], where the inverse yields the timescale to lose all cold gas to RPS+O (at constant RPS+O). We calculate the median pre-infall sRPS+O, and find where the sRPS+O peaks. For all 259 jellyfish without cold gas at $z = 0$, the maximum sRPS+O (shortest timescale) occurs at one of the last 3 snapshots that the galaxy has some cold gas. This peak value is typically $\sim 10^{-8}\,{\rm yr}^{-1}$, which is approximately the inverse time between snapshots $1/\Delta t_{\rm snap} \approx 1/(150\,{\rm Myr})$. Then we go backwards from this peak until the running median of the sRPS+O over $N_{\rm snaps} = 7$ ($\sim$ 1 Gyr) returns to the pre-infall average, and this time defines the onset of RPS. In Figs. 7.12, 7.13, this "RPS sRPS" onset is marked with olive ticks.

For galaxies that lose all cold gas approximately within the first orbit or by the first pericentric passage, such as the example in Fig. 7.12, the "RPS sRPS" onset is typically $\approx \pm 2$ snapshots ($\approx \pm 300$ Myr) of the infall time (Figure 7.14, top panel). While the sRPS+O generally increases between infall and pericentric passage, the sRPS+O may plateau or decrease near apocenter. Sometimes this apocentric decrease may bring the sRPS+O back to the pre-infall average. In

these cases, then the "RPS sRPS" onset occurs on the second infall, such as for the example in Fig. 7.13. This leads to a number of galaxies with "RPS sRPS" onsets significantly after infall, shown in Fig. 7.14 (bottom panel). This definition estimates that these galaxies actually undergo multiple periods of ram-pressure stripping. However for determining the entire duration of RPS, splitting the entire RPS process into multiple periods is not helpful. Thus, we choose the infall time as the onset of RPS.

8 The Cooler Past of the Intracluster Medium in TNG-Cluster

This chapter is based on the article Rohr et al. submitted., which I led as the first author and has been submitted to MNRAS, currently awaiting the referee report. I conducted the main scientific direction of the paper, performed the analysis, created the figures, and wrote the text. Additional authors and their contributions include: Annalisa Pillepich, who assisted in the scientific direction, helped organize the structure and main figures of the text, and edited the text; Dylan Nelson, who provided the Mg II *masses for all gas cells, assisted in the scientific direction, and edited the text; Mohammadreza Ayromlou, who provided valuable insights to the analysis in § 8.4 and comments to the text; Céline Péroux, who provided valuable insights to the analysis in § 8.5.2 and comments to the text; and Elad Zinger, who provided valuable insights to the analysis in § 8.4.1 and comments to the text.*

The TNG-Cluster simulation was led by PIs Dylan Nelson and Annalisa Pillepich and executed on a various machines: the HoreKa supercomputer, funded by the Ministry of Science, Research and the Arts Baden-Württemberg and by the Federal Ministry of Education and Research; the bwForCluster Helix supercomputer, supported by the state of Baden-Württemberg through bwHPC and the German Research Foundation (DFG) through grant INST 35/1597-1 FUGG; the Vera cluster of the Max Planck Institute for Astronomy (MPIA), as well as the Cobra and Raven clusters, all three operated by the Max Planck Computational and Data Facility (MPCDF); and the BinAC cluster, supported by the High Performance and Cloud Computing Group at the Zentrum für Datenverarbeitung of the University of Tübingen, the state of Baden-Württemberg through bwHPC and the German Research Foundation (DFG) through grant no INST 37/935-1 FUGG. TNG-Cluster is based on the AREPO *code and employs the TNG galaxy formation model from the IllustrisTNG team (PI: Volker Springel; additional references can be found on the TNG website here), which is a follow-up of the original Illustris simulation. Additional analysis was carried out on the Vera supercomputer from the MPCDF.*

ABSTRACT

The intracluster medium (ICM) today is comprised largely of hot gas, with clouds of cooler gas of unknown origin and lifespan. We analyze the evolution of cool gas (temperatures $\lesssim 10^{4.5}$ K) in the ICM of 352 galaxy clusters from the TNG-Cluster simulations, with present-day mass $\sim 10^{14.3-15.4}$ $M_\odot$. We follow the main progenitors of these clusters over the past $\sim$ 13 billion years (since $z \lesssim 7$) and find that, according to TNG-Cluster, the cool ICM mass increases with redshift at fixed halo mass, implying that this cooler past of the ICM id due to more than just halo growth. The cool cluster gas at $z \lesssim 0.5$ is mostly located in and around satellite galaxies, while at $z \gtrsim 2$ cool gas can also be fed by filaments from the intergalactic medium. Lower-mass clusters and clusters at higher-redshifts are more susceptible to cooling. The cool ICM mass correlates with the number of gaseous satellites and inversely with the central supermassive black hole (SMBH) mass. The average number of gaseous satellites decreases since $z = 2$, potentially explaining the decrease in cool ICM mass with cosmic time. Concurrently, strong SMBH feedback shifts the ICM temperature distribution, decreasing the cool ICM mass inside-out. At intermediate redshifts, the predicted Mg II column densities are in the ballpark of recent observations, where satellites and other halos contribute significantly to the total Mg II column density. Suggestively, a non-negligible amount of the ICM cool gas forms stars in-situ at early times, reaching $\sim 10^2$ $M_\odot$ yr^{-1} and an Hα surface brightness of $\sim 10^{-17}$ erg s^{-1} cm^{-2} arcsec^{-2} at $z = 2$, detectable with Euclid and JWST observations.

8.1 Introduction

The nature of gas in and around cluster of galaxies, the intracluster medium (ICM), is sensitive to both the cosmology and feedback processes of the cluster members, providing one of the best astrophysical laboratories for testing our theories of hierarchical structure formation and galaxy evolution. The ICM today is mostly hot at temperatures $\sim 10^{7.5-8}$ K that emit via thermal bremsstrahlung emission in the X-ray (e.g., Sarazin, 1986; Bulbul et al., 2024). The ICM is, however, not at a single temperature but instead multiphase in nature (McCarthy et al., 2004; Olivares et al., 2019). Local clusters contain reservoirs of warm $\sim 10^{5.5}$ K, cool $\sim 10^{4.5}$ K gas, and cold $\sim 10^2$ K, molecular gas, which is observable via thermal and kinetic Sunyaev-Zel'dovich effect (Mroczkowski et al., 2019), Hα filaments and nebulae (Fabian et al., 2003; Crawford et al., 2005), H I and Mg II emission and absorption in background quasar spectra (McNamara et al., 1990; Lanzetta et al., 1995; Chen et al., 1997), and molecular CO emission in both the central galaxies and in cooling filaments (Salome et al., 2006; McNamara et al., 2014; Omoruyi et al., 2024). At higher redshifts $z \gtrsim 2$, clusters and their progenitors, or protoclusters, have already assembled their hot ICM (Tozzi et al., 2022; Di Mascolo et al., 2023), which still contain multiphase gas observable as Lyα nebulae (Steidel et al., 2000; Matsuda et al., 2012), optical absorption features (Prochaska et al., 2013), and even radio emission from cold, molecular gas (Chen et al., 2024). In fact, some observations of gas cooling in local and higher redshift $z \gtrsim 1$ clusters suggest that the ICM may even be able

to cool to the point of forming stars (McNamara & O'Connell, 1989; Webb et al., 2015; Hlavacek-Larrondo et al., 2020; Barfety et al., 2022). At even higher redshifts $z \gtrsim 4$, there may exist large reservoirs of neutral gas in the proto-cluster ICM, as inferred by Lyα absorption (Heintz et al., 2024). The exact nature of cool halo gas and how it evolves with cosmic time remains largely unknown.

Cluster progenitors form in the early Universe at the strongest density perturbations in the centers of their dark matter halos. They grow by accreting material – namely dark matter, gas, and smaller satellite galaxies or subhalos – from the intergalactic medium (IGM; e.g., Springel et al., 2001, 2005b). Infalling gas is thought to be shock heated to the virial temperature of the halo, forming a hydrostatic halo supported by thermal pressure (Rees & Ostriker, 1977; Silk, 1977; White & Rees, 1978). However, halos less massive than some critical threshold mass $\sim 10^{12}\,M_\odot$ at $z \sim 2$ cannot sustain hot atmospheres (Binney, 1977; Birnboim & Dekel, 2003; Katz et al., 1991; Fardal et al., 2000). Simulations suggest that cool- or cold-mode accretion is likely the main source of growth for lower-mass halos, followed by a hot-mode accretion for higher-mass halos (e.g., Kereš et al., 2005; Dekel & Birnboim, 2006; Kereš et al., 2009; Faucher-Giguere et al., 2011; Nelson et al., 2013), although the exact details depend on numerics and baryonic feedback (van de Voort et al. 2011; Nelson et al. 2015; Mitchell et al. 2020; see also Vogelsberger et al. 2020; Crain & Van De Voort 2023 for recent reviews of galaxy formation models in cosmological simulations). Note however that these works focus on lower halo masses at the group mass scale and below, whose evolution may not be directly comparable to cluster progenitors.

There are a number of additional physical complications that impact the multiphase nature of the ICM. Hot halo gas can cool down due to thermal instabilities enhanced by local density perturbations (e.g., Sharma et al., 2012a; McCourt et al., 2012; Voit et al., 2017; Choudhury et al., 2019). For example, using the cosmological magneto-hydrodynamical (MHD) simulations from the IllustrisTNG project, Nelson et al. (2020); Ramesh et al. (2023b) show that the passage of satellites provides strong density perturbations, triggering gas cooling in the halo gas of luminous red galaxies at intermediate redshifts and in the circumgalactic medium (CGM) of Milky Way-like galaxies today. Furthermore, gaseous satellites may deposit their mostly cold interstellar medium (ISM) directly into halos, which has been ubiquitously observed in jellyfish galaxies (e.g., Cortese et al., 2006; Poggianti et al., 2017b; Roberts et al., 2021b; Cortese et al., 2021; Boselli et al., 2022) and recently suggested in cosmological simulations (Rodríguez et al., 2022; Rohr et al., 2023; Weng et al., 2024; Chaturvedi et al., 2024). We again note, however, that these numerical works have largely studied low-mass clusters and groups.

Feedback from the central supermassive black hole (SMBH) may also affect the halo baryons by redistributing gas, driving material from the central galaxy into the halo and beyond, heating the halo gas to super-virial temperatures, inducing turbulence as a form of non-thermal pressure support, and providing the perturbations to trigger gas cooling (e.g., Li & Bryan, 2014; Qiu et al., 2019; Beckmann et al., 2019; Nelson et al., 2019b; Zinger et al., 2020). Recently, the Manhattan project, a suite of ~ 100 zoom simulations of clusters with $z = 2$ mass $\gtrsim 10^{14}\,\mathrm{M}_\odot$ predict large amounts of cool, neutral gas in the proto-clusters at high redshifts $z \gtrsim 2 - 5.5$ (Rennehan, 2024; Heintz et al., 2024). Idealized MHD simulations of galaxy clusters have also shown that both SMBH feedback and magnetic fields may be important for the creation and survival of cool gas in clusters (Fournier et al., 2024; Hong et al., 2024). For the latter, there is an extensive body of literature studying a cool gas cloud in motion with respect to the ambient hot medium, that is, the cloud-crushing problem (e.g., Li et al. 2020; Sparre et al. 2020; Fielding & Bryan 2022; Gronke et al. 2022; this is typically studied from the perspective of a slow-moving cold gas cloud being accelerated by a fast wind, but the same physics applies to a cold gas cloud moving through the ICM).

In this work, we analyze the history and evolution of the ICM, concentrating on the cool gas, using the TNG-Cluster project (Nelson et al., 2024, Pillepich et al. in prep.). With its sample of 352 simulated high-mass galaxy clusters, we study the cool ICM of temperatures $\sim 10^{4-4.5}$ K (and star-forming gas), where the IllustrisTNG galaxy formation model (TNG hereafter) has already been shown to naturally produce multiphase gas in the CGM and in group-mass halos (Nelson et al., 2020, 2021; Ramesh et al., 2023a, albeit at better resolution than in TNG-Cluster). We then focus on how the total cool ICM mass and the significance of the relevant physical processes evolve across cosmic time, and on how this is connected to both internal and global properties of the clusters. Our work combines a statistical study of the cool ICM in cosmological simulations of massive galaxy clusters from the first billion years until today including magnetic fields, hierarchical structure formation and infalling satellites, and SMBH feedback from a well-tested galaxy formation model.

The remainder of the paper is organized as follows. In § 8.2 we describe the main methods, including the TNG-Cluster simulation, TNG galaxy formation model, and the cool ICM definition. In the results in § 8.3, we present the evolution of the cool ICM over the past ≈ 13 billion years, since $z \sim 7$. We then delve into the sinks and sources affecting the evolution of the cool ICM in § 8.4. In § 8.5 we discuss the observational implications of the cool ICM. Lastly in § 8.6, we summarize the main results and conclusions.

8.2 Methods

8.2.1 TNG-Cluster

TNG-Cluster[1] is a suite of 352 massive galaxy cluster simulations, spanning halo masses $M_{200c} \approx 10^{14.3-15.4}\,M_\odot$ (Nelson et al., 2024, Pillepich et al. in prep.). The technical details of TNG-Cluster are given in Nelson et al. (2024) and briefly summarized here.

The re-simulated clusters were drawn from a $\approx$ 1 Gpc box-size parent dark matter only simulation based only on $z = 0$ halo mass such that: (i) all $\approx$ 90 halos with mass[2] $> 10^{15}\,M_\odot$ are included; and (ii) halos with mass $10^{14.3-15.0}\,M_\odot$ were randomly selected such that the halo mass distribution is flat over this mass range.

The TNG-Cluster simulation employs the well-tested TNG galaxy formation model (Weinberger et al., 2017; Pillepich et al., 2018a). In short, the TNG and TNG-Cluster simulations evolve gas and cold dark matter from $z = 127$ until today, including: gas heating and cooling (including metal cooling) down to $\approx 10^4$ K; ideal MHD (Pakmor et al., 2011; Pakmor & Springel, 2013); reionization via an ultra-violet background, star formation, stellar population evolution, stellar metal return, and galactic winds (Pillepich et al., 2018a); SMBH formation, growth, merging, and feedback, where the growth and feedback are either via a high-accretion-rate thermal or low-accretion-rate kinetic mode (Weinberger et al., 2017). The simulations use the Arepo code[3](Springel, 2010b; Weinberger et al., 2020), where the fluid dynamics are discretized and solved on a moving Voronoi mesh. Star formation occurs in dense gas $> 10^{-1}\,\mathrm{cm}^{-1}$, following an effective equation of state (Springel & Hernquist, 2003); for this analysis we adopt 10^3 K as the temperature of star-forming gas.

The baryon mass resolution of TNG-Cluster is $m_{\rm bar} = 1.1 \times 10^7\,M_\odot$, the same resolution as TNG300 from the original TNG simulation suite (Pillepich et al., 2018b; Nelson et al., 2018a; Naiman et al., 2018; Marinacci et al., 2018; Springel et al., 2018). We note that the TNG galaxy formation model at TNG-Cluster mass resolution has already been at least partially validated in the low-mass cluster regime (e.g., Nelson et al., 2018a; Donnari et al., 2021a; Truong et al., 2020; Donnari et al., 2021b) and in the TNG-Cluster first results papers (Ayromlou et al., 2023a; Lee et al., 2024; Lehle et al., 2024; Nelson et al., 2024; Rohr et al., 2024; Truong et al., 2024). In this analysis we only consider high resolution particles and cells, whose masses are similar to the target masses listed below and are located in the targeted zoom regions.

We adopt the same cosmology as TNG and TNG-Cluster, consistent with the Planck Collaboration et al. (2016) results: $\Omega_{\Lambda,0} = 0.6911$, $\Omega_{\rm m,0} = \Omega_{\rm bar,0} + \Omega$dm, 0 = 0.3089, Ωbar, 0 =

[1] www.tng-project.org/cluster/

[2] In this work, we refer to the halo mass as M_{200c}, the mass enclosed by the halo radius R_{200c} such that the total average enclose density is equal to 200 times the critical density of the universe at that time.

[3] www.arepo-code.org

0.0486, $\sigma_8 = 0.8159$, $n_s = 0.9667$, and $h = H_0/(100\,\mathrm{km\,s^{-1}\,Mpc^{-1}}) = 0.6774$, where H_0 is the Hubble parameter.

8.2.2 Cluster Sample and ICM Definitions

In this work, we exclusively focus on the 352 primary zoom targets from the TNG-Cluster project. We refer to the central galaxy within each of these clusters as the brightest cluster galaxy (BCG). The galaxy stellar mass $M_\star$ is the stellar mass enclosed within twice the stellar half mass radius. We define the most massive supermassive black hole within each BCG as the main SMBH, which usually becomes the most massive SMBH in the BCG at $z = 0$.

Dark matter halos are identified using the Friends-of-Friends (FoF) algorithm with a linking length $b = 0.2$, run only using the dark matter particles (Davis et al., 1985). Then the baryonic components are connected to the same halos as their closest dark matter particle. Throughout this paper, we use "FoF group," "halo," and "cluster" synonymously. Galaxies are then identified using the SUBFIND algorithm, which identifies gravitationally bound sets of particles and cells (Springel et al., 2001; Dolag et al., 2009). We use the terms "subhalo" and "galaxy" interchangeably even though, in general, SUBFIND objects may contain no stars and-or gas whatsoever (that is, they may be composed entirely of dark matter). Typically, the most massive subhalo within a cluster is the "main" or "primary subhalo," and is called the "central galaxy" or "brightest cluster galaxy;" all other subhalos may then be considered "satellite galaxies (satellites)" or "cluster members," although at times we consider all other galaxies within a given aperture as satellites (see § 8.2.2 for more details). We follow the evolution of galaxies using SUBLINK_GAL , which constructs merger trees for subhalos by searching for descendants with common stellar particles and star-forming gas cells (Rodriguez-Gomez et al., 2015).

Throughout, by intracluster medium (ICM) gas, we mean all FoF gas within the cluster-centric aperture $[0.15,\ 1.0]\,R_{200c}$, irrespective of temperature, excluding gas gravitationally bound to satellites, but including gas bound to the BCG. By construction, we also exclude all gas that belongs to other nearby halos. We check that our results remain qualitatively similar when using instead only gas that is gravitationally bound to the BCG. The adopted BCG-ICM boundary at $0.15R_{200c}$ ensures that we do not include extended cool interstellar medium (ISM) gas in our measure of the cool ICM. Further, at distances outside the ICM-IGM boundary $> R_{200c}$, the cool gas mass tends to decrease rapidly. This remains true when including all gas in the entire zoom simulation, that is, beyond the FoF membership. We expand on the spatial extent of the cool gas in § 8.3.2.

We consider cool gas as all gas with temperatures $\leq 10^{4.5}$ K, which, by definition and construction in our galaxy formation model, includes all star-forming gas. We also use the

terms ICM and BCG at all cosmic times, while we may refer to the cluster in its entirety as a "cluster progenitor" or "protocluster" at redshifts $z > 0$.

8.3 The Cooler Past of the ICM

8.3.1 The ICM Was Cooler in the Past

In Fig. 8.1 we show the evolution of the ICM temperatures: according to TNG-Cluster, the cluster progenitors had more cool gas, larger cool ICM to total halo mass fractions, and larger cool ICM to total ICM mass fractions than their descendants today.

More specifically, in the main panel of Fig. 8.1, for each cluster of present-day mass $\sim 10^{15}\,\mathrm{M}_\odot$ (51 clusters), we plot the gas mass distribution of ICM temperatures as thin curves, colored by redshift. We include the cluster-wide medians at each redshift as thick curves. All FoF gas in the aperture $[0.15R_{200c}, R_{200c}]$, excluding satellites, constitutes the ICM (see §8.2.2), and we define cool gas to be all gas with temperatures $\leq 10^{4.5}$ K (§8.2.2), denoted by the shaded region.

Today at $z = 0$ for clusters of mass $M_{200c} \sim 10^{15}\,\mathrm{M}_\odot$, the majority of the ICM is hot at temperatures $\approx 10^{7.5-8}$ K ($kT \approx 3 - 9$ keV), approximately at the virial temperature and primarily heated via shocks when the gas was accreted (White & Rees, 1978). The position of this peak at the virial temperature depends on the cluster mass $T_{\rm vir} \propto M_{200c}^{2/3}$. As the halo mass grow, so do its gravitational potential well and the amount of gravitational potential energy that accreting gas converts into thermal energy. In the inset, we show how the $z = 0$ ICM temperature distribution varies with cluster mass. The virial temperature and gas mass at this temperature increase with cluster mass, as expected.

At super-virial temperatures $\gtrsim 10^8$ K, the gas radiates efficiently via free-free bremsstrahlung emission, and the gas mass at these temperatures decreases exponentially. The other features of the ICM temperature distribution depend largely on the cooling function, which is only indirectly related to halo mass. At sub-virial temperatures $\sim 10^{5-7}$ K, in addition to bremsstrahlung radiation, the gas can cool via recombination and metal cooling, where the relative importance of the latter increases with increasing gas metallicity and decreasing halo mass. At cooler temperatures there are two peaks in the distribution at $\approx 10^{4.2}$, $10^{4.8}$ K where cooling via bound-bound collisional excitation of atomic Hydrogen H I and singly ionized Helium He II dominate the cooling function respectively. Then, due to the TNG cooling floor at temperature 10^4 K, there is no ICM of lower temperatures, except for the star-forming gas, which we manually place at 10^3 K (offset slightly for visibility; see § 8.2.1, 8.5.1 for details).

At higher redshifts, along the progenitors of the simulated clusters, the position of the hot, virial temperature peak moves to cooler temperatures, partly because the halo masses were

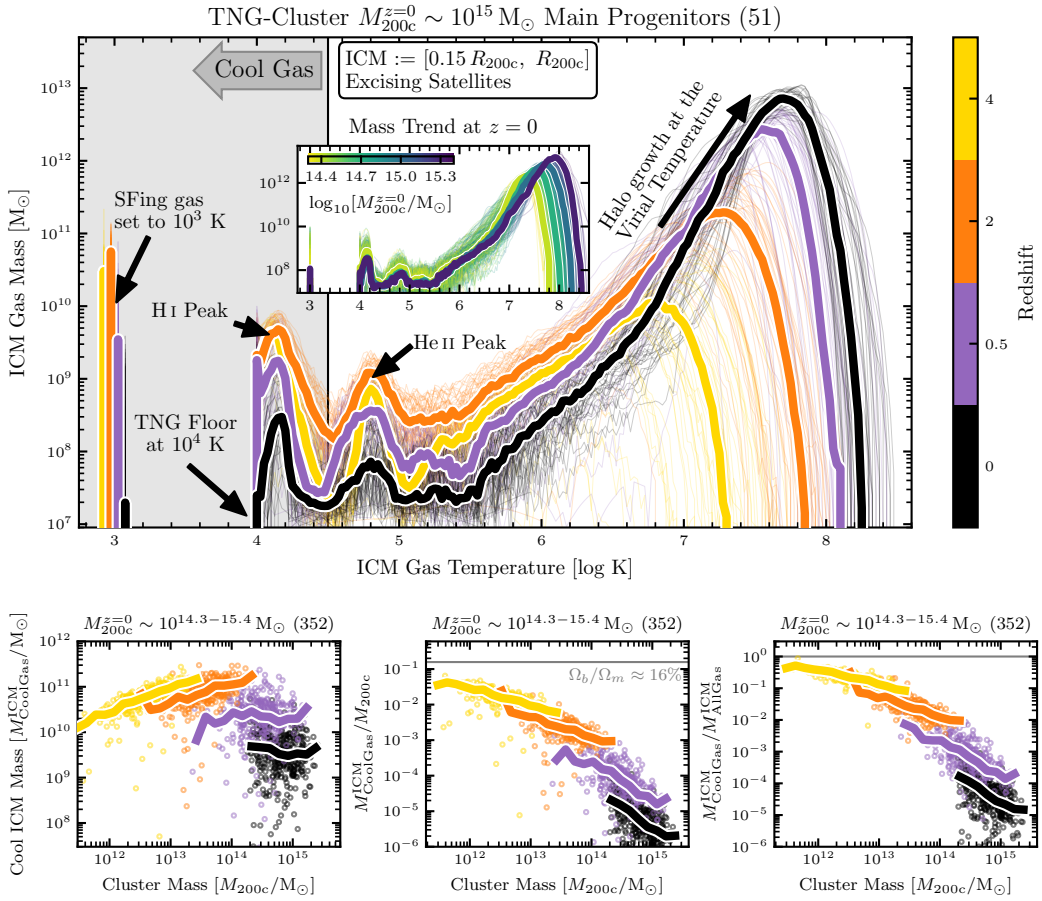

Figure 8.1: **The evolution of the ICM temperatures, cool gas masses, cool ICM to total halo, and cool ICM to total ICM mass fractions in TNG-Cluster since $z = 4$.** The ICM is all FoF gas in the aperture $[0.15, 1.0]R_{200c}$, excising satellites. Cool gas has temperatures $\leq 10^{4.5}$ K. *Main Panel*: The distribution of ICM temperatures of each cluster of $z = 0$ mass $\sim 10^{15}$ M$_\odot$ (51 clusters) as thin curves and the median of this sample as thick curves, where the color denotes the redshift. In the inset we show how the ICM temperature distribution varies with cluster mass today. We label prominent features in the ICM temperature distribution (see text for details; we offset the star-forming gas temperatures slightly for visibility). *Bottom Panels*: The cool ICM mass (left), cool ICM to total cluster (center), and cool ICM to total ICM (right) mass fractions as functions of cluster mass and redshift for all 352 clusters in TNG-Cluster. We plot each cluster as circles and the median trend with mass as thick curves, colored by redshift. According to TNG-Cluster, the ICM of cluster progenitors were cooler, having more total cool gas, cooler average temperatures, and a larger ICM mass fraction in cool gas.

smaller in the past. The relative amplitude of this peak, however, decreases due to both halo growth and an increased ability for cool gas to exist in the ICM. Despite the cluster progenitors having on average lower ICM metallicities (not shown), a larger fraction of their ICM is at sub-virial temperatures ($\lesssim 10^7$ K) in comparison to their descendants, implying that gas is cooling more efficiently. This increased cooling efficiency at higher redshift comes from the average increased density of Universe at earlier times, as the gas cooling time decreases with density – we extensively expand upon this in § 8.4.1. Additionally both the absolute and relative amplitudes of the peaks at H I and He II increase with redshift.

Is a dependence of cool ICM mass ($M^{\rm ICM}_{\rm ColdGas}$) with cluster mass $M_{\rm 200c}$ and redshift expected? In the bottom left panel of Fig. 8.1, we plot all 352 clusters (circles) and the median trend with mass (thick curves) at four example redshifts (color). For the $z = 0$ clusters, there is little to no trend in $M^{\rm ICM}_{\rm ColdGas}$ with cluster mass, and the clusters host on average $\sim 10^{9.5}$ M$_\odot$ of cool ICM. At $z = 0.5$, there is again an approximately flat trend with mass, but the normalization is now higher at $\sim 10^{10}$ M$_\odot$. At higher redshifts $\gtrsim 2$, the cool ICM mass increases with halo mass. Between redshifts $\sim 2 - 4$, the power law index (slope in the log-log plot) of $M^{\rm ICM}_{\rm ColdGas}$ as a function of $M_{\rm 200c}$ remains approximately constant, but the normalization still increases with redshift. That is, while a protocluster of mass $M_{\rm 200c} \sim 10^{13}$ at $z \approx 2$ has $\sim 10^{10.5}$ M$_\odot$ of cool gas in the ICM, at $z \approx 4$ a similar mass cluster has $\sim 10^{11}$ M$_\odot$ of cool ICM. We speculate that at these early times while the BCGs are largely still star-forming, their gaseous atmospheres have not yet been significantly affected by kinetic mode feedback from the central SMBH, which could either heat up cool or prevent the cooling of hot ICM; see § 8.4.3 for a discussion on this.

The cool ICM to total halo fraction is quantified in Fig. 8.1, bottom center, where we include the global baryon fraction $\Omega_b/\Omega_m \approx 0.16$ for reference (gray line; constant with redshift). At all redshifts and masses considered, the cool ICM fraction decreases with cluster mass. At low redshift $\lesssim 0.5$, the flat cool ICM mass trends with cluster mass (bottom left) translate to power law indices of the cool ICM fraction trends of ≈ -1, where the normalization also decreases with redshift. That is, a cluster of mass $\sim 10^{15}$ M$_\odot$ at $z = 0$ has a cool ICM to total halo fraction of $\sim 10^{-5.5}$, while at $z = 0.5$ a similar mass cluster has a fraction of $\sim 10^{-5}$. At higher redshifts $z \gtrsim 2$, slopes of the cool ICM fraction trends are still negative but flatter than those at lower redshifts, a reflection of the positive cool ICM mass trend at these redshifts (bottom left). The slopes are similar at redshifts $\sim 2 - 4$, but the normalization increases with redshift. A protocluster of mass $\sim 10^{13}$ M$_\odot$ at redshift ~ 2 has a cool ICM to total halo fraction of $\sim 10^{-2.5}$, while a similar mass cluster at $z = 4$ has a fraction of $\sim 10^{-2}$. The lowest mass protoclusters considered here – $M_{\rm 200c} \sim 10^{11.5}$ M$_\odot$ at redshift ~ 4 – have cool ICM to

total halo fractions $\sim 10^{-1}$, meaning that ≈ 60 per cent of the baryons within the cluster are in the cool ICM.

Lastly we examine the fraction of ICM that is cool (Fig. 8.1, bottom right), where we mark where the fraction is one, where the entire ICM is cool (gray line). At all redshifts, the cool to total ICM mass fraction decreases with halo mass with similar power law indices, but the normalizations increase with redshift. A cluster of mass $\sim 10^{15}\,\mathrm{M}_\odot$ today has only 10^{-5} of its total ICM in the cool phase, while a similar mass cluster at redshift ~ 0.5 has $\sim 10^{-4}$ of its ICM in the cool phase. The ICM in the lowest mass protoclusters considered here at $\sim 10^{11.5}\,\mathrm{M}_\odot$ at redshift ~ 4 is ≈ 50 per cent cool.

To summarize, according to TNG-Cluster, at a fixed cluster mass, clusters had more cool gas in their ICM at earlier times. While smaller clusters have cooler virial temperatures and a higher fraction of ICM in the cool phase, the conditions at higher redshifts were more conducive for either cooling hot ICM and-or maintaining cool ICM.

8.3.2 The Cool Cluster Gas Across Space and Time

We show in Fig. 8.2 the cool gas density radial profiles, normalized by the virial radius R_{200c} at the given redshift (see Appendix 8.7 for different normalizations). Here we show clusters of $z = 0$ mass $\sim 10^{15}\,\mathrm{M}_\odot$ (51 clusters, thin curves; see Appendix 8.8 for the trend with halo mass today) and the median of this sample at each redshift (color). We label the regions of interest and their definitions for this work: BCG at distances $< 0.15R_{200c}$; ICM in the aperture $[0.15R_{200c},\ R_{200c}]$; and IGM at distances $> R_{200c}$. These present-day clusters have on average little cool gas in their BCGs, reflecting the lack of cool gas available to, for example, form stars as a majority of the BCGs in TNG-Cluster are quenched at $z = 0$ (Nelson et al., 2024). In the cluster outskirts at $\gtrsim R_{200c}$, the cool gas density begins to drop exponentially. We note that cool gas profile still drops exponentially when including all gas in the simulation.

At higher redshifts, the cool gas density at a fixed cluster-centric distance increases at all distances. Especially at redshifts $\gtrsim 2$, there is a significant amount of cool gas within the BCG at distances $< 0.15R_{200c}$, agreeing with expectations that the cluster cores tend to be more cool-cored with increasing redshift (Lehle et al., 2024). Additionally, the cool gas densities are higher than what would be expected from the cosmic evolution, which scales as $\propto (1+z)^3$, affirming that the conditions for cool gas are more conducive at higher redshifts. These results motivate our fiducial definition of the ICM: all FoF gas in the aperture $[0.15R_{200c},\ 1.0R_{200c}]$ that is not bound to satellites. We note that in general, the ICM extends beyond the virial radius. Especially at later times $z \lesssim 1$, the shock radius is likely located beyond the virial radius (e.g., Birnboim & Dekel, 2003; Voit et al., 2003; Zinger et al., 2018a), and satellite stripping

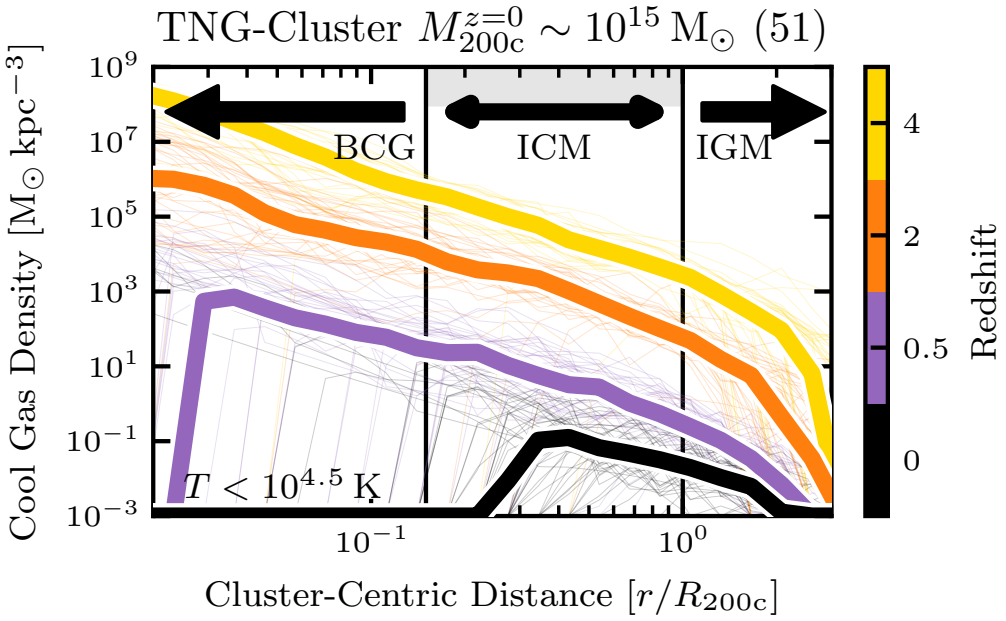

Figure 8.2: **The evolution of the cool gas radial profiles in TNG-Cluster since $z = 4$.** We plot the cool gas density radial profiles of the 51 clusters with present-day mass $\sim 10^{15}\,M_\odot$ (thin curves) and the medians of this sample (thick curves), where the color denotes redshift. We normalize the radial profiles by the virial radius R_{200c} at that redshift. At all redshifts and cluster-centric distances considered, the cool gas density increases with redshift. Outside of the adopted ICM-IGM boundary at R_{200c}, the cool gas densities begin to drop exponentially.

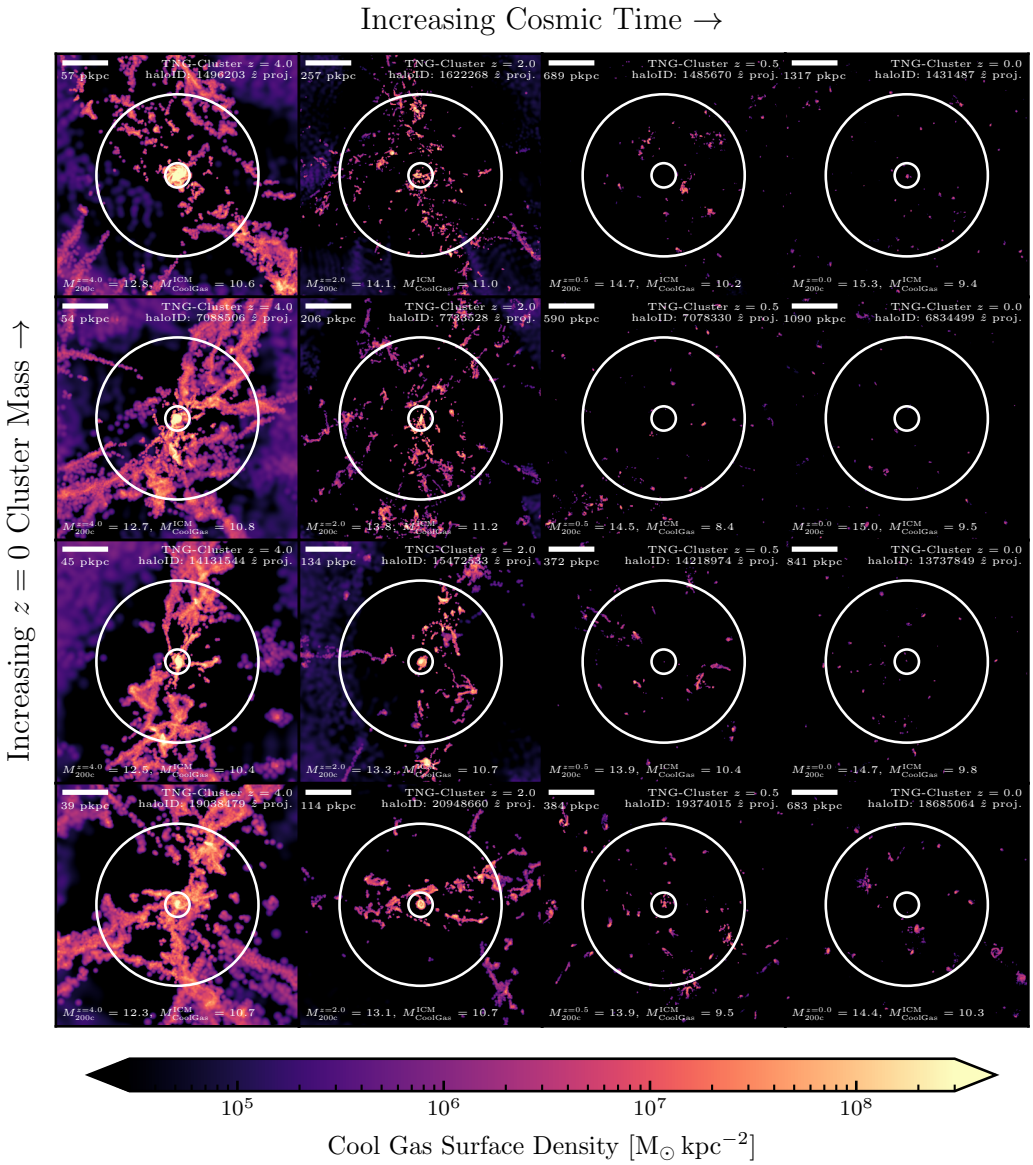

Figure 8.3: **Examples of the cool gas surface density as functions of cosmic time and cluster mass in TNG-Cluster systems.** Each panel shows the total cool gas (temperature $\leq 10^{4.5}$ K) surface density, including the BCG and potential satellites, within a cube of $3R_{200c}$ centered on the BCG, where we project the gas cells using a cubic spline of variable kernel size according to the gas cell size. The white circles mark the adopted BCG-ICM and ICM-IGM boundaries at $0.15R_{200c}$, R_{200c}, and the scale in the upper-left is $0.5R_{200c}$ in size. We include the halo ID at the given redshift in the top right, and the halo M_{200c} and cool ICM mass $M^{\rm ICM}_{\rm ColdGas}$ at each redshift in the lower-left in units of [$\log_{10}$ $M_\odot$]. Each row shows the evolution of an individual cluster, and each column shows the mass trend at a fixed redshift. According to TNG-Cluster, at all halo masses, clusters tends to have less cool gas today than at earlier times.

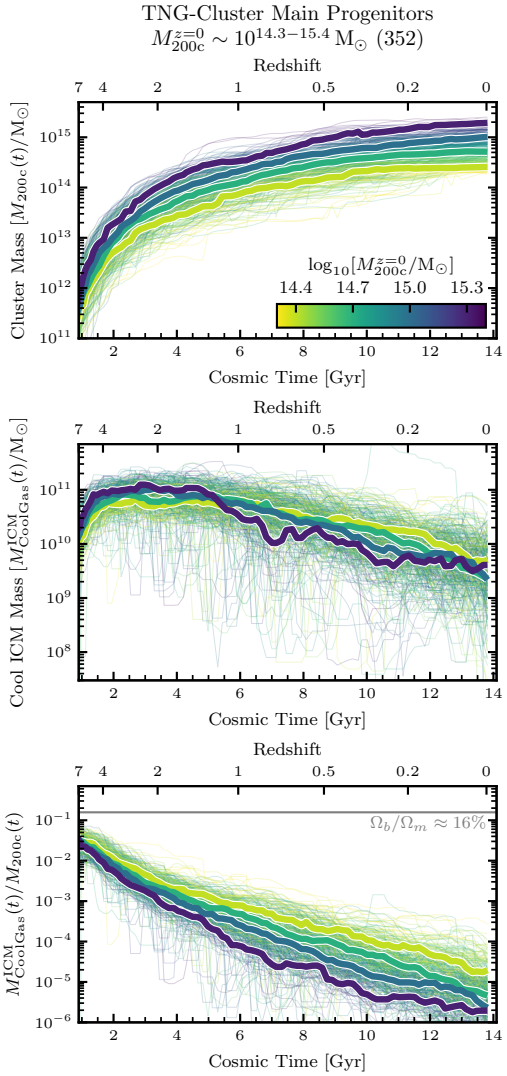

Figure 8.4: **The evolution of individual clusters and their cool ICM since $z = 7$.** For all 352 clusters in TNG-Cluster we plot the evolution of the cluster mass M_{200c} (top panel), cool ICM mass $M_{\rm ColdGas}^{\rm ICM}$ (center panel), and cool ICM to total halo mass fraction (bottom panel) as thin curves colored by their $z = 0$ cluster mass, and we include the median evolutionary trends at a fixed $z = 0$ cluster mass (thick curves). The cool ICM mass and cool ICM to total halo fraction curves are averaged over five snapshots, corresponding to ≈ 750 Myr. While the cool ICM mass and cool ICM to total halo fraction for individual clusters (center and bottom panels) evolve in a complicated manner, increasing or decreasing by more than an order of magnitude at times, the median trends show an average decrease in cool ICM mass and cool ICM to total halo fraction since $z \lesssim 4$, according to TNG-Cluster.

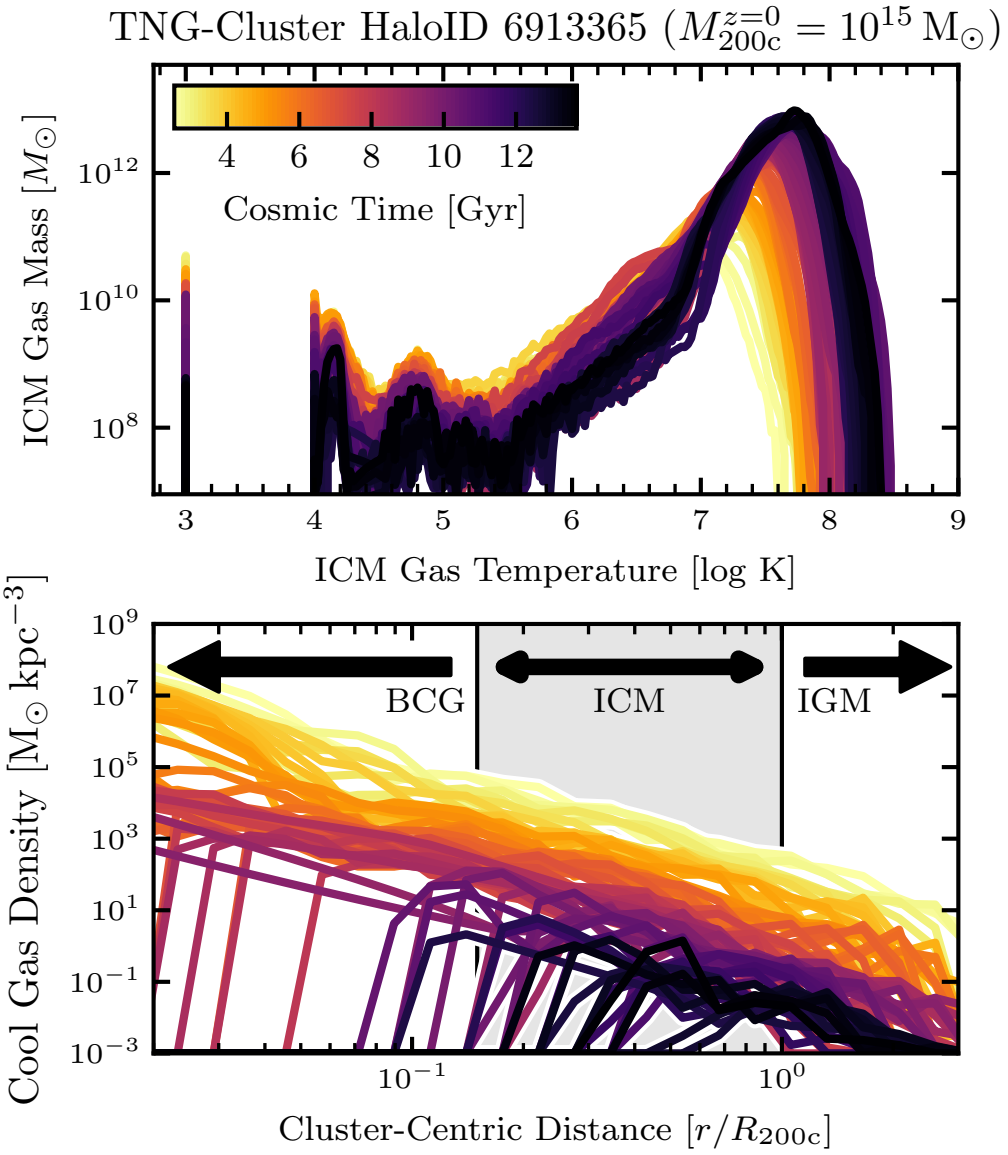

Figure 8.5: **Evolution of the ICM temperatures and external cool gas profile for an example halo from TNG-Cluster.** We plot the evolution of the ICM temperature distribution (top panel) and external cool gas radial profile (bottom panel) for an example cluster of $z = 0$ mass $\sim 10^{15}$ M$_\odot$. Over the past ≈ 10 billion years, the hot ICM mass near the virial temperature increases while the cool gas density decreases at all radii, but with more evident suppressions proceeding inside-out.

likely begins outside of the virial radius (e.g., Bahé et al., 2013; Ayromlou et al., 2021b; Rohr et al., 2023; Zinger et al., 2024).

Studying the evolution of individual objects allows us to better understand the population trends across redshift. In Fig. 8.3 we show the cool gas surface density for four example individual clusters (rows) at four example redshifts (columns). Each image includes all cool gas, including the BCG and satellites, within a cube of $3R_{200c}$ centered on the BCG, where we project the gas surface density using a cubic spline of variable kernel size according to the gas cell size. The white circles mark the BCG-ICM and ICM-IGM boundaries at $0.15R_{200c}$, R_{200c} respectively, and the scale in the upper-left is $0.5R_{200c}$ in size. For each of the example clusters, their high redshift $z \gtrsim 2$ progenitors had more cool gas than their descendants today. Especially at $z = 4$, large scale cool filaments are present and directly feeding cool gas into the ICM, where no such cool filaments are present at later times $z \lesssim 0.5$, as expected (e.g., Zinger et al., 2016; Birnboim et al., 2016). Many gaseous satellite galaxies are visible at all redshifts, but at $z \sim 4$ many satellites are co-spatial with the cool filaments. The BCGs at these high redshifts are largely still star-forming, and there are morphological signs of cool gas disks in these protoclusters. At a fixed time, the cool gas maps have qualitatively similar morphologies across cluster masses. At $z \gtrsim 2$, the total cool ICM, excluding satellites, increases with cluster mass, while at later times there is no trend with cluster mass (see also § 8.3.1).

From individual systems to the whole population, Fig. 8.4 shows the evolution of the cluster mass M_{200c} (top panel), cool ICM mass $M^{\rm ICM}_{\rm ColdGas}$ (center panel), and cool ICM to total halo mass fraction (bottom panel) since $z = 7$ of all 352 clusters (thin curves) colored by their $z = 0$ mass. The median trends at a fixed mass are given with thick curves. The cool ICM mass and cool ICM to total halo fraction curves are averaged over five snapshots ≈ 750 Myr. While the evolution of individual cluster masses (top panel) may be complex, involving discrete jumps in mass likely due to merger events, the median trends in TNG-Cluster smoothly and monotonically increase with time. Generally more massive clusters today tend to be more massive at all times. Therein, more massive $z = 0$ clusters tend to reach a given characteristic halo mass at earlier times; for an example characteristic halo mass at 10^{13} $M_\odot$, a massive cluster of mass $\sim 10^{15.3}$ $M_\odot$ today was already at this mass by redshift ≈ 4, while a less massive $z = 0$ cluster of mass $\sim 10^{14.3}$ $M_\odot$ reached this mass at $z \approx 3$, ~ 1 Gyr later.

The evolution of the cool ICM mass (center panel) and cool ICM to total halo mass fraction (bottom panel) are more complex. At early times $z \gtrsim 4$, clusters were gaining more cool gas with time. At $z \sim 2 - 4$ the average cool ICM mass is maximum for all clusters, interestingly corresponding with the peak of cosmic star formation. At a fixed time here, more massive protoclusters have more cool gas in their ICM than lower mass ones (see also Fig. 8.1, bottom left panel). At $z \lesssim 2$, the cool ICM masses tend to decrease with time. We note that the

median curve of the most massive clusters today ($M_{200c} \sim 10^{15.3}\,M_\odot$) is lower than, but within the scatter of, the trends for the other mass bins, and this population has the lowest number statistics. In individual systems, the evolution of the cool ICM may be much more complicated. Many clusters show large jumps the cool ICM mass and thereby the cool ICM to total halo mass fraction (bottom panel) by one to two orders of magnitude, before potentially returning to the average value. For the cool ICM to total halo mass fraction (bottom panel), the median fractions decrease with time since $z \sim 4$. At all times since $z \sim 4$, but especially so at later times $z \lesssim 2$, more massive (proto) clusters have lower cool gas to total mass fractions (see also Fig. 8.1, bottom center).

Lastly in Fig. 8.5, we demonstrate how the distribution of ICM temperatures (top panel) and the cool gas density radial profile (bottom panel) evolve for an individual system. With cosmic time, both the amplitude and the position of the hot gas peak near the virial temperature increase. Simultaneously the ICM mass decreases at all cool temperatures $\lesssim 10^{4.5}$ K. At all radii considered, the cluster exhibits less cool gas with cosmic time, and more prominently so in the inner regions of the ICM or BCG. The cool gas density profiles approximate power laws in the BCG and ICM at earlier times, before declining exponentially in the IGM. With increasing cosmic time, the cool gas density decreases to below the TNG-Cluster resolution limit and it does so in an inside-out fashion: this suggests that processes in the BCG may be crucial for determining the cool ICM content.

8.4 Why Was There More Cool Gas in the Past?

The growth and evolution of galaxy clusters is the result of hierarchical structure formation convolved with baryonic physics and galactic feedback. In Fig. 8.6 we visualize the complexity and inter-connectedness of these various processes with the goal of understanding not only how the cool ICM mass changes with time, on non-cosmological time scales, but also why it ubiquitously decreases over the past $\sim$ 10 billion years (see also Péroux & Howk 2020; Donahue & Voit 2022 for recent reviews of the cosmic baryon cycle).

In particular, in Fig. 8.6, we plot the mass-weighted temperature map of an example protocluster at $z = 4$ from TNG-Cluster, including all gas within a cube of $3R_{200c}$ centered on the BCG and projected using a cubic spline kernel, where the annotations are as in Fig. 8.3. Throughout the cluster and its environment there are complex, multiphase structures. In the following, we list and describe sources and sinks of cool gas in the ICM, noticing that its amount can change due to both mass fluxes across the ICM "boundaries" (at fixed cool gas temperature) as well as changes in temperature (at a fixed spatial location). Once we identify the physical processes that may affect the production, destruction, or survival of cool gas in the

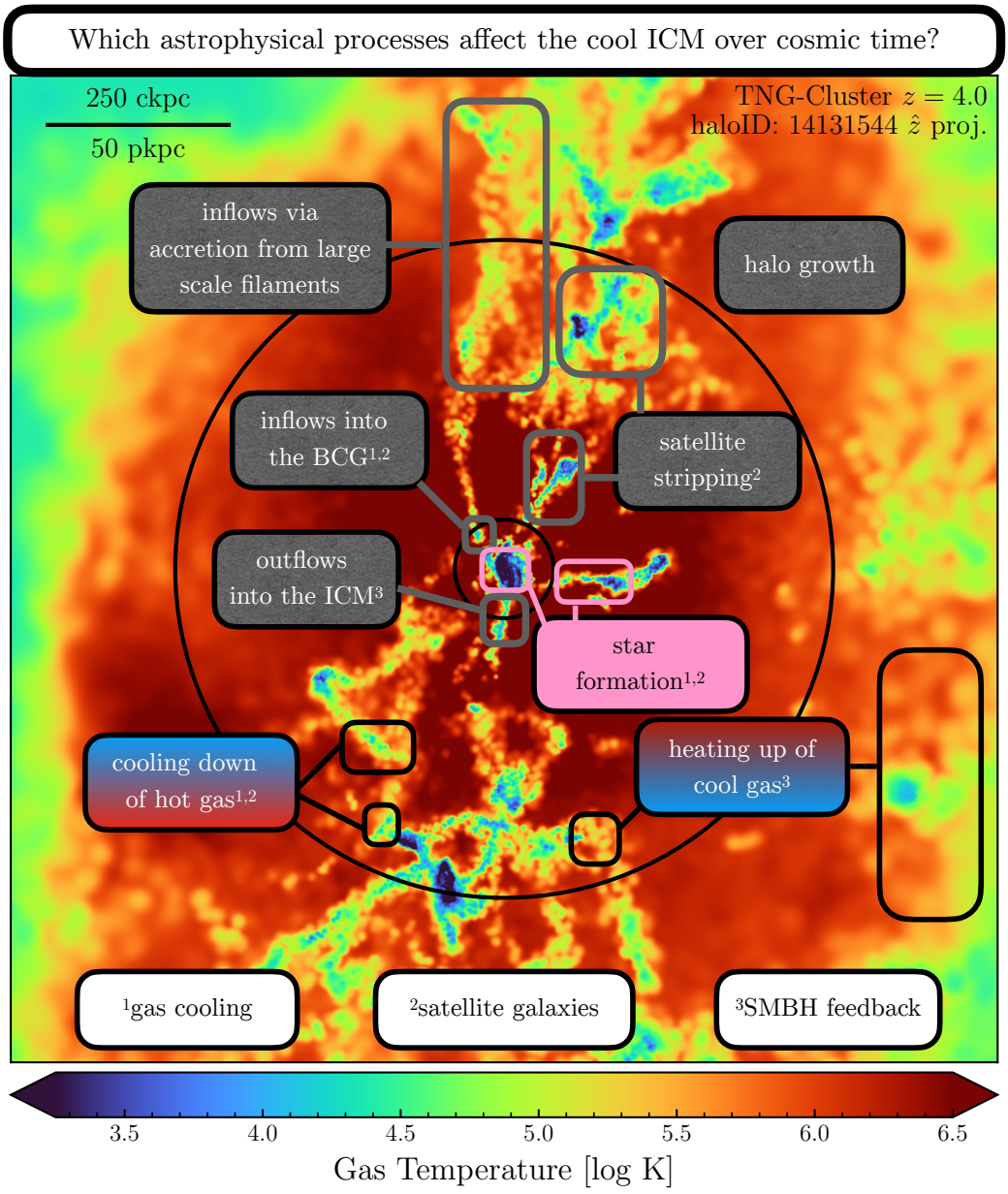

Figure 8.6: **Schematic detailing the physical mechanisms responsible for the amount of cool ICM.** We plot the mass-weighted temperature map of an example protocluster at $z = 4$, including all gas within a cube of $3R_{200c}$ using a cubic spline kernel. The annotations are as in Fig. 8.3. We label the various ways – namely fluxes at a fixed gas temperature (gray) and changes of gas phase at a fixed spatial location (blue-red and pink) – in which the cool ICM mass can change and ascribe the dominant astrophysical phenomena (bottom, numbered) responsible for either the production, destruction, or survival of cool gas on non-cosmological time scales. Many of these processes are interconnected and their relevant importance change with redshift; see text for details.

otherwise hot ICM, we assess whereas, and how, the prevalence of such individual processes may change across cosmic epochs as clusters assemble and evolve.

Halo growth and cool ICM. First, halo growth is disfavorable for the cool ICM. As shown in Figs. 8.1, 8.4, and 8.5, the amount of cool ICM decreases as clusters grow, because of their growth in mass. The mode of the temperature distributions at the virial temperature increases with halo mass and time, which then increases the temperature contrast between the volume filling hot gas and the cooler gas clouds: this decreases the chances of cool gas survivability (e.g., Sparre et al., 2020; Fielding & Bryan, 2022).

Mass fluxes of cool gas in the outer regions. Clusters do not grow in isolation nor in the absence of galactic feedback. Therefore, both the cosmological growth of structure and galaxy evolution processes can potentially affect the ways in which the cool ICM mass change via cool gas fluxes at the ICM spatial boundaries. Here we firstly consider the ICM-IGM boundary. Large scale filaments, which are visible in the figure as elongated structures of cool gas (see also Fig. 8.3, especially the left-most columns), can channel cool gas from the ICM into the IGM, at times even directly into the BCG. As described in the introduction, the clusters likely grew by accreting cool gas at high redshifts $\gtrsim 2$ and hot gas at lower redshift $\lesssim 2$. That is, this source of cool gas at high redshifts is much less prominent at lower redshifts, where clusters progenitors at $z = 2$ had $\approx 100\times$ higher cool gas accretion rates than their descendants today, according to TNG-Cluster (see also Fig. 8.3, right-most columns). According to our analysis of the simulated systems, many satellite galaxies are also located co-spatially to these filaments, and in general, it is expected that satellites tend to accrete along filaments rather than spherically (e.g. Fielding et al., 2020; Kuchner et al., 2022). We return to the role of satellite galaxies below in § 8.4.2. In the other direction, according to modern simulations of clusters including feedback, cool gas can also leave the ICM in the form of outflows driven by SMBH or stellar feedback, most prominently originating within the BCGs. At $z = 0$, the clusters have little outflowing gas going into the ICM, and the outflowing gas that does exist tends to be hot (Ayromlou et al., 2023b,a). At lower host masses both today and in the past for the cluster progenitors, the stellar- and SMBH-driven outflows in the TNG model can extend beyond R_{200c}, but the outflows tend to be shock heated (Weinberger et al., 2017; Nelson et al., 2019b; Pillepich et al., 2021). We check that the cool gas outflow rates at R_{200c} are on average $\lesssim 10^{-1}\,\mathrm{M}_\odot\,\mathrm{yr}^{-1}$ at all studied cluster masses and redshifts in TNG-Cluster.

Mass fluxes of cool gas in the inner regions. According to TNG-Cluster and the TNG model in general, there can be a cool gas flux also at the BCG-ICM boundary at $0.15R_{200c}$ (e.g.

Nelson et al., 2019b). Feedback from the SMBH in kinetic mode and from supernovae in the form of galactic winds can drive cool gas outflows out of the innermost galaxy regions. However, within the TNG model, as the gas is pushed outwards, it also heats up via shocks before reaching the ICM (Weinberger et al., 2017; Pillepich et al., 2021). Conversely, cool gas may return to the BCG via galactic fountains or precipitation onto the BCG, acting as fuel for star formation (Fraternali & Binney, 2008; Voit et al., 2015). A majority of the BCGs of TNG-Cluster are still star-forming at high redshift $z \gtrsim 3$, while the opposite is true today (Nelson et al., 2024). Thereby, while some cool gas falls onto the BCG at early times, this becomes negligible at later times, at least partially contributing to the decrease in the cool ICM mass since $z \lesssim 4$.

In-situ changes of gas temperature. Within the ICM itself – assuming no gas fluxes – gas can change phase in three distinct ways: (i) hot gas can cool down; (ii) cool gas can heat up; or (iii) cool gas can form stars. We return to the ICM in-situ star formation in § 8.5.1. Gas cooling and heating are affected by multiple factors: as halos and their virial temperatures grow with time, it becomes both more difficult for cool gas to survive in the hotter environments and more difficult for hot gas to cool down. In fact, hot gas may cool into cold clouds (e.g. Sharma et al., 2012a,b; Voit et al., 2017). That is, a cool phase may condensate out of a hot medium via thermal instabilities, facilitated by density perturbations, which in turn may eventually rain down onto the BCG (Voit et al., 2015; Voit, 2021). In a cosmological context, density perturbations could be caused by the passage of satellites (Nelson et al., 2020; Fielding et al., 2020; Ramesh et al., 2023b), and satellites can directly deposit their cool ISM into the ICM via ram pressure stripping (e.g., Nelson et al., 2020; Rodríguez et al., 2022; Rohr et al., 2023; Saeedzadeh et al., 2023). At the same time, in a galaxy evolution context, feedback from the central SMBH of the BCG (or other massive cluster galaxies) can both directly heat up cool gas (see above) or increase the cooling time of the hot ICM (Truong et al., 2020; Zinger et al., 2020). In fact, SMBH driven outflows could also create density perturbations and facilitate cooling.

In the remainder of this analysis, we use TNG-Cluster to further and explicitly quantify the thermal instability cooling framework in the ICM in a full cosmological context (§ 8.4.1) and to evaluate and highlight the role of satellites and the effects of SMBH on the cool ICM (§ 8.4.2 and § 8.4.3, respectively).

8.4.1 The Decreasing Importance of ICM Cooling Towards $z = 0$

An important source of cool halo gas is the cooling of the ambient, volume-filling hot gas. When the cooling time $t_{\rm cool}$ compared to the dynamical free-fall time $t_{\rm ff}$ drops below some

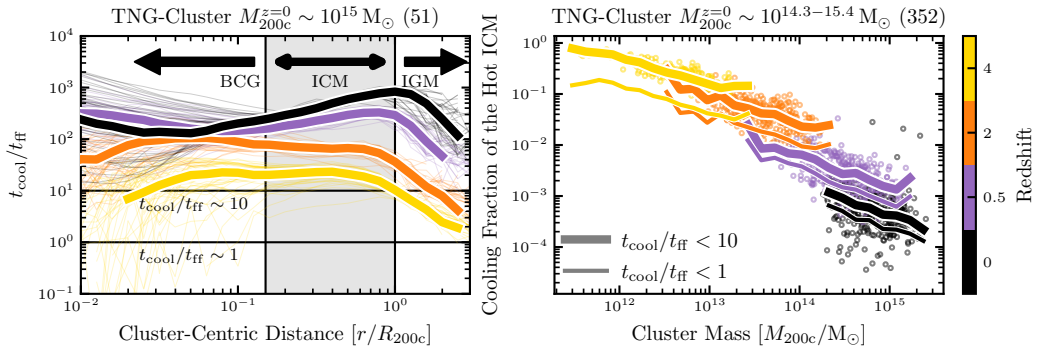

Figure 8.7: **The ICM in TNG-Cluster progenitors was more prone to cooling in the past.** We examine the ability of the hot ICM (in the aperture $[0.15R_{200c}, R_{200c}]$ with temperatures $> 10^{4.5}$ K, excising satellites) to cool, using the canonical criterion of cooling to free-fall ratio $t_{cool}/t_{ff} < 10$ as a proxy for cooling gas. *Left panel*: We plot the radial azimuthally averaged profile of the cooling to free-fall time for the 51 systems from TNG-Cluster with $z = 0$ mass $\sim 10^{15}$ $M_\odot$ (thin curves) and the medians of this sample (thick curves), where the color denotes redshift. We normalize the radial profiles by the virial radius R_{200c} at that redshift. We include horizontal lines at the classical (catastrophic) cooling to free-fall ratios $t_{cool}/t_{ff} \sim$ (1) 10. The average cooling to free-fall ratio in the ICM increases with cosmic time, meaning that the ICM is less susceptible to cooling today than it was in the past. *Right panel*: The mass fraction of the hot ICM that is susceptible to cooling, with cooling to free-fall time < 10, for all clusters in TNG-Cluster (circles) as a function of cluster mass and redshift, where we include the median trend with mass as thick curves. We also mark the median trend of the fraction of ICM with cooling to free-fall time < 1 as thin curves. At a fixed redshift, the cooling fraction of the hot ICM decreases with cluster mass; at a fixed cluster mass, the cooling fraction increases with redshift.

threshold, the hot gas will tend to cool faster than it can be re-heated by the surrounding medium. Expressions for the cooling and free-fall times are

$$t_{\rm cool} = \frac{3}{2}\frac{(n_e + n_i)k_b T}{n_e n_i \Lambda_{\rm cool}} \tag{8.1}$$

$$t_{\rm ff} = \left(\frac{3\pi}{32 G \rho_{\rm tot}(<r)}\right)^{1/2} \approx \sqrt{2}\left(\frac{2r^3}{G M_{\rm tot}(<r)}\right)^{1/2} \tag{8.2}$$

where n_e, n_i are the electron and ion abundances, $k_b T$ is the thermal energy, $\Lambda_{\rm cool}$ is the instantaneous note cooling rate, G is the gravitational constant, ρ is the average total internal density, and $M_{\rm tot}(<r)$ is the total internal mass. Thereby, the cooling time is a local measurement that depends on the properties of the gas, whereas the free-fall time is spherically averaged and depends only on cluster-centric distance. A canonical criterion for gas cooling is $t_{\rm cool}/t_{\rm ff} < 10$ (e.g., Sharma et al., 2012a; Voit et al., 2017), whereas catastrophic cooling or cooling in the presence of gravity can occur when $t_{\rm cool}/t_{\rm ff} < 1$ or < 10, respectively (McCourt et al., 2012). In fact, such a threshold can be higher in the presence of large local density perturbations (Choudhury et al., 2019). In the following we consider gas fulfilling the $t_{\rm cool}/t_{\rm ff} < 10$ criterion to be susceptible to cooling, although in general, not all hot gas with $t_{\rm cool}/t_{\rm ff} > 10$ may cool and with $t_{\rm cool}/t_{\rm ff} < 10$ may not cool (Choudhury et al., 2019; Saeedzadeh et al., 2023).

Because the cooling time is proportional to the inverse of the gas density and the free-fall time to the inverse square root of the total density, gas becomes more susceptible to cooling if the local and-or the global density increases. The global density increases with redshift as $\rho \propto (1+z)^3$, meaning that in general, $t_{\rm cool}/t_{\rm ff} \propto (1+z)^{-3/2}$ and global cooling is more efficient at higher redshifts. Additionally, the local density can be perturbed, for example, by the passage of satellites or by the presence of already existing over-dense, cool gas clouds (e.g., Nelson et al., 2020; Fielding et al., 2020; Ramesh et al., 2023b). Perhaps these perturbations occurred more frequently at higher redshift (see § 8.4.2).

In Fig. 8.7 we examine the ability for the ICM to cool across cosmic epochs. We plot the mass-weighted cooling to free-fall time radial profile for all TNG-Cluster systems with $z = 0$ mass $\sim 10^{15}\,{\rm M}_\odot$ (51 clusters; left panel) as individual curves colored by redshift. We include the median curve at each redshift as thick curves and mark both the adopted ICM region and the canonical cool criteria. Here, we only consider hot gas with temperatures $> 10^{4.5}$ K that is cooling $\Lambda_{\rm cool} < 0$. In the ICM, the average cooling to free-fall time decreases with redshift, showing that the higher-redshift ICM is in fact more susceptible to cooling, as expected. That is, at a cluster centric radius $\sim 0.5 R_{\rm 200c}$, the average cluster today has cooling to free-fall time ratio of $\sim 10^{2.5}$ while a proto-cluster may have ~ 20, more than order of magnitude lower. However, the average ratios (averaged both across clusters and spherically within each cluster)

are always (or typically) at $t_{\rm cool}/t_{\rm ff} > 10$, suggesting that on average the ICM is in fact not cooling significantly. At lower host masses $\sim 10^{12.5-14}$ $M_\odot$ the cooling to free-fall time ratio in the CGM tends to still be > 10, although there is gas at all radii fulfilling $t_{\rm cool}/t_{\rm ff} < 10$, which tends to be infalling, (Nelson et al., 2020). At higher-redshifts $z \gtrsim 2$, the radial profiles are approximately flat or even decrease with cluster-centric distance, while the profiles at lower redshfits $z \lesssim 0.5$ increase with cluster-centric distance. In the ICM for present-day clusters, the cooling to free-fall time ratio tends to increase with cluster mass, while the ratio in the inner regions depends on whether the object is a cool core cluster (Lehle et al., 2024).

The radial profiles of Fig. 8.7 (left panel) are spherically averaged and represent the mass-weighted average of a possibly wide distribution of cooling to free-fall times. To probe the ICM that is susceptible to cooling, we compute the mass fraction of the ICM fulfilling the (catastrophic) cooling criterion $t_{\rm ff}/t_{\rm cool} < (1)\ 10$ compared to the total hot ICM mass (Fig. 8.7 right panel). We then plot this cooling fraction of the hot ICM as a function of cluster mass and redshift for all 352 clusters (circles) and include the median mass trend at a fixed redshift as thick curves (thin curves show the median trend of the fraction of the hot ICM fulfilling the catastrophic cooling criterion $t_{\rm cool}/t_{\rm ff} < 1$). According to TNG-Cluster, at a fixed redshift, the cooling fraction of the hot ICM decreases with cluster mass, such that lower mass clusters likely have more cooling proportional to their total ICM. At a fixed cluster mass, the cooling fraction increases with redshift, agreeing with expectations. In fact, $\approx$ 100 per cent of the ICM in protoclusters of mass $\sim 10^{12}$ $M_\odot$ at $z \sim 4$ are able to cool, and $\approx$ 10 per cent may cool catastrophically.

In summary, the ICM gas cooling was more significant in the past than it is today, at least partially explaining why the cool ICM mass decreases with time. What perturbed it to cool and what happens to it after cooling remains unanswered. We consider below one of the causes of these perturbations, satellite galaxies, and discuss this gas cooling to the point of forming stars in-situ in the ICM in § 8.5.1.

8.4.2 The Decreasing Importance with Cosmic Time of Satellites as Sources for Cool ICM

It is plausible that satellites can increase the cool ICM mass both via direct deposition of their cool ISM gas into the ICM via ram pressure stripping and by triggering hot gas to cool via density perturbations. The stripped gas is, in many cases, more metal rich than the ICM. This seeding of metals can also contribute to the enhanced cooling. Satellites are in principle also able to accrete cool gas from the surrounding medium, but in general, it is expected that the satellite accretion is negligible within the cluster environment (Larson et al., 1980; Balogh & Morris, 2000; van de Voort et al., 2017; Rohr et al., 2023). In the following, we quantitatively

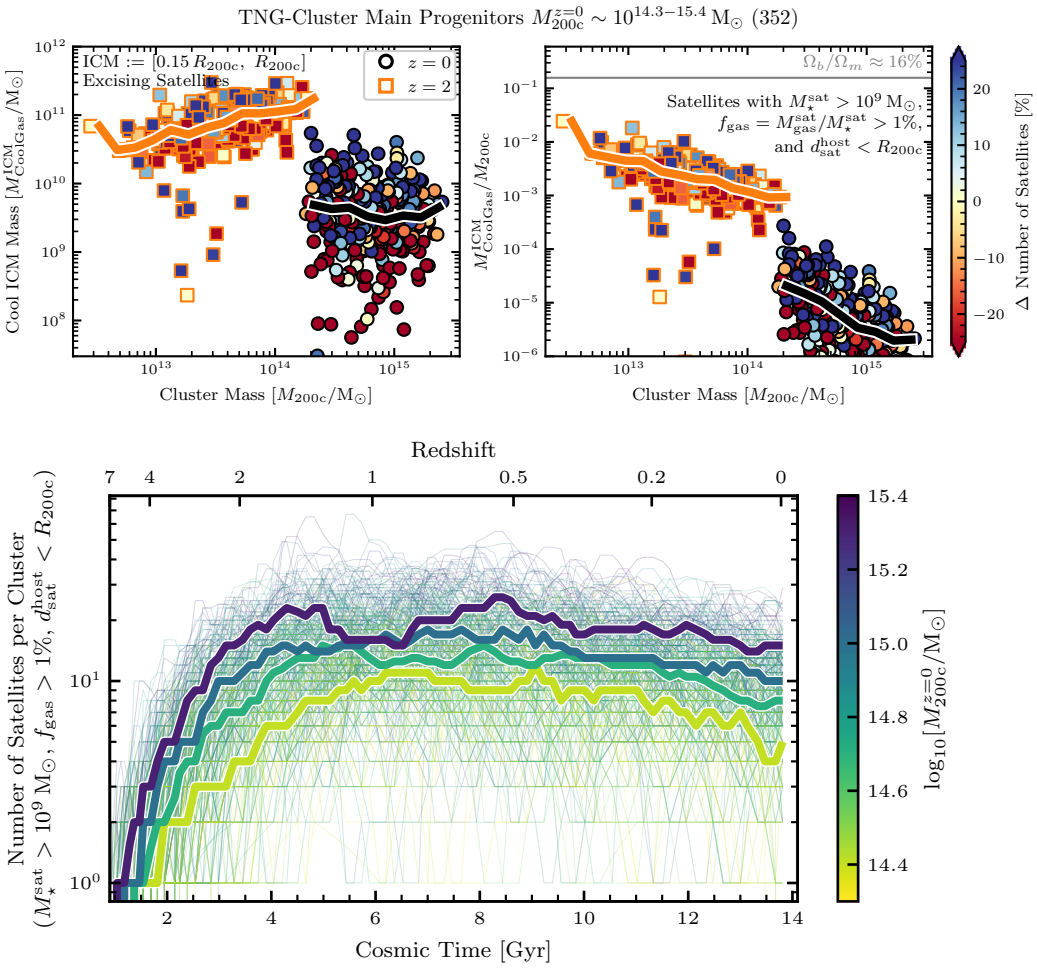

Figure 8.8: **According to TNG-Cluster, at a fixed cluster mass and redshift, the cool ICM mass correlates with the number of gaseous satellites, and clusters tend to have fewer gaseous satellites today than in the past.** *Top Panels*: At $z = 0$ and 2 (black-outlined circles, orange-outlined squares), we demonstrate that at a fixed redshift the cool ICM mass increases with the relative number of satellites, that is, with the percentage difference between the number of satellites in a given cluster and the average number in a corresponding narrow bin of halo mass. Here, we only consider satellites with a stellar mass $> 10^9\,M_\odot$, a gas to stellar mass fraction > 1 per cent, and within a cluster-centric distance $< R_{200c}$. *Bottom Panel*: We show the evolution of the number of gaseous satellites per cluster over the past ≈ 13 billion years for all 352 clusters (thin curves), colored by their $z = 0$ cluster mass (medians within a $z = 0$ cluster mass bin as thick curves). Namely for all considered masses today, clusters have fewer gaseous satellites today than in the past at $z \approx 1 - 2$, at least partially explaining why the cool ICM mass decreases with time.

demonstrate that, in general, the cool ICM mass at a fixed cluster mass and redshift increases with the number of gaseous satellites.

In Fig. 8.8, we show that, at a fixed cosmic time, the number of gaseous satellites – all galaxies with stellar mass $> 10^9\,M_\odot$, gas to stellar mass fraction > 1 per cent, and within a cluster-centric distance $< R_{200c}$ – increases with cluster mass (bottom panel). Therefore, to see trends of cool ICM mass with both the number of gaseous satellites and cluster mass (top panels), we compute the relative number of satellites per halo: within a narrow bin of halo mass at a fixed redshift, we compute the median number of gaseous satellites per cluster and consider the percent difference between a given cluster and its similar-massed companions. At all redshifts considered (here only showing redshifts $z \sim 0,\ 2$ for clarity), the amount of cool ICM (top left) and the cool ICM to total halo mass fraction (top right) increase with the number of gaseous satellites, at a fixed halo mass. That is, for a given cluster, the more gaseous satellites it hosts, the more cool gas it tends to have in its ICM.

While at fixed redshift the cool ICM mass increases with the relative number of gaseous satellites, we want to understand how satellites can cause the cool ICM mass to decrease with time. Stripping of cool satellite gas via ram pressure becomes more effective at higher halo masses, which also increases with time. This is also reflected in, for example, the fraction of gaseous satellites that are jellyfish, which increases with cosmic time (Zinger et al., 2024). However, the total cool gas deposited into the ICM from satellites depends not only on the effective strength of cool gas stripping but also on the number of gaseous satellites themselves, which are known to undergo environmental effects and more so the longer they orbit in massive systems (e.g. Donnari et al., 2021b, within the TNG model). We hence compute the number of satellites per cluster over the past ≈ 13 billion years (Fig. 8.8 bottom panel). We plot the evolution for each of the 352 clusters from TNG-Cluster (thin curves) colored by their $z = 0$ halo mass, and we include the medians within a $z = 0$ halo mass bin (thick curves). At all times, the number of gaseous satellites increases with halo mass, a natural consequence of hierarchical structure formation. In contrast, the number of gaseous satellites per cluster decreases for all average cluster masses since redshifts $\sim 1 - 2$. That is, while a cluster of mass $\sim 10^{15}\,M_\odot$ today may host 10 gaseous satellites of stellar mass $> 10^9\,M_\odot$, its progenitor at $z \sim 1$ may have hosted twice as many. So while satellites are important sources of cool ICM, they may become less crucial at later times due to their decreasing abundance.

We note that these results depend, in part, on the type of satellites that are being considered. In Appendix 8.9 we include two additional versions of Fig. 8.8 using different definitions for satellites, and we summarize the results here. Recently, Chaturvedi et al. (2024) suggest that it is the number of massive satellites, not the total number of satellites, that is important when considering satellites as sources of cool ICM. When considering only gaseous satellites of stellar

mass $> 10^{10}\,M_\odot$ (instead of $> 10^9\,M_\odot$), the same qualitative trends hold, and the average number of gaseous satellites per cluster decreases for all halo masses since $z \lesssim 1-2$. For this regime then, we conclude that satellite stellar mass may not be significant for the total amount of cool ICM, although it may still be important for the survivability of individual cool gas clouds (Gronke et al., 2022; Roy et al., 2024). We also consider removing the gaseous criterion – that is, only requiring a stellar mass $> 10^9\,M_\odot$ and cluster-centric distance $< R_{200c}$ – and the stellar mass criterion – that is, only requiring the subhalos to be within R_{200c} (not shown). In TNG-Cluster, most $z = 0$ cluster satellites of stellar mass $\sim 10^{9-10}\,M_\odot$ are gas-poor and quenched, and those that are gas-rich tend to be recent infallers (Rohr et al., 2024). Thereby, the number of gaseous satellites proxies the number of recent infallers. However, the number of satellites (or subhalos in total) traces the overall hierarchical assembly of clusters and tends to increase monotonically with time, modulo satellites that have been tidally disrupted and satellite-satellite mergers. In these cases, the relative number of satellites still correlates with the cool ICM mass at a fixed cluster mass, but the number of satellites per cluster continues to increase with time until today. Therefore, while these definitions are still important for the amount of cool ICM, where gas-poor satellites or starless subhalos may still trigger gas cooling, the evolution of these satellites does not provide an explanation for why the cool ICM decreases towards $z = 0$.

8.4.3 How SMBH Feedback Decreases the Cool Cluster Gas Mass

Feedback from the central SMBH affects the ICM even out to, and at times extending beyond, the virial radius. In the TNG galaxy formation model, the kinetic, low-accretion mode feedback from SMBHs is largely responsible for quenching central galaxies (Weinberger et al., 2018; Nelson et al., 2018a) by both ejecting the interstellar medium gas and by offsetting the cooling times of the gaseous reservoirs in the halos (e.g., Nelson et al., 2018b, 2019a; Truong et al., 2020; Davies et al., 2020; Zinger et al., 2020). We henceforth examine exactly how the cool ICM mass changes once the central SMBHs starts to provide kinetic feedback.

In Fig. 8.9, for all 352 clusters (thin curves), we find the redshift when the main SMBH underwent a kinetic mode feedback event for the first time and plot the evolution of the cool ICM mass normalized to this time (main panel), colored by the redshift at the first kinetic mode feedback event. Before the onset of kinetic mode feedback, all clusters grew rapidly in their cool ICM mass. Interestingly at the onset of kinetic mode feedback, all clusters here have on average $\sim 10^{10.5}\,M_\odot$ of cool ICM, regardless of when in cosmic time they in fact switch from thermal to kinetic mode feedback. This suggests that there may be a characteristic cool ICM mass at which the SMBHs tend to switch to kinetic mode feedback, even though these two quantities are spatially disconnected. In the first $\sim 1-2$ Gyr after the onset of kinetic

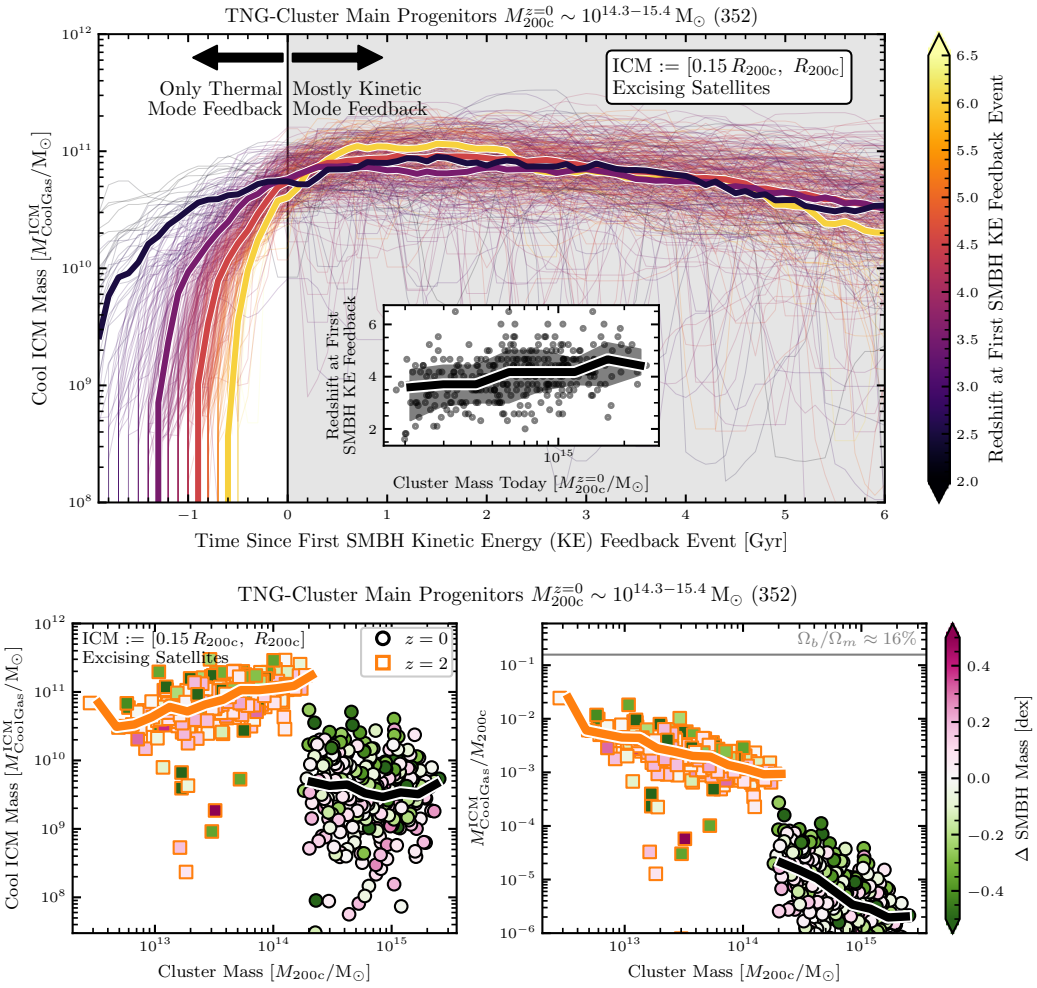

Figure 8.9: **Kinetic mode feedback from the SMBH causes the growth of the cool ICM mass to flatten and its total amount to decrease with time in TNG-Cluster.** *Main Panel*: We show the evolution of the cool ICM mass since the first kinetic mode feedback event for all 352 clusters (thin curves), colored by the redshift at the first kinetic mode feedback event (medians as thick curves). Before this first kinetic mode event, all SMBH feedback was only in thermal mode, whereas afterwards a majority is in kinetic mode. In the inset we show that SMBHs in more massive clusters today tended to switch to kinetic mode at higher redshifts (earlier in cosmic time, although the effect is small at ≈ 500 Myr over one dex in cluster mass today). Before the onset of kinetic mode feedback, the cool ICM mass increases with time; afterwards, the cool ICM mass tends to flatten and decrease until today. *Bottom Panels*: the effect of relative SMBH mass on the cool ICM mass and cool ICM to total halo mass fraction. Similar to Fig. 8.8, we now show how the relative difference in the central SMBH mass correlates with the cool ICM mass. At both redshifts considered here ($z \sim 2$, orange-outlined squares; $z \sim 0$, black-outlined circles), clusters with undermassive SMBHs tend to have more cool ICM at fixed cluster mass. This effect is stronger at later times and demonstrates that feedback from SMBH affects the amount of cool gas in the ICM, at least according to TNG-Cluster.

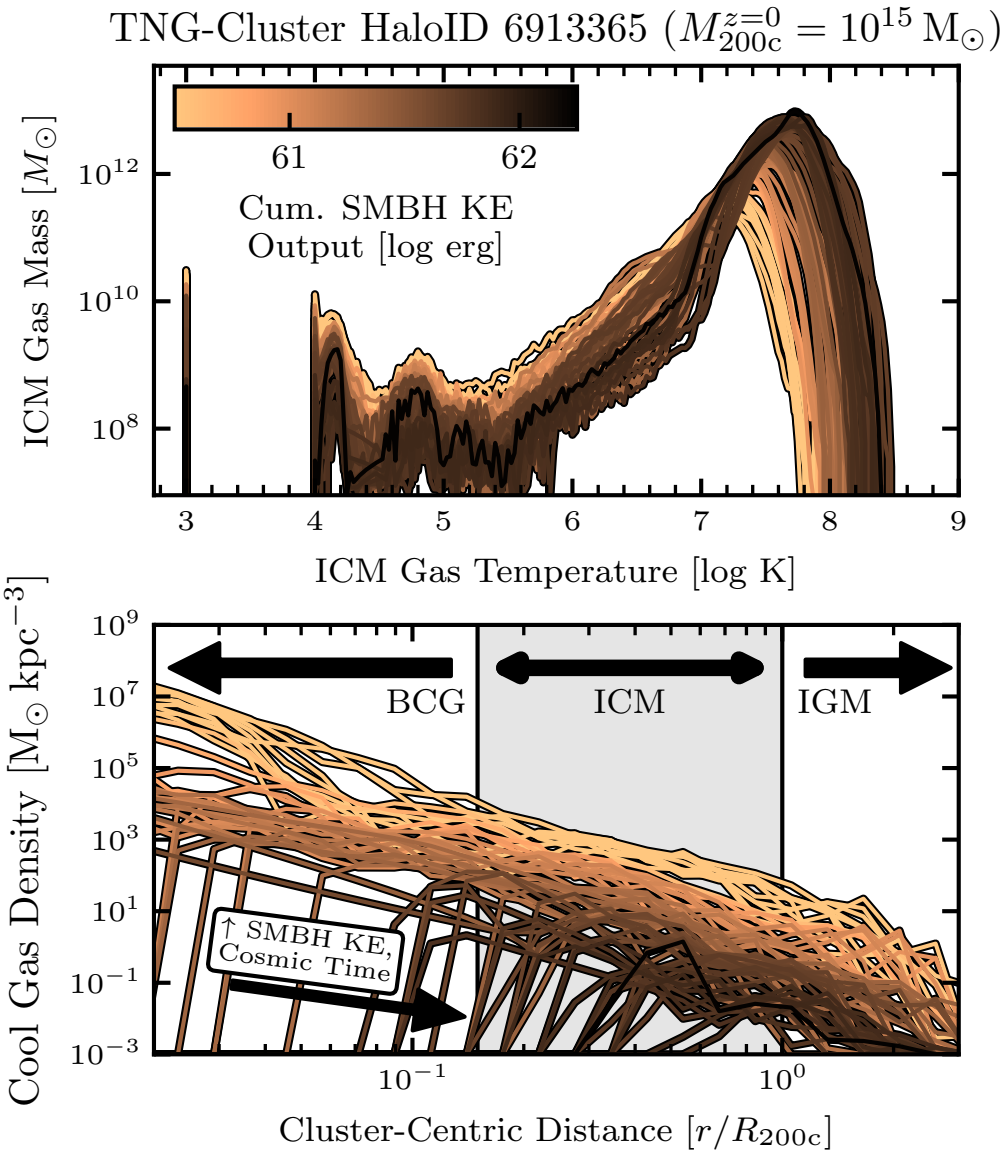

Figure 8.10: **Kinetic mode feedback from the central SMBH decreases the cool ICM mass.** Similar to Fig. 8.5, we now use the cumulative kinetic energy (KE) injected from the central SMBH in kinetic mode as the color. As the cumulative energy output increases with time, the cool gas density at all radii decreases, including in the ICM, and the decrease occurs inside-out, suggesting that feedback from the SMBH drives the cool ICM mass.

mode feedback, the growth of the cool ICM mass flattens out at approximately the same maximum cool ICM mass of $\sim 10^{10.5-11}$ $M_\odot$ regardless of when in cosmic time this occurs (the median trends are within the scatter of each other).

We note that SMBHs in more massive $z = 0$ clusters tended to have their first kinetic mode feedback event at higher redshfits, at earlier cosmic times (inset), although the effect is relatively small at ≈ 500 Myr difference across $\sim$ one dex in cluster mass. The central SMBHs of TNG-Cluster systems switched from thermal to kinetic mode in the redshift range $z = 3-5$. They do so upon crossing some approximate halo mass threshold: as more massive $z = 0$ clusters tend to cross this threshold at earlier times, their SMBHs also begin their kinetic mode feedback earlier (see also Fig. 8.4). In general after the first kinetic mode feedback event, SMBHs may switch between kinetic and thermal mode feedback; however, a majority of both the time and energy output in these massive systems occurs in kinetic mode and the majority are in kinetic mode feedback at $z = 0$. Within the TNG model, we note that kinetic mode feedback, rather than the thermal mode feedback, is mainly responsible for affecting the low redshift ICM.

Similarly to the number of satellites per cluster (Fig. 8.8), the average SMBH mass increases with cluster mass. Because of this and because the mass of SMBHs is proportional to the cumulative energy ever injected in SMBH feedback, we compute the relative SMBH mass as the difference (in dex) between a given SMBH and the average SMBH mass for all clusters of a similar mass and correlate it with the cool ICM mass (Fig. 8.9 bottom panels). At a fixed cluster mass and redshift, clusters with undermassive SMBHs tend to have more cool ICM. The effect appears slightly stronger at later times. In Appendix 8.10, we repeat these panels colored instead by the cumulative kinetic energy output since birth and since the last snapshot (≈ 150 Myr). Briefly, the same qualitative trend holds for both of these SMBH properties, although there is more scatter, especially for the kinetic energy output since the last snapshot. We conclude that the cumulative kinetic mode feedback is more strongly correlated with the formation and/or survival of the cool ICM than recent feedback history.

Finally, we demonstrate in Fig. 8.10 how the ICM temperatures and cool gas radial profile evolve with the cumulative kinetic mode feedback. Similar to the evolution with cosmic time (Fig. 8.5), the hot ICM mass increases and cool ICM mass decreases with cumulative kinetic mode feedback. This heating of the ICM is also related to the lengthening of the cooling times, functioning as a form of preventative feedback (Zinger et al., 2020; Voit et al., 2024). We note that, in lower mass hosts, SMBH feedback tends to heat and redistribute the halo gas in the TNG model (Nelson et al., 2019a; Zinger et al., 2020; Truong et al., 2021). For these clusters, we then conclude that the SMBH feedback heats up the cool ICM inside-out,

redistributes some of the ICM to larger distances, potentially driving X-ray cavities (Truong et al., 2024), and likely lengthens the cooling times of the hot ICM.

8.5 Observational Signatures of the Cool ICM

8.5.1 In-Situ Star Formation in the ICM and Hα Emission

In-situ star formation in the ICM – that is, star formation that occurs in ICM gas that is not bound to any satellite – has been seen in early zoom-in simulations (Puchwein et al., 2010; Mandelker et al., 2018), in the most massive groups or low mass clusters of TNG50 (Ahvazi et al., 2024a), and in observations of runaway cooling clusters (McNamara & O'Connell, 1989; Webb et al., 2015; Hlavacek-Larrondo et al., 2020). The fate of this in-situ star formation is likely to become part of the intracluster light (ICL), perhaps by forming star clusters (Mandelker et al., 2018; Ahvazi et al., 2024b). However, to what degree such in-situ ICM star formation may contribute to the ICL remains observationally unconstrained and theoretically difficult to assess: the aforementioned studies suggest around $\approx 10-30$ per cent of the total ICL today (Puchwein et al., 2010; Ahvazi et al., 2024a), but we anticipate that this in fact may strongly depend on halo mass and other factors. In the following, we examine this phenomenon in TNG-Cluster.

We have seen that a non negligible amount of ICM gas in TNG-Cluster systems is star-forming, and that the star-forming ICM mass generally increases with redshift (Fig. 8.1, main panel). We now quantify further this in-situ ICM star formation. As a reminder, star formation in TNG-Cluster occurs in gas with densities $> 0.1\,\mathrm{cm}^{-3}$ (see § 8.2.1), with no additional physically motivated considerations for star formation to occur. We hence acknowledge from the onset that the following results likely depend on this simplified criterion, and that the ICM star formation rates may in fact change with different star formation models (see also discussions in Puchwein et al., 2010; Ahvazi et al., 2024a).

With this caveat in mind, we examine a possible observable consequence: Hα emission from star forming gas. Throughout, we convert the SFRs predicted in the TNG-Cluster simulated systems to Hα luminosity via

$$\log_{10}[\mathrm{H}\alpha/\mathrm{erg\,s}^{-1}] = \log_{10}[\mathrm{SFR}/\mathrm{M}_\odot\,\mathrm{yr}^{-1}] + \log_{10} C_{\mathrm{H}\alpha} \tag{8.3}$$

with a calibration factor $\log_{10} C_{\mathrm{H}\alpha} = 41.27$ (Hao et al., 2011; Murphy et al., 2011; Kennicutt & Evans, 2012). We note that this simple approximation assumes that Hα emission originates exclusively from star formation, that all star formation is totally unobscured (dust free), and

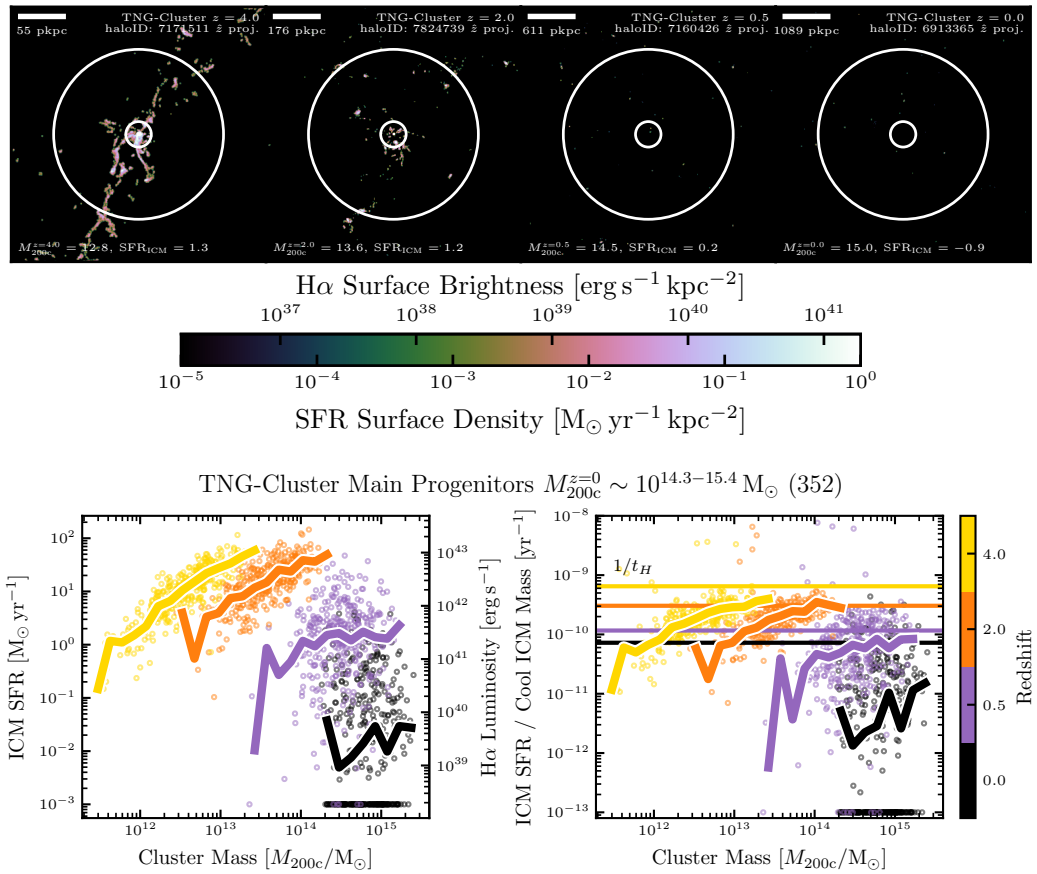

Figure 8.11: **Cluster progenitors in TNG-Cluster had (higher) in-situ ICM star formation rates than their descendants.** We include the Hα surface brightness (top) and luminosity (bottom) using the unobscured SFR to Hα conversion from Hao et al. (2011); Murphy et al. (2011); Kennicutt & Evans (2012); see text for details. *Top Panels*: We show the evolution of the star formation rate surface density for an example cluster of $z = 0$ mass $\sim 10^{15}$ M$_\odot$, including all gas (including satellites) within a cube of $3R_{200c}$ centered on the BCG, where we project the gas cells using a cubic spline of variable kernel size according to the gas cell size. The annotations are as in Fig. 8.3, and we additionally include the total ICM star formation rate in units of [$\log_{10}$ M$_\odot$ yr^{-1}] in the lower-left. *Bottom panels*: The ICM SFR (left) and ICM SFR to cool ICM mass (right) as functions of cluster mass for all 352 clusters (circles), colored by redshift, where we include the median trend with mass as thick curves. We place clusters with ICM SFRs and ICM SFR to cool ICM mass below our resolution level at 10^{-3} M$_\odot$ yr^{-1}, 10^{-13} yr^{-1} respectively. We mark the the age of the universe $1/t_H$ at each redshift as horizontal lines. The most extreme clusters at $z = 2$ have ICM SFRs of $\sim 10^2$ M$_\odot$ yr^{-1}, corresponding to an Hα surface brightness of $\sim 10^{-17}$ erg s^{-1} cm^{-2} arcsec^{-2}, making it detectable with the Euclid Space Telescope or James Webb Space Telescope, according to TNG-Cluster.

that this conversion calibrated using star formation in local galaxies holds at high redshift and in the ICM.

8.5.1.1 Spatial Distribution of the Hα Emission

In the top panels of Fig. 8.11, we show the evolution since $z \lesssim 4$ of the SFR surface density and Hα surface brightness of an individual cluster from TNG-Cluster of $z = 0$ mass $\sim 10^{15}\,\mathrm{M}_\odot$. In the images, we include all gas within a cube of size $3R_{200c}$, including satellites, centered on the BCG. Annotations are as in previous maps. In the bottom left of each stamp we include the halo mass M_{200c} and the in-situ ICM SFR, which excludes gas bound to satellites, in units of $[\log_{10}\mathrm{M}_\odot]$ and $[\log_{10}\mathrm{M}_\odot\,\mathrm{yr}^{-1}]$, respectively.

At $z = 4$ (left panel), there is cluster wide star formation from within the BCG, throughout the ICM, and even stretching into the IGM. Inside the BCG, the star formation qualitatively appears to occur in a disk like structure. In the ICM, the star formation occurs in elongated structures in the directions of large scale filaments and the tails of stripped satellite galaxies. At $z = 2$, there is still extended SFR in the ICM, although some of the star forming structures appear to be near satellite galaxies. At lower redshifts $z \lesssim 0.5$, there is almost no extended star formation in the ICM, and nearly all star formation that does exist occurs in the interstellar media of satellite galaxies. However, at least some of the stripped intersteller media from satellite galaxies is expected to form stars in the TNG and TNG-Cluster simulations (Göller et al., 2023; Lora et al., 2024). In fact, the total in-situ SFR in the ICM at $z = 0$ is $\sim 10^{-1}\,\mathrm{M}_\odot\,\mathrm{yr}^{-1}$, and it is plausible to speculate that this gas stems from stripped satellites.

The simulated cluster of Fig. 8.11 is representative of the whole TNG-Cluster sample and, upon visual inspection of the maps, we believe that much of the star-forming ICM originates from satellite galaxies, which tend to be found co-spatially with filaments, where the star formation occurs at least partially in the elongated, ram pressure stripped tails of the satellites. This is consistent with the previous findings by Puchwein et al. (2010) but not with the claims of Ahvazi et al. (2024a), which are based on the same galaxy formation model as our simulations. In particular, previously, Ahvazi et al. (2024a) find that, in the progenitors of the three most massive $z = 0$ halos of TNG50 (total halo mass $\sim 10^{13.7-14.3}\,\mathrm{M}_\odot$), widespread ICM star formation occurs in small cloudlets within filamentary structures following the distribution of neutral hydrogen and loosely that of the underlying dark matter distribution. They suggest that the star-forming gas is not related to the ram pressure tails of stripped satellites. Puchwein et al. (2010), on the other hand, suggest that a majority of the star-forming ICM in their cluster simulations of present day mass $\sim 10^{14}\,\mathrm{M}_\odot$ has distinct properties and origins compared to the rest of the ICM, where most of the star-forming ICM came from

stripped satellites. More detailed analysis and comparisons will be required to clarify the situation.

8.5.1.2 Expected Total Hα Luminosities

In the bottom panels of Fig. 8.11, we extend the analysis of the in-situ ICM SFR to the total amount in all TNG-Cluster systems and their progenitors since $z \lesssim 4$. We plot the in-situ ICM SFR (excluding satellites; left) and the ICM SFR to cool ICM mass ratio (right) as functions of cluster mass for all 352 clusters (circles), colored by redshift. We include the median mass trend at a fixed redshift as thick curves, and in the right panel we include the inverse age of the universe at that redshift as horizontal lines. We place clusters with SFRs below our resolution limit manually at $10^{-3}\,\mathrm{M_\odot\,yr^{-1}}$ (left) and $10^{-13}\,\mathrm{yr^{-1}}$ (right).

At $z = 0$, the ICM SFR has an approximately flat trend with cluster mass at $\sim 10^{-2}\,\mathrm{M_\odot\,yr^{-1}}$ (Hα $\sim 10^{39.5}\,\mathrm{erg\,s^{-1}}$). This median trend represents two populations of clusters today: $\approx$ 40 per cent of clusters have ICM SFRs $\lesssim 10^{-3}\,\mathrm{M_\odot\,yr^{-1}}$ ($\lesssim 10^{38}\,\mathrm{erg\,s^{-1}}$); the other $\approx$ 60 per cent of clusters have SFRs ranging up to $\sim 1\,\mathrm{M_\odot\,yr^{-1}}$ ($\sim 10^{41}\,\mathrm{erg\,s^{-1}}$). For comparison, in the three most massive objects in TNG50, Ahvazi et al. (2024a) measure ICM SFRs of $\sim 1\,\mathrm{M_\odot\,yr^{-1}}$, approximately an order of magnitude higher than the median ICM in TNG-Cluster, although still within the range of $z = 0$ clusters. We note the objects studied by Ahvazi et al. (2024a) are less massive $\sim 10^{13.7-14.3}\,\mathrm{M_\odot}$ than the clusters in TNG-Cluster $\sim 10^{14.3-15.4}\,\mathrm{M_\odot}$. Additionally, the difference in resolution may play a role in the creation, survival, and potential star formation of cool clouds in the halo (Nelson et al., 2020). Namely, the mass resolution in TNG50 $\approx 8.5 \times 10^4\,\mathrm{M_\odot}$ is $\approx$ 130 times better than in TNG-Cluster at $\approx 1.1 \times 10^7\,\mathrm{M_\odot}$, and in general with the TNG galaxy formation model, star formation rates slightly increase with increasing resolution (Pillepich et al., 2018a).

At higher redshifts $z \gtrsim 0.5$, the ICM SFR increases with cluster mass, and at a fixed cluster mass, the ICM SFR increases with redshift. Compared to a similar mass cluster at $z = 0$, a $z = 0.5$ cluster may have $\approx 10 - 30$ times more star formation in the ICM. The most actively star-forming ICM at redshift $z \approx 0.5$ have SFRs up to $\approx 10^{1.5}\,\mathrm{M_\odot\,yr^{-1}}$, corresponding to an H$\alpha$ flux of $\sim 10^{-18}\,\mathrm{erg\,s^{-1}\,cm^{-2}\,arcsec^{-2}}$. At $z \approx 2$, the most extreme objects may be have ICM SFRs of $\sim 10^2\,\mathrm{M_\odot\,yr^{-1}}$ ($\sim 3 \times 10^{43}\,\mathrm{erg\,s^{-1}}$), which corresponds to $\sim 10^{-17}\,\mathrm{erg\,s^{-1}\,cm^{-2}\,arcsec^{-2}}$ in Hα.

Importantly, the in-situ star formation predicted by TNG-Cluster in the ICM of $z \approx 2$ proto-clusters may be observable in the near-infrared within current surface brightness limits of the Euclid Space Telescope and James Webb Space Telescope, providing a test of star formation and galaxy formation models.

The ICM SFR to cool ICM mass ratio (right panel), akin to the star formation efficiency in nearby galaxies, details how efficient the cool ICM is at forming stars. Across the redshifts and cluster masses considered, the ICM SFR to cool ICM mass ratio increases with mass at a fixed redshift and vice versa; that is, the star-forming efficiency in the ICM increases with cluster mass at a fixed redshift, and with redshift at a fixed cluster mass. At $z = 0$, the median ICM SFR to cool ICM mass ratio is significantly smaller than the inverse age of the Universe, by $\approx 1 - 2$ dex, meaning that it would take many Hubble times to deplete the cool ICM gas at that constant SFR. For redshifts $z \gtrsim 0.5$, the median trends approach the inverse Hubble time, especially at large cluster masses at each redshift. The median star-forming efficiency in the ICM is maximum at $z \approx 2$, where ≈ 65 per cent of clusters have ICM SFR to cool ICM mass ratios greater than the inverse Hubble time. At all redshifts, there are individual clusters with ICM SFR to cool ICM mass ratio much larger than the inverse Hubble time.

8.5.2 The Cool Cluster Gas in Mg II Absorption

Cool halo gas can also be detected as absorption features in spectra of background quasars or galaxies both in observations and simulations (Péroux et al., 2020). Here we focus on Mg II in absorption to compare with recent observational studies with large sample statistics (Mishra & Muzahid, 2022; Anand et al., 2022; Fresco et al., 2024).

We compute the number of Mg II atoms on a cell-by-cell basis, following Nelson et al. (2018a, 2024). Briefly, we use the total magnesium mass as stored by the simulation and compute the ionization states using CLOUDY (Ferland et al., 2013, 2017, version c17), including both collisional and photoionization with the UV + X-ray background from Faucher-Giguère et al. (2009, with the 2011 update), ensuring the self-consistency between the simulation and post-processing. We ignore local sources of radiation. CLOUDY was run in single-zone mode and iterated to equilibrium, employing the fitting function for the frequency-dependent shielding from the background field at high density from Rahmati et al. (2013). We then compute the column density of absorbers along a given line-of-sight (LoS) by projecting the clusters and summing the number of Mg II atoms. We include high resolution gas in the zoom simulation within a LoS velocity $< 2000\,\mathrm{km\,s^{-1}}$ of the LoS velocity of the BCG, mimicking the selection from the observations (see below for details). In the TNG-Cluster simulation suite, however, the high-resolution zoom region does not sustain the path length corresponding to a Hubble expansion of $\pm 2000\,\mathrm{km\,s^{-1}}$, which would be $> 10 R_{200c}$ from the BCG. We subsequently underestimate the total number of Mg II atoms originating from other satellites and halos, which may be significant in the projected column densities (Rahmati et al., 2015; Nelson et al., 2018b; Weng et al., 2024).

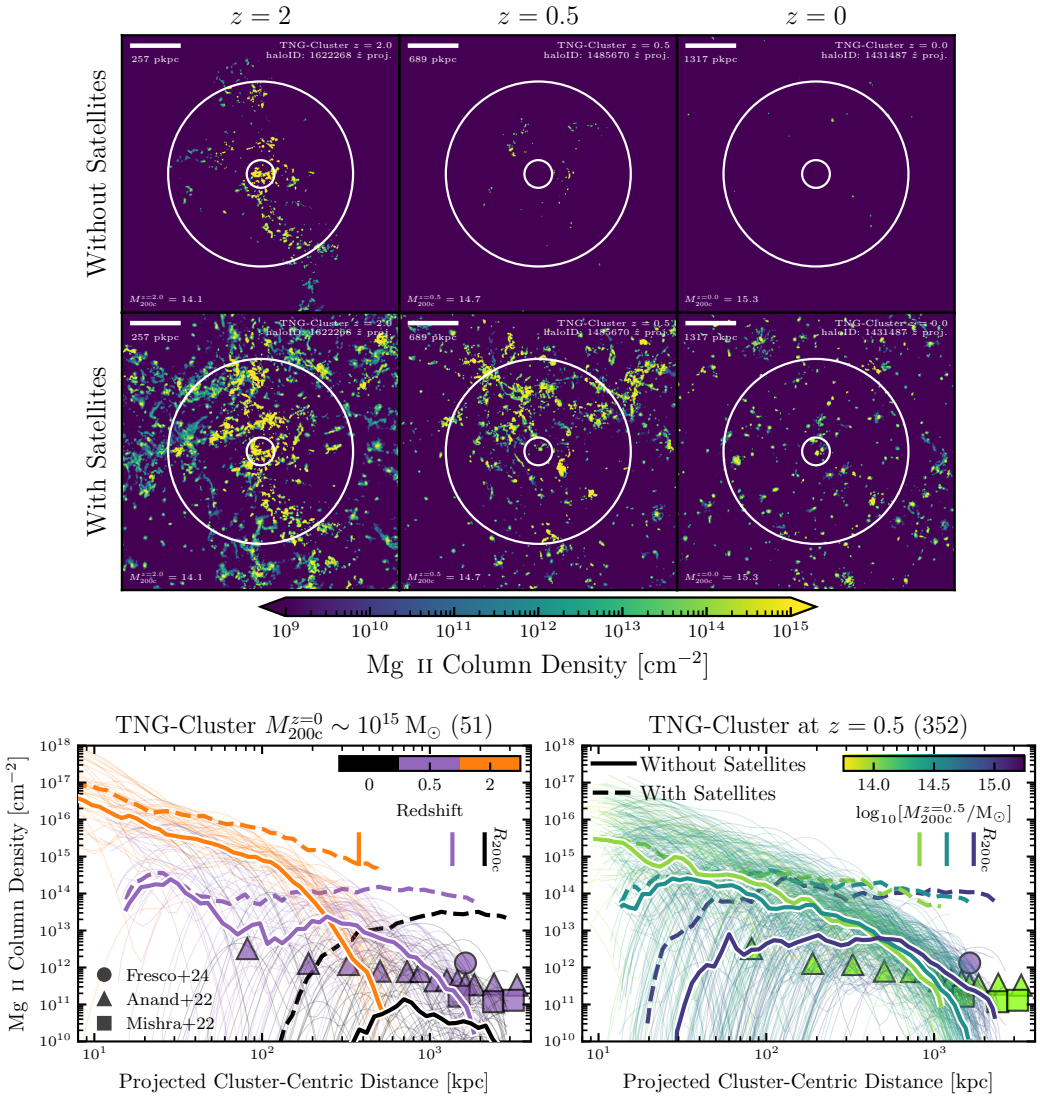

Figure 8.12: **Clusters and their progenitors contain Mg II gas in TNG-Cluster.** *Top panels*: We show the evolution of the Mg II column density for an example cluster of $z = 0$ mass $\sim 10^{15.3}$ M$_\odot$, including gas (top: excluding satellites; bottom: including satellites and foreground+background halos) within a line-of-sight velocity < 2000 km s^{-1} of the BCG. The annotations and method are as in Fig. 8.3. *Bottom panels*: The Mg II column density radial profiles in clusters of present-day mass $\sim 10^{15}$ M$_\odot$ across cosmic time (left) and for all clusters of mass $\sim 10^{13.75-15.25}$ M$_\odot$ at $z = 0.5$. The thin curves show the profiles for individual clusters, including gas within the a line of sight velocity < 2000 km s^{-1} of the BCG and excluding satellites, where we include the medians as thick curves. The dashed curves show the median profiles when also including satellites. We include stacked observational comparisons of clusters from Fresco et al. (2024, circle), Anand et al. (2022, triangles), and Mishra & Muzahid (2022, squares), which are colored to match the average redshift (left) and cluster mass (right); see text for details.

We present the results and comparisons with observations in Fig. 8.12. In particular, we provide quantification both with and without satellites and foreground and background objects. In the figure annotations by "satellites" we refer to both to gas bound to cluster satellites, as determined by the SUBFIND and Friends-of-Friends algorithms, and to gas from other halos that lie within the projected field of view and LoS velocity. That is, the "with satellites" results include both FoF satellites and foreground+background halos, commonly referred to as the "2-halo" or "other-halo" term (Nelson et al., 2018b, 2020). Other studies may choose to separate these into different origins (e.g., Weng et al., 2024), or maybe even include other halos in fiducial choice (Rahmati et al., 2015). We exclude both gas bound to cluster satellites and to other halos, including the central and satellite galaxies of the other halos, because sightlines near satellites and other halos may be associated with these other objects rather than the cluster itself.

8.5.2.1 Spatial Distribution of Mg II Absorbers

In the top panels of Fig. 8.12, we show the evolution since $z = 2$ of the Mg II column density for a single cluster of $z = 0$ mass $\sim 10^{15.3}\,M_\odot$, including all gas within a LoS velocity $< 2000\,\mathrm{km\,s^{-1}}$ of the BCG, excluding satellites (top row) and including satellites (bottom row). For this example (and others as well, quantified below), satellites provide a large amount of Mg II absorbers in the ICM across redshifts and cluster centric distances, agreeing with expectations from lower mass hosts at $z = 0$ (Weng et al., 2024). Clusters at lower redshifts $\lesssim 0.5$ have few extended reservoirs of Mg II absorbers. Instead they tend to be small cloudlets throughout the ICM. When including satellites, the amount of Mg II absorbers increases, and there is some extended mission in the circumgalactic media or in the ram pressure stripped tails of these satellite galaxies. In general, the number of Mg II absorbers tends to increase with redshift. At $z \approx 2$, there are greater numbers of Mg II absorbers throughout the ICM and their covering fraction is higher. Without satellites, there exists a filamentary structure of Mg II absorbers, extending from within the BCG through the ICM to the IGM. When considering satellites, there are many such filaments connecting the satellites throughout the ICM.

8.5.2.2 Mg II Column Densities in the ICM

In the bottom panels of Fig. 8.12, we compute the radial profiles of the Mg II column density for clusters across cosmic time (left) and mass (right). We include the radial profiles – without satellites – for individual clusters as thin curves colored by redshift (left) and mass (right) and include the median trend with redshift (left) and mass (right) as thick curves. We also

include the median radial profiles when counting absorbers associated to satellites as dashed curves. We mark the average virial radius for each of the median radial profiles. Across all redshifts, cluster masses, and cluster-centric distances considered, satellites contribute to the total column density of Mg II absorbers, and their contribution increases with cosmic time, cluster mass, and cluster-centric distance.

In the bottom left panel of Fig. 8.12, we examine the evolution of Mg II column density radial profiles for clusters in TNG-Cluster of present-day mass $\sim 10^{15}$ $M_\odot$ (51 clusters). A majority of present-day clusters (black) have little to no Mg II absorbers at small cluster-centric distance $\lesssim$ 100 kpc, reflecting that many of these clusters have little to no cool gas in their centers (Nelson et al., 2024; Lehle et al., 2024). Their progenitors at $z \approx 0.5$ contained on average $\approx 1-3$ orders of magnitude more Mg II absorbers throughout the ICM. At redshift ≈ 2, there were large amounts of Mg II even in the cluster centers, reaching values of $\sim 10^{16}$ cm^{-2} at $\sim$ 10 kpc, reflecting that the average cluster progenitor at this time had cool gas in and around its core (Figs. 8.2, 8.3). Here, there is a larger Mg II contribution from the ICM itself in the inner regions $\lesssim$ 100 kpc, and satellites mostly contribute at larger distances.The stacked observational data lie approximately between the median trends at redshifts 0 and 0.5 from TNG-Cluster out to $\approx R_{200c}$; we return to this comparison below.

In the right panel, we show how the Mg II column density profile varies with cluster mass at a fixed time of $z \approx 0.5$. In the inner regions of clusters $\lesssim$ 100 kpc, there is a clear separation between the low and high mass clusters in their numbers of absorbers. Namely, lower-mass clusters tend to have much higher column densities of Mg II absorbers $\sim 10^{14-15}$ cm^{-2} compared to high mass clusters $\sim 10^{12-13}$ cm^{-2}, reflecting that the fraction of non-cool clusters in TNG-Cluster tends to increase with cluster mass (Lehle et al., 2024). In the outer regions $\gtrsim$ 300 kpc, there is little trend of the average column density of Mg II absorbers with mass until $\approx R_{200c}$ for the respective clusters, where the column density begins to drop exponentially. The observational data lie within the space covered by TNG-Cluster, although we caution a direct comparison.

8.5.2.3 Preliminary Comparisons to Available Observational Results

In the bottom panels of Fig. 8.12, we juxtapose our TNG-Cluster outcome to results from recent stacked observations of clusters from Fresco et al. (2024, circle), Anand et al. (2022, triangles), Mishra & Muzahid (2022, squares), which are colored to match the sample's average redshift (left) and cluster mass (right).

In general, the stacked observational data lie within the Mg II column density space probed by TNG-Cluster. From the simulations, we model the number of Mg II absorbers on a cell-by-cell basis for all clusters across distance, mass, and cosmic time. The observations rely on

an equivalent width absorption feature on the background quasar spectrum through a given sightline near a cluster and then convert this equivalent width to a column density. Then by stacking tens to hundreds of thousands of these absorption features, either detected or non-detected, around different clusters at different projected distances, masses, and redshifts, one obtains the statistical properties of the cool ICM.

Namely, Fresco et al. (2024) consider $\approx$ 16, 000 quasar spectra from the (extended) Baryonic Oscillation Spectroscopic Surveys (BOSS Dawson et al. 2013 and eBOSS Dawson et al. 2016) from the Sloan Digital Survey Survey (SDSS) data release 16 (DR16 Lyke et al., 2020; Ahumada et al., 2020) around $\approx$ 1000 X-ray selected clusters from the SPectroscopic IDentification of ERosita Sources (SPIDERS Comparat et al., 2020; Clerc et al., 2020) at all projected distances $\lesssim$ 2 Mpc, of mass $\sim 10^{15}$ $M_\odot$, and at redshifts $\sim 0.3 - 0.6$ (average redshift ≈ 0.41); Anand et al. (2022) cross-match $\approx$ 155, 000 known Mg II absorbers from SDSS DR 16 spectra (Anand et al., 2021) with $\approx$ 70, 000 spectroscopically identified galaxy clusters from the Dark Energy Spectroscopic Instrument (DESI) Legacy Imaging Surveys (Dey et al., 2019; Zou et al., 2021) at projected cluster-centric distances $\lesssim$ 5 Mpc, of mass $\sim$ a few $\times 10^{14}$ $M_\odot$, and at redshifts $\sim 0.4 - 0.8$; Mishra & Muzahid (2022) study $\approx$ 81, 000 quasar-cluster pairs from $\approx$ 64, 000 unique quasars from SDSS DR16 (Lyke et al., 2020) around $\approx$ 38, 000 clusters from the Wen & Han (2015) SDSS cluster catalog at projected distances $\sim$ 1 – 4 Mpc, of mass $\sim$ a few$\times 10^{14}$ $M_\odot$, and at redshifts $\sim 0.4 - 0.75$ (median redshift at ≈ 0.55). The studies from Fresco et al. (2024); Mishra & Muzahid (2022) rely on stacking many spectra to obtain a statistical Mg II absorption feature, while Anand et al. (2022) utilize the $\approx$ 2700 individually detected Mg II quasar-cluster absorbers identified by Anand et al. (2021). The observed cluster samples are relatively complete, while TNG-Cluster is only volume-complete above cluster masses $> 10^{15}$ $M_\odot$ at $z = 0$ (above masses $\gtrsim 10^{14.5}$ $M_\odot$ at $z = 0.5$; see Nelson et al. 2024 for details).

The role of satellites, other halos, and intervening material at large distances are all critical for an apples-to-apples comparison with the observations. The observational studies tend to consider the Mg II absorbing gas within a LoS velocity of $\lesssim 2000\,\mathrm{km\,s^{-1}}$ of the BCG, and we apply the same cut, additionally either removing satellites and other halos or including their contributions (but in no cases including the low resolution gas that would still be within a LOS velocity $\lesssim 2000\,\mathrm{km\,s^{-1}}$ of the BCG).

In cluster outskirts, TNG and TNG-Cluster satellites can both retain some of their own circumgalactic media (Rohr et al., 2024) and begin depositing their metal-enriched ISM into the ICM (e.g. Rohr et al., 2023; Zinger et al., 2024), both of which may contribute to absorption features (Weng et al., 2024). Anand et al. (2022); Mishra & Muzahid (2022) conclude that much of the cool, metal enrich gas in cluster outskirts is associated with satellites

and may have been stripped from them in the past. This includes ISM, CGM, and (some) ram pressure stripped gas from the satellites. When we include gas associated with satellites and other halos, the average column density of Mg II absorbers in cluster outskirts $\gtrsim R_{200c}$ increases by orders of magnitude at all cluster masses and redshifts, confirming their significance to cool, metal-enriched cluster gas.

Overall, the observational data lie in the Mg II column density space predicted by the simulations, where the total Mg II column density (including satellites) from the simulations is higher than observed, but follow up studies that match the observational selection functions, forward-model the simulations to create mock spectra, and appropriately treat the contribution from cluster satellites and other halos are needed to fairly compare the observations with predictions from TNG-Cluster. Any discrepancies can shed light on the thermodynamic state of the ICM in the simulations and the associated role of SMBH feedback in forming and-or destroying Mg II in the cluster mass regime (see also the discussion in Nelson et al., 2024).

8.6 Summary and Conclusions

In this work, we analyze the intracluster medium (ICM) in 352 clusters of $z = 0$ mass $\sim 10^{14.3-15.4}\,M_\odot$ from the TNG-Cluster simulation suite across cosmic epochs. We focus on halo gas in the aperture $[0.15R_{200c},\ R_{200c}]$, excluding satellites. We follow the progenitors of these clusters over the past $\sim$ 13 billion years, since $z \sim 7$ and study the cool ICM of temperatures $\leq 10^{4.5}$ K, as opposed to the much more abundant and hot virial-temperature gas of $\sim 10^{7-8}$ K. Such a study of the cool ICM over cosmic time and cluster mass for $\gtrsim 350$ clusters – including processes and effects such as magnetic fields, gas cooling, SMBH feedback, satellite galaxies, and accretion from the large scale filaments – is only possible with TNG-Cluster.

We summarize the main results and conclusions of our analysis:

- According to TNG-Cluster, the cool ICM mass today is roughly constant across the considered cluster mass range. On the other hand, cluster progenitors unambiguously had more cool ICM, a higher cool ICM to total halo mass fraction, and a higher cool to total ICM mass fraction than their descendants today. At a fixed cluster mass, the cool ICM mass increases with increasing redshift, demonstrating that the cooler past of the ICM is due to more than just halo growth (§ 8.3.1, Fig. 8.1).

- The cool cluster gas today is spatially scattered throughout the ICM in the form of more-or-less compact clouds, and a majority of the BCGs today have little to no cool gas. At higher redshifts ($z \gtrsim 2$), large, cool filaments feed cool gas into the ICM from

the IGM. Many of the higher-z BCGs are still star-forming and exhibit extended, cool gaseous disks. At all times, cool gas can be found both in and around satellites (§ 8.3.2, Figs. 8.2, 8.3).

- The azimuthally averaged cooling to free-fall time ratio in the ICM decreases with redshift and increases with cluster mass, as does the fraction of the hot ICM fulfilling the canonical $t_{\rm cool}/t_{\rm ff} < 10$ criterion. This implies that the ICM in lower mass clusters and clusters at higher redshifts are more susceptible to cooling (§ 8.4.1, Fig. 8.7).

- The cool ICM mass correlates with the relative number of gaseous satellites at a fixed cluster mass and redshift, and this holds at all times since $z \lesssim 4$. The average number of gaseous satellites per cluster decreases by approximately a factor of two since redshifts $z \sim 1-2$, partially explaining why the cool ICM mass decreases with time (§ 8.4.2, Fig. 8.8).

- The onset and cumulative effect of SMBH kinetic mode feedback correlates with the time evolution of the cool ICM mass. The cool ICM mass is maximal at $\approx 10^{10.5-11}\,{\rm M}_\odot$, $\approx 1-2$ Gyr after the onset of SMBH kinetic mode feedback, and then decreases to an average mass of $\sim 10^{9.5}\,{\rm M}_\odot$ today. Most SMBHs in TNG-Cluster tend to switch to kinetic mode feedback at a characteristic cool ICM mass of $\sim 10^{10.5}\,{\rm M}_\odot$ at around $z \sim 3-5$), despite these two properties being spatially separated. At fixed redshift and cluster mass, the cool ICM mass increases in clusters hosting undermassive SMBHs. As the cumulative kinetic energy output from the SMBH increases, the cool ICM density decreases outside-in. We speculate that the cumulative kinetic energy from the SMBH, which has been shown within the TNG model to be the cause for star formation quenching in central and massive satellite galaxies, is likely the primary factor that sets the cool ICM mass (§ 8.4.3, Figs. 8.9, 8.10).

- Within the TNG-Cluster model, and quite directly depending on the choices of the star formation criteria therein, a non-negligible amount of ICM is star-forming, especially at higher redshifts. This star-forming gas potentially has observational signatures in the form of Hα emission, where this in-situ ICM star formation reaches rates of $\sim 10^2\,{\rm M}_\odot\,{\rm yr}^{-1}$ at $z \approx 2$, corresponding to a maximum Hα surface brightness of $\sim 10^{-17}\,{\rm erg\,s^{-1}\,cm^{-2}\,arcsec^{-2}}$, within current surface brightness limits of the Euclid Space Telescope and James Webb Space Telescope (§ 8.5.1, Fig. 8.11).

- The cool ICM of TNG-Cluster contains significant Mg II absorption, including large contributions from satellites and other halos. The column density of Mg II absorbers increases with redshift and decreases with cluster mass. Observations lie within the

predicted range of TNG-Cluster, although more thorough comparisons are needed to draw stronger conclusions (§ 8.5.2, Fig. 8.12).

With this work, we demonstrate that current cosmological (magneto-)hydrodynamical simulations of galaxy formation and evolution like TNG-Cluster naturally return a multi-phase ICM, at least down to $\sim 10^4$ K. In general, understanding how the cool ICM mass evolves is a multi-faceted, inter-connected problem, which we try to visualize in Fig. 8.6 in § 8.4. We extend previous findings on multi-phase gaseous halos in the TNG simulations, for the CGM of Milky Way-mass galaxies (Ramesh et al., 2023b) and the intra-group medium of luminous red galaxies (Nelson et al., 2020), to the high-mass end.

All the results and interpretations discussed in this paper are based on the TNG-Cluster simulation and underlying physical model, and hence there are a few caveats to consider. First, the effects of SMBH feedback on the halo gas may depend on the choice of feedback model: however, in general, many modern cosmological simulations implement some form of ejective and/or preventative SMBH feedback (e.g., Davies et al., 2020; Terrazas et al., 2020; Ayromlou et al., 2023b; Wright et al., 2024, see also Vogelsberger et al. 2020; Crain & Van De Voort 2023 for recent comparisons of hydrodynamic cosmological simulations of galaxies). Additionally, some of the results related to the mass and size distribution of cool gas clouds or the ram pressure stripping of satellites and subsequent mixing of the cool tails with the ambient medium may not be converged at the resolution of TNG-Cluster. Specifically, the mass and covering fraction of the cool halo gas and the ram pressure stripping of jellyfish galaxies tend to increase with resolution even at TNG50 resolution, which is ≈ 100 times better than in TNG-Cluster (e.g., Nelson et al., 2020; Ramesh et al., 2024; Zinger et al., 2024). Lastly, there could be additional physical processes not modeled within the simulation, such as thermal conduction or cosmic rays, which may be important for the gas cooling and the survival of cool gas clouds. With these caveats in mind, we expect these results and interpretations to hold at least qualitatively across galaxy formation models, resolution levels, and in the real Universe, where future studies can be used to inform the models for the next generation of cosmological simulations.

Finally, a majority of our discussion assumes that there is an already existing cool gas reservoir at early cosmic epochs, which has been expected analytically and in early hydrodynamical simulations: for an unprecedented sample of massive clusters in a suite of cosmological galaxy-formation simulations, we show that these results still hold. Our analysis focuses on understanding how the cool ICM mass changes with time by studying the sources and sinks of cool gas and how their relative importance evolves. The TNG-Cluster simulation also yields, for example, observable predictions for the warm ($\sim 10^{4.5-5.5}$ K) ICM related to emission or absorption of He II. To understand both the net effects on the cluster scale but also the

small-scale effects on individual gas clouds within a cosmological context, we must combine efforts and results across scales of simulations, continuing to learn and inform models via comparisons with observations. Understanding the spatial and temperature structure of halo gas across redshifts is a viable next step to constraining our models of galaxy formation and evolution.

Acknowledgments

ER is a fellow of the International Max Planck Research School for Astronomy and Cosmic Physics at the University of Heidelberg (IMPRS-HD). AP acknowledges funding from the European Union (ERC, COSMIC-KEY, 101087822, PI: Pillepich). DN and MA acknowledge funding from the Deutsche Forschungsgemeinschaft (DFG) through an Emmy Noether Research Group (grant number NE 2441/1-1). ER would like to thank colleagues Eduardo Bañados Urmila Chadayammuri, Seok-Jun Chang, Dimitris Chatzigiannakis, Max Häberle, Nico Winkel, Simon White, and Zhang-Liang Xie for insightful conversations that improved the analysis.

This research was supported by the International Space Science Institute (ISSI, https://www.issibern.ch/) in Bern, through ISSI International Team project #564 (The Cosmic Baryon Cycle from Space).

The TNG-Cluster simulation suite has been executed on several machines: with compute time awarded under the TNG-Cluster project on the HoreKa supercomputer, funded by the Ministry of Science, Research and the Arts Baden-Württemberg and by the Federal Ministry of Education and Research; the bwForCluster Helix supercomputer, supported by the state of Baden-Württemberg through bwHPC and the German Research Foundation (DFG) through grant INST 35/1597-1 FUGG; the Vera cluster of the Max Planck Institute for Astronomy (MPIA), as well as the Cobra and Raven clusters, all three operated by the Max Planck Computational Data Facility (MPCDF); and the BinAC cluster, supported by the High Performance and Cloud Computing Group at the Zentrum für Datenverarbeitung of the University of Tübingen, the state of Baden-Württemberg through bwHPC and the German Research Foundation (DFG) through grant no INST 37/935-1 FUGG.

Data Availability and Software Used

The TNG-Cluster simulation will be made public one year after the first publications by the team, probably in the first quarter of 2025. The data will be organized as for all other TNG simulations, which are already publicly available at https://www.tng-project.org/ and described

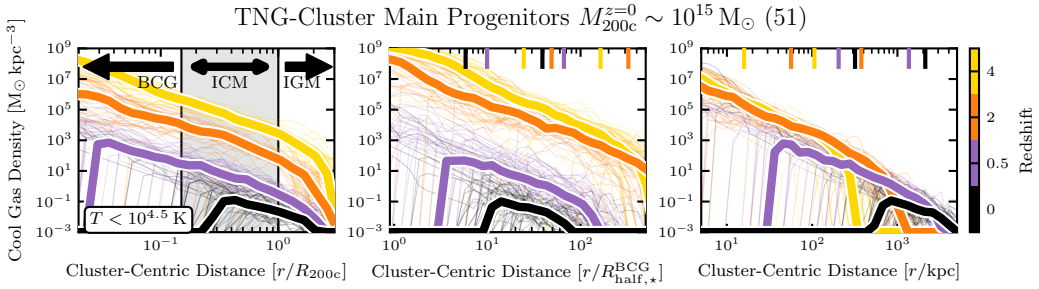

Figure 8.13: The effect of different normalizations on cool gas radial profiles. From left to right, the radial profiles are normalized by the virial radius, normalized by the BCG stellar half mass radius, and in physical coodinates. For the latter two, we mark on the top x-axis where the average adopted BCG-ICM and ICM-IGM boundaries are at $0.15R_{200c}$, R_{200c} respectively. All profiles are only for clusters whose $z = 0$ mass is $\sim 10^{15}\,M_\odot$ (51 clusters; thin curves), and we include the medians at each redshift as thick curves. At all overlapping radii and redshifts since $z \sim 4$, cluster progenitors had more cool gas than their descendants today.

in Nelson et al. (2019a). All codes used to analyze the TNG-Cluster data and to produce the figures in this paper are publicly available at https://github.com/ecrohr/TNG_RPS.

Software used: Python (Van Der Walt et al., 2011); Numpy (Van Der Walt et al., 2011; Harris et al., 2020); Scipy (Virtanen et al., 2020); Matplotlib (Hunter, 2007); Jupyter (Kluyver et al., 2016).

This work made extensive use of the NASA Astrophysics Data System and https://arxiv.org/ preprint server.

8.7 Appendix A: The Effect of Different Normalizations on Cool Gas Radial Profiles

In Fig. 8.13 we show how cool gas radial profiles for clusters of $z = 0$ mass $\sim 10^{15}\,M_\odot$ evolve with redshift, as was shown in Fig. 8.2. Here, we show the effect of different normalizations on the cool gas radial profiles. From left to right, the profiles are normalized by the virial radius R_{200c} (this figure is the same as Fig. 8.2), by the stellar half mass radius of the BCG $R_{half,\star}^{BCG}$, and in physical coordinates. For the the latter two, we mark on the top x-axis where the positions of the average adopted BCG-ICM and ICM-IGM boundaries at $0.15R_{200c}$, R_{200c}, respectively.

For all normalizations considered, the cool gas density decreases as an approximate power law in the ICM and exponentially in the IGM; lower-redshift clusters tend to have little cool gas in their BCGs while their higher-redshift progenitors tend to have cool gas in their

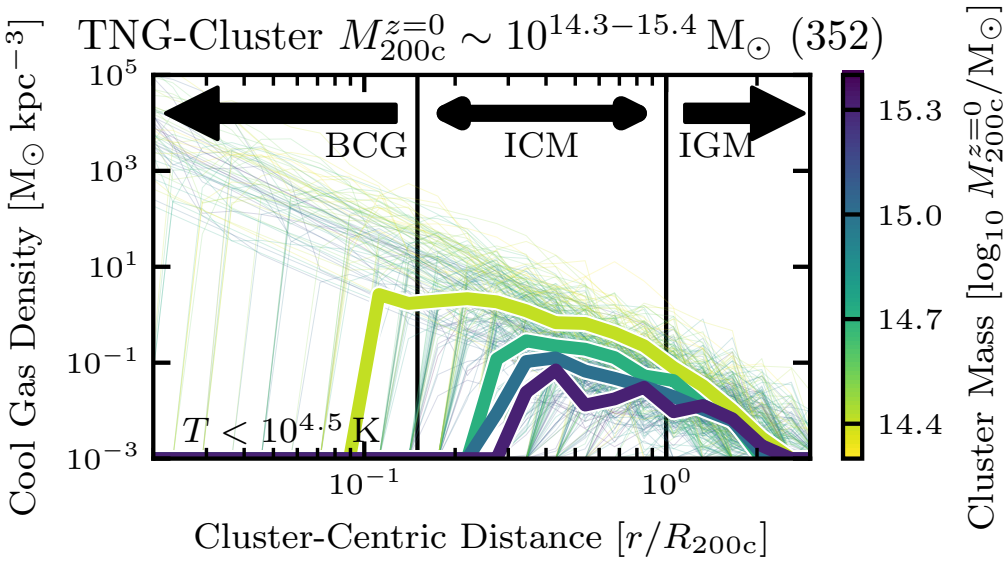

Figure 8.14: Similar to Fig. 8.2 but for all clusters at $z = 0$. We plot the external cool gas radial profile for all 352 clusters today (thin curves) colored by their mass, and we include the medians at a fixed mass (thick curves). Lower mass clusters tend to have higher cooler gas densities in the ICM.

cores. When normalizing the radial profiles by the stellar half mass radius of the BCG (center panel), the cool gas density increase with redshift at all cluster-centric distance. However, the definition of the ICM in units of the stellar half mass radius changes significantly across redshifts, which likely reflects a morphological transformation from discy star-forming galaxies at higher redshift to an elliptical, quenched BCG today. In physical units (right panel), the cool gas density increases with redshift in the ICM regions, but there is little overlap between the redshifts in physical spaces due to the halos growing in size with time.

8.8 Appendix B: The Effect of Cluster Mass on the Cool Gas Radial Profiles Today

In Fig. 8.14 we show the effect of $z = 0$ cluster mass on the cool gas radial profiles, in a similar fashion to Fig. 8.2. Lower-mass clusters tend to have higher cool gas densities in their ICM, although the effect is small compared to trend with redshift (Fig. 8.2). There are a number of clusters with non-negligible cool gas masses in their BCGs, which are likely cool-core clusters and are potentially even star-forming (Lehle et al., 2024; Nelson et al., 2024).

8.9 Appendix C: Different Definitions of Satellites and Their Correlations with Cool ICM Mass

In § 8.4.2 and Fig. 8.8 we demonstrate that the cool ICM mass increases with the number of gaseous satellites – namely satellites with stellar mass $> 10^9$ $M_\odot$ and gas to total baryonic mass fraction $f_{\rm gas} = M^{\rm sat}_{\rm gas}/M^{\rm sat}_\star > 1$ per cent – and relative to similar mass clusters at the same redshift. We also show that the average number of gaseous satellites per cluster decreases by factors of $\approx 1.5-2$ since redshifts $\lesssim 1-2$, partially explaining the cool ICM mass decreases with cosmic time. As a reminder, the majority of TNG-Cluster satellites are gas-poor at $z = 0$, and more recent-infallers and more massive satellites are more likely to be gas-rich (Rohr et al., 2024). Therein, considering gaseous satellites is a proxy for a combination of recent-infalling and massive satellites, not necessarily the total number of satellites. Gaseous satellites are able to directly deposit their cool ISM into the ICM via ram pressure stripping and outflows, in addition to causing hydrodynamical instabilities that lead to gas cooling (e.g., Rohr et al., 2023). Recently, Chaturvedi et al. (2024) suggest that massive satellites, not all satellites, are significant sources of cool gas in the ICM, and that only massive satellites deposit large enough clouds of cool gas to survive for cosmological timescales in the ICM (Gronke et al., 2022; Roy et al., 2024). Moreover, gas-poor satellites, or even dark subhalos without baryonic material, may still be able to cause density perturbations leading to gaseous cooling. We now consider different definitions of satellites in Fig 8.15.

These figures are similar in style as Fig. 8.8 (here only showing the correlations with the cool gas mass), where the left panels show how the number of satellites relative to similar mass halos affect the cool ICM mass as functions of cluster mass and redshift; the right panels shows the time evolution of the number of satellites per cluster over the past ≈ 13 billion years, since redshift $\lesssim 7$. In the top panels of Fig. 8.15 we consider massive, gaseous satellites with stellar mass $M^{\rm sat}_\star > 10^{10}$ $M_\odot$ and gas to total baryonic mass fraction > 1 per cent. The cool ICM mass tends to increase with relative number of massive satellites, which is qualitatively consistent when considering gaseous satellites with stellar mass $> 10^9$ $M_\odot$. Additionally, the average number of massive, gaseous satellites decreases by factors of $\approx 1.5-2$ since redshift $\lesssim 1$, although there are low number statistics, again similarly to the number of gaseous satellites with stellar mass $> 10^9$ $M_\odot$. Due to the similarities in these results, we conclude that not only massive satellites are relevant to determining the cool ICM mass and its decline with cosmic time, but gaseous satellites all together.

In the bottom panels of Fig. 8.15 we consider all satellites with stellar mass $> 10^9$ $M_\odot$, regardless of their gaseous content. The results are qualitatively similar with both definitions of satellites. The cool ICM mass still tends to increase with the relative number of satellites, but

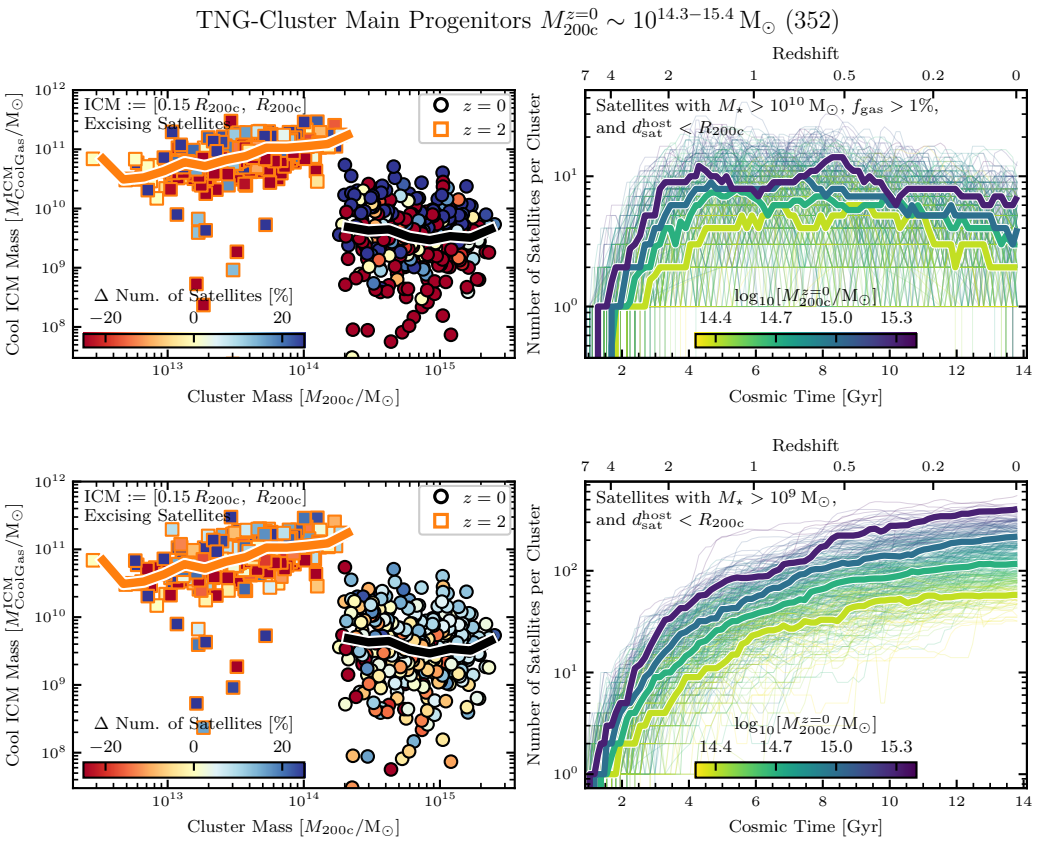

Figure 8.15: Similar to Fig. 8.8, now only considering massive satellites of stellar mass $> 10^{10}\,M_\odot$ (top panels) or all satellites of stellar mass $> 10^{9}\,M_\odot$ regardless of their gas content (that is, including gas-poor galaxies as well; bottom panels). The results are qualitatively similar when only considering massive satellites, so we conclude that is not only massive satellites that are relevant to determining the cool ICM mass. The correlations of cool ICM mass with relative number of all satellites regardless of their gas content are similar (albeit slightly weaker) to the fiducial choice (only gaseous satellites), but the number of satellites monotonically increases with time, and thereby is not as helpful in explaining why the cool ICM mass decreases.

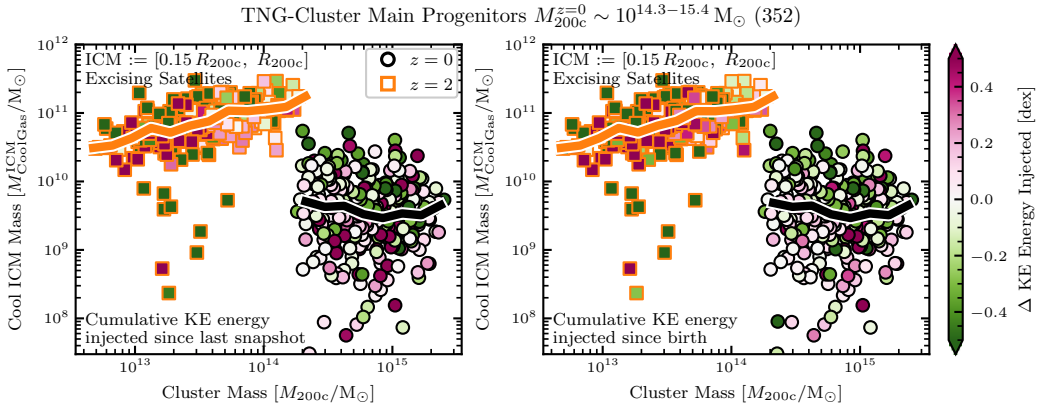

Figure 8.16: Similar to Fig. 8.9 bottom panels, but showing two additional SMBH properties: the amount of kinetic energy injected since the last snapshot (left) and the cumulative kinetic energy injected since birth (right). The qualitative results are similar, albeit stronger for the SMBH mass and cumulative energy since birth than for the energy injected since the last snapshot, suggesting that the cumulative SMBH kinetic feedback is more important than the recent feedback history in affecting the cool ICM mass.

the trends become qualitatively weaker than when considering gaseous satellites. Unlike when considering gaseous satellites, however, here the average number of satellites monotonically increases with cosmic time. In this sense, the evolution of the number of satellites does not reflect the evolution of the cool ICM mass, and thereby cannot help explain its decrease since redshifts $\approx 2-3$. The same results qualitatively hold when considering all subhalos, regardless of their baryonic content (not shown). However, the total number of satellites, especially above a stellar mass or brightness threshold, follows the evolution of the total cluster mass and can be calibrated to estimate cluster mass, known as the mass-richness relation (e.g., Costanzi et al., 2019; Abdullah et al., 2020, 2023, see also fig. 1 from Rohr et al. 2024).

8.10 Appendix D: Different SMBH Properties and Their Effects on the Cool ICM

In § 8.4.3 and Fig. 8.9 we demonstrate how the onset of kinetic energy feedback from the central SMBH coincides with the maximum cool ICM mass and that the cool ICM mass correlates with the SMBH mass relative to similar mass clusters. In Fig. 8.16 we consider how the cool ICM mass correlates with two alternative SMBH properties: the cumulative kinetic energy output since the previous snapshot (left) and the total cumulative kinetic energy output since birth (right). The kinetic energy output since the previous snapshot, which corresponds to ≈ 150 Myr, proxies recent SMBH activity and feedback, while the latter proxies the total

cumulative output, similar to the SMBH mass. There exist weak trends with the kinetic energy output since the last snapshot, but the trends with the cumulative kinetic energy output and SMBH mass are more apparent. We therefore conclude that it is the cumulative kinetic energy from the SMBH, likely not the recent SMBH feedback, that sets the cool ICM mass, especially at later times.

III. Summary and Outlook

9 Summary of Scientific Results

In this thesis, I studied how the gas contents of satellite galaxies are affected by the gaseous atmospheres of their hosts, and in turn, how satellite galaxies contribute to the circumgalactic and intracluster medium. To achieve this, I combined the results from the TNG-Cluster and TNG50 simulations, which cover present-day satellite stellar masses of $\sim 10^{8-12}\,\mathrm{M}_\odot$ in hosts of mass $\sim 10^{11.5-15.4}\,\mathrm{M}_\odot$. These simulations are state-of-the-art cosmological magneto-hydrodynamical simulations of galaxy formation and evolution in two different regimes. Both simulations employ the well-tested and validated TNG galaxy formation model, which includes ideal MHD; gas heating and cooling to temperatures $\gtrsim 10^4$ K; star formation; stellar population evolution and chemical enrichment, galactic winds from supernovae; and the formation, growth, and merging of SMBHs, where the accretion and feedback are in a two-mode scheme: a thermal "quasar" mode at high accretion rates and a kinetic "wind" mode at low accretion rates.

TNG-Cluster is a collection of 352 cosmological zoom-in simulations around massive galaxy clusters of total mass $\sim 10^{14.3-15.4}\,\mathrm{M}_\odot$ today, with a baryonic mass resolution of $\approx 1.1 \times 10^7\,\mathrm{M}_\odot$. The TNG-Cluster simulation suite is especially useful for studies of BCGs, cluster satellites, and the ICM, where the large cluster sample naturally produces a continuum of cluster properties today, such as cool-coredness, relaxedness, and cluster richness. These 352 galaxy clusters and their $\approx 90,000$ cluster members of stellar mass $> 10^9\,\mathrm{M}_\odot$ are the primary focus in Chapters 6 and 8. TNG50 is a full-volume cosmological simulation of box size ≈ 50 Mpc with the baryon mass resolution of $\approx 8.5 \times 10^4\,\mathrm{M}_\odot$, uniquely providing TNG50 with both the resolution of Milky-Way-like zoom-in simulations and the sample size of a full cosmological simulation. TNG50 naturally produces over 500 unique jellyfish galaxies, which comprises the main sample of galaxies I studied in Chapter 7.

While these simulations have been shown to produce realistic galaxy populations at $z = 0$, their true strength lies in following the evolution of galaxies and their gaseous reservoirs across cosmic time. Throughout this thesis, I tracked the evolution of satellites and their hosts across cosmic time, capturing critical transition periods in their histories, such as the first infall of satellites into their hosts and when the central SMBH first switches to kinetic-mode accretion and feedback. This style of analysis – considering all gas gravitationally bound to

galaxies, or at times even all gas in the entire simulation, and across cosmic time over the past ≈ 13 billion years – can be quite computationally demanding. I condensed tens to hundreds of terabytes of data into individual quantitatively precise and qualitatively accurate figures that can summarize the complex interplay of galaxy evolution. Below, I provide a synopsis of the main scientific results of this thesis[1], highlighting the novel findings that challenge long-standing theories about galaxy evolution and propose observational tests based on the simulations.

1. Massive satellite galaxies (stellar masses $M_\star \sim 10^{10-12}\,\mathrm{M}_\odot$) in galaxy clusters are able to retain at least part of their hot, X-ray emitting CGM today, despite the environmental effects of the cluster environment. This satellite CGM can be detected in the soft X-ray, sometimes even without subtracting the background emission from the cluster itself, and the stacked X-ray excess around massive satellites can be up to one dex above the background and extend out to tens to hundreds of kpc from the satellite. Overall, approximately 10% of the total soft X-ray flux in cluster outskirts comes from the CGM of massive satellite galaxies.

    - The presence of the satellite CGM changes the satellite-host dynamic likely, decreasing the effective ram pressure felt by the ISM, altering how satellite outflows may interact with the ICM, and increasing the ability of the satellite to continue accreting gas from the surrounding medium.
    - The contribution from the CGM of satellites must be considered in soft X-ray studies of both individual and stacked galaxy clusters, especially in the cluster outskirts.
    - The chemo-thermodynamic properties of the satellite CGM are likely different from the ICM, potentially producing different distributions of ions that contribute to either metal-line emission or absorption. That is, the satellite CGM may be even more apparent compared to the ICM in future X-ray missions like the Line Emission Mapper or in UV absorption features of background quasars.

2. The total ram pressure stripping phase of cool gas in jellyfish galaxies occurs over a broad range of timescales, ranging from ≈ 1 − 8 billion years after infall and mostly at intermediate to large host-centric distances of ≈ $0.2 - 2.0 R_{200c}$, although a majority of the cool gas lost due to RPS occurs quickly between first infall and pericenter passage.

[1] Detailed summaries of each science chapter can be found in the final section of the respective chapter.

- The host halo mass first and foremost sets the average ram pressure stripping duration, where the satellite stellar mass, satellite gas mass at infall, and orbital parameters are all secondary effects.
- The chemo-thermodynamic properties of the jellyfish tails are similar to the interstellar medium of the jellyfish (i.e., cold and metal-enriched), suggesting that the jellyfish tails originate from the stripped ISM, which subsequently mixes with the surrounding gas.
- Despite losing a significant amount of cool gas quickly after infall, the jellyfish continue forming stars until they have lost $\gtrsim$ 98% of their ISM, quenching their star formation only after almost all of their gas has been stripped.

3. Jellyfish galaxies deposit their cool ISM into their host halos. Jellyfish, and the more general satellite galaxy population, deposit more cool gas into the halos than exist in the halos today. Since $z \lesssim 4$, the cool intracluster medium mass correlates with the number of gaseous satellites.
    - The column density of Mg II in clusters is dominated by satellites galaxies, especially in the cluster outskirts.
    - Some of the stripped satellite ISM is able to form stars and, as this gas is not gravitationally bound to the satellite, may become a source of intracluster light. In extreme cases, this star formation in the ICM may be observable with the Euclid or James Webb Space Telescopes.
    - The average number of gaseous satellites per cluster decreases by factors of $\approx 1.5-2$ since $z \sim 1-2$, potentially explaining part of the decrease in cool ICM mass since then.

4. The onset of and cumulative energy injection from kinetic mode feedback from the SMBH correlates with the evolution of the cool ICM mass, where the cool ICM mass is maximal $\approx 1-2$ Gyr after the SMBH switches from thermal to kinetic mode feedback. As the cumulative kinetic energy injection increases, the cool ICM density decreases in an inside-out fashion. At a fixed redshift and cluster mass, clusters with undermassive SMBHs tend to have higher cool ICM masses.
    - The SMBHs in all galaxy clusters considered tend to switch to kinetic mode feedback at a characteristic cool ICM mass of $\sim 10^{10.5}$ $M_\odot$ at redshifts $\sim 3-5$, even though the ICM and the SMBH in the center of the BCG are spatially disconnected from each other.

- The preliminary comparisons of the Mg II column density between TNG-Cluster and observational data may suggest a surplus of Mg II gas in the simulations. If true, this may imply that the SMBH feedback in TNG-Cluster does not sufficiently destroy or prevent the formation of this gas in the cluster mass regime.

To summarize, the long-standing notion about satellite galaxies is that at infall, they are immediately stripped of their CGM, quickly lose their ISM and quench their star formation, and have little to no effect on their host. These results emphasize the need to revise this canonical picture, where massive satellites are able to retain their own CGM, ram pressure stripping and quenching can last up to many billions of years after infall, and satellites are a significant source of cool gas for their host halos. The satellite contributions to the multiphase halo gas have observational implications, where the satellite CGM shines in the soft X-ray, the stripped ISM provides Mg II ions that are detectable either in emission or in absorption of background quasar spectra, and some of the stripped material may continue cooling to the point of forming stars. Comparing these simulation outcomes with data from current and upcoming surveys will sharpen our understanding of galaxy formation and evolution, ultimately guiding the development of more sophisticated galaxy formation models for next-generation cosmological simulations.

10 Scope of the Results and Future Work

10.1 The Broader Context of Each Science Chapter

All new results presented in Chapters 6, 7, and 8, which are summarized above in Chapter 9, are part of the growing body of knowledge related to galaxy formation and evolution. These chapters were inspired by hundreds of preceding works that built up the foundations, and I, along with my collaborators, broadened these ideas. Here, I highlight how the papers I led fit into the recent work from the larger TNG community, where I am a coauthor on a number of these other papers.

TNG-Cluster First Results Splash

On the 14th of November, 2023, six papers presenting the first results of the new TNG-Cluster simulation appeared on the arXiv pre-print server: Ayromlou et al. (2023a); Lee et al. (2024); Lehle et al. (2024); Nelson et al. (2024); Rohr et al. (2024); Truong et al. (2024). TNG-Cluster enjoys a better spatial resolution compared to other recent cosmological hydrodynamical simulations of galaxy clusters – FLAMINGO (Schaye et al., 2023) and MillenniumTNG (Pakmor et al., 2023) – due to TNG-Cluster being a collection of zoom-ins rather than a full-volume simulation. While the full-volume studies are better suited for studies of the large scale structure, TNG-Cluster has the comparative advantage in studies of the BCG, cluster members, and the ICM. Accordingly, all six first results papers focus on the ICM, where I specifically concentrate on the interaction between the satellite CGM and ambient ICM. These theoretical efforts are accompanied by the recent and upcoming results from the eROSITA All Sky Survey Predehl et al. (eRASS; 2012) and Euclid Space Telescope (Euclid Collaboration et al., 2022).

I directly contributed as a coauthor to three of the first results works: Nelson et al. (2024); Lehle et al. (2024), and Ayromlou et al. (2023a). Nelson et al. (2024) present an overview of the TNG-Cluster simulation, where, at face value, TNG-Cluster reproduces many cluster scaling relations, validating the simulation. In this overview, Nelson et al. (2024) suggest that

satellites can contribute to a number of scaling relations by, for example, adding to the ICM magnetic field strength, depositing cool neutral Hydrogen gas in the ICM via ram pressure stripping, and adding tidally stripped stars to the intracluster light. Lehle et al. (2024) study the cluster cores, finding a continuum of strong cool-cores, weak cool-cores, and non-cool-cores across the 352 clusters. Satellites on radial orbits traveling close to the cluster cores can both deposit cool gas and perturb the surrounding gas to cool, affecting the thermodynamic properties of the cluster cores, and major mergers with massive cluster satellites can potentially even disrupt cool core clusters. Lastly, Ayromlou et al. (2023a) present an atlas of gas motions throughout the ICM, studying the radial velocities, velocity dispersions, and velocity structure function from the inner cluster regions $\lesssim 0.1 R_{200c}$ to the cluster outskirts $\sim R_{200c}$. While galaxy clusters tend to be baryonically closed (Ayromlou et al., 2023b) – meaning that the baryon to total matter mass fraction equals the global value $\Omega_{\mathrm{bar},0}/\Omega_{m,0}$ – there can still be large coherent and incoherent gas motions in the cluster outskirts, some of which may be caused by the bulk supersonic motions of satellite galaxies (Yun et al., 2019). Additionally, unrelaxed halos, which tend to be undergoing major mergers with massive satellites, have higher inflow and outflow gas velocities on average, demonstrating an effect of satellites on the ICM kinematics.

Beyond the coauthored papers, I actively participated in the collaboration during the initial analysis and discussion phases. This included, for example, improving the publicly released data analysis scripts and producing catalogs of backsplash and pre-processed galaxies. These contributions to the community facilitate future TNG-Cluster studies.

Cosmological Jellyfish Project with the IllustrisTNG Simulations

The results from Chapter 7 were originally presented as part of the *Jellyfish Galaxies with the IllustrisTNG* collaboration – along with Zinger et al. (2024), who presented the project itself, and Göller et al. (2023), who studied the star-forming activity of jellyfish galaxies. These two papers plus my own are based on the results from the Cosmological Jellyfish Project, which was hosted on the Zooniverse website[1], and these results are based on an internal pilot study by Yun et al. (2019). These statistical studies of simulated jellyfish from the IllustrisTNG simulations are complemented by the recent observational efforts from the LOFAR Two-meter Sky Survey Shimwell et al. (LoTSS 2017); Roberts et al. (LoTSS 2021a,b), the OSIRIS Mapping of Emission-line Galaxies (OMEGA Chies-Santos et al., 2015; Roman-Oliveira et al., 2018), and, perhaps most importantly, the GAs Stripping Phenomena in galaxies with MUSE (GASP Poggianti et al., 2017b).

[1] https://www.zooniverse.org/projects/apillepich/cosmological-jellyfish

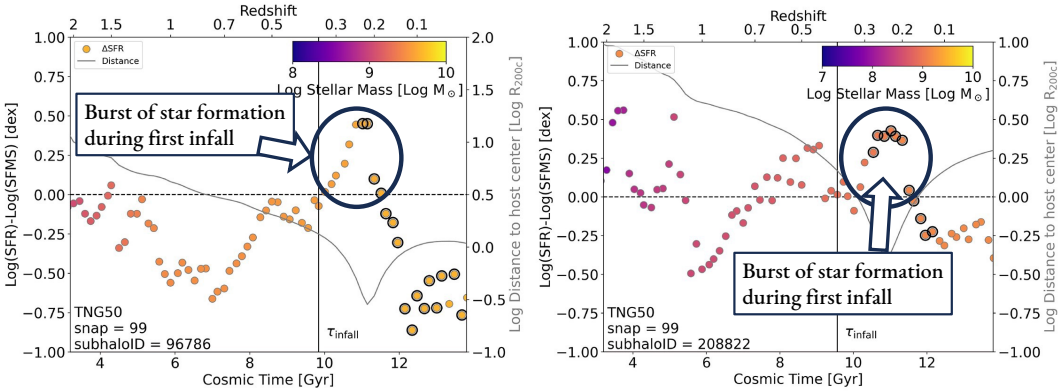

Figure 10.1: **Jellyfish undergo bursts of star formation during first infall**. Between infall (vertical black line marked by $\tau_{\rm infall}$) and pericentric passage (the minimum of the thin black curve), these two example jellyfish branches experience bursts of star-formation, putting their star formation rate (SFR) $\approx$ 0.5 dex above the star-forming main sequence (SFMS) for their stellar mass. Adapted from Göller et al. (2023).

I contributed as a coauthor to Zinger et al. (2024) and Göller et al. (2023), where I was a leading coauthor on Göller et al. (2023). Zinger et al. (2024) present the Cosmological Jellyfish Project, which asked trained citizen science volunteers whether images of gas surface density of satellite galaxies look like jellyfish galaxies or not. The volunteers classified $\approx$ 80, 000 galaxies from TNG50 and TNG100, resulting in $\approx$ 5300 ($\approx$ 6.6%) jellyfish galaxies , by far the largest sample of simulated or observed jellyfish galaxies to date. I then tracked the jellyfish across the snapshots, where many of the galaxies were inspected at different points in their evolution (at different snapshots). This resulted in 5023 and 9052 unique inspected branches in TNG50 and TNG100 respectively, where 935 ($\approx$ 19%) and 922 ($\approx$ 10%) branches in TNG50 and TNG100 were classified as a jellyfish at least once in their lifetime. Göller et al. (2023) find no enhanced population-wide star-formation in the TNG50 jellyfish, perhaps in contradiction to recent results from GASP (Vulcani et al., 2018). However, $\approx$ 75% of the jellyfish undergo a period of enhanced star-formation during the first infall, which is thought to be caused by a compressed ISM due to the ram pressure (Roberts et al., 2022b). Fig. 10.1 shows the evolution of the star formation activity, here as the difference between the instantaneous star formation rate and the star-forming main sequence (SFMS), for two example jellyfish galaxies. Between infall (the vertical black line marked by $\tau_{\rm infall}$ and pericentric passage (when the thin black curves reach a minimum), the star formation rate increases to $\approx$ 0.5 dex above the SFMS. Additionally, Göller et al. (2023) find that star formation occurs not only within the stellar bodies but also in the jellyfish tails in the TNG simulations. Some of this star-forming gas and

these newly formed stars are not gravitationally bound to the jellyfish galaxy, meaning that they may contribute to the halo star formation rate discussed further in Chapter 8.

Lastly, I am co-supervising Shalini Kurinchi-Vendhan, a former Fulbright Fellow now Master Student, who is studying the effect of ram pressure on AGN fractions in jellyfish galaxies. This work is still in preparation, but preliminary results show that jellyfish galaxies have more luminous SMBHs and, thereby, higher AGN fractions than the overall population of satellite galaxies at the same mass. I expect these results to be published soon.

With the release of these papers, our collaboration publicly released the results of the Cosmological Jellyfish Project, where I contributed jellyfish branches[2]. Additionally, based on the successes of this project, observational groups have also began using the Zooniverse platform to classify jellyfish galaxies[3].

Understanding the Evolution and Structure of Cool Halo Gas

The study of the evolution of the cool cluster gas in Chapter 8 is part of a series of papers studying the multiphase halo gas in TNG and TNG-like halos, where the results presented in this thesis are the first to extend to the multiphase halo results to a statistical sample of massive clusters. Earlier works have studied the cool halo gas around Milky Way- and Andromeda-like hosts (Ramesh et al., 2023b) and elliptical galaxies (Nelson et al., 2020), finding that some of the cool halo gas is associated to satellite galaxies.

However, other results presented in Chapter 8, such as the correlation of the evolution of the cool ICM mass with the onset of kinetic mode feedback from the SMBH, has currently only been studied in TNG-Cluster, limiting the scope of these results. In Fig. 10.2, I expand the initial stages of this analysis across the three flagship TNG simulations, in addition to TNG-Cluster. Here I plot the cool halo gas mass, where the cool halo gas here is all gas gravitationally bound to the central galaxy in the radial aperture $[0.1R_{200c}, 1.0R_{200c}]$ with temperature $\leq 10^{4.5}$ K, as a function of host mass at redshifts 2 (left), 0.5 (center), and 0 (right). By widening the halo mass range of interest, the structure and evolution of the cool halo gas mass - total halo mass relation becomes more apparent. Of particular interest here is how the characteristic total halo and cool halo gas mass – where the cool halo gas mass begins to flatten out or even decrease rather than increase with halo mass – change with redshift. At $z = 2$ (left), these masses are not covered even by the TNG-Cluster, as the cool halo gas mass increases with halo mass for all halo masses considered. At lower redshifts $z \lesssim 0.5$, however, this is no longer the case. At $z = 0.5$, the cool halo gas mass - total halo gas mass relation flattens out at a halo mass of $\sim 10^{14}$ $M_\odot$, at a cool halo gas mass of $\sim 10^{10.5-11}$ $M_\odot$;

[2] https://www.tng-project.org/data/docs/specifications/#sec5_3
[3] https://www.zooniverse.org/projects/cbellhouse/fishing-for-jellyfish-galaxies

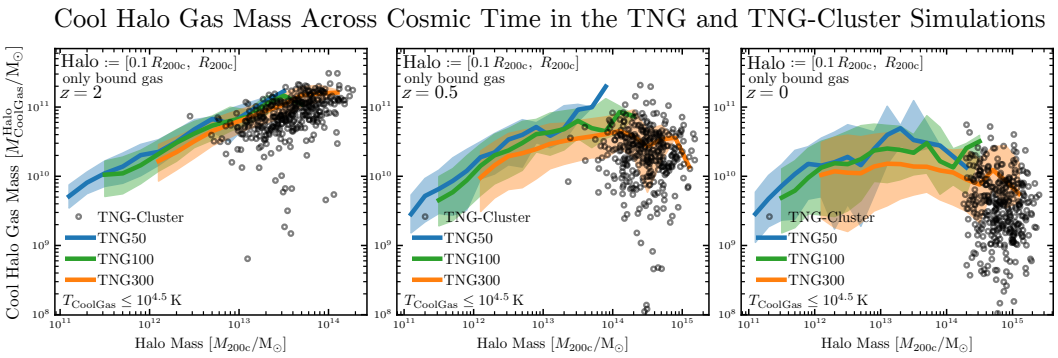

Figure 10.2: **Cool halo gas evolution in the TNG and TNG-Cluster simulations** From left to right, I plot the cool halo gas mass as a function of halo mass for TNG-Cluster and the three flagship TNG simulations at redshifts 2, 0.5, and 0. At $z = 2$, the cool halo gas mass increases with halo mass across the halo mass ranges considered. At $z = 0.5$, the cool halo gas mass increases with halo mass until $M_{200c} \sim 10^{14}\,M_\odot$, where the trend then flattens out with halo mass. Today, the cool halo mass increase with halo mas until $M_{200c} \sim 10^{13-13.5}\,M_\odot$, where it flattens out. The characteristic cool halo gas mass, where the trend with halo mass begins to flatten, appears to be redshift, and perhaps resolution, dependent. Understanding the evolution of this relation is the focus on an upcoming work (Rohr et al. in prep.).

today, at $z = 0$, this occurs at a halo mass of $\sim 10^{13-13.5}\,M_\odot$, at a cool halo gas mass of $\sim 10^{10-10.5}\,M_\odot$. Additionally, at a fixed halo mass, the average cool halo gas mass increases by factors of $\lesssim 2$ from TNG300 to TNG50, suggesting that numerical resolution could be important, although the median relations are all within the scatter of each other (see below for more details on numerical resolution). The exact description of this relation across halo mass, cosmic time, and numerical resolution is the focus of an upcoming work (Rohr et al. in prep.).

10.2 Limitations of the Numerical Resolution and Galaxy Formation Model

The results of this thesis are first and foremost based on the outcomes of the TNG-Cluster and TNG50 cosmological galaxy simulations, which employ the TNG galaxy formation model (see Chapter 4.3 for details). These simulations have been shown to reproduce a number of observed scaling relations across a range galaxy stellar masses, host halo masses, and numerical resolutions, affirming the realism of these simulations. Regardless, other cosmological simulations with other galaxy formation models may yield different results (see Chapter 4.2 for an overview; see also Vogelsberger et al. 2020; Crain & Van De Voort 2023

for recent reviews). Some of the results may even depend on the resolution of the simulation, while still using the same galaxy formation model. Here, I briefly reiterate the key results that may vary in other simulations before proposing a new style of simulation that could solve many issues present here.

Starting from the small scale, the structure of cool gas clouds moving with respect to a hot background, such as ram pressure stripped cool clouds in the ICM, is likely not converged even at the mass resolution of TNG50 ($m_{\rm bar} \approx 8.5{\times}10^4\,{\rm M}_\odot$), which is a factor of ≈ 130 times better resolution than in TNG-Cluster ($m_{\rm bar} \approx 1.1 \times 10^7\,{\rm M}_\odot$) (Nelson et al., 2020; Ramesh et al., 2024). Cloud-crushing simulations suggest that at least ≈ 16 resolution elements are necessary to accurately resolve the cool gas clouds (e.g., Sparre et al., 2020; Fielding & Bryan, 2022; Gronke et al., 2022), which corresponds to a cool cloud mass of $\sim 10^6\,{\rm M}_\odot$ in TNG50 (which is achieveable; Ramesh et al., 2024) or $\sim 10^{8.5}\,{\rm M}_\odot$ in TNG-Cluster (likely only achievable in the largest cool clouds). This can manifest itself in population averaged quantities, such as in the total number and mass of cool halo gas (Nelson et al., 2020; Ramesh et al., 2024, Fig. 10.2). This may also affect ram pressure stripping, the survival of the stripped gas (alternatively, the mixing of the stripped gas with the ambient medium), or simply the ability to identify jellyfish-like features, where TNG50 has a higher fraction of jellyfish galaxies than TNG100, even when controlling for the satellite stellar and total host mass (Zinger et al., 2024). There could also be other physical processes, such as radiation pressure, cosmic rays, non-ideal MHD, viscous momentum transfer, thermal evaporation, and explicit modeling of molecular gas, which may be important for the survival of cool clouds and are not implemented here (e.g.; Cowie & Binney, 1977; Nulsen, 1982, see also Zinger et al. 2018b; Kukstas et al. 2022). Despite this, the TNG simulations still return satellite quenched fractions and gas contents that are consistent with the observed populations (e.g., Stevens et al., 2019; Donnari et al., 2021a; Stevens et al., 2021).

Star formation in the TNG model is based on a density criterion, where gas denser than $> 0.1\,{\rm cm}^{-3}$ follows an effective equation of state and is allowed to form stars without any additional physically-motivated criteria. This has been shown work well within galactic disks, reproducing observables such as the galaxy stellar mass function and stellar-halo mass relation (Pillepich et al., 2018b), the size-mass relation (Genel et al., 2018), and the mass-metallicity relation (Torrey et al., 2019); however, it is unclear how well this model works for star-formation that occurs outside of the galactic disk, namely either in ram pressure stripped tails of jellyfish galaxies (Göller et al., 2023; Lora et al., 2024) or in the halo itself, away from any galaxy (Ahvazi et al., 2024b, Chapter 8). Thereby, the total amount of star formation occurring outside of the disk in these simulations may change with a more physically-motivated model for star formation (see also discussions in Puchwein et al., 2010; Mandelker et al., 2018).

Additionally, the choice of stellar feedback in the form of decoupled winds may impact the gas to total halo fraction, the closure radius, the radius within which the baryon fraction reaches the global average, and the mass inflow and outflow rates throughout the halo (Ayromlou et al., 2023b; Wright et al., 2024).

Lastly, the thermodynamic composition of both the ISM and halo gas (CGM and maybe ICM) likely depend on the SMBH accretion and feedback model. In low mass halos $\lesssim 10^{12}\,M_\odot$ in TNG, SMBHs tend to be in a high-accretion state and release thermal energy into the surrounding ISM. Because much of this ISM is star-forming and therefore on the effective equation of state, the temperature of this gas is non-physical and may not be as effective. However, even when using the effective equation of state, thermal SMBH feedback can still impact the stellar and gaseous contents in low mass halos (Pillepich et al., 2018a), and the exact details depend on the implementation (e.g., Koudmani et al., 2022). This may affect the effect the SMBHs in jellyfish galaxies, where recent observations suggest that galaxies undergoing ram pressure have elevated AGN activity compared to satellites and centrals of the same mass (Poggianti et al., 2017a; Peluso et al., 2022). In massive halos $\gtrsim 10^{12}\,M_\odot$, the SMBHS tend to accrete in a low-accretion mode, where the feedback is in the form of kinetic energy. While this mode is primarily responsible for quenching star-formation in the galaxy itself (Weinberger et al., 2017; Nelson et al., 2018a), it also has important effects on the density and temperature, for example, of the halo gas (Zinger et al., 2020). Different implementations of SMBH feedback in massive halos yield different halo gas fractions, closure radii, and inflow and outflow rates (Davies et al., 2020; Terrazas et al., 2020; Ayromlou et al., 2023b; Wright et al., 2024). It is also unclear if the kinetic mode feedback is strong enough at the cluster scale $\sim 10^{15}\,M_\odot$, where the BCG stellar masses are $\approx 0.1-0.2$ dex above observations (Nelson et al., 2024), and there may be an excess of cool Mg II gas in the halos compared to observations (Chapter 8).

In short, the TNG model quite successfully reproduces a broad range of observable scaling relations across a range of galaxy stellar and total halo masses, but no model is perfect. Knowing the potential short-comings of the model allows for better interpretation of the results, and disagreements with observations open avenues for improvement.

10.2.1 The Future of Idealized Jellyfish Simulations

Beyond cosmological simulations, jellyfish galaxies can also be simulated in idealized wind tunnel experiments (see Section 7.1 for details and references). While these wind tunnels allow for high resolution simulations and controlled experiments, they lack cosmological realism and applicability to observed jellyfish galaxies. In Fig. 10.3, I present a new idealized simulation scheme to study jellyfish galaxies and the halo gas in detail. Here, an idealized disk

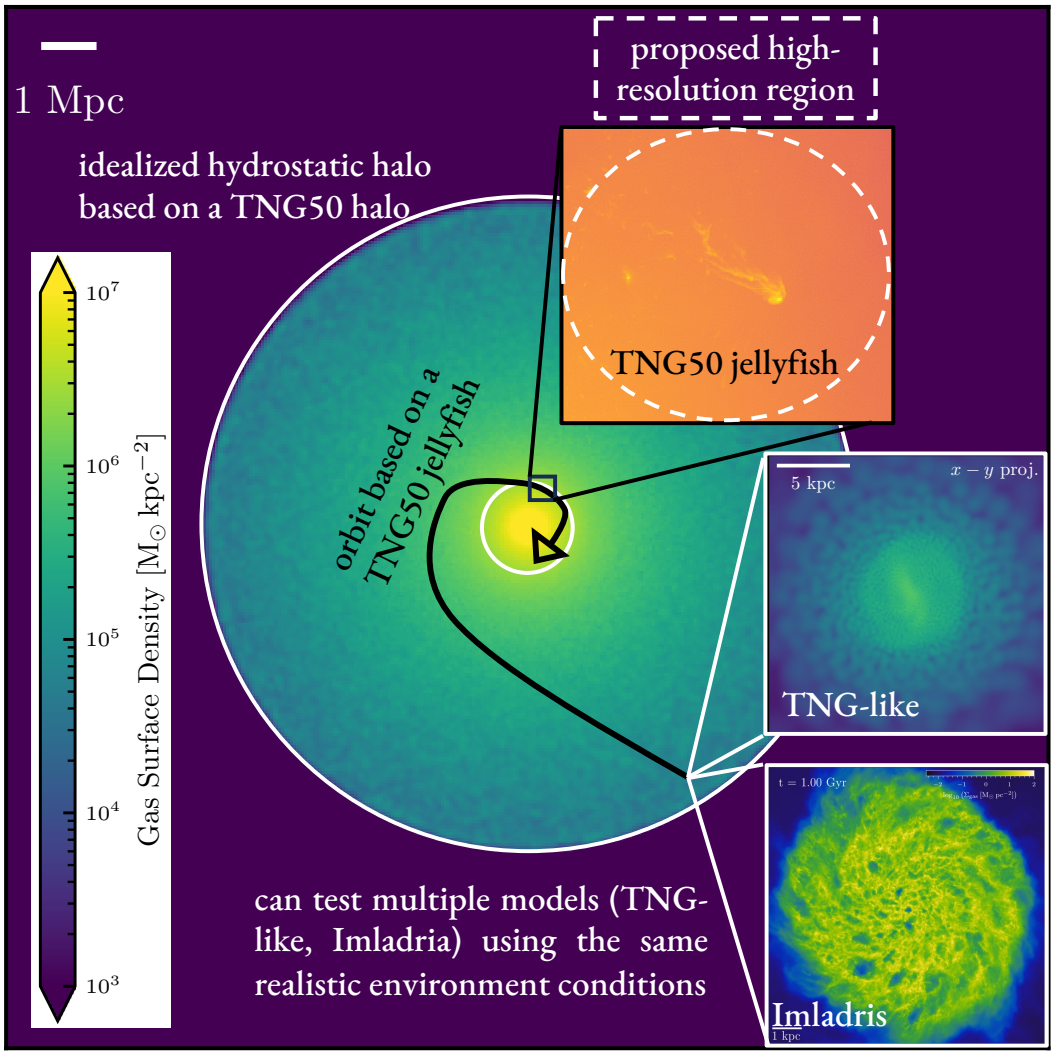

Figure 10.3: **Schematic for the new idealized jellyfish simulation**. This simulation takes an idealized disk galaxy, based on some stellar and gaseous parameters and employing a model for galaxy formation, and evolves it through a hydrostatic halo following the orbit of a TNG50 jellyfish (black inset). The halo gas properties, satellite stellar and gaseous properties, and the orbital parameters are based on the outcomes of the cosmological simulation TNG50, and all of these can be varied in the simulation setup. Here, I show two LMC-like satellites (white insets), one of which uses a TNG-like galaxy formation model at TNG50 resolution $m_{\rm bar} \approx 8.5 \times 10^4\,{\rm M}_\odot$ and one using the Imladris model (see text for details) at $m_{\rm bar} \approx 20\,{\rm M}_\odot$ resolution. I propose to increase the resolution only in the vicinity of the satellite galaxy, allowing for much higher resolution than what would otherwise be possible. The inner white circle marks the virial radius, and the outer white circle marks the approximate edge of the simulated halo's extent at $\sim 7R_{\rm 200c}$. Image credit for the LMC-like galxy run with the Imladris model: Matthew C. Smith.

galaxy is injected into the outskirts of a hydrostatic halo and follows the orbital trajectory of a TNG50 jellyfish galaxy. The thermodynamic properties of the halo gas, the stellar and gas masses of the satellite, and the orbital parameters are inspired from the outcome of the cosmological simulation TNG50. This ensures a control baseline for all experiments, since the outcome from TNG50 is already known and trusted (black outlined inset). This concept of throwing a idealized satellite into a halo has been used before (Tonnesen & Bryan, 2009), but the novelty of this setup is the proposed refinement scheme to better the numerical resolution only near the satellite. In doing so, the satellite and local ambient halo gas are resolved in high resolution, while the portions of the halo are left at lower resolution, significantly decreasing the total computational time required compared to running the entire simulation at the highest resolution. Additionally, I propose to restrict the gas cooling within the core of the halo $\lesssim 0.1 R_{200c}$, which saves additional computational time and prevents the halo from collapsing on itself.

This setup allows for varying parameters related to the halo, the satellite, the orbit, or even the galaxy formation model itself. In Fig. 10.3, I show two idealized LMC-like galaxies (white insets in the lower right), one using a TNG-like model (i.e., an effective equation of state and similar galactic winds) at TNG50 resolution $m_{\rm bar} \approx 8.5 \times 10^4\,{\rm M}_\odot$ and one using the Imladris model at $m_{\rm bar} \approx 20\,{\rm M}_\odot$ resolution (Smith et al. in prep.). The Imladris model includes an explicit treatment of the multiphase ISM to temperatures $\gtrsim 10$ K; a Jeans mass threshold for star formation; stellar feedback from winds, Type Ia supernovae, and Type II supernovae; local radiation effects from photoionization and photoelectric feedback; and the ability to track individual massive stars and their supernovae (Smith et al., 2018, 2021, Smith et al. in prep.). Such a sophisticated galaxy formation model is intended to be used only at high resolution $m_{\rm bar} \lesssim 10^2\,{\rm M}_\odot$, which is currently not feasible in cosmological simulations run to $z = 0$. This setup however, where the high resolution region is confined to the vicinity of the jellyfish, allows for a comparison of galaxy formation models where it would otherwise not be possible.

In the initial simulation suite, I plan to investigate the following questions by comparing the outcomes of the TNG-like and Imladris models:

- How do the jellyfish in a TNG-like model relate to those in the Imladris model? How do these relate to the jellyfish in TNG50?
- How does ram pressure affect the ISM gas properties? Is there an increased star-formation rate in galaxies undergoing strong ram pressure?
- When and where does star-formation occur in the tails of jellyfish galaxies? How does stellar feedback affect the jellyfish tails?

- What happens to the stripped gas in the tails once it is no longer bound to the galaxy? Does the cold gas remain cold? What is the role of magnetic fields here?
- How does ram pressure affect the SMBH accretion rate? How does thermal SMBH feedback affect the ISM in jellyfish galaxies?

After the initial study, I plan to expand on the realism of this setup by increasing the sophistication of the halo gas. Cosmological halos are not in fact in constant hydrostatic equilibrium but instead have large velocity motions due to accretion, galactic feedback, and satellites, and this velocity structure can significantly impact the effective ram pressure felt by the infalling satellite (Ayromlou et al., 2021b). One way to mimic this would be to include gas cooling and a galaxy formation model for the central galaxy as well, in a way such that the halo remains stable on cosmological timescales and that simulation runs to completion within the timescale of a post-doc position. If achieved, this simulation setup may become standard in the field for studies of both satellite galaxies and the halo itself.

11 Concluding Thoughts

At the beginning of the Ph.D., I did not even know what a jellyfish galaxy was; I had heard of ram pressure stripping only in an introductory astronomy course during my undergraduate studies, and the cosmic baryon cycle sounded like nothing more than a buzz-word to me. Four years later and I am being invited to international conferences around the world to present the latest cutting-edge results on these topics. What an amazing journey this has been.

I have become an expert in using the TNG-Cluster and IllustrisTNG cosmological simulations to understand how satellites are affected by their hosts and how satellites affect their hosts in return. I have learned how to critically evaluate not only my own results but also the results from others, whether they use the same simulations, other simulations, or observations. I have shown where the canonical theories of galaxy evolution hold, and, perhaps more importantly, where they do not. I have approached these astrophysical problems from the perspective of wanting to learn something about how galaxies evolve using the simulations, but also from questioning the simulations' validity by providing observational tests based on these implications. In this thesis, I have demonstrated that I understand the simulation outputs, that I can put these results into a broader context, and that I can provide these falsifiable tests of the models.

The future is bright for this field. The observations are catching up, or have even caught up, to the simulation predictions from the past roughly ten years. It has been incredible to work with the most well-cited and, in my opinion, most successful cosmological simulations of galaxies and galaxy clusters, but there is always room for improvement. After the four years of the Ph.D., I am feeling more motivated and confident than ever that I can help write and run the next set of simulations. More than anything, I am excited to see which tensions between observations and the current simulations can be resolved in future models. I am on my way to helping develop galaxy formation models for the next generation of cosmological simulations!

List of Figures

List of Tables

Publications List

As a first author (all except item 1. were used in this thesis):

4. Rohr, E., Pillepich, A., Nelson, D., et al. in review with MNRAS: "The cooler past of the intracluster medium in TNG-Cluster".
3. Rohr, E., Pillepich, A., Nelson D. et al. (2024): "The hot circumgalactic media of massive cluster satellites in the TNG-Cluster simulation: existence and detectability". A&A, 686, A86.
2. Rohr, E., Pillepich, A., Nelson D. et al. (2023): "Jellyfish galaxies with the IllustrisTNG simulations - when, where, and for how long does ram pressure stripping of cold gas occur?". MNRAS, 524, 3502.
1. Rohr, E., Feldmann, R., Bullock, J. et al. (2022): "The galaxy-halo size relation of low-mass galaxies in FIRE". MNRAS, 510, 3967.

As a contributing author (each work was used in this thesis):

5. Ayromlou, M., Nelson, D., Pillepich A. et al. incl. Rohr, E. accepted: "An Atlas of Gas Motions in the TNG-Cluster Simulation: from Cluster Cores to the Outskirts". A&A. arXiv.2311.06339.
4. Lehle, K., Nelson D., Pillepich A. et al. incl. Rohr, E. (2024): "The heart of galaxy clusters: demographics and physical properties of cool-core and non-cool-core halos in the TNG-Cluster simulation". A&A, 687, A129.
3. Nelson, D., Pillpeich, A., Ayromlou M. et al. incl. Rohr, E. (2024). "Introducing the TNG-Cluster Simulation: overview and physical properties of the gaseous intracluster medium". A&A, 686, A157.
2. Zinger, E., Pillepich, A., Joshi, G. et al. incl. Rohr, E. (2024): "Jellyfish galaxies with the IllustrisTNG simulations - citizen-science results towards large distances, low-mass hosts, and high redshifts". MNRAS, 527, 8257.
1. Göller, J., Joshi, G., Rohr, E. et al. (2023): "Jellyfish galaxies with the IllustrisTNG simulations - No enhanced population-wide star formation according to TNG50". MNRAS, 525, 3551.

Bibliography

Abdullah M. H., Wilson G., Klypin A., Old L., Praton E., Ali G. B., 2020, ApJS, 246, 2

Abdullah M. H., Wilson G., Klypin A., Ishiyama T., 2023, ApJ, 955, 26

Agertz O., Kravtsov A. V., 2015, ApJ, 804, 18

Agertz O., Teyssier R., Moore B., 2011, MNRAS, 410, 1391

Agertz O., Kravtsov A. V., Leitner S. N., Gnedin N. Y., 2013, ApJ, 770, 25

Ahumada R., et al., 2020, ApJSS, 249, 3

Ahvazi N., et al., 2024a, arXiv, p. arXiv:2403.04839

Ahvazi N., Sales L. V., Doppel J. E., Benson A., D'Souza R., Rodriguez-Gomez V., 2024b, MNRAS, 529, 4666

Allen S. W., Evrard A. E., Mantz A. B., 2011, ARA&A, 49, 409

Alpher R. A., Bethe H., Gamow G., 1948, PhRv, 73, 803

Anand A., Nelson D., Kauffmann G., 2021, MNRAS, 504, 65

Anand A., Kauffmann G., Nelson D., 2022, MNRAS, 513, 3210

Ayromlou M., Nelson D., Yates R. M., Kauffmann G., White S. D., 2019, MNRAS, 487, 4313

Ayromlou M., Nelson D., Yates R. M., Kauffmann G., Renneby M., White S. D., 2021a, MNRAS, 502, 1051

Ayromlou M., Kauffmann G., Yates R. M., Nelson D., White S. D., 2021b, MNRAS, 505, 492

Ayromlou M., et al., 2023a, arXiv:2311.06339

Ayromlou M., Nelson D., Pillepich A., 2023b, MNRAS, 524, 5391

Babcock W. H., 1939, LicOB, 498, 41

Babyk I. V., McNamara B. R., Nulsen P. E. J., Hogan M. T., Vantyghem A. N., Russell H. R., Pulido F. A., Edge A. C., 2018, ApJ, 857, 32

Bagla J. S., 2002, JApA, 23, 185

Bahé Y. M., McCarthy I. G., 2015, MNRAS, 447, 969

Bahe Y. M., McCarthy I. G., Crain R. A., Theuns T., 2012, MNRAS, 424, 1179

Bahé Y. M., McCarthy I. G., Balogh M. L., Font A. S., 2013, MNRAS, 430, 3017

Baldry I. K., et al., 2012, MNRAS, 421, 621

Balogh M. L., Morris S. L., 2000, MNRAS, 318, 703
Barfety C., et al., 2022, ApJ, 930, 25
Barnes J., Hut P., 1986, Nature, 324, 446
Barnes D. J., et al., 2018, MNRAS, 481, 1809
Baugh C. M., 2006, RPPh, 69, 3101
Beckmann R. S., et al., 2019, A&A, 631, A60
Behroozi P. S., Conroy C., Wechsler R. H., 2010, ApJ, 717, 379
Bekki K., 2009, MNRAS, 399, 2221
Bell E. F., et al., 2004, ApJ, 608, 752
Benítez-Llambay A., Navarro J. F., Abadi M. G., Gottlöber S., Yepes G., Hoffman Y., Steinmetz M., 2013, ApJL, 763, L41
Berger M. J., Colella P., 1989, JCoPh, 82, 64
Berger M. J., Oliger J., 1984, JCoPh, 53, 484
Berlind A. A., Weinberg D. H., 2002, ApJ, 575, 587
Binney J., 1977, ApJ, 215, 483
Birnboim Y., Dekel A., 2003, MNRAS, 345, 349
Birnboim Y., Padnos D., Zinger E., 2016, ApJL, 832, L4
Bluck A. F., et al., 2020, MNRAS, 499, 230
Blumenthal G. R., Pagels H., Primack J. R., 1982, Nature, 299, 37
Blumenthal G. R., Faber S. M., Primack J. R., Rees M. J., 1984, Nature, 311, 517
Bogdan A., et al., 2013, ApJ, 772, 97
Bond J. R., Szalay A. S., Turner M. S., Bond J. R., Szalay A. S., Turner M. S., 1982, PhRvL, 48, 1636
Bond J. R., Kofman L., Pogosyan D., 1996, Nature, 380, 603
Bondi H., 1952, MNRAS, 112, 195
Bondi H., Hoyle F., 1944, MNRAS, 104, 273
Borgani S., Plionis M., Kolokotronis V., 1999, MNRAS, 305, 866
Boselli A., Fossati M., Sun M., 2022, A&ARv, 30, 1
Brinchmann J., Charlot S., White S. D., Tremonti C., Kauffmann G., Heckman T., Brinkmann J., 2004, MNRAS, 351, 1151
Bromm V., Yoshida N., 2011, ARAA, 49, 373
Brown T., et al., 2016, MNRAS, 466, 1275
Bryan G. L., et al., 2014, ApJSS, 211, 19
Bulbul E., et al., 2024, A&A, 685, A106
Burchett J. N., Tripp T. M., Daniel Wang Q., Willmer C. N., Bowen D. V., Jenkins E. B., 2018, MNRAS, 475, 2067

Bykov A. M., Churazov E. M., Ferrari C., Forman W. R., Kaastra J. S., Klein U., Markevitch M., de Plaa J., 2015, SSRv, 188, 141
Campitiello M. G., et al., 2021, ApJ, 911, 144
Cavaliere A., Fusco-Femiano R., 1976, A&A, 49, 137
Cayatte V., van Gorkom J. H., Balkowski C., Kotanyi C., Cayatte V., van Gorkom J. H., Balkowski C., Kotanyi C., 1990, AJ, 100, 604
Cayatte V., Kotanyi C., Balkowski C., van Gorkom J. H., Cayatte V., Kotanyi C., Balkowski C., van Gorkom J. H., 1994, AJ, 107, 1003
Chabrier G., 2003, PASP, 115, 763
Chadayammuri U., Bogdan A., Oppenheimer B., Kraft R., Forman W., Jones C., 2022, ApJL, 936, L15
Chaturvedi A., Tonnesen S., Bryan G. L., Popping G., Hilker M., Serra P., Genel S., 2024, arXiv:2404.16926
Chen H. W., Lanzetta K. M., Webb J. K., Barcons X., 1997, ApJ, 498, 77
Chen Z., et al., 2024, MNRAS, 527, 8950
Chies-Santos A. L., et al., 2015, MNRAS, 450, 4458
Choi W., Kim C.-G., Chung A., 2022, ApJ, 936, 133
Choudhury P. P., Sharma P., Quataert E., 2019, MNRAS, 488, 3195
Churazov E., et al., 2012, MNRAS, 421, 1123
Cicone C., et al., 2014, A&A, 562, A21
Clerc N., et al., 2020, MNRAS, 497, 3976
Cole S., Lacey C. G., Baugh C. M., Frenk C. S., 2000, MNRAS, 319, 168
Colless M., et al., 2001, MNRAS, 328, 1039
Comparat J., et al., 2020, A&A, 636, A97
Comparat J., et al., 2022, A&A, 666, A156
Cortese L., Gavazzi G., Boselli A., Franzetti P., Kennicutt R. C., O'Neil K., Sakai S., 2006, A&A, 453, 847
Cortese L., Catinella B., Smith R., 2021, PASP, 38, e035
Costanzi M., et al., 2019, MNRAS, 488, 4779
Couchman H. M. P., 1991, ApJL, 368, L23
Cowie L. L., Binney J., 1977, ApJ, 215, 723
Crain R. A., Van De Voort F., 2023, ARAA, 61, 473
Crain R. A., et al., 2015, MNRAS, 450, 1937
Crawford C. S., Hatch N. A., Fabian A. C., Sanders J. S., 2005, MNRAS, 363, 216
Croton D. J., et al., 2006, MNRAS, 365, 11
Cui W., et al., 2018, MNRAS, 480, 2898

Dalla Vecchia C., Schaye J., 2012, MNRAS, 426, 140
Davé R., Anglés-Alcázar D., Narayanan D., Li Q., Rafieferantsoa M. H., Appleby S., 2019, MNRAS, 486, 2827
Davies L. J., et al., 2019, MNRAS, 483, 5444
Davies J. J., Crain R. A., Oppenheimer B. D., Schaye J., 2020, MNRAS, 491, 4462
Davis M., Efstathiou G., Frenk C. S., White S. D. M., 1985, ApJ, 292, 371
Dawson K. S., et al., 2013, AJ, 145, 10
Dawson K. S., et al., 2016, AJ, 151, 44
Dehnen W., 2000, ApJ, 536, L39
Dekel A., Birnboim Y., 2006, MNRAS, 368, 2
Dekel A., Birnboim Y., 2008, MNRAS, 383, 119
Dekel A., Silk J., 1986, ApJ, 303, 39
Dey A., et al., 2019, AJ, 157, 168
Di Mascolo L., et al., 2023, Nature, 615, 809
Di Matteo T., Springel V., Ilernquist L., 2005, Nature, 433, 604
Di Valentino E., et al., 2021, CQGra, 38, 153001
Dolag K., Borgani S., Murante G., Springel V., 2009, MNRAS, 399, 497
Donahue M., Voit G. M., 2022, PhR, 973, 1
Donnari M., et al., 2019, MNRAS, 485, 4817
Donnari M., et al., 2021a, MNRAS, 500, 4004
Donnari M., Pillepich A., Nelson D., Marinacci F., Vogelsberger M., Hernquist L., 2021b, MNRAS, 506, 4760
Dressler A., 1980, ApJ, 236, 351
Dressler A., Lynden-Bell D., Burstein D., Davies R. L., Faber S. M., Terlevich R., Wegner G., 1987, ApJ, 313, 42
Dressler A., Smail I., Poggianti B. M., Butcher H., Couch W. J., Ellis R. S., Oemler Jr. A., 1999, ApJSS, 122, 51
Driver S. P., et al., 2022, MNRAS, 513, 439
Dutta R., et al., 2023, MNRAS, 522, 535
Ebeling H., Stephenson L. N., Edge A. C., 2014, ApJL, 781, L40
Eggen O. J., Lynden-Bell D., Sandage A. R., 1962, ApJ, 136, 748
Einasto J., 1965, TrAlm, 5, 87
Einasto J., Saar E., Kaasik A., Chernin A. D., 1974, Nature, 252, 111
Einstein A., 1916, AnP, 354, 769
Emerick A., Low M.-M. M., Grcevich J., Gatto A., 2016, ApJ, 826, 148
Emsellem E., et al., 2022, A&A, 659, A191

Engler C., et al., 2020, MNRAS, 500, 3957
Euclid Collaboration et al., 2022, A&A, 662, A112
Faber S. M., Jackson R. E., 1976, ApJ, 204, 668
Fabian A. C., 1994, ARA&A, 32, 277
Fabian A. C., 2011, ARA&A, 50, 455
Fabian A. C., Sanders J. S., Crawford C. S., Conselice C. J., Gallagher J. S., Wyse R. F., 2003, MNRAS, 344, L48
Fall S. M., Efstathiou G., 1980, MNRAS, 193, 189
Fardal M. A., Katz N., Gardner J. P., Hernquist L., Weinberg D. H., Davé R., 2000, ApJ, 562, 605
Faucher-Giguère C.-A., Oh S. P., 2023, ARA&A, 61, 131
Faucher-Giguère C. A., Lidz A., Zaldarriaga M., Hernquist L., 2009, ApJ, 703, 1416
Faucher-Giguere C. A., Keres D., Ma C. P., 2011, MNRAS, 417, 2982
Ferland G. J., et al., 2013, RMxAA, 49, 137
Ferland G. J., et al., 2017, RMxAA, 53, 385
Ferrarese L., Merritt D., 2000, ApJL, 539, L9
Ferrière K. M., 2001, RvMP, 73, 1031
Field G. B., Goldsmith D. W., Habing H. J., Field G. B., Goldsmith D. W., Habing H. J., 1969, ApJL, 155, L149
Fielding D. B., Bryan G. L., 2022, ApJ, 924, 82
Fielding D. B., et al., 2020, ApJ, 903, 32
Fournier M., Grete P., Brüggen M., Glines F. W., O'Shea B. W., 2024, arXiv:2406.05044
Franchetto A., et al., 2021, ApJL, 922, L6
Fraternali F., Binney J. J., 2008, MNRAS, 386, 935
Freedman W. L., et al., 2001, ApJ, 553, 47
Fresco A. Y., Peroux C., Merloni A., Comparat J., Szakacs R., Weng S., 2024, A&A, 684, A136
Friedmann A., 1922, ZPhy, 10, 377
Fujita Y., 2004, PASJ, 56, 29
Fukugita M., Hogan C. J., Peebles P. J. E., 1998, ApJ, 503, 518
Fumagalli A., Costanzi M., Saro A., Castro T., Borgani S., 2024, A&A, 682, A148
Gaburov E., Nitadori K., 2011, MNRAS, 414, 129
Garling C. T., Peter A. H., Spekkens K., Sand D. J., Hargis J., Crnojević D., Carlin J. L., 2024, MNRAS, 528, 365
Gavazzi G., Jaffe W., 1987, A&A, 186, L1
Gavazzi G., Scodeggio M., 1996, A&A, 312, L29

Gavazzi G., Boselli A., Mayer L., Iglesias-Paramo J., Vilchez J. M., Carrasco L., 2001, ApJL, 563, L23

Gebhardt K., et al., 2000, ApJ, 539, L13

Geller M. J., Huchra J. P., 1989, Science, 246, 897

Genel S., Vogelsberger M., Nelson D., Sijacki D., Springel V., Hernquist L., 2013, MNRAS, 435, 1426

Genel S., et al., 2014, MNRAS, 445, 175

Genel S., et al., 2018, MNRAS, 474, 3976

Gingold R. A., Monaghan J. J., 1977, MNRAS, 181, 375

Giovanelli R., Haynes M. P., Giovanelli R., Haynes M. P., 1985, ApJ, 292, 404

Göller J., Joshi G. D., Rohr E., Zinger E., Pillepich A., 2023, MNRAS, 525, 3551

Goto T., Yamauchi C., Fujita Y., Okamura S., Sekiguchi M., Smail I., Bernardi M., Gomez P. L., 2003, MNRAS, 346, 601

Goubert P. H., Bluck A. F., Piotrowska J. M., Maiolino R., 2024, MNRAS, 528, 4891

Goulding A. D., et al., 2016, ApJ, 826, 167

Grishin K. A., Chilingarian I. V., Afanasiev A. V., Fabricant D., Katkov I. Y., Moran S., Yagi M., 2021, Nature Astronomy, 5, 1308

Gronke M., Oh S. P., Ji S., Norman C., 2022, MNRAS, 511, 859

Gullieuszik M., et al., 2017, ApJ, 846, 27

Gullieuszik M., et al., 2020, ApJ, 899, 13

Gunn J. E., Gott J. Richard I., 1972, ApJ, 176, 1

Guth A. H., 1981, PhysRevD, 23, 347

Haardt F., Madau P., 2012, ApJ, 746, 125

Hahn O., Abel T., 2011, MNRAS, 415, 2101

Hansen S. M., Sheldon E. S., Wechsler R. H., Koester B. P., 2009, ApJ, 699, 1333

Hao C. N., Kennicutt R. C., Johnson B. D., Calzetti D., Dale D. A., Moustakas J., 2011, ApJ, 741, 124

Harris C. R., et al., 2020, Nature, 585, 357

Hayes M., et al., 2013, ApJL, 765, L27

Heintz K. E., et al., 2024, arXiv:2407.06287

Helmi A., 2008, A&ARv, 15, 145

Henriques B. M., White S. D., Thomas P. A., Angulo R., Guo Q., Lemson G., Springel V., Overzier R., 2015, MNRAS, 451, 2663

Hernquist L., 1990, ApJ, 356, 359

Herzog G., Benítez-Llambay A., Fumagalli M., 2023, MNRAS, 518, 6305

Hess K. M., Kotulla R., Chen H., Carignan C., Gallagher J. S., Jarrett T. H., Kraan-Korteweg R. C., 2022, A&A, 668, A184

Hill R., Masui K. W., Scott D., 2018, ApSpe, 72, 663

Hlavacek-Larrondo J., et al., 2020, ApJL, 898, L50

Hlavacek-Larrondo J., Li Y., Churazov E., 2022, AGN Feedback in Groups and Clusters of Galaxies. Springer Nature Singapore, doi:10.1007/978-981-16-4544-0_122-1, https://ui.adsabs.harvard.edu/abs/2022hxga.book....5H/abstract

Hockney R., Eastwood J., 1988, Computer Simulation Using Particles. CRC Press, doi:10.1201/9780367806934, https://www.taylorfrancis.com/books/mono/10.1201/9780367806934/computer-simulation-using-particles-hockney-eastwood

Hong W. S., Zhu W., Wang T. R., Yang X., Feng L. L., 2024, MNRAS, 529, 4262

Hopkins P. F., 2015, MNRAS, 450, 53

Hopkins P. F., Quataert E., 2011, MNRAS, 415, 1027

Hopkins P. F., Hernquist L., Cox T. J., Di Matteo T., Robertson B., Springel V., 2006, ApJSS, 163, 1

Hopkins P. F., Quataert E., Murray N., 2012a, MNRAS, 421, 3488

Hopkins P. F., Quataert E., Murray N., 2012b, MNRAS, 421, 3522

Hopkins P. F., Kereš D., Oñorbe J., Faucher-Giguère C. A., Quataert E., Murray N., Bullock J. S., 2014, MNRAS, 445, 581

Hopkins P. F., et al., 2018, MNRAS, 480, 800

Hou M., Li Z., Jones C., Forman W., Su Y., 2021, ApJ, 919, 141

Hou M., et al., 2024, ApJ, 961, 249

Hoyle F., Lyttleton R. A., 1939, Proceedings of the Cambridge Philosophical Society, 35, 405

Hubble E., 1929, PNAS, 15, 168

Hunter J. D., 2007, CSE, 9, 90

Ignesti A., et al., 2022, ApJ, 924, 64

Jáchym P., et al., 2017, ApJ, 839, 114

Johnson R. E., Markevitch M., Wegner G. A., Jones C., Forman W. R., 2010, ApJ, 710, 1776

Joshi G. D., Pillepich A., Nelson D., Marinacci F., Springel V., Rodriguez-Gomez V., Vogelsberger M., Hernquist L., 2020, MNRAS, 496, 2673

Joshi G. D., Pillepich A., Nelson D., Zinger E., Marinacci F., Springel V., Vogelsberger M., Hernquist L., 2021, MNRAS, 508, 1652

Jung S. L., Choi H., Wong O. I., Kimm T., Chung A., Yi S. K., 2018, ApJ, 865, 156

Kaiser N., Squires G., 1993, ApJ, 404, 441

Kannan R., Garaldi E., Smith A., Pakmor R., Springel V., Vogelsberger M., Hernquist L., 2022, MNRAS, 511, 4005

Katz N., Gunn J. E., Katz N., Gunn J. E., 1991, ApJ, 377, 365
Katz N., Hernquist L., Weinberg D. H., 1992, ApJL, 399, L109
Katz H., et al., 2023, OJAp, 6, 44
Kauffmann G., White S. D. M., Guiderdoni B., Kauffmann G., White S. D. M., Guiderdoni B., 1993, MNRAS, 264, 201
Kawata D., Mulchaey J. S., 2008, ApJ, 672, L103
Kelvin W. T., 1884, Baltimore lectures on molecular dynamics and the wave theory of light, founded on Mr. A. S. Hathaway's stenographic report of twenty lectures delivered in Johns Hopkins university, Baltimore, in October 1884: followed by twelve appendices on allied subjects by Lord Kelvin. 1904, London, C.J. Clay and Sons, London
Kenney J. D. P., van Gorkom J. H., Vollmer B., 2004, AJ, 127, 3361
Kennicutt Jr. R. C., 1998, ApJ, 498, 541
Kennicutt R. C., Evans N. J., 2012, ARAA, 50, 531
Kereš D., Katz N., Weinberg D. H., Davé R., 2005, MNRAS, 363, 2
Kereš D., Katz N., Fardal M., Davé R., Weinberg D. H., 2009, MNRAS, 395, 160
King R. I., 1972, ApJL, 174, L123
Klessen R. S., Glover S. C., 2023, ARAA, 61, 65
Kluyver T., et al., 2016, in Positioning and Power in Academic Publishing: Players, Agents and Agendas - Proceedings of the 20th International Conference on Electronic Publishing, ELPUB 2016. IOS Press, pp 87–90, doi:10.3233/978-1-61499-649-1-87, https://ebooks.iospress.nl/doi/10.3233/978-1-61499-649-1-87
Klypin A. A., Shandarin S. F., 1983, MNRAS, 204, 891
Klypin A., Kravtsov A. V., Valenzuela O., Prada F., 1999, ApJ, 522, 82
Kormendy J., Ho L. C., 2013, ARAA, 51, 511
Koudmani S., Sijacki D., Smith M. C., 2022, MNRAS, 516, 2112
Kraft R., et al., 2022, arXiv:2211.09827
Krishnarao D., et al., 2022, Nature, 609, 915
Kroupa P., 2001, MNRAS, 322, 231
Kuchner U., et al., 2022, MNRAS, 510, 581
Kukstas E., et al., 2022, MNRAS, 518, 4782
Kulier A., et al., 2023, ApJ, 954, 177
Lacey C. G., et al., 2016, MNRAS, 462, 3854
Lagos C. d. P., Tobar R. J., Robotham A. S., Obreschkow D., Mitchell P. D., Power C., Elahi P. J., 2018, MNRAS, 481, 3573
Lanzetta K. M., Bowen D. V., Tytler D., Webb J. K., Lanzetta K. M., Bowen D. V., Tytler D., Webb J. K., 1995, ApJ, 442, 538

Larson R. B., 1974, MNRAS, 169, 229
Larson R. B., Tinsley B. M., Caldwell C. N., Larson R. B., Tinsley B. M., Caldwell C. N., 1980, ApJ, 237, 692
Lea S. M., Silk J., Kellogg E., Murray S., Lea S. M., Silk J., Kellogg E., Murray S., 1973, ApJL, 184, L105
Leavitt H. S., Pickering E. C., 1912, HarCi, 173, 1
Leclercq F., et al., 2022, A&A, 663, A11
Lee J., Kimm T., Katz H., Rosdahl J., Devriendt J., Slyz A., 2020, ApJ, 905, 31
Lee S., Sheen Y. K., Yoon H., Jaffé Y., Chung A., 2022a, MNRAS, 517, 2912
Lee J., Kimm T., Blaizot J., Katz H., Lee W., Sheen Y.-K., Devriendt J., Slyz A., 2022b, ApJ, 928, 144
Lee W., Pillepich A., Zuhone J., Nelson D., Jee M. J., Nagai D., Finner K., 2024, A&A, 686, A55
Lehle K., Nelson D., Pillepich A., Truong N., Rohr E., 2024, A&A, 687, A129
Lemaître G., 1927, ASSB, 47, 49
Li Y., Bryan G. L., 2014, ApJ, 789, 153
Li Z., Hopkins P. F., Squire J., Hummels C., 2020, MNRAS, 492, 1841
Li H., Wang H., Mo H. J., Wang Y., Luo X., Li R., 2023, ApJ, 942, 44
Linde A. D., 1982, PhLB, 108, 389
Lora V., et al., 2024, ApJ, 969, 24
Lucchini S., D'Onghia E., Fox A. J., Bustard C., Bland-Hawthorn J., Zweibel E., 2020, Nature, 585, 203
Lucy L. B., 1977, AJ, 82, 1013
Lyke B. W., et al., 2020, ApJSS, 250, 8
Magorrian J., et al., 1998, ApJ, 115, 2285
Maier C., Ziegler B. L., Haines C. P., Smith G. P., 2019a, A&A, 621, A131
Maier C., Hayashi M., Ziegler B. L., Kodama T., 2019b, A&A, 626, A14
Maier C., Haines C. P., Ziegler B. L., 2022, A&A, 658, A190
Mandelker N., Dokkum P. G. v., Brodie J. P., Bosch F. C. v. d., Ceverino D., 2018, ApJ, 861, 148
Marinacci F., Vogelsberger M., Mocz P., Pakmor R., 2015, MNRAS, 453, 3999
Marinacci F., et al., 2018, MNRAS, 480, 5113
Markevitch M., et al., 2000, ApJ, 541, 542
Martín-Navarro I., Pillepich A., Nelson D., Rodriguez-Gomez V., Donnari M., Hernquist L., Springel V., 2021, Nature, 594, 187
Matsuda Y., et al., 2012, MNRAS, 425, 878

McCarthy I. G., Balogh M. L., Babul A., Poole G. B., Horner D. J., 2004, ApJ, 613, 811
McCarthy I. G., Frenk C. S., Font A. S., Lacey C. G., Bower R. G., Mitchell N. L., Balogh M. L., Theuns T., 2008, MNRAS, 383, 593
McCourt M., Sharma P., Quataert E., Parrish I. J., 2012, MNRAS, 419, 3319
McGee S. L., Balogh M. L., Bower R. G., Font A. S., McCarthy I. G., 2009, MNRAS, 400, 937
McGee S. L., Bower R. G., Balogh M. L., 2014, MNRAS, 442, L105
McNamara B. R., O'Connell R. W., 1989, AJ, 98, 2018
McNamara B. R., Bregman J. N., O'Connell R. W., McNamara B. R., Bregman J. N., O'Connell R. W., 1990, ApJ, 360, 20
McNamara B. R., et al., 2014, ApJ, 785, 44
McPartland C., Ebeling H., Roediger E., Blumenthal K., 2016, MNRAS, 455, 2994
Merritt D., 1995, AJ, 111, 2462
Mishra S., Muzahid S., 2022, ApJ, 933, 229
Mistani P. A., et al., 2016, MNRAS, 455, 2323
Mitchell P. D., Schaye J., Bower R. G., 2020, MNRAS, 497, 4495
Mo H. J., Mao S., White S. D., 1998, MNRAS, 295, 319
Monaghan J. J., 1992, ARA&A, 30, 543
Moore B., Katz N., Lake G., Dressler A., Oemler A., 1996, Nature, 379, 613
Moore B., Lake G., Katz N., 1998, ApJ, 495, 139
Moore B., Ghigna S., Governato F., Lake G., Quinn T., Stadel J., Tozzi P., 1999, ApJ, 524, L19
Moster B. P., Naab T., White S. D., 2013, MNRAS, 428, 3121
Mroczkowski T., et al., 2019, SSRv, 215, 17
Müller A., Ignesti A., Poggianti B., Moretti A., Ramatsoku M., Dettmar R.-J., 2021, Galaxies, 9, 116
Murphy E. J., et al., 2011, ApJ, 737, 67
Naab T., Ostriker J. P., 2017, ARAA, 55, 59
Naiman J. P., et al., 2018, MNRAS, 477, 1206
Navarro J. F., Frenk C. S., White S. D. M., 1996, ApJ, 462, 563
Nelson D., Vogelsberger M., Genel S., Sijacki D., Kereš D., Springel V., Hernquist L., 2013, MNRAS, 429, 3353
Nelson D., Genel S., Vogelsberger M., Springel V., Sijacki D., Torrey P., Hernquist L., 2015, MNRAS, 448, 59
Nelson D., Genel S., Pillepich A., Vogelsberger M., Springel V., Hernquist L., 2016, MNRAS, 460, 2881
Nelson D., et al., 2018a, MNRAS, 475, 624

Nelson D., et al., 2018b, MNRAS, 477, 450
Nelson D., et al., 2019a, ComAC, 6, 1
Nelson D., et al., 2019b, MNRAS, 490, 3234
Nelson D., et al., 2020, MNRAS, 498, 2391
Nelson D., Byrohl C., Peroux C., Rubin K. H., Burchett J. N., 2021, MNRAS, 507, 4445
Nelson D., et al., 2023, MNRAS, 522, 3665
Nelson D., Pillepich A., Ayromlou M., Lee W., Lehle K., Rohr E., Truong N., 2024, A&A, 686, A157
Nulsen P. E. J., 1982, MNRAS, 198, 1007
Ocvirk P., et al., 2020, MNRAS, 496, 4087
Olivares V., et al., 2019, A&A, 631, A22
Oman K. A., Bahé Y. M., Healy J., Hess K. M., Hudson M. J., Verheijen M. A., 2021, MNRAS, 501, 5073
Omoruyi O., et al., 2024, ApJ, 963, 1
Oort J., 1940, ApJ, pp 91–273
Ostriker J. P., Peebles P. J. E., Yahil A., 1974, ApJL, 193, L1
Pakmor R., Springel V., 2013, MNRAS, 432, 176
Pakmor R., Bauer A., Springel V., 2011, MNRAS, 418, 1392
Pakmor R., Pfrommer C., Simpson C. M., Springel V., 2016, ApJL, 824, L30
Pakmor R., et al., 2017, MNRAS, 469, 3185
Pakmor R., et al., 2023, MNRAS, 524, 2539
Pallero D., Gómez F. A., Padilla N. D., Bahé Y. M., Vega-Martínez C. A., Torres-Flores S., 2022, MNRAS, 511, 3210
Pasquali A., Gallazzi A., van den Bosch F. C., 2012, MNRAS, 425, 273
Peebles P. J. E., 1969, ApJ, 155, 393
Peebles P. J. E., 1982, ApJL, 263, L1
Peeples M. S., et al., 2019, ApJ, 873, 129
Peluso G., et al., 2022, ApJ, 927, 130
Peng Y.-j., et al., 2010, ApJ, 721, 193
Peng Y. J., Lilly S. J., Renzini A., Carollo M., 2012, ApJ, 757, 4
Perlmutter S., et al., 1999, ApJ, 517, 565
Péroux C., Howk J. C., 2020, ARAA, 58, 363
Péroux C., Nelson D., Van De Voort F., Pillepich A., Marinacci F., Vogelsberger M., Hernquist L., 2020, MNRAS, 499, 2462
Pillepich A., Porciani C., Reiprich T. H., 2012, MNRAS, 422, 44
Pillepich A., et al., 2018a, MNRAS, 473, 4077

Pillepich A., et al., 2018b, MNRAS, 475, 648
Pillepich A., Reiprich T. H., Porciani C., Borm K., Merloni A., 2018c, MNRAS, 481, 613
Pillepich A., et al., 2019, MNRAS, 490, 3196
Pillepich A., Nelson D., Truong N., Weinberger R., Martin-Navarro I., Springel V., Faber S. M., Hernquist L., 2021, MNRAS, 508, 4667
Planck Collaboration et al., 2016, A&A, 594, A13
Planck Collaboration et al., 2020, A&A, 641, A1
Poggianti B. M., Smail I., Dressler A., Couch W. J., Barger A. J., Butcher H., Ellis R. S., Oemler Jr. A., 1999, ApJ, 518, 576
Poggianti B. M., et al., 2017a, Nature, 548, 304
Poggianti B. M., et al., 2017b, ApJ, 844, 48
Poggianti B. M., et al., 2019, ApJ, 887, 155
Pratt G. W., Croston J. H., Arnaud M., Böhringer H., 2009, A&A, 498, 361
Predehl P., Nandra K., Collaboration E., 2012, in Half a Century of X-ray Astronomy, Proceedings of the conference held 17-21 September, 2012 in Mykonos Island, Greece. Online at http://www.astro.noa.gr/xcosmo/, id.96. p. 96, https://ui.adsabs.harvard.edu/abs/2012hcxa.confE..96P/abstract
Presotto V., et al., 2012, A&A, 539, A55
Press W. H., Schechter P., 1974, ApJ, 187, 425
Prochaska J. X., Hennawi J. F., Simcoe R. A., 2013, ApJL, 762, L19
Puchwein E., Springel V., Sijacki D., Dolag K., 2010, MNRAS, 406, 936
Qiu Y., Bogdanović T., Li Y., Park K., Wise J. H., 2019, ApJ, 877, 47
Rahmati A., Pawlik A. H., Raičevic M., Schaye J., 2013, MNRAS, 430, 2427
Rahmati A., Schaye J., Bower R. G., Crain R. A., Furlong M., Schaller M., Theuns T., 2015, MNRAS, 452, 2034
Ramesh R., Nelson D., Pillepich A., 2023a, MNRAS, 518, 5754
Ramesh R., Nelson D., Pillepich A., 2023b, MNRAS, 522, 1535
Ramesh R., Nelson D., Ramesh R., Nelson D., 2024, MNRAS, 528, 3320
Rees M. J., Ostriker J. P., 1977, MNRAS, 179, 541
Rennehan D., 2024, arXiv:2406.06672
Rieder M., Teyssier R., 2016, MNRAS, 457, 1722
Riess A. G., Press W. H., Kirshner R. P., Riess A. G., Press W. H., Kirshner R. P., 1995, ApJL, 438, L17
Riess A. G., et al., 1998, AJ, 116, 1009
Roberts I. D., Parker L. C., 2020, MNRAS, 495, 554

Roberts I. D., Parker L. C., Brown T., Joshi G. D., Hlavacek-Larrondo J., Wadsley J., 2019, ApJ, 873, 42
Roberts I. D., et al., 2021a, A&A, 650, A111
Roberts I. D., Van Weeren R. J., McGee S. L., Botteon A., Ignesti A., Rottgering H. J., 2021b, A&A, 652, A153
Roberts I. D., Van Weeren R. J., Timmerman R., Botteon A., Gendron-Marsolais M., Ignesti A., Rottgering H. J., 2022a, A&A, 658, A44
Roberts I. D., et al., 2022b, ApJ, 941, 77
Rodriguez-Gomez V., et al., 2015, MNRAS, 449, 49
Rodríguez S., Garcia Lambas D., Padilla N. D., Tissera P., Bignone L., Dominguez-Tenreiro R., Gonzalez R., Pedrosa S., 2022, MNRAS, 514, 6157
Rohr E., Pillepich A., Nelson D., Zinger E., Joshi G. D., Ayromlou M., 2023, MNRAS, 524, 3502
Rohr E., Pillepich A., Nelson D., Ayromlou M., Zinger E., 2024, A&A, 686, A86
Roman-Oliveira F. V., Chies-Santos A. L., del Pino B. R., Aragón-Salamanca A., Gray M. E., Bamford S. P., 2018, MNRAS, 484, 892
Rosdahl J., et al., 2018, MNRAS, 479, 994
Roy M., Su K. Y., Tonnesen S., Fielding D. B., Faucher-Giguère C. A., 2024, MNRAS, 527, 265
Rubin V. C., Ford W. Kent J., 1970, ApJ, 159, 379
Russell H. R., et al., 2019, MNRAS, 490, 3025
Saeedzadeh V., et al., 2023, MNRAS, 525, 5677
Salome P., et al., 2006, A&A, 454, 437
Samuel J., Pardasani B., Wetzel A., Santistevan I., Boylan-Kolchin M., Moreno J., Faucher-Giguère C. A., 2023, MNRAS, 525, 3849
Sarazin C. L., 1986, RvMP, 58, 1
Sarazin C. L., 2002, ASSL, 272, 1
Scannapieco C., et al., 2012, MNRAS, 423, 1726
Schaefer A. L., et al., 2017, MNRAS, 464, 121
Schaefer A. L., et al., 2019, MNRAS, 483, 2851
Schaller M., Gonnet P., Chalk A. B., Draper P. W., 2016, PASCC, p. 2
Schawinski K., Thomas D., Sarzi M., Maraston C., Kaviraj S., Joo S. J., Yi S. K., Silk J., 2007, MNRAS, 382, 1415
Schaye J., et al., 2015, MNRAS, 446, 521
Schaye J., et al., 2023, MNRAS, 526, 4978
Schmidt M., 1959, ApJ, 129, 243

Schuecker P., Böhringer H., Reiprich T. H., Feretti L., 2001, A&A, 378, 408
Setton D. J., Besla G., Patel E., Hummels C., Zheng Y., Schneider E., Salem M., 2023, ApJL, 959, L11
Sharma P., Mccourt M., Quataert E., Parrish I. J., 2012a, MNRAS, 420, 3174
Sharma P., McCourt M., Parrish I. J., Quataert E., 2012b, MNRAS, 427, 1219
Shimwell T. W., et al., 2017, A&A, 598, A104
Sijacki D., Springel V., Di Matteo T., Hernquist L., 2007, MNRAS, 380, 877
Sijacki D., Vogelsberger M., Genel S., Springel V., Torrey P., Snyder G. F., Nelson D., Hernquist L., 2015, MNRAS, 452, 575
Silk J., 1977, ApJ, 211, 638
Silk J., Rees M. J., 1998, A&A, 331, L1
Simionescu A., et al., 2019, SSRv, 215, 1
Smith R. K., Brickhouse N. S., Liedahl D. A., Raymond J. C., 2001, ApJL, 556, L91
Smith B., Sigurdsson S., Abel T., 2008, MNRAS, 385, 1443
Smith R. J., et al., 2010, MNRAS, 408, 1417
Smith M. C., Sijacki D., Shen S., 2018, MNRAS, 478, 302
Smith M. C., Bryan G. L., Somerville R. S., Hu C. Y., Teyssier R., Burkhart B., Hernquist L., 2021, MNRAS, 506, 3882
Smith R., et al., 2022, ApJ, 934, 86
Somerville R. S., Davé R., 2015, ARAA, 53, 51
Somerville R. S., Hopkins P. F., Cox T. J., Robertson B. E., Hernquist L., 2008, MNRAS, 391, 481
Sparre M., Pfrommer C., Ehlert K., 2020, MNRAS, 499, 4261
Sparre M., Pfrommer C., Puchwein E., 2024, MNRAS, 527, 5829
Springel V., 2005, MNRAS, 364, 1105
Springel V., 2010a, ARA&A, 48, 391
Springel V., 2010b, MNRAS, 401, 791
Springel V., Hernquist L., 2003, MNRAS, 339, 289
Springel V., Hernquist L., 2005, ApJL, 622, L9
Springel V., Yoshida N., White S. D., 2001, New Astronomy, 6, 79
Springel V., Di Matteo T., Hernquist L., 2005a, MNRAS, 361, 776
Springel V., et al., 2005b, Nature, 435, 629
Springel V., Frenk C. S., White S. D., 2006, Nature, 440, 1137
Springel V., et al., 2018, MNRAS, 475, 676
Springel V., Pakmor R., Zier O., Reinecke M., 2021, MNRAS, 506, 2871
Starobinsky A. A., 1982, PhLB, 117, 175

Steidel C. C., Adelberger K. L., Shapley A. E., Pettini M., Dickinson M., Giavalisco M., 2000, ApJ, 532, 170
Stevens A. R. H., et al., 2019, MNRAS, 483, 5334
Stevens A. R. H., et al., 2021, MNRAS, 502, 3158
Strateva I., et al., 2001, ApJ, 122, 1861
Sun M., Jones C., Forman W., Nulsen P. E. J., Donahue M., Voit G. M., 2006, ApJL, 637, L81
Sun M., Jones C., Forman W., Vikhlinin A., Donahue M., Voit M., 2007, ApJ, 657, 197
Sun M., Donahue M., Roediger E., Nulsen P. E., Voit G. M., Sarazin C., Forman W., Jones C., 2009, ApJ, 708, 946
Sutherland R. S., Dopita M. A., 1993, ApJS, 88, 253
Terrazas B. A., et al., 2020, MNRAS, 493, 1888
Teyssier R., 2002, A&A, 385, 337
Thomas P. A., Couchman H. M., 1992, MNRAS, 257, 11
Tonnesen S., Bryan G. L., 2009, ApJ, 694, 789
Toomre A., Toomre J., Toomre A., Toomre J., 1972, ApJ, 178, 623
Torrey P., et al., 2019, MNRAS, 484, 5587
Tozzi P., et al., 2022, A&A, 662, A54
Truong N., et al., 2020, MNRAS, 494, 549
Truong N., Pillepich A., Nelson D., Werner N., Hernquist L., 2021, MNRAS, 508, 1563
Truong N., Pillepich A., Nelson D., Zhuravleva I., Lee W., Ayromlou M., Lehle K., 2024, A&A, 686, A200
Tully R. B., Fisher J. R., 1977, A&A, 54, 661
Tumlinson J., Peeples M. S., Werk J. K., 2017, ARAA, 55, 389
Uhlig M., Pfrommer C., Sharma M., Nath B. B., Enßlin T. A., Springel V., 2012, MNRAS, 423, 2374
Van Der Walt S., Colbert S. C., Varoquaux G., 2011, CSE, 13, 22
Vikhlinin A., Markevitch M., Murray S. S., 2001, ApJ, 551, 160
Vikhlinin A., et al., 2009, ApJ, 692, 1033
Villumsen J. V., 1989, ApJSS, 71, 407
Virtanen P., et al., 2020, Nature Methods, 17, 261
Vogelsberger M., Genel S., Sijacki D., Torrey P., Springel V., Hernquist L., 2013, MNRAS, 436, 3031
Vogelsberger M., et al., 2014a, MNRAS, 444, 1518
Vogelsberger M., et al., 2014b, Nature, 509, 177
Vogelsberger M., et al., 2018, MNRAS, 474, 2073

Vogelsberger M., Marinacci F., Torrey P., Puchwein E., 2020, NatRP, 2, 42
Voit G. M., 2005, RvMP, 77, 207
Voit G. M., 2021, ApJL, 908, L16
Voit G. M., Balogh M. L., Bower R. G., Lacey C. G., Bryan G. L., 2003, ApJ, 593, 272
Voit G. M., Donahue M., Bryan G. L., McDonald M., 2015, Nature, 519, 203
Voit G. M., Meece G., Li Y., O'Shea B. W., Bryan G. L., Donahue M., 2017, ApJ, 845, 80
Voit G. M., Oppenheimer B. D., Bell E. F., Terrazas B., Donahue M., 2024, ApJ, 960, 28
Vollmer B., Cayatte V., Balkowski C., Duschl W. J., 2001, ApJ, 561, 708
Vulcani B., et al., 2018, ApJ, 866, L25
Vulcani B., et al., 2020, ApJ, 892, 146
Vulcani B., et al., 2024, A&A, 682, A117
Wakker B., Howk J. C., Chu Y.-H., Bomans D., Points S. D., 1998, ApJ, 499, L87
Wang B., 2022, MNRAS, 516, 4293
Wang D., Lagos C. D., Croom S. M., Wright R. J., Bahe Y. M., Bryant J. J., Van De Sande J., Vaughan S. P., 2023, MNRAS, 523, 6020
Warmels R. H., Warmels H. R., 1988a, A&AS, 72, 19
Warmels R. H., Warmels H. R., 1988b, A&AS, 72, 427
Webb T. M. A., et al., 2015, ApJ, 814, 96
Wechsler R. H., Tinker J. L., 2018, ARAA, 56, 435
Weinberger R., et al., 2017, MNRAS, 465, 3291
Weinberger R., et al., 2018, MNRAS, 479, 4056
Weinberger R., Springel V., Pakmor R., 2020, ApJSS, 248, 32
Wen Z. L., Han J. L., 2015, ApJ, 807, 178
Weng S., Péroux C., Ramesh R., Nelson D., Sadler E. M., Zwaan M., Bollo V., Casavecchia B., 2024, MNRAS, 527, 3494
Werle A., et al., 2022, ApJ, 930, 43
Wetzel A. R., Tinker J. L., Conroy C., 2012, MNRAS, 424, 232
Wetzel A. R., Tinker J. L., Conroy C., van den Bosch F. C., 2013, MNRAS, 432, 336
White S. D. M., Rees M. J., 1978, MNRAS, 183, 341
White S. D. M., Frenk C. S., Davis M., Efstathiou G., 1987, ApJ, 313, 505
Wiersma R. P., Schaye J., Smith B. D., 2009a, MNRAS, 393, 99
Wiersma R. P., Schaye J., Theuns T., Dalla Vecchia C., Tornatore L., 2009b, MNRAS, 399, 574
Winkel N., Pasquali A., Kraljic K., Smith R., Gallazzi A., Jackson T. M., 2021, MNRAS, 505, 4920

Wright R. J., Lagos C. D. P., Davies L. J., Power C., Trayford J. W., Ivy Wong O., 2019, MNRAS, 487, 3740

Wright R. J., Lagos C. d. P., Power C., Mitchell P. D., 2020, MNRAS, 498, 1668

Wright R. J., Lagos C. d. P., Power C., Stevens A. R., Cortese L., Poulton R. J., 2022, MNRAS, 516, 2891

Wright R. J., Somerville R. S., Lagos C. D. P., Schaller M., Davé R., Anglés-Alcázar D., Genel S., 2024, MNRAS, 532, 3417

York D. G., et al., 2000, AJ, 120, 1579

Yun K., et al., 2019, MNRAS, 483, 1042

Zel'dovich Y. B., 1970, A&A, 5, 84

Zhang H., Zaritsky D., Behroozi P., Werk J., 2019, ApJ, 880, 28

Zhang Y., et al., 2024, arXiv:2401.17308

Zhu J., Tonnesen S., Bryan G. L., 2024, ApJ, 960, 54

Zinger E., Dekel A., Birnboim Y., Kravtsov A., Nagai D., 2016, MNRAS, 461, 412

Zinger E., Dekel A., Kravtsov A. V., Nagai D., Zinger E., Dekel A., Kravtsov A. V., Nagai D., 2018a, MNRAS, 475, 3654

Zinger E., Dekel A., Birnboim Y., Nagai D., Lau E., Kravtsov A. V., 2018b, MNRAS, 476, 56

Zinger E., et al., 2020, MNRAS, 499, 768

Zinger E., Joshi G. D., Pillepich A., Rohr E., Nelson D., 2024, MNRAS, 527, 8257

Zoldan A., De Lucia G., Xie L., Fontanot F., Hirschmann M., 2017, MNRAS, 465, 2236

Zou H., et al., 2021, ApJSS, 253, 56

Zwicky F., 1933, Helvetica Physica Acta, 6, 110

de Vaucouleurs G., 1961, ApJS, 5, 233

van de Voort F., Schaye J., Booth C. M., Haas M. R., Dalla Vecchia C., 2011, MNRAS, 414, 2458

van de Voort F., Bahé Y. M., Bower R. G., Correa C. A., Crain R. A., Schaye J., Theuns T., 2017, MNRAS, 466, 3460